Advanced Gas Turbine

AGT

Technology Project

DOE/NASA/0168-9
NASA CR-175018
EDR 12070

1984 Annual Report

Allison
GAS TURBINE DIVISION
General Motors Corporation
P.O. Box 420
Indianapolis, Indiana 46206-0420

June 1985

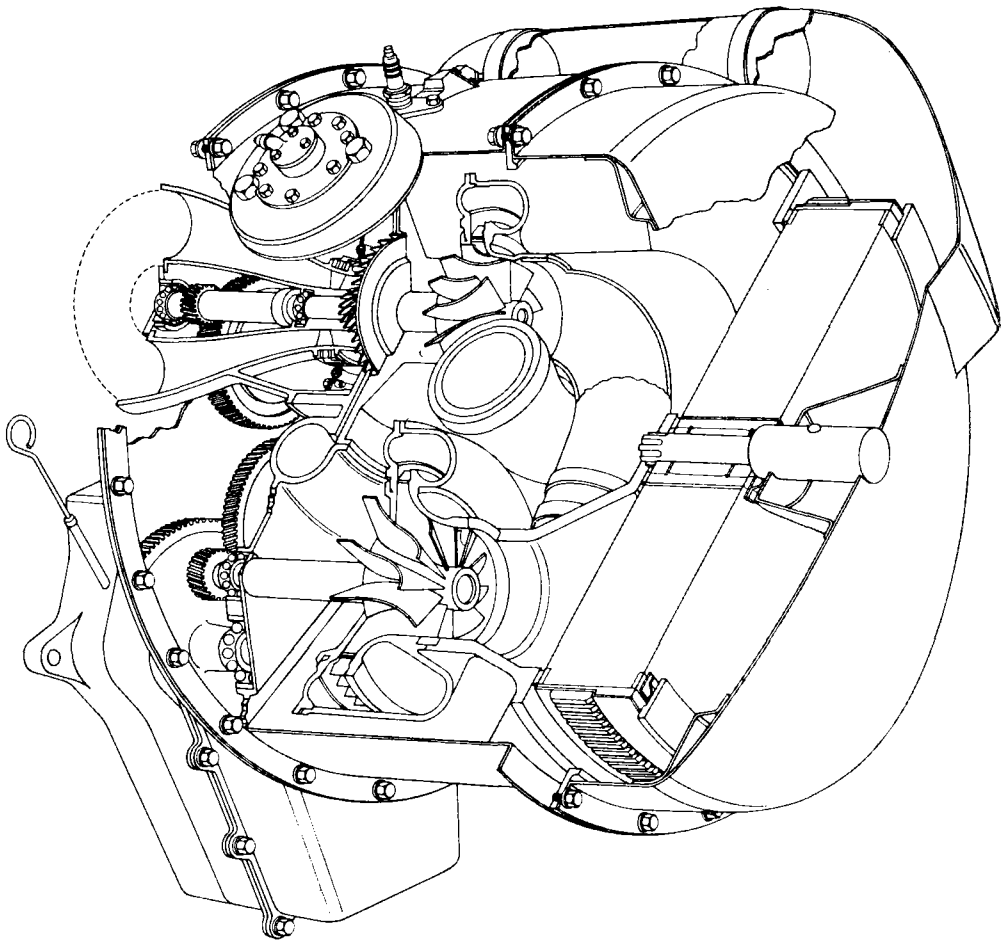

Prepared for
National Aeronautics
and Space Administration
Lewis Research Center
Cleveland, Ohio 44135
Contract DEN 3-168

For U. S. Department of Energy
Conservation and Renewable Energy
Office of Transportation Systems

NOTICE

DOE/NASA/0168-9
NASA CR-175018

EDR12070

Advanced Gas Turbine
AGT
Technology Project

1984 Annual Report

Allison Gas Turbine Division
General Motors Corporation
Indianapolis, Indiana 46206-0420

June 1985

Prepared for
NATIONAL AERONAUTICS AND SPACE ADMINISTRATION
Lewis Research Center
Under Contract DEN 3-168

for
U.S. Department of Energy
Conservation and Renewable Energy
Office of Transportation Systems

FOREWORD

This report presents a technical summary of the Allison Gas Turbine project to develop an automotive gas turbine power-train system under NASA Contract DEN 3-168 (Department of Energy funding). The report covers the 1984 calendar year.

The basic objective of this project is to develop the technology base for an advanced automotive gas turbine that will, when installed in a Pontiac Phoenix class vehicle of 1360 kg (3000 lbm) inertia weight, achieve a fuel economy of 18 km/L (42.5 mpg), meet or exceed the Federal emission requirements, and have alternate fuel capability.

Several General Motors Divisions and other companies are major contributors to this effort. They are as follows: Pontiac Motor Division — vehicle and cost studies, Delco Remy Division — starter/boost motor, Corning Glass Works — regenerator, The Carborundum Company and GTE — ceramics.

The Allison Program Manager for the AGT 100 is H. E. (Gene) Helms; design effort is directed by Leonard Lindgren; materials effort is directed by Dr. Peter Heitman; and project effort is directed by Richard Johnson. The Pontiac effort is headed by Leighton Smith. The NASA AGT 100 Project Manager is Paul T. Kerwin.

TABLE OF CONTENTS

*No activity this period

TABLE OF CONTENTS (cont)

*No activity this period

LIST OF ILLUSTRATIONS

LIST OF ILLUSTRATIONS (cont)

LIST OF ILLUSTRATIONS (cont)

LIST OF ILLUSTRATIONS (cont)

LIST OF TABLES

SUMMARY

Engine testing, ceramic component fabrication and evaluation, component performance rig testing, and producibility experiments at Pontiac highlighted AGT 100 activities of the past year. The technical challenges remain great; however, progress was witnessed in all areas.

Engine testing saw much activity, and significant accomplishments were recorded. Two experimental engines were available and allowed the evaluation of eight experimental assemblies (builds). Operating time accumulated was 115 hr of burning and 156 hr total. Total cumulative engine operating time is now 225 hr. Build numbers 11 and 12 of engine S/N 1 totaled 28 burning hours and constituted a single assembly of the engine core — the compressor, both turbines, and the gearbox. Build number 11 of engine S/N 1 included a 1:07 hr continuous test at 100% gasifier speed (86,000 rpm). The combustor main fuel nozzle has, on occasion, performed erratically due to coking of DF-2 individual delivery tubes. Build number 8 of engine S/N 2 was the first engine test with a ceramic turbine rotor. Posttest inspection revealed failed blade tips. The rotor hub and the rotor/shaft attachment were intact.

Engine testing has shown most design modifications to be effective, and continues to be absent of any major failures. A mechanical loss test of an engine assembly revealed the actual losses to be near the original design allowance. Engine testing included mapping of the combustion system operating range. Builds subsequent to number 11 of S/N 1 experienced case vibration and shaft displacement (whip) levels high enough to prevent operation to rated speed. The ceramic combustor case and regenerator disk and bulkhead continue to operate satisfactorily in the engine, and turbine vanes and piston rings have been added to the list of successfully engine-tested components.

Component development activity included rig testing of the compressor, combustor, and regenerator. Compressor testing was initiated on a rig modified to control the transfer of heat between flow path, lubricating oil, and structure. Results show successful thermal decoupling of the rig and lubricating/cooling oil. Rig evaluation of a reduced-friction compressor was initiated. Combustor testing covered qualification of ceramic parts for engine use, mapping of operating range limits, and evaluation of a relocated igniter plug. Several seal refinements were tested on the hot regenerator rig. An alternate regenerator disk, extruded MAS, was examined and found to be currently inadequate for the AGT 100 application. Also, a new technique for measuring leakage was explored on the regenerator rig. It is based upon measuring the concentration of a tracer gas ($C0_2$) at two stations. Any change in concentration is due to the dilution produced by inflowing leakage that is either void of or at a grossly different concentration level than the tracer gas.

Ceramic component activity has focused on the development of state-of-the-art material strength characteristics in full-scale hardware. Injection-molded sintered α-SiC rotors were produced at Carborundum in an extensive process and tool optimization study. Correlation of spin-to-burst rotor tests with fracture surface analyses revealed that backface flow and knit-line indications were the frequent cause of rotor bursts at relatively low speeds. A modified fabrication/rework procedure, for both green and sintered rotors, was identified whereby these surface imperfections may be removed. The exploration of injection molded GTE Si_3N_4 rotors included evaluation of 10 hot isostatically pressed (HIP) rotors. Burst testing demonstrated that HIP processing raised burst speed.

Gasifier turbine scroll assemblies, in SiC material, are being fabricated by both Carborundum and Norton. Carborundum units are awaiting hot-rig test; engine test will follow successful rig testing.

Fiber reinforced glass-ceramic composite turbine backplates were fabricated by the Corning Glass Works. Different materials were considered, and evaluation was initiated with room temperature bend testing of test bars.

INTRODUCTION

This is one of a series of annual reports documenting work performed on an Advanced Gas Turbine (AGT) Technology Development Project for automotive applications. The work is being conducted by Allison Gas Turbine Division of General Motors Corporation under NASA/DOE contract DEN-168.

The objectives of the project, as highlighted in Table I, are to develop an experimental power-train system that demonstrates the following: (1) the potential of a combined cycle fuel economy of 18.1 km/L (42.5 mpg) using diesel fuel No. 2 in a 1985 automobile of 1364 kg (3000 lbm) weight on a 15°C (59°F) day, (2) emission levels less than federal standards, and (3) the ability to use a variety of fuels. It is intended that the technology demonstrated through this project would assist the automotive industry in making a go/no-go decision regarding the production engineering development of gas turbine power trains.

In meeting the project objectives, the engine will be designed to accomplish the following, also outlined in Table I: (1) achieve reliability and life comparable to conventional 1985 vehicles, (2) achieve initial and life-cycle power-train costs competitive with 1985 power trains, (3) demonstrate vehicle acceleration suitable for safety and maneuverability, and (4) meet 1985 federal vehicle noise and safety standards.

Initially, the project scope included the fabrication and chassis dynamometer testing of the engine, transmission, and electronic control system installed in a 1985 Pontiac Phoenix passenger car. However, Government funding constraints after the first year made it necessary to reduce the program scope.

Activities eliminated included fabrication and testing of the transmission and vehicle. The electronic control scope was narrowed from that of controlling the engine, transmission, and vehicle to controlling an engine on a dynamometer. Figure 1 depicts the activity areas and schedule for the revised project.

The AGT 100 design was originally matched to the Pontiac Phoenix X-body car, shown in Figure 2. A front-wheel-drive car, it was one of General Motors' advanced passenger cars, emphasizing efficiency of space and weight to combine comfort and function with high fuel economy. The AGT 100 will also fit into the Pontiac A6000, an A-body car that is slightly larger and is the latest GM front-wheel design with potential to replace the X-body car in the Pontiac future marketing of cars. The Fiero, a Pontiac midengine personal car, can be powered by the AGT 100 engine.

The AGT 100, shown in Figures 3 and 4, is a two-shaft, regenerative gas turbine engine. In all respects, this engine design is tailored for high-volume application to fuel-efficient passenger cars. Its two-shaft configuration allows (1) the use of conventional transmissions, manual or automatic, and (2) turbine tip speeds (approximately 503 m/s [1650 ft/sec]) commensurate with available ceramic material properties (strength and variability). Single-shaft configurations were rejected by Allison because of the corresponding requirement for a continuously variable transmission and for approximately 40% higher turbine rotor ceramic material strength (for equal reliability). Careful attention was given to component arrangement for both vehicle installation and management of potentially high heat losses. All hot-section components are grouped together, bounded on one end by the regenerator, on the other end by the gearbox, and enclosed by a well-insulated cylindrical case. High-cycle temperature is possible through the use of ceramic hot-section parts. This, coupled with high aerodynamic component efficiencies, produces low fuel consumption and a 50% improvement in composite miles per gallon (30% energy efficiency improvement). Most important is that the AGT 100 uses existing technologies for shafts, bearings, cases, control system, accessories, etc, and thereby provides a reliable test device for evaluating ceramic and aerodynamic components.

Design goals of fuel economy and vehicle performance are shown in Figures 5 and 6. The fuel economy design goal is 18.1 km/L (42.5 mpg) for a

Table I.
AGT 100 project and design objectives.

Project objectives:	System design objectives:
• 18.1 km/L (42.5 mpg) in 1985 automobile	• comparable reliability and life
• alternate fuels capability	• competitive initial and life-cycle costs
• meet 1985 emission standards	• competitive accelerations
	• meet noise/safety standards

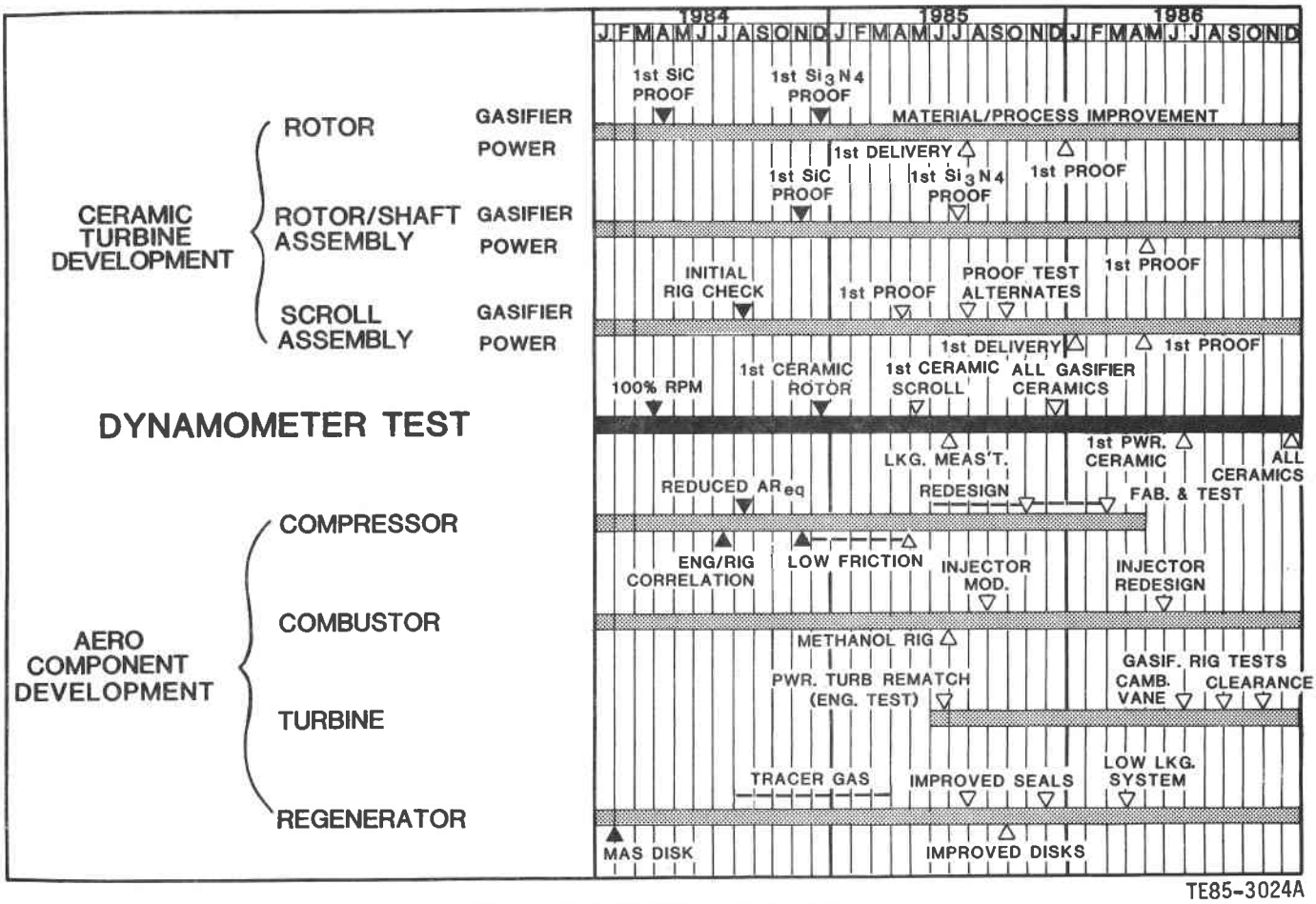

Figure 1. AGT 100 project plan.

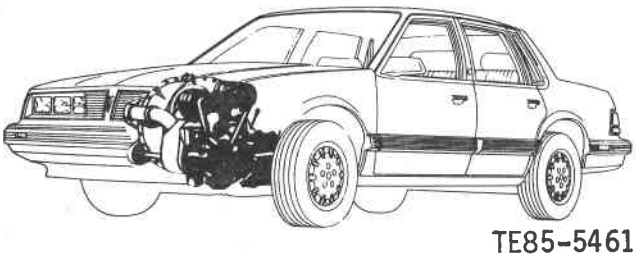

Figure 2. AGT 100 engine in Pontiac A6000.

composite driving cycle comprising a 55-45% mix of urban and highway cycles. Peak roadload fuel economy is over 25.5 km/L (60 mpg) at approximately 56 km/h (35 mph). Average driving cycle velocity is 43 km/h (27 mph). Figure 6 shows the velocity versus time relationship following a wide-open throttle acceleration from stop. The gas turbine powered vehicle is fastest at all except the very early times.

The main development challenges in the program are in building small, high-performance gas turbine components and developing ceramic components for the required high engine cycle temperatures that are

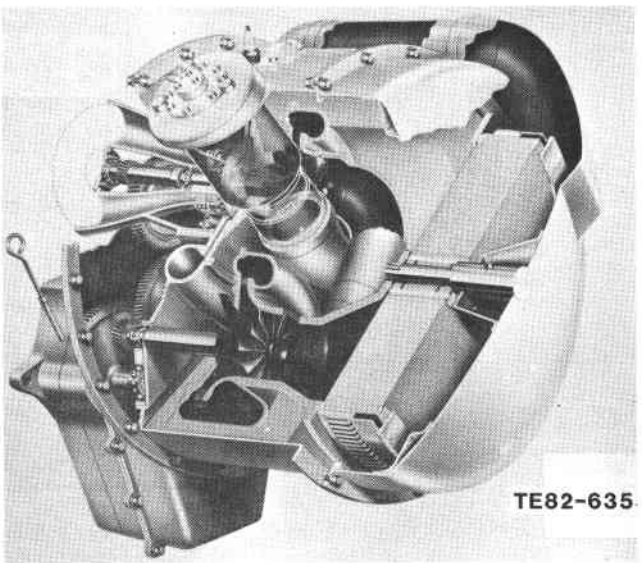

Figure 3. AGT 100 advanced gas turbine engine.

price competitive and can be produced in an automotive production environment. The AGT 100 ceramic components are shown in Figure 7.

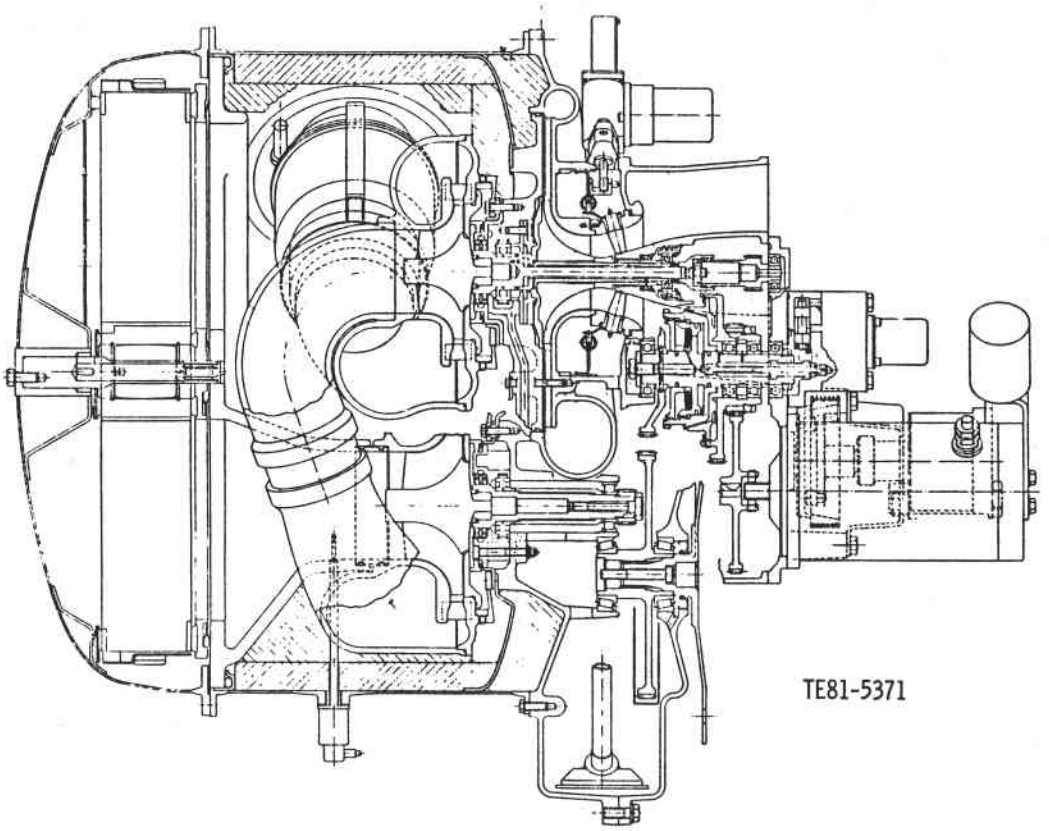

Figure 4. Cross section of AGT 100 gas turbine engine.

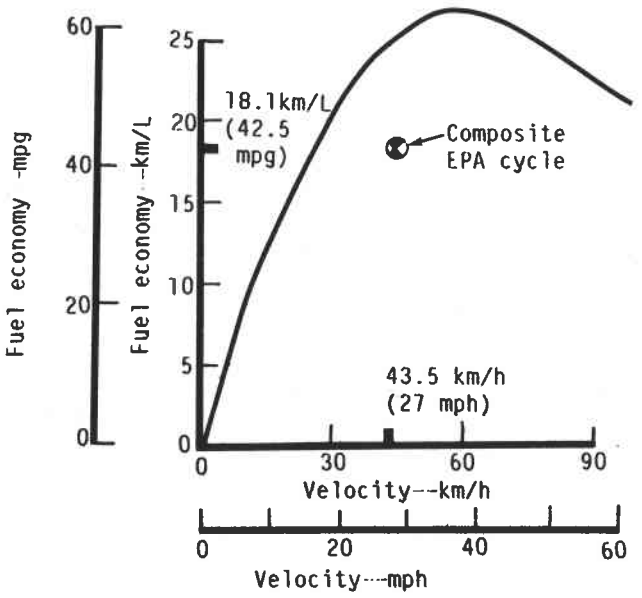

Road-Load
Fuel Economy*

EPA Driving Cycle Fuel Economy*

	km/L	mpg
Urban	15.1	35.5
Highway	23.8	56.0
Composite**	18.1	42.5

*Based on diesel No. 2 fuel and 15°C (59°F) day

**55-45% mix

TE85 3025

Figure 5. Design fuel economy goal for a 1364 kg (3000 lbm) automobile powered by AGT 100 gas turbine.

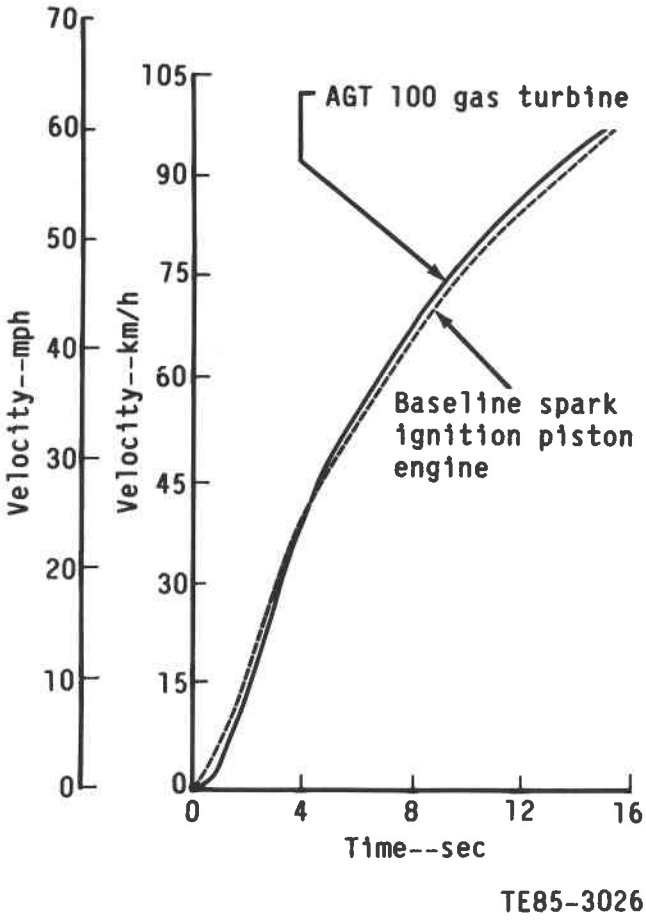

Figure 6. Design goal of vehicle wide-open throttle performance.

Because of the small-size engine (0.35 kg/s [0.76 lbm/sec] airflow), extensive rig testing, outlined in Table II, is being performed in component development. A major ceramic component development program is being pursued, and the ultimate success of the engine depends on the success of this activity.

Mechanical development of the engine is being conducted in two essential phases. The first incorporates early available ceramic components with metal substitutes for those components requiring further development. This phase includes metal turbine rotors and engine operation at 1080°C (1976°F) turbine inlet temperature. The second phase includes engine demonstration of all ceramic component types at 1288°C (2350°F) turbine inlet temperature. The transition from the first to second phase will occur in steps as each new ceramic component becomes available.

A team concept is used in this project, with many of the team members being General Motors divisions. Allison is the prime contractor and team leader with responsibility for the overall power train and controls. Pontiac Motor Division (PMD) has vehicle design and cost analysis responsibility, and Delco Remy will develop the starter/boost system for the engine. The primary non-GM groups on the team are Carborundum Company (CBO), Corning Glass Works (CGW), and GTE Laboratories, Inc (GTE), who are involved in the ceramic effort.

This report is structured on a component basis (e.g., all work relating to the gasifier turbine rotor, including rig work and ceramic rotor development, is

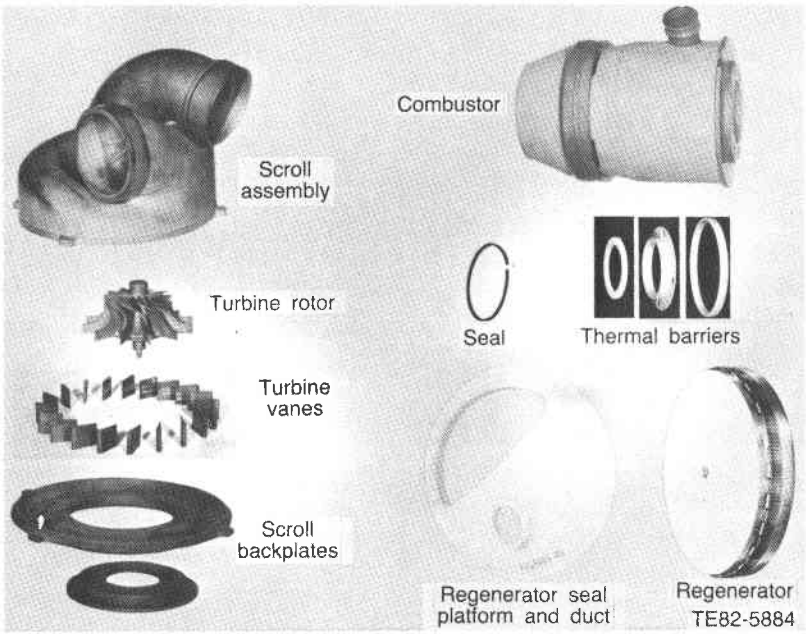

Figure 7. AGT 100 ceramic components.

discussed as a part of the gasifier turbine section). Exceptions to this are functional areas that are not peculiar to any one major component: engine subsystems, cover structures, gearbox and power transfer, rotor bearings, shafts/seals, and secondary flow. There are separate sections for materials development and controls development.

Certain sections are omitted in this report because no effort was expended in those areas. These sections are identified in the Table of Contents to preserve continuity.

Table II.
Aerodynamic component rigs.

Component	Builds	Hours
Compressor	11	419
Combustor	18	193
Turbines		
Gasifier	2	204
Power	1	26
Interturbine duct	3	239
Regenerator		
Cold side flow distribution	8	110
Hot side flow distribution	1	72
Seal leaf leakage	7	70
Hot simulator rig	79	495
Ceramic seal platform	Seven units	40
		1868

II. ENGINE DEVELOPMENT

2.2 EXPERIMENTAL ENGINE

2.2.1 *Fabrication*

No major engine fabrication efforts were initiated this period. However, several projects previously initiated were completed. These included compressor impellers and diffuser, as well as turbine hardware for incorporating an improved gasifier vane shape and a resized power turbine flow capacity.

The engine test program required the replacement of certain consumable parts, replacement of failed parts, parts rework per design modifications, and fabrication of parts to implement new designs.

2.2.2 Experimental Engine Testing

During the previous reporting period, engine serial number 1 (S/N 1) had progressed through Build 10 (BU10), with a total running time of 38:17 hr, including 20:40 hr of burn time. A second engine (S/N 2) had been introduced into the test program, and two builds had been tested for a total running time of 37:59 hr, including 20:39 hr of burn time.

The test program goal during the present reporting period continued to be to identify engine-related mechanical and aerodynamic problems as well as engine component modifications necessary to improve engine operation, durability, and performance. During this current reporting period, engine S/N 1 acquired two additional builds with an additional 33:36 hr (27:45 hr of burning) of running time. Engine S/N 2 added 90:52 hr (66:08 hr of burning) of running time during an additional 6 builds. Total running time on both engines stood at 224:31 hr (156:14 hr of burning) at the end of this reporting period.

Figure 8 graphically displays the burning operating time, in a cumulative manner, for the two experimental engines. Operating time per build is increasing. Builds 11 and 12 of engine S/N 1 shared the same flow-path assembly (compressor, both turbines) and thus had an effective time of 27:45 hr.

Each build configuration and test accomplished in the present reporting period is discussed in the following pages. The tests are reviewed in chronological order. Detailed discussion of the condition of the component parts after test can be found in the report section discussing that component.

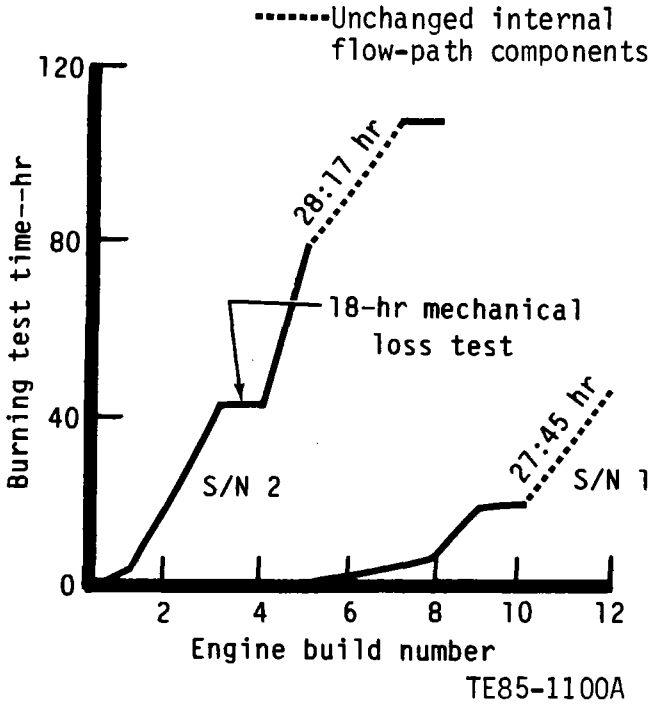

Figure 8. Cumulative burning test hours of AGT 100 experimental engines.

Engine S/N 2 BU3 and Test

The previous test of engine S/N 2 (BU2) revealed that a high pressure existed in the nominally vented insulated cavity between the hot and cold sections of the engine. This indicated excessive leakage at graphite ball seals at the scroll hold down springs. For BU3 those seals were replaced with metal ball seals. Additionally, carbon shaft seals were replaced, a gearbox splitline seal was improved, and the engine was returned to test.

Test time and data were obtained at 60, 70, 80, and 90% synchronous speeds under thermally stabilized conditions. The engine was at 90% speed for 10 minutes, during which time vibration and shaft displacement (whip) increased to undesirable levels. Gasifier shaft displacement, measured at the cold end, rose from 0.102 to 0.292 mm (0.004 to 0.0115 in.) while at speed. Most of this rise occurred at a steady speed of 77,500 rpm. Vibration levels at other positions on the engine reacted in concert.

It was concluded that the gasifier rotor was changing balance, possibly as a result of some degree of rubbing. A test run of the engine was com-

pleted to determine if gasifier shaft displacement had changed at lower speeds. At 60% speed, gasifier whip was 0.104 mm (0.0041 in.) compared with 0.064 mm (0.0025 in.) prior to the 90% speed run. The data implied a permanent balance change and, therefore, no further running was attempted at the higher speeds.

Other data acquired showed success with the replacement of the graphite ball seals with Haynes 188 material at the scroll hold-down locations. On the previous build, air leakage at that point produced 110.3 kPa (16 lb/in.^{2}) gage in the vented cavity between the hot and cold engine sections. Observed pressure seen for this current build did not exceed 6.2 kPa (0.9 lb/in.^{2}) gage.

Engine operation at low speed continued to be satisfactory. Testing continued to add to durability information and to accomplish two more elements of the test schedule. One of these was the initial tryout of the clutch. This test involved locking the clutch with rotor speeds already at nearly synchronous speeds. Clutch actuation oil pressure was controlled manually from the electronic control unit. The clutch was locked at 60% speed with data acquired at 60 and 70% subsequently. No problems were apparent during this exercise. More testing to confirm load carrying capacity and slipping clutch operation will be conducted when operation at higher speeds is routine.

Specific tests were run to determine the thermal effects of normal engine shutdown. All testing to date has involved motoring the engine after shutdown to ensure maintenance of very conservative levels of bearing temperature. Bearing temperature limits were raised for this evaluation to maximum values consistent with long life. Two shutdowns were made from 60% speed, one from 982°C (1800°F) turbine inlet temperature (TIT) and one from 1038°C (1900°F) TIT. The only bearing to reach its limit was the No. 5 bearing at the cold end of the power turbine shaft. A limit here of 204°C (400°F) on the outer race was nearly reached during the 982°C (1800°F) test and was reached on the 1038°C (1900°F) test. No immediate problem is perceived as a result of the test. Further test programs will use less conservative temperature limits than originally used to further explore soakback.

The test program on this build was terminated after the previously discussed testing was completed. Teardown of the engine showed all three seals on the gasifier shaft to be damaged with minor rub on the compressor impeller and turbine rotor. The No. 2 bearing (impeller end) showed distress on the separator. This bearing had been preloaded with an extra shim, probably the source of the separator distress. The seals were damaged by the radial excursion of the rotors due to out of balance forces. After teardown the rotors were reassembled for a balance check. This check confirmed that the rotors were out of balance. Improvements for obtaining and retaining improved balance are under way. This engine build did not incorporate the new viscous vibration damper fabricated for use at the impeller end bearing. This damper is expected to minimize the effect of rotor unbalance.

This build obtained 23:47 hr running time with a burn time of 21:02 hr, for a total on engine S/N 2 of 61:46 hr.

Engine S/N 2 BU4 and Test

Engine S/N 2 BU4 was configured and assembled for mechanical loss test to determine power loss of the gears, bearings, and oil system. Bladeless turbine rotors, together with a simple sleeve to replace the compressor impeller, were used to eliminate aerodynamic loads. Neither the burner nor the regenerator was installed.

Testing was accomplished by driving the gearbox through a torquemeter coupled to the starter shaft, with oil temperatures of 38°C (100°F), 93°C (200°F), and 121°C (250°F), to obtain no-load friction horsepower of the gasifier gear train and the complete gear train. Testing was also performed with the complete gear train loaded by a hydraulic pump at the power output shaft. This load was limited by the power transfer clutch to 10 horsepower.

The mechanical loss was obtained at speeds to 100% on both shafts during early testing; however, at an oil temperature of 121°C (250°F) some increase in vibration and an audible noise occurred at 98-100% speed on the gasifier shaft. This speed was avoided during subsequent power loss determination. A list and discussion of measured losses are provided in Section VIII for both the gasifier-only case and the complete drivetrain (i.e., gasifier plus power turbine). At full speed, actual loss was somewhat higher than estimated. However, at part-speed, where most of the driving cycle time is spent, the measured power loss matches the design estimate.

Testing, in addition to loss measurement, consisted of several runs to identify the engine vibration that occurred at 100% speed when the oil temperature was 102°C (215°F) or higher. Two other oils, a lower viscosity and a higher viscosity, were used to attempt to separate a viscosity effect from a temperature effect. The results were inconclusive in that no vibration occurred with either alternate oil but returned with a return to the original Dexron oil. Testing of the complete engine S/N 1 BU 11 did not experience vibration. It was concluded that the vibration was caused by rotation of the No. 3 outer bearing race in

its aluminum pocket. Plans were formulated to lock that race in position.

This testing on engine S/N 2 added 18:17 hr to the running time. Total time on engine S/N 2 was 80:03 hr.

Engine S/N 1 BU 11 and Test

The previous build (BU10) of engine S/N 1 experienced high vibration. During BU 11 a rotor balance investigation was made. Several iterations of measurement, assembly, and unbalance determination were completed without obtaining satisfactory repeatability of unbalance amount and position. Since it is necessary to disassemble the gasifier rotor after balance correction in order to reassemble into an engine build, repeatability is necessary. A further study of the rotor resulted in parts modification for several dimensional changes to achieve improved fit. A subsequent unbalance repeatability program produced satisfactory results.

Included in this engine build was a new viscous vibration damper, installed at the No. 2 bearing (gasifier shaft impeller end) in place of the spring bar mass isolators at that location. New mass isolator spring bars of improved dimensional accuracy were installed at the turbine end of both the gasifier and power turbine shafts. At the gasifier turbine bearing location, two of the mass isolator spring bars were instrumented with strain gages. These gages were calibrated so that a shaft displacement (whip) signal could be obtained during running. This build also included improved seals at the turbine scroll hold-down rods to prevent excessive leakage into the cavity between hot and cold engine sections. Two gasifier turbine vanes were incorporated into BU10.

Test operation of this build ran through the complete speed range and included 1:07 hr at a gasifier shaft mechanical speed of 100%. Shaft displacement and vibration levels were very low during all test operation. During the 100% speed operation on the gasifier, thermally stabilized data were acquired at power turbine mechanical speeds of 100, 90, 80, and 70%, all with turbine inlet temperatures in the range of 1049°C (1920°F) to 1071°C (1960°F). Data at all speeds, from 60% up, were acquired to assist in performance analysis, including data at 90% gasifier speed with two power turbine speeds and three values of turbine inlet temperature. Figure 9 contains time histories of speed, turbine temperature, shaft displacement, and case vibration during this high speed test.

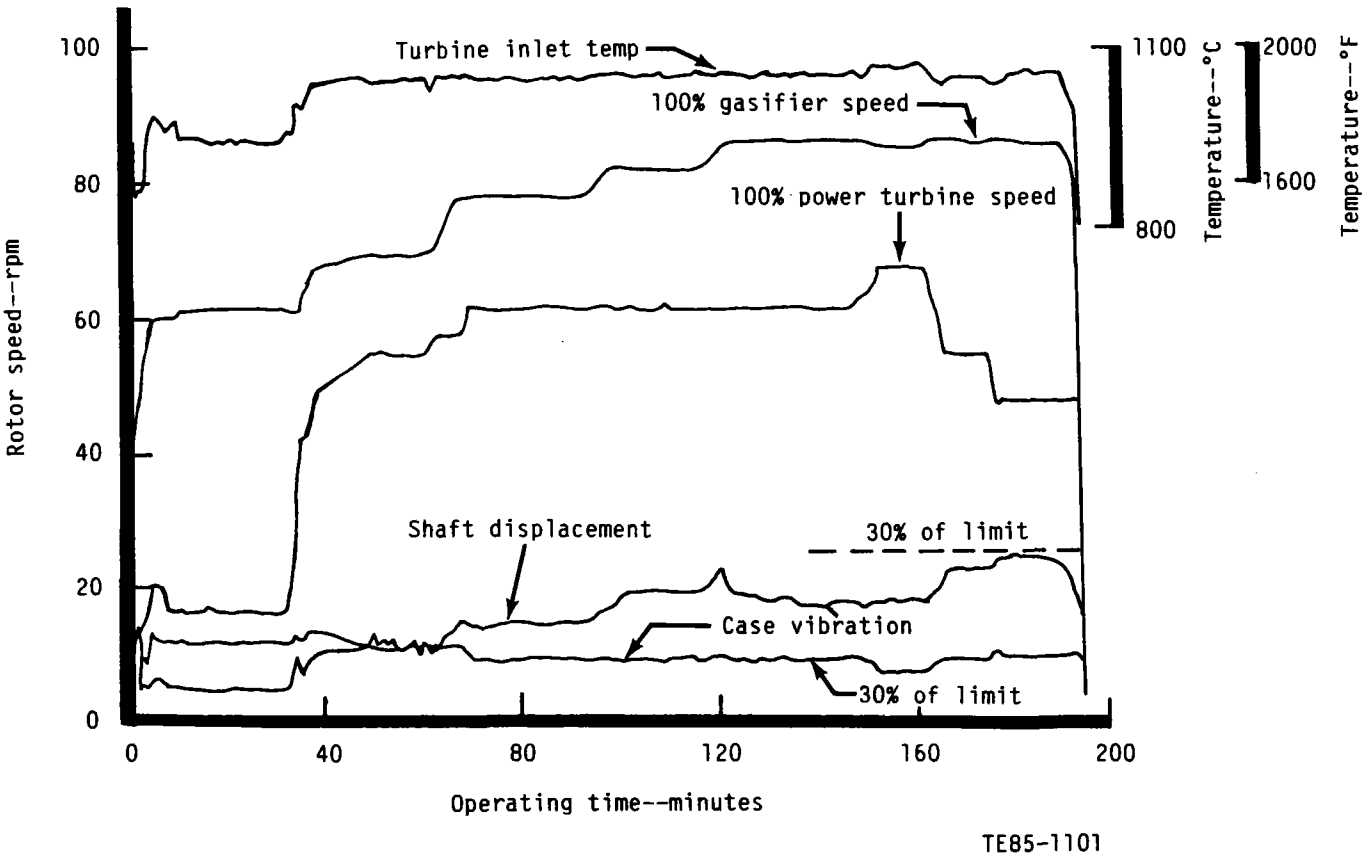

Figure 9. AGT 100 high-speed engine test (S/N 1 BU 11).

During early testing there were occurrences of combustor flashback, i.e., ignition of the fuel in the prevaporization chamber. A thorough review of the combustor-associated hardware revealed the fact that thermal insulation material had been inadvertently assembled into an airflow path that feeds the prevaporization chamber. This substantially reduced the velocity of gas out of this chamber, allowing the flame front to move into the chamber. A review of previous data indicated that this situation had probably occurred on some earlier engine builds. After modifying the insulation, no further flashbacks were experienced.

The pilot combustor continued to flame out during engine running, as during running on other recent builds. The pilot nozzle was modified to add a shroud onto the air swirler to aid in mixing fuel and air. While some improvement was shown, instability was still present. The burner variable geometry schedule was therefore adjusted for the fact that the lean blowout fuel/air ratio is different without a pilot flame. For the remaining testing period, the combustor was trouble-free.

Testing was terminated by low engine oil pressure, due to a stuck relief valve in the engine oil pump. Teardown, which was confined to the gearbox section of the engine, also revealed that the brass separator of the No. 2 bearing had cracked. A study for long term corrections for the bearing and oil pump was initiated.

Running time on the build was 16:02 hr, with a burn time of 11:52 hr. Total running time on engine S/N 1 stood at 54:19 hr.

Engine S/N 1 BU12 and Test

The teardown of BU 11 involved only the gearbox. The No. 2 bearing (gasifier shaft impeller end) was replaced with one with a heavier separator. It was determined that the oil pump required a redesign of the relief valve. In the interim, the gear case was modified to allow an external oil pump to supply engine oil requirements.

The engine was reassembled as BU12 and placed on test. Testing was accomplished up to a speed of 86% on the gasifier, at which point the pressure measured in the vented cavity between the hot and cold engine sections reached 172 kPa (25 lb/in.^{2}) gage, a value previously established as a limit. This pressure is caused by leakage past the scroll hold-down rod seals. These seals were Haynes 188 material on this build and were not as well seated as in the last test of engine S/N 2 when the vent cavity pressure remained very low.

As a result of reaching this limiting pressure, no speeds higher than 86% were tested on this build. Durability testing at 60% and 70% speed was continued, however, until engine time accumulated to approximately 15 hr on this build. Extensive modifications were then made to the fuel system as part of a planned upgrading of the control function. Engine testing continued during this checkout of the control system. The changes proved to be satisfactory and the engine was then removed from the test stand.

Teardown of the engine showed all parts to be in good condition, with only minor exceptions. Most ceramic combustor and regenerator parts showed no distress, nor did the two gasifier ceramic turbine vanes installed as a trial. The ceramic combustor dome was chipped where it bears against a metal locating pin. Minor rubs on gasifier and power turbine shrouds occurred. The gasifier turbine carbon seal was severely oxidized. Data taken during testing showed that seal air pressures had become unbalanced as a result of increased seal clearances, permitting hot turbine gases to backflow through the seal.

Total engine time on BU12 was 17:34 hr, with a burn time of 15:53 hr. The total of BU 11 and BU12 (gearbox only teardown between) was 33:36 hr. Total engine S/N 1 time to date stood at 71:53 hr.

Engine S/N 1 BU13 Preparation

The next build of engine S/N 1 will be configured as a leakage test vehicle. To this end, provisions for gas sampling probes are being made in the gasifier scroll at combustor outlet, gasifier turbine outlet, and power turbine outlet. A provision for adding helium or $C0_2$ at the combustor will be provided by using a combustor fuel nozzle assembly modified to accept gas injection tubes. Tracer gas will also be injected upstream of the compressor inlet. Other modifications to the engine for BU13 include seal clearance reduction, scroll hold-down rod seal improvement, replacement of the gasifier turbine due to progressive accumulation of blade tip erosion, and addition of several ceramic vanes in the power turbine.

This next build will also be used as a vehicle for flow calibration testing of the turbine nozzles. A partial build, using both gasifier and power rotors in turn, will be supplied with measured Test Facility cold air to determine turbine flow versus nozzle pressure ratio.

Engine S/N 2 BU5 and Test

During this build, the gasifier rotor unbalance was checked several times in an investigation similar to that on engine S/N 1. The repeatability of the unbalance magnitude (i.e., repeat cycles of balance, dis-

assembly, reassembly, and balance) was not as good as with engine S/N 1 but was deemed adequate considering the use of the viscous damper. Two gasifier and two power turbine ceramic vanes were installed in the engine. SiC ceramic combustor body fabricated by Asahi glass was installed. The gear case was modified to allow for the use of an external oil pump. Instrumentation was added to better define burner inlet temperature and compressor impeller discharge temperature.

Testing was initiated by obtaining performance data at gasifier speeds of 55% through 88%. At 90% speed, vibration velocity limits exceeded a preestablished conservative limit of 16.5 mm/s (0.65 in./sec). This value occurred only at the accelerometer positioned on the splitline near the air inlet. Rotor shaft displacement measured at the cold end of the gasifier shaft was less than 0.102 mm (0.004 in.) double amplitude. This value is considered to be very safe; operation at any value under 0.254 mm (0.010 in.) is considered to be safe. Vibration levels at other engine external measuring points were low.

Testing continued at speeds below 80% while vibration analysis was conducted. During these test runs some difficulty was experienced with apparent combustor instability. Several instances of both combustor flameout and rich flashback (RFB) occurred. The engine was borescoped, showing no damage to the burner hardware. Data analysis indicated that the burner variable geometry was not being positioned by the control to the desired schedule. Several changes were made to the software of the electronic control unit to refine the variable geometry positioning algorithm. Also an improved electric ground potential was established for the ECU. A recalibration of the fuel valve (fuel flow versus electric current) did not show any discrepancy.

The main fuel nozzle was found to have somewhat restricted flow characteristics, probably from a degree of fuel coking. The main nozzle was replaced with a new alternate design that incorporates a cooling chamber surrounding the small diameter fuel tubes internally. This cooling chamber, during current development work, uses circulating water for cooling, as does the fuel manifold cooling jacket, also part of the main nozzle. The additional cooling chamber was intended to prevent fuel coking in the small tubes.

Engine testing continued. During several more hours of running at intermediate speeds, there continued to be occasional shutdowns due to combustor instability. At certain of these unstable points the data indicated that the burner variable geometry was positioned such that no instability should be present, according to burner rig data.

Inspection of the engine internal regions around the burner cold end showed that a portion of the thermal insulation was potentially disturbing the flow into the combustor. This was successfully trimmed back while the engine remained on the test stand. During subsequent testing, both types of main fuel nozzles were used. This testing resulted in continued occurrence of RFB.

An increased potential for RFB is believed to result when either fuel or air is admitted to the prevaporization chamber in a nonuniform manner. RFB on engine S/N 1 had apparently been stopped by proper repositioning of insulation that appeared to have been adversely affecting the airflow into the prevaporization chamber. The last 20 hr of running on engine S/N 1 had been free of RFB.

One difference between engine S/N 1 and this build of engine S/N 2 is that engine S/N 2 incorporates a combustor made by Asahi. Prior S/N 1 testing was with a CBO combustor. Some dimensional differences between them had been noted but considered to be unimportant. To check the validity of that belief, the engine was returned to the assembly area to replace the Asahi combustor with the CBO combustor previously used.

This build obtained 41:36 hr running time with a burn time of 37:51 hr. Total running time on engine S/N 2 advanced to 121:39 hr.

Engine S/N 2 BU6 and Test

At disassembly of BU5 the metal foil used to package some of the thermal insulation was found to be out of place, such that airflow past the combustor would be impeded over a 100-deg arc. Since this face could explain the combustor instability encountered, the foil and thermal insulation were properly repositioned and the engine reassembled as BU6 without replacing the Asahi combustor.

The test plan with BU6 was to run each type of main fuel nozzle for 6 hr to check for RFB. In fact, RFB occurred at the end of the 6-hr tests with each type of main fuel nozzle.

Because combustor instability was not eliminated by the insulation improvements of BU6, the engine was removed from the test stand for a further configuration change. Testing on BU6 of engine S/N 2 added 12:19 hr of running time, 11:59 hr of which was burn time. Engine S/N 2 total time rose to 133:58 hr.

Engine S/N 2 BU7 and Test

The engine was reassembled as BU7 with the CBO combustor body that had already operated for

80 hr of engine time. The purpose of the change was to determine if stability differences existed between the two combustor bodies. No other change was made, nor was any other area of the engine disassembled.

Testing of BU7 showed some degree of instability in that the temperature sensor indicated RFB, but recovery could be made without shutting down. Recovery depended upon immediate change in combustor performance parameters, i.e., an increase in fuel flow and BVG. However, this test result was taken to mean that the exchange of cmbustor parts did not satisfactorily improve operation.

As previously explained, the combustor is believed to be more prone to RFB when either air or fuel entry into the prevaporization chamber is nonuniform. With the two types of main fuel nozzles in use, the original type experiences a degree of coking in the small fuel delivery tubes, while the alternate type with the cooling jacket around the tubes experiences instead a coking on the fuel evaporation surface. In both cases, coking is believed to cause uneven fuel distribution.

To reduce the incidence of coking, the test facility was modified to supply JP-5 fuel to the engine. JP-5 fuel will sustain a higher temperature before coking. The alternate type main fuel nozzle was installed, and the engine fired with no difficulty on JP-5. Some combustor instability did occur at crossover from the start nozzle to the main nozzle, but no engine shutdown was required. This may be related to control transients and is being studied.

With this fuel and combustor setup, a previously planned test program of the lubrication system was initiated. The purpose of this program was to obtain data relating bearing temperature to oil flow rate to contribute to the goal of reducing bearing soakback temperatures. Oil flow meters and pressure control valves were installed in the oil lines to the oil galleries for No. 1, No. 4, and No. 5 bearings. Oil pressure was varied at the outlet of the auxiliary oil pump being used to supply engine main oil pressures as well as at the oil gallery. Data were acquired at 65% speed and at 85% speed.

During the test run at 85% speed, temperature of the No. 4 (power turbine) bearing rose rapidly, accompanied by an increase in vibration and power turbine shaft whip. The engine was removed from test for diassembly and inspection. The test time on engine S/N 2 stood at 151:25 hr at the end of BU7, of which 107:49 hr was burn time.

Engine S/N 2 BU7 was disassembled after a test program that had obtained 66:08 hr of burn time on all parts but the combustor. The No. 4 (power turbine) bearing was found to be damaged. The adjacent area, between the carbon seal and the bearing, was found to be "coked" to the extent that the oil drainage hole was partially blocked. It is believed that the No. 4 bearing failure resulted from inadequate oil cooling, caused partly by oil coking occurring during the total test run and aggravated by the reduced oil flow during the bearing temperature and cooling investigation at the end of the run. An oil jet flow bench test showed that oil jet targeting was compromised by a "burr" in the jet. Parts rework to increase oil drainage flow area was implemented.

The bearing failure allowed the power turbine rotor to rub the turbine scroll. Inspection of the turbine rotor showed that 0.89 mm (0.035 in.) of material was removed from the turbine exducer; however, the rotor is reusable.

Certain ceramic parts exhibited distress. The combustor body had some chipping at the pilot flame tube hole (the flame tube itself also had chipping at its interface with the metal support). Both parts are usable. The flame tube is destined to be eliminated by the pilotless combustor configuration; thus, these chipped areas are not of great concern. The combustor dome was broken at the o.d. of its flange and was no longer serviceable. One of the gasifier turbine ceramic vanes was found to have a chip out at midchord at one end.

The gasifier rotor assembly was not removed from its bearing support at teardown. This build of the gasifier rotor assembly produced excessive vibration at speeds higher than 88%. Data indicated that rotor unbalance existed. While building an engine it is necessary to disassemble a rotor after unbalance correction in order to reassembly it in its bearing support for installation in the engine. Thus, the possibility exists that parts are not properly reassembled, resulting in unbalance. A new fixture that permits the rotor assembly unbalance to be checked in its final assembly form was developed. The rotor assembly, on engine bearings and in the gasifier turbine bearing support, is mounted in the fixture, which is fastened to the turbine bearing support and, in turn, provides a bearing support for the No. 2 (cold end) bearing. The whole assembly is then mounted on the balance machine.

This new fixture was used to check the unbalance of the gasifier rotor assembly as removed from the engine. The unbalance was found to be 11 times blueprint limit at the turbine bearing and 2 times blueprint limit at the cold end bearing. These values are believed to be consistent with the dynamics data obtained during test.

Engine S/N 2 BU8 and Test

Engine S/N 2 BU8 was configured as a test vehicle for the first engine test using a ceramic gasifier turbine. The goals of this first test were to expose the ceramic rotor to the engine assembly process, to rotate the ceramic turbine to idle speed, and to add a moderate increase in turbine inlet temperature. To that end a 60 kW electric heater was installed on the engine test stand. Piping was provided to duct air from the engine compressor outlet to the heater and return the heated air to the regenerator inlet. A turbine inlet temperature of 427-482°C (800-900°F) was expected. Ceramic inlet vanes at the turbines were replaced with metal ones.

The engine was motored at 43% speed, and the electric heater was subsequently activated. After 48 minutes, speed was slowly increased. Shortly thereafter, whip and vibration increased at an increased rate. This circumstance is illustrated by Figure 10. In this figure several variables are plotted against data acquisition record number, with data acquired at a rate of one record per second. As speed (N_1) increased from record number 2941 to 2967, so too did gasifier shaft whip, WP1, and compressor inlet vibration, VP2H. Starter torque was reduced to allow speed to decrease. Shortly afterward, torque was reapplied to maintain a reduced speed. Soon thereafter, whip and vibration increased excessively with little speed change, and the test program was terminated.

Teardown inspection revealed that the ceramic gasifier turbine had failed, losing approximately 15.2 mm (0.6 in.) from all vane tips at the inducer. Examination of Figure 10 indicates that the failure may have initiated at the point labeled F, where temperature drop across the turbine begins to change. Details of turbine failure analysis are given in subsection 9.2.1.

At the end of BU8, running time for engine S/N 2 stood at 152:38 hr (107:49 hr burning). Total time on both engines was 224:31 hr (156:14 hr burning).

At the end of this reporting period, engine S/N 2 was being readied to test either a ceramic gasifier scroll or another ceramic rotor. The ceramic scroll was in the process of being thermally proof tested in a bench test rig, while a rotor was in the process of fabrication and spin test.

2.2.3 Performance Analysis

Performance analysis of AGT 100 data was concentrated on test data obtained from engine S/N 1 BU 11, Record 10584, which was the maximum gasifier rotor speed and power turbine rotor speed data point obtained. The resulting analysis and a comparison with goal engine performance are shown in Table III with power and fuel accountabilities for the differences in each of the performance parameters shown. The analysis and comparison were made at observed ambient conditions, rotor speeds, and gasifier turbine inlet temperature.

The analysis procedure was to calculate compressor performance based on observed airflow, inlet total pressure and temperature (2.2°C [4°F] was added to the observed compressor inlet temperature to account for inlet heating observed during BU8 testing), discharge static pressure, and discharge temperature measured at the diffuser vanes. The observed flow was 11% less than the goal, and computed efficiency was 3.7 points less than the goal.

Estimated flow leakages bypassing the gasifier turbine (14.5%) and power turbine (13.5%) were obtained by internal flow analysis and were based on the summation of computed leakage flows through known seal clearances, estimated leakage through clamped joints, and rig based 7% regenerator leakage. These leakages exceed the goal leakages by 5.6% (gasifier turbine bypass) and 4.9% (power turbine bypass).

Gasifier turbine performance was computed based on observed vane inlet temperature, static pressure (adjusted to total pressure at the scroll inlet assuming 0.1 Mach number and 0.7% scroll pressure loss), computed turbine flow from measured compressor inlet flow and estimated leakage, and exit static pressure (adjusted to total pressure assuming 0.2 Mach number). The gasifier turbine power balance with computed compressor work minus observed starter input power plus mechanical loss (from engine S/N 2 BU4 mechanical loss test) resulted in gasifier turbine flow match and efficiency differences from goal of −15% and +0.1 points.

Power turbine performance was computed based on observed vane inlet temperature, static pressure (adjusted to total pressure at the vane inlet assuming 0.1 Mach number), computer turbine flow from measured compressor inlet flow and estimated leakage, and exit static pressure (adjusted to total pressure assuming 0.2 Mach number). The power turbine power balance with observed output power plus mechanical loss (from engine S/N 2 BU4 mechanical loss test) resulted in power turbine flow match and efficiency differences from goal of −12% and −8.9 points.

Table III shows a 1.4 kW (1.9 hp) increase in mechanical loss compared with the goal based on the results of engine S/N 2 BU4 mechanical loss test. Other computer differences from goal to test were +0.5 points regenerator effectiveness, +0.9% pressure loss, and +1.0 kg/h (+2.2 lb/hr) heat rejection measured in terms of equivalent fuel.

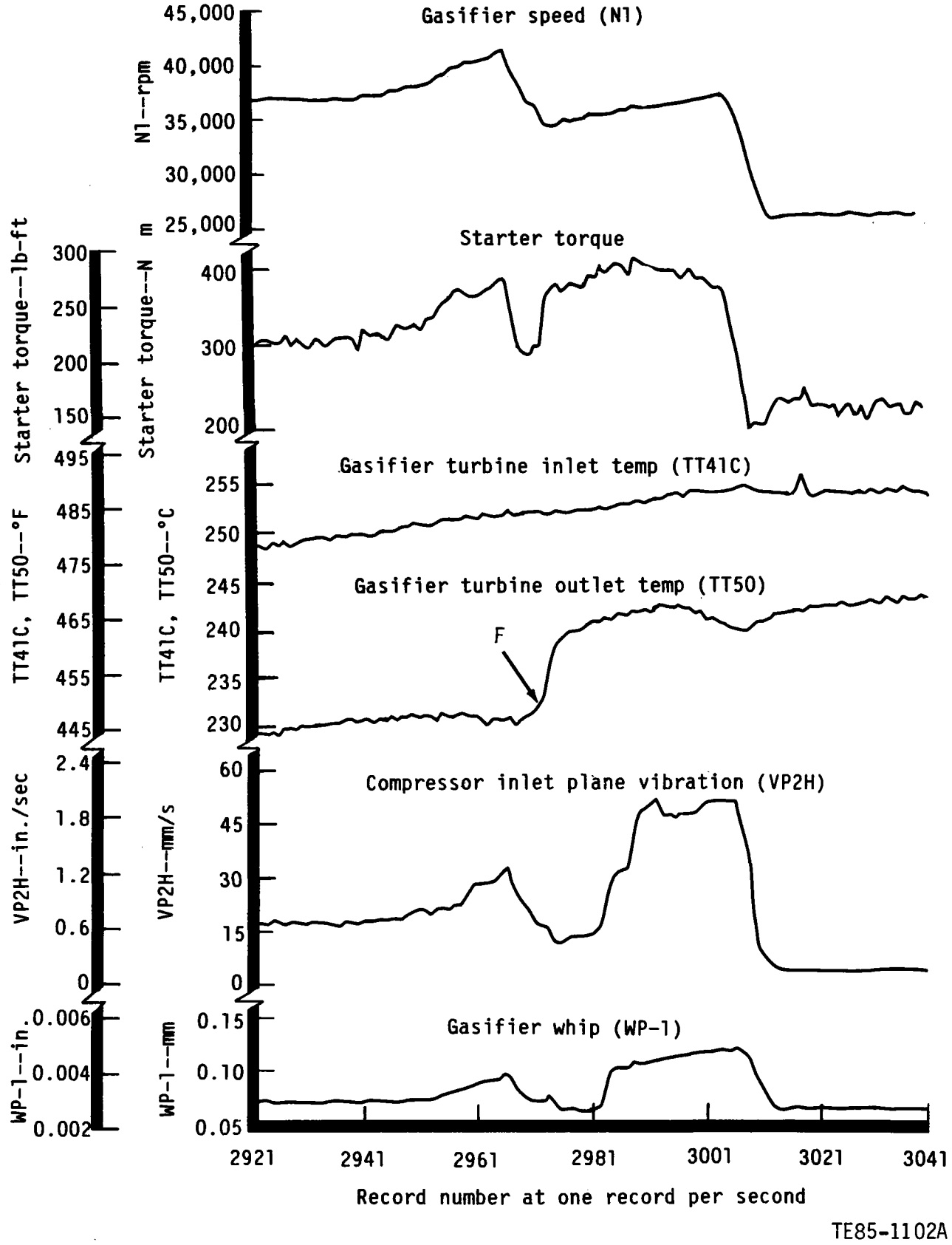

Figure 10. Ceramic rotor engine test after 48 minutes.

Table III.
AGT 100 (S/N 1 BU 11, record 10584) performance analysis.

			Accountability	
	Goal	Record 10584	Power— kW (hp)	Fuel flow— kg/h (lb/hr)
Net power	26.6 kW (35.6 hp)	10.7 kW (14.3 hp)	−15.9 (−21.3)	— —
Fuel flow	9.6 kg/h (21.2 lb/hr)	8.7 kg/h (19.2 lb/hr)	— —	−0.9 (−2.0)
Compressor				
Airflow	0.291 kg/s (0.640 lb/sec)	0.259 kg/s (0.571 lb/sec)	−5.6 (−7.5)	−1.5 (−3.3)
Efficiency	77.3%	73.6%	−2.9 (−3.9)	0.0 (0.0)
Leakage				
Gasifier turbine bypass	8.9%	14.5%	−3.4 (−4.6)	0.0 (−0.1)
Power turbine bypass	8.6%	13.5%	−3.3 (−4.4)	−0.1 (−0.2)
Gasifier turbine				
Flow match	0.162 kg/s (0.356 lb/sec)	0.138 kg/s (0.303 lb/sec)	−0.7 (−0.9)	−0.4 (−0.9)
Efficiency	81.3%	81.7%	+0.2 (+0.3)	0.0 (0.0)
Power turbine				
Flow match	0.318 kg/s (0.700 lb/sec)	0.280 kg/s (0.617 lb/sec)	+5.9 (+7.9)	+0.7 (+1.5)
Efficiency	78.7%	69.8%	−4.0 (−5.3)	−0.2 (−0.5)
Mechanical loss				
Power	5.0 kW (6.7 hp)	6.4 kW (8.6 hp)	−1.4 (−1.9)	0.0 (0.0)
Regenerator				
Effectiveness	92.3%	92.8%	0.0 (0.0)	−0.1 (−0.2)
Pressure loss				
Delta P	13.4%	14.3%	−0.9 (−1.2)	0.0 (0.0)
Heat rejection				
Equivalent fuel	0.2 kg/h (0.4 lb/hr)	1.3 kg/h (2.9 lb/hr)	0.0 (0.0)	+1.1 (+2.5)
Totals			−16.1 (−21.5)	−0.5 (−1.2)

Notes:

329.5 m (1081 ft) pressure altitude
48.3°C (119°F) compressor inlet temperature
99% gasifier and power turbine rotor mechanical speeds
1071°C (1959°F) gasifier turbine inlet temperature

Using power and fuel flow trade factors for the parameters listed in Table III and based on the goal cycle level of performance, the combined effects of the differences in all the performance parameters between computed or observed test results, as well as the goal cycle, accounted for 16.1 kW (21.5 hp) and 0.5 kg/h (1.2 lb/hr) of the total observed differences in power (15.9 kW [21.3 hp]) and fuel flow (0.9 kg/h [2.0 lb/hr]), respectively.

Examination of the power accountability column of Table III shows that the greatest net power improvements can be made by improved compressor performance (increased flow and efficiency) and decreased engine leakage.

Results of planned rig testing of the engine compressor hardware will be used to develop correlations with engine test results. These correlatins will further aid the analysis of engine test data.

Planned flow calibrations of both turbines and engine leakage tests using tracer gas (carbon dioxide or helium) will assist in determining the split between leakage and turbine flows, further aiding the analysis of engine test data.

III. COMPRESSOR DEVELOPMENT

In the current reporting period, compressor development activities were dedicated to the fabrication, assembly, and checkout of a modified compressor performance rig and the initiation of a series of extensive performance tests on previously tested engine S/N 1 compressor hardware and several new alternate configurations.

3.1 COMPRESSOR AERODYNAMIC DEVELOPMENT

Since previous test data based on engine S/N 1 running have consistently indicated lower flow and efficiency in comparison with compressor rig CX40 BU3 data, an engine to rig correlation test was devised to resolve any discrepancies in the results due to differences in compressor hardware and/or system thermal inertia and heat losses. Such a test necessitated modifications to the existing compressor rig to accommodate the engine compressor hardware. Also, additional modifications were made to improve the thermal characteristics of the rig. These changes will be discussed in more detail in subsection 3.2.

Analysis of test data, as stated in Section III of the Eighth Semiannual Report, EDR 11684 (CR 174798) has indicated that improved compressor efficiency is an important key to improved overall engine efficiency. Preliminary design studies have shown higher levels of compressor efficiency with reduced impeller equivalent area ratio (AREQ). In an effort to quantify this, two configurations—type 1A and type 1B (as illustrated in Figure 11)—were selected. Both of these designs feature flow-path changes to alleviate a potential "tight" (low flow area) knee region and thinner airfoils. Figure 12 shows the thickness distrubtion as compared with the compressor rig BU3 design.

Since several modifications to improve the system thermal inertia and reduce heat loss were made, a prelude to ensure proper results involved a series of systematic rig checkout tests to evaluate the effects of the following:

- thermal stabilization time
- rig sensitivity to bearing oil temperatures
- rig insulation

All the checkout tests were carried out using the S/N 1 engine compressor hardware.

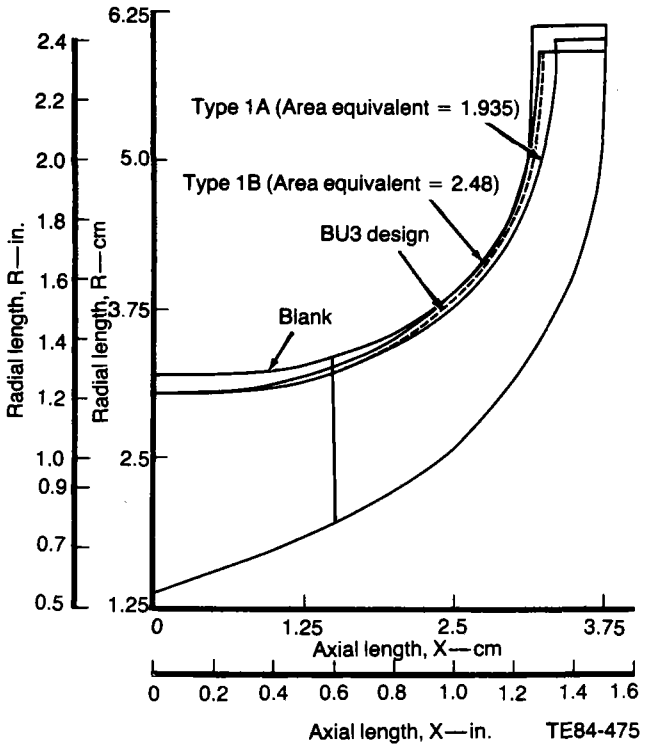

Figure 11. Meridional flow-path evaluation.

Thermal Stabilization Time

In a small flow machine such as the AGT 100, heat transfer affects the compressor indicated performance significantly. Hence, it was necessary to establish the amount of time for the rig to stabilize to obtain true results and not be misled by nonstable performance. Rig stabilization times were determined by running the compressor with one layer of 51 mm (2 in.) fiberglass insulation at 50, 70, and 90% corrected speed ($N/\sqrt{\theta}$). Data points were obtained every 5 minutes. Figure 13 indicates compressor performance versus time for 50% speed. From cold start, stabilization required approximately 45 minutes. This was decidedly longer than the time encountered earlier in BU3 and BU5 rigs and can be attributed to the presence of the large aluminum shroud cover in the engine as opposed to the small steel shroud in previous compressor rigs. A theoretical analysis of the rig revealed a stabilization time of 75 minutes. Further tests also revealed that 10 minutes were required for each new data point on the same speed line and 20 min-

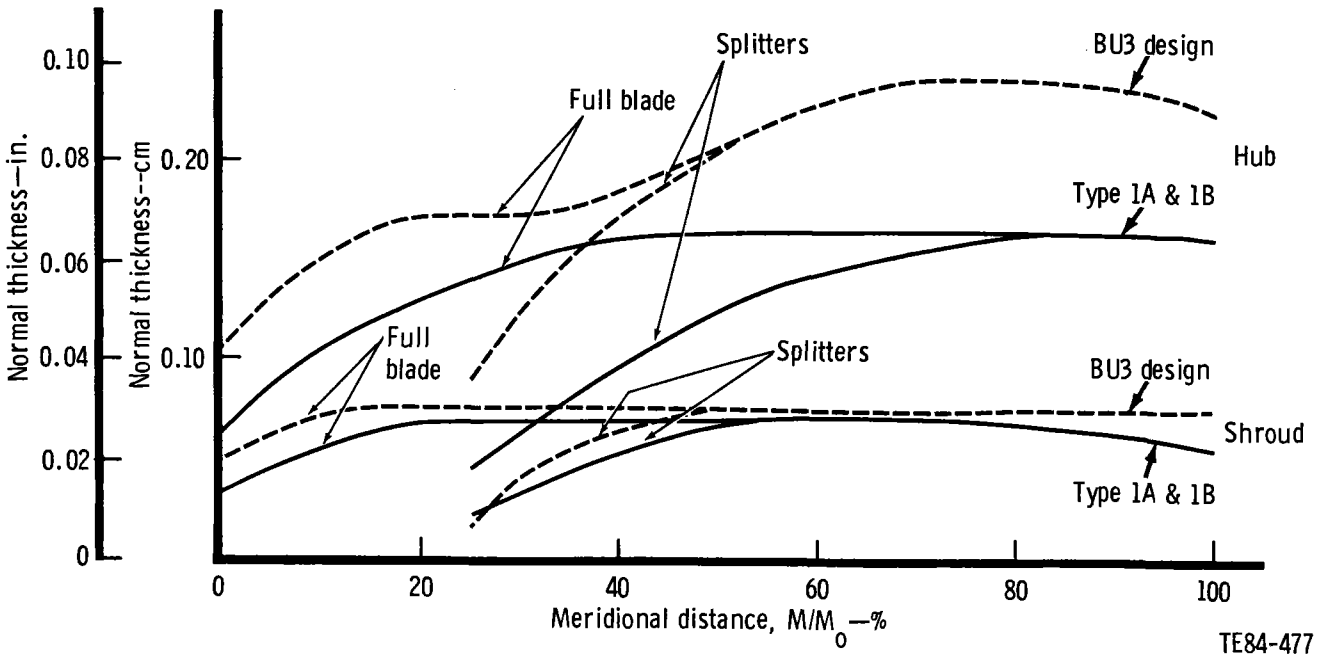

Figure 12. Impeller blade normal thickness distribution.

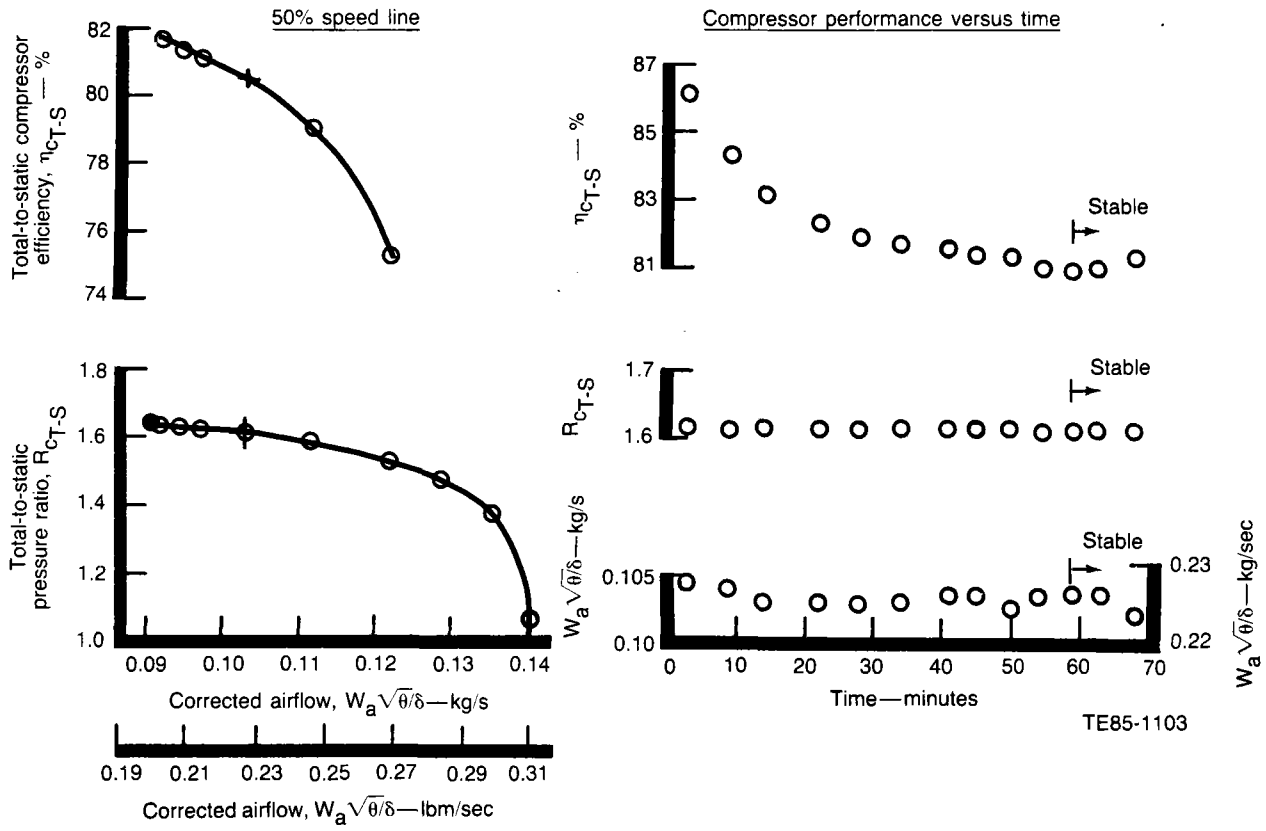

Figure 13. CX53 rig stabilization study at 50% corrected speed.

utes for small speed changes, i.e., 50-60%, 80-90%, etc. The stabilization times determined held true for all other speeds. (Engine testing also exhibits stabilization times of 10 to 20 minutes.)

Rig Sensitivity to Front and Rear Oil Temperatures

Data from previous compressor rig tests have revealed that front and rear bearing oil temperatures

contributed significantly to "indicated" compressor efficiency. Thus, having determined the thermal stabilization time, the oil temperatures of the front and rear bearings were perturbed to determine their individual effects on the rig. Testing was performed at 50, 70, and 90% corrected speed with the following combinations of oil temperatures.

	Front bearing
Base	27-32°C (80-90°F)
Alt 1	27-32°C (80-90°F)
Alt 2	93°C (200°F)

	Rear bearing
Base	Near CDT—<135°C (<275°F)
Alt 1	32°C (90°F)
Alt 2	Near CDT—<135°C (<275°F)

Figure 14 illustrates that altering the rear bearing oil temperature has essentially no effect on indicated performance, whereas increasing front bearing oil temperature significantly reduced indicated compressor efficiency. It was thus determined to maintain the oil temperature in the front bearing at a level similar to that of the engine's rear ambient temperature levels. (Note: Sensitivity to oil temperature was also examined for an insulated rig as described in the Sensitivity of Oil Temperature subsection.)

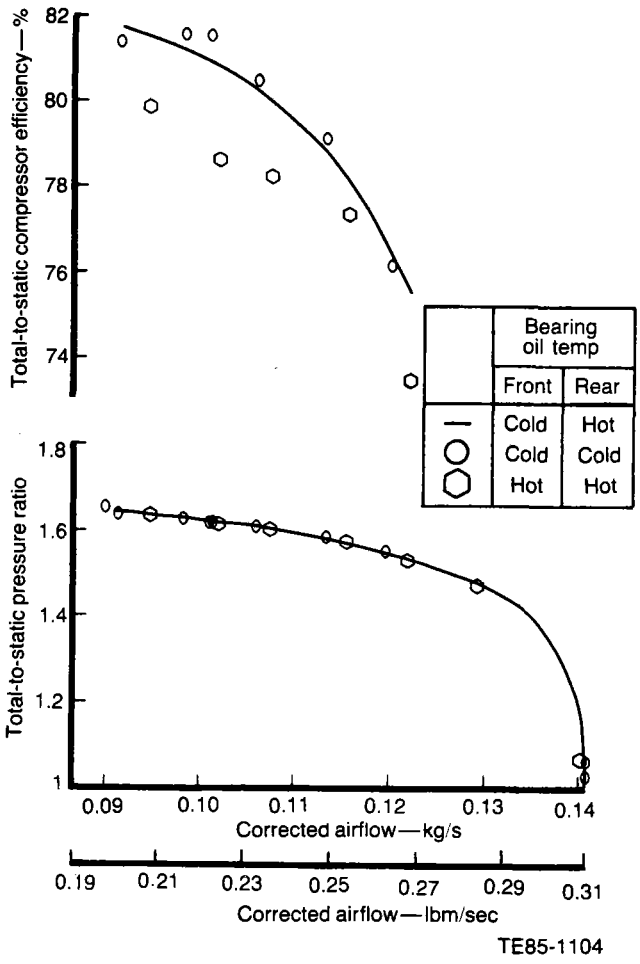

Figure 14. Effect of lubrication oil temperature on CX53 rig at 50% corrected speed.

Effect of Rig Insulation

It was the intent of this test to determine the effect of insulation on indicated compressor efficiency and eliminate any heat transfer to and from the rig. The following tests were conducted at 50, 80, and 100% corrected speed.

- 0 layers of 51 mm (2 in.) fiberglass insulation
- 1 layer of 51 mm (2 in.) fiberglass insulation
- 2 layers of 51 mm (2 in.) fiberglass insulation
- 4 layers of 51 mm (2 in.) fiberglass insulation

The results of these tests are shown in Figure 15 with 80% corrected speed selected as the representative speed. The results of the tests revealed that the amount of insulation on the rig did affect the indicated compressor efficiency significantly and that four layers of insulation were required to properly assess compressor performance. It was thus prescribed to map the compressor with four layers of insulation. (This effect may be due to clearance changes and will be further evaluated with dynamic clearance probes on future testing.)

Sensitivity of Oil Temperature

Since the previous test was performed with the baseline oil rig temperature settings (front at 32°C [90°F] and rear <135°C [<275°F]), a further test of oil temperature effects on the fully insulated rig was performed to eliminate any possibility of obtaining erroneous indicated performance. The test revealed, as previously, that the rear bearing had been successfully isolated whereas the front bearing still had an effect. This further reinforced maintaining the front bearing oil near ambient and the rear bearing oil at CDT (<135°C [<275°F]).

Sequence of Testing and Results

Having established the various salient factors that strongly influence the indicated performance of the AGT compressor, the following tests were carried out to obtain a better understanding of the compression system.

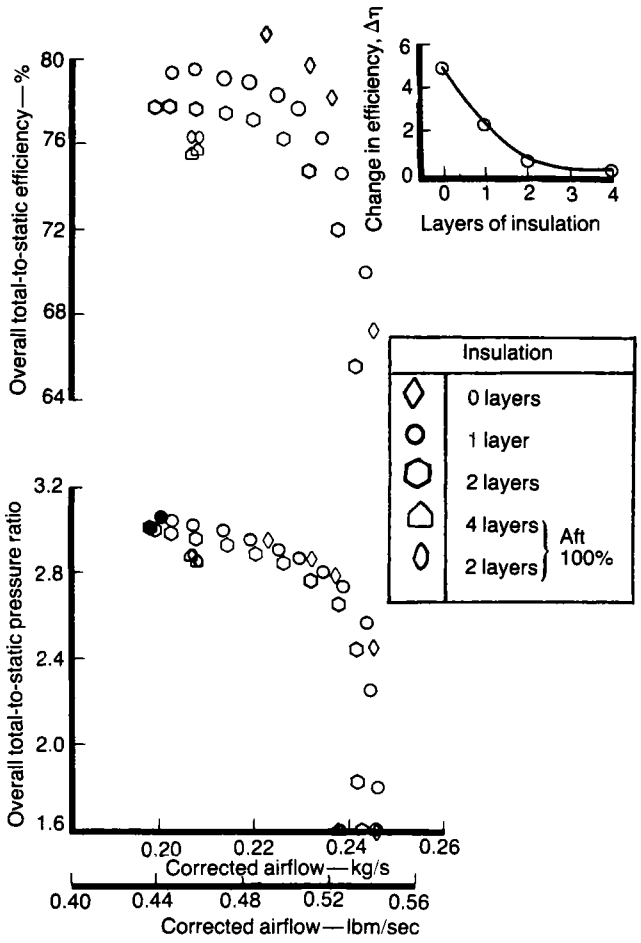

TE85-1105

Figure 15. Effect of exterior insulation on CX53 rig at 80% corrected speed.

Baseline Map (Engine S/N 1 Hardware)

The engine S/N 1 hardware is designated as the CX53 BU1 and BU2 rigs. To match previous engine S/N 1 running, a 0 deg IGV setting was used for the baseline map. Figure 16 compares the compressor performance for CX40 BU3 and CX53 BU2 for comparable measuring stations (inlet plenum to compressor discharge). Agreeing with previous engine data, the results confirmed that CX53 BU2 was down in flow and efficiency but had a marked improvement in surge margin and range over CX53 BU3. Inspection records on the diffuser eliminated the possibility of a small diffuser as a basis for these differences. In an effort to investigate the findings of this test, fully instrumented tests were planned.

Performance Sensitivity to Clearance

Since the variable IGV actuator mechanism prevented the installation and use of a dynamic running clearance probe, the compressor was built to a cold clearance of 0.20 mm (0.008 in.) between the exducer and shroud. (Cold build clearance was maintained the same as S/N 1 engine clearances.) However, since the rig does not have the hot oil surrounding the compressor shroud, the thermal properties of the rig can be assumed to be different, resulting in different running clearances. It was an effort to quantify such effects without causing irreversible damage to hardware as a result of hard rub that the cold clearance was opened 0.13 mm (0.005 in.) to 0.33 mm (0.013 in.).

Figure 17 illustrates the overlay of the open clearance map on the baseline map. There are no marked differences in flow or pressure ratio at 50% as inducer losses outweigh the clearance losses. However at higher speeds (80, 90, and 100%), clearance losses play a significant role and result in 3, 4, and 3.5% reduction in flow capacity, respectively, accompanied by loss of work. Figure 18 shows that, for these higher speeds, there is a 2-2.5% reduction in overall compressor efficiency with a 0.5-1% decrement at 50%. These data, along with those shown for insulation effects, indicate that the changes in overall indicated compressor efficiency due to insulation effects may result primarily from clearance changes. This will be further evaluated with dynamic clearance probes.

Since clearance strongly influences compressor performance, the feasibility of installing running clearance probes was considered and will be included in compressor testing to monitor running clearances closely. It was also necessary to keep clearances down to a safe minimum to assess the performance of the AGT 100 reasonably.

Performance Testing of Type 1A Compressor

The compressor rig test of the type 1A hardware (designated as CX53 BU3) incorporated an impeller with thinner blades and reduced overall diffusion (decreased impeller exit width). The design also included a newly designed diffuser to match the impeller. The design of the diffuser, albeit new, remained unchanged in design philosophy. The performance map for type 1A was obtained through the same speed range as the baseline map while also maintaining the system thermal conditions defined by previous tests. On completion of the initial tests, the inlet guide vanes were reset open (10 deg) at high speed to determine their effect on the thinner blades and radially repositioned diffuser.

Figures 19 and 20 show the previously described CX53 BU3 test results. Comparing these results with the baseline map (Figures 21 and 22), the overlay of the results from the two tests show very little differ-

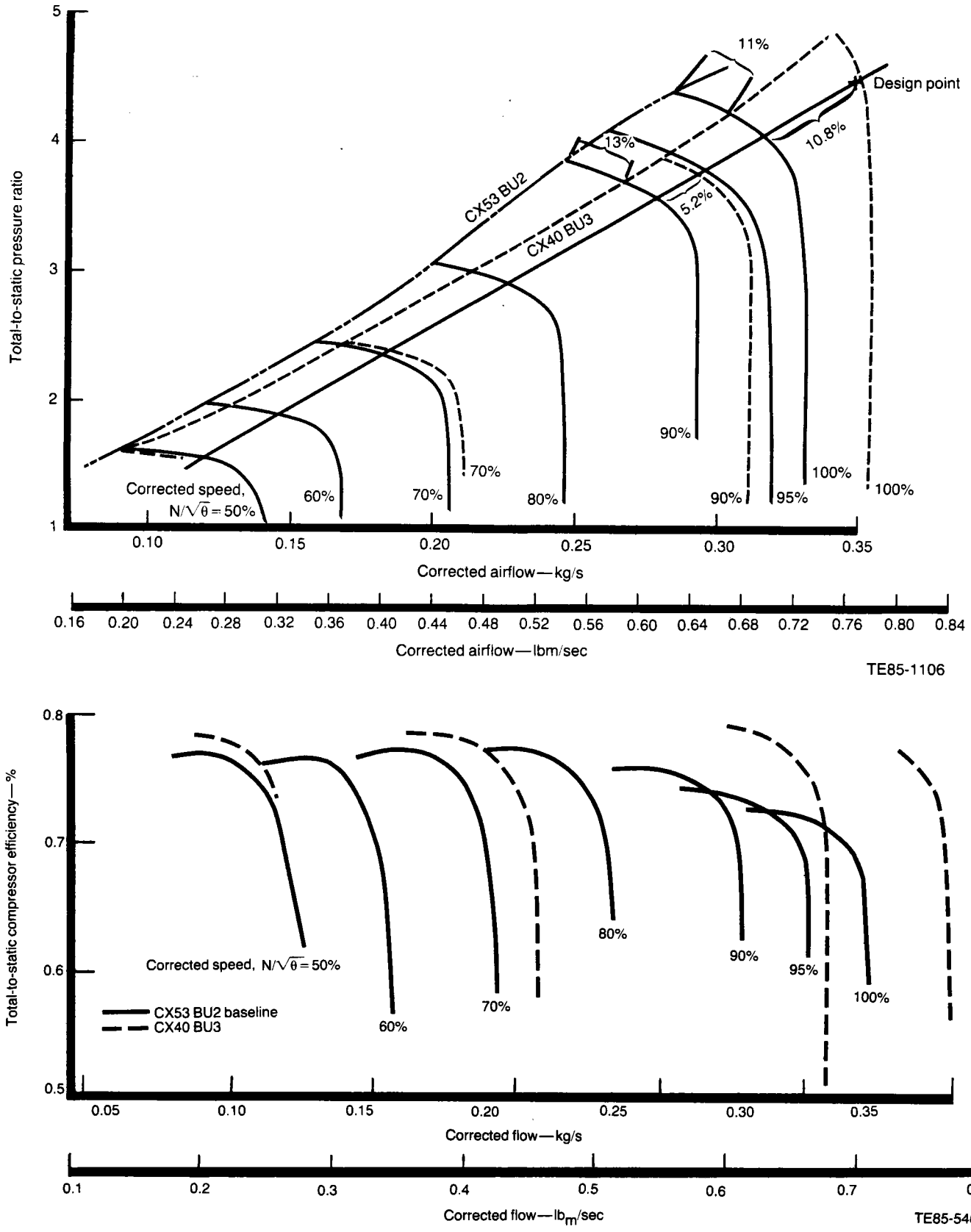

Figure 16. Overall compressor performance for CX40 BU3 and CX53 BU2 rigs.

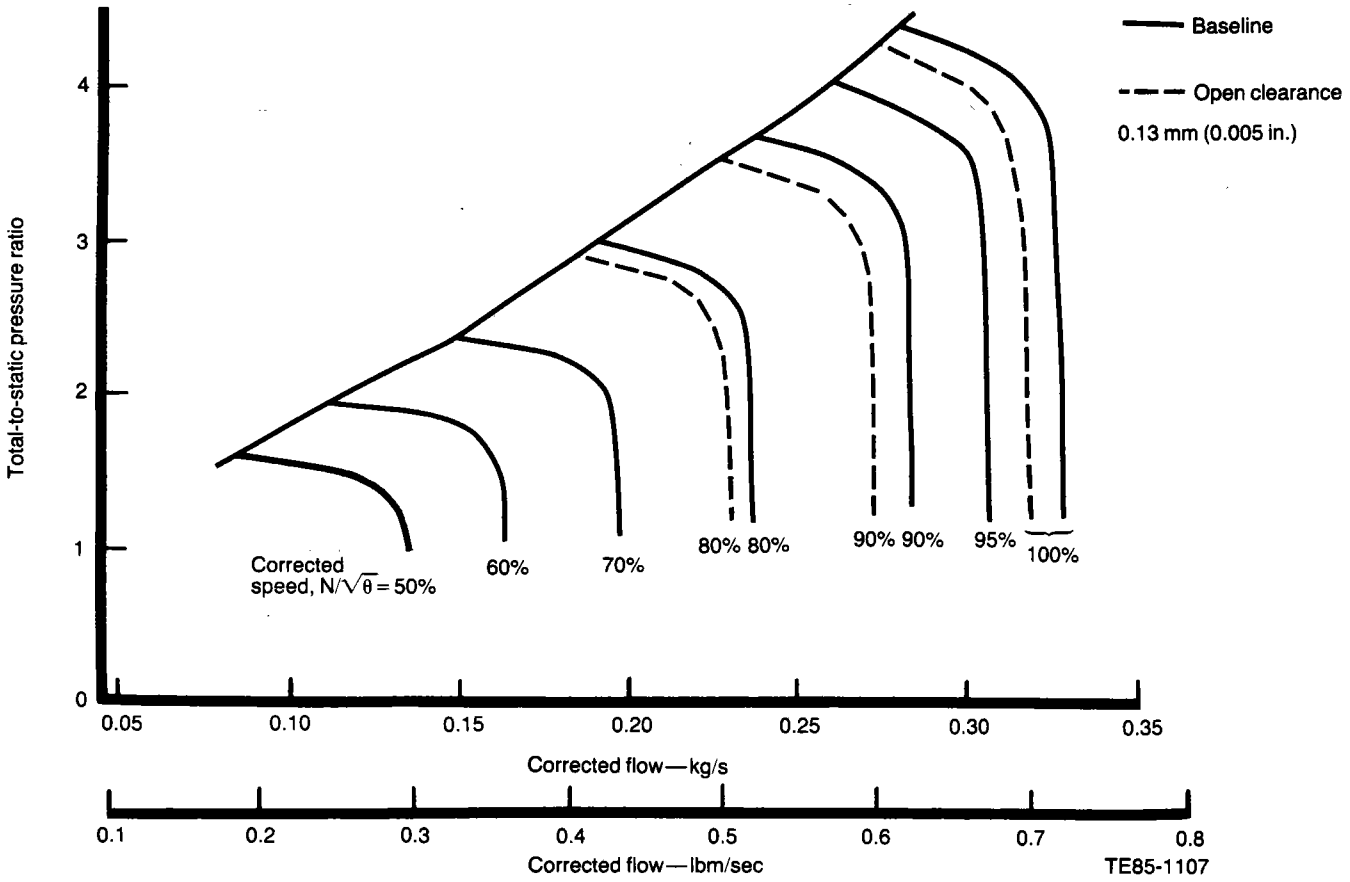

Figure 17. CX53 BU2 rig performance sensitivity to exducer-shroud clearance.

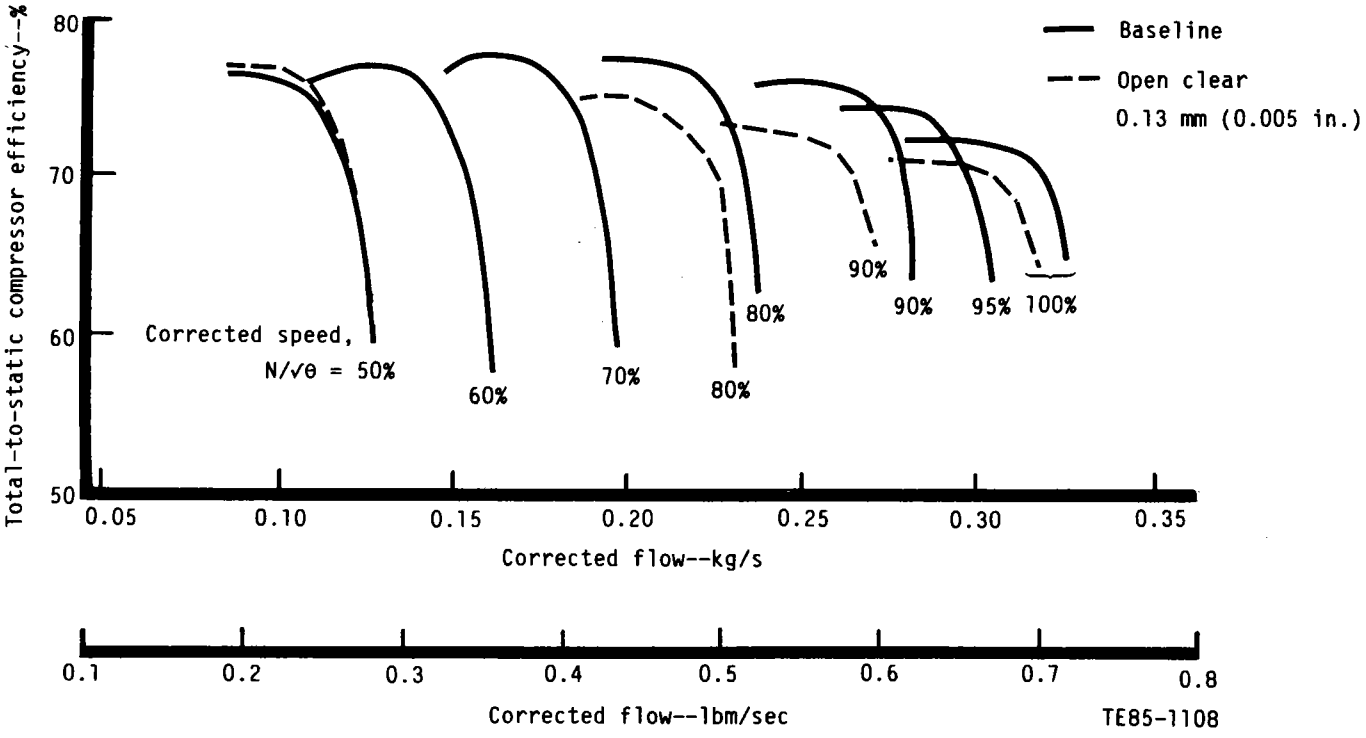

Figure 18. CX53 BU2 rig efficiency sensitivity to exducer-shroud clearance.

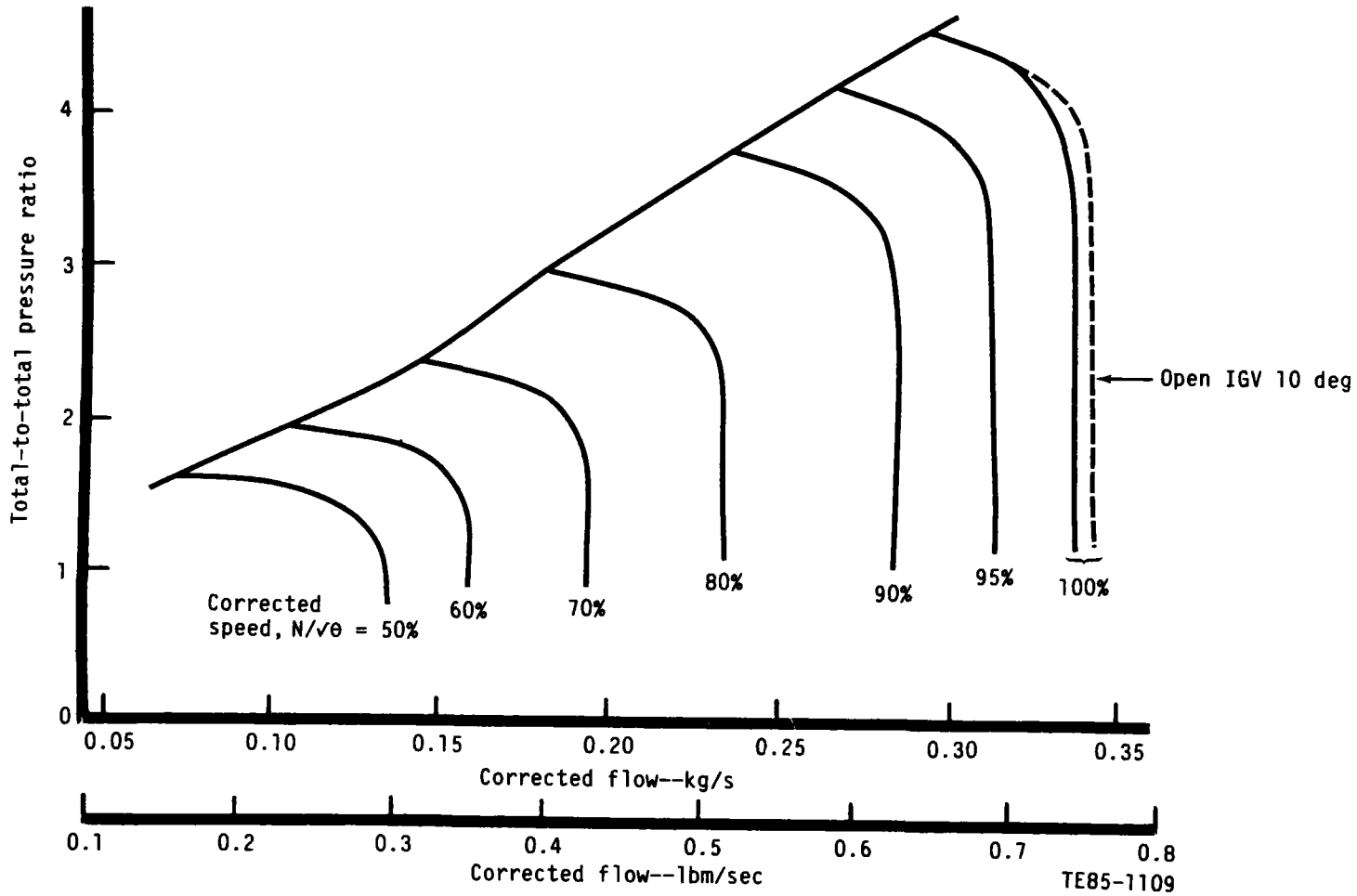

Figure 19. CX53 BU3 rig performance.

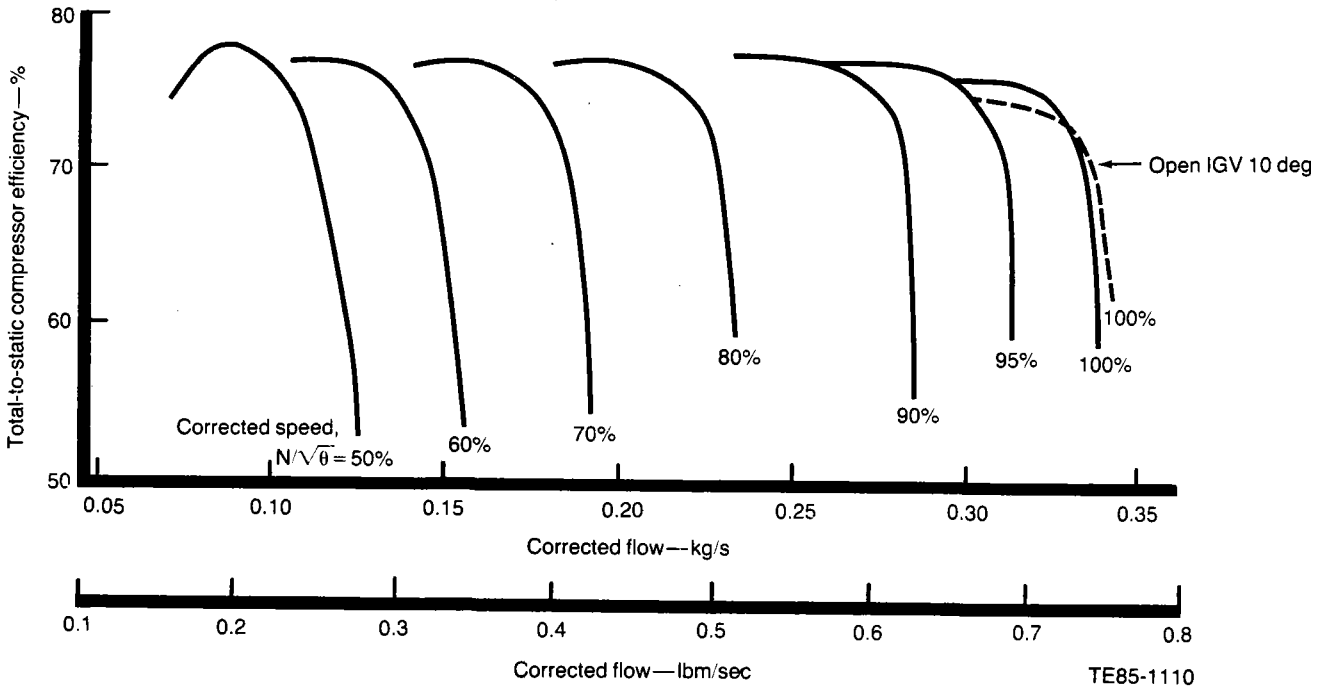

Figure 20. CX53 BU3 rig efficiency.

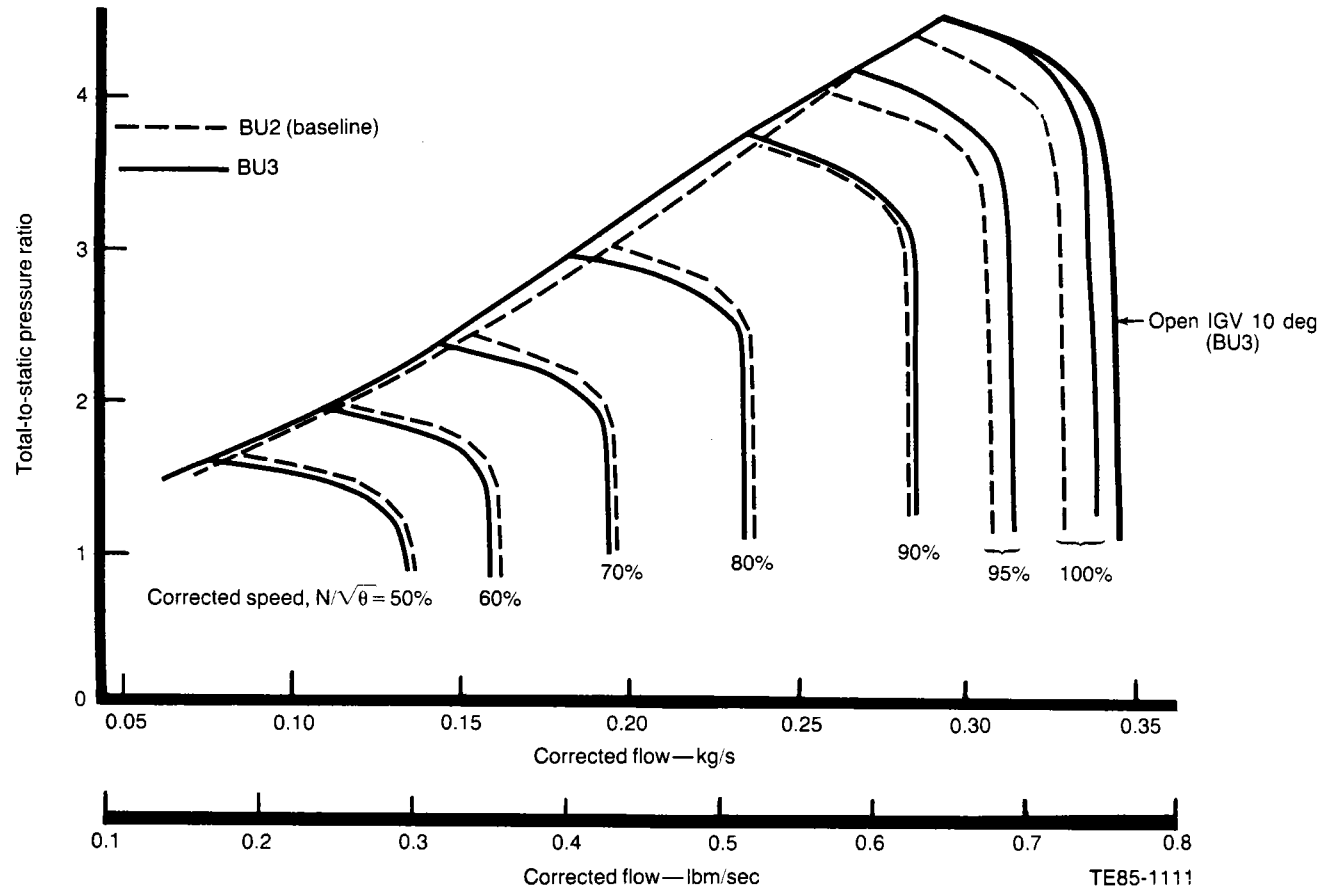

Figure 21. CX53 rig performance comparison for BU2 and BU3.

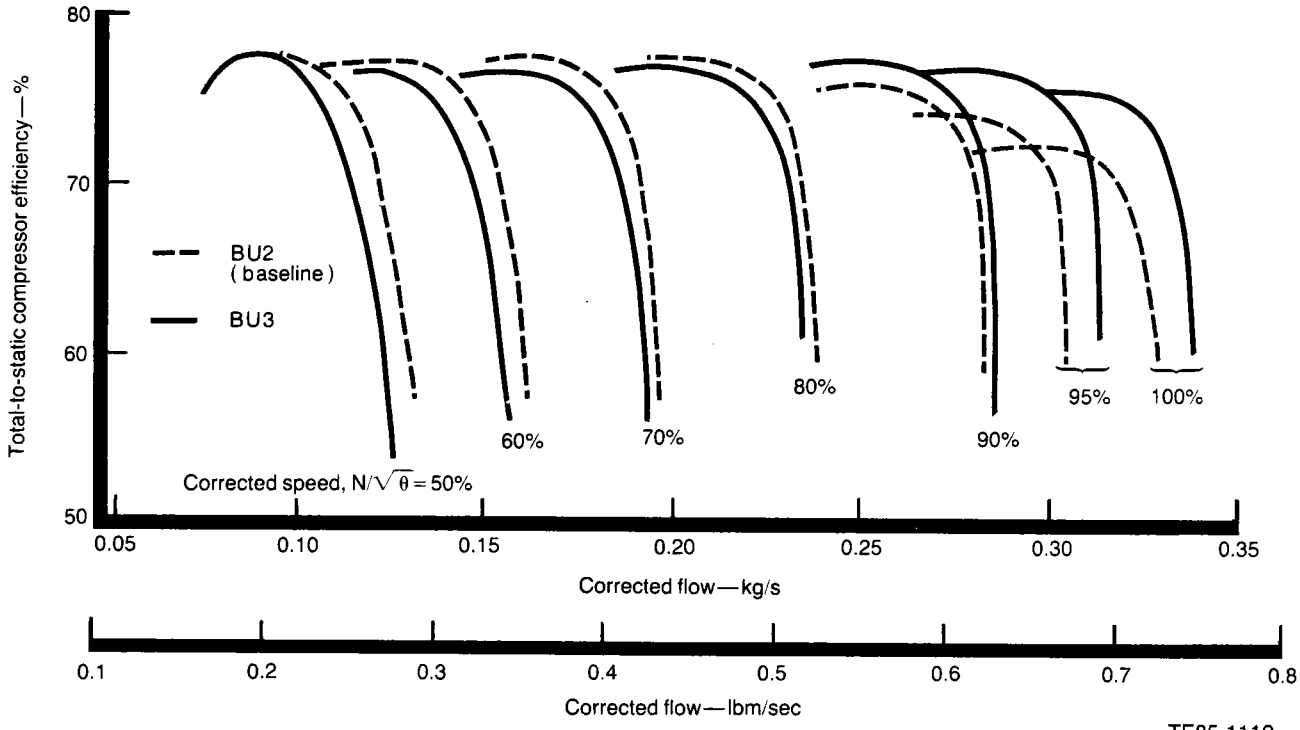

Figure 22. CX53 rig efficiency comparison for BU2 and BU3.

ence in flow and pressure ratio through 90% speed, with a significant increase in flow and pressure ratio at 95% and 100% speeds. The efficiency overlay shows a small loss for the modified compressor at part speed (<1%) and significantly improved high speed efficiency at 90, 95, and 100% (with the largest improvement at 100%).

Testing of Double Splitter Modification

Since the combined effect of reduced diffusion and thinner blades is favorable, a further modification to the type 1A impeller was devised to investigate the effects of impeller blade friction. The impeller splitter blades were cut back to the 60% meridional distance location, and every other full blade was cut back to the original splitter location (30%). This will result in an impeller with 8 full blades, 8 splitters starting at 30%, and 16 secondary splitters at 60% meridional distance. Figures 23 and 24 show the meridional flowpath elevation and comparative photographs of the modified impeller. This modification would enable the determination of any potential performance improvement with reduced blade friction losses.

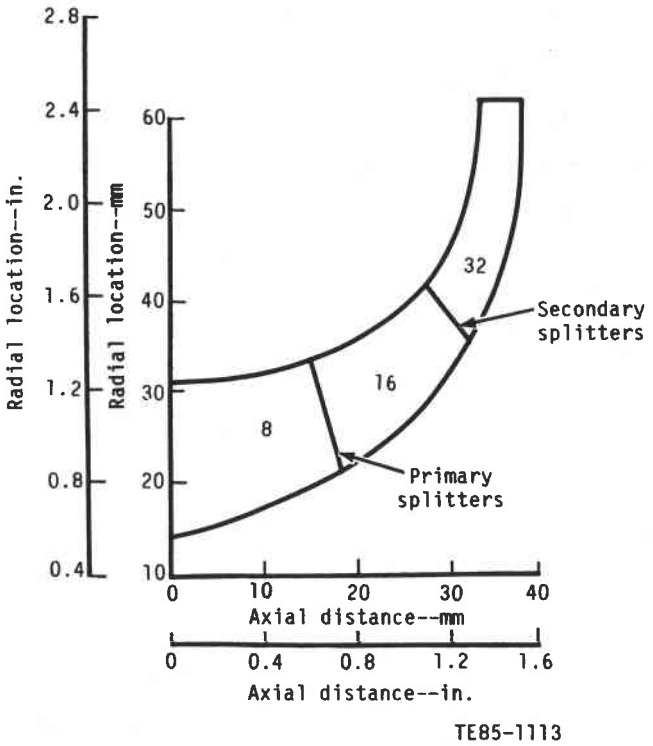

Figure 23. Flow-path meridional elevation for reduced blade friction impeller.

Initial testing of this hardware showed excessively high vibration problems in the static structure at 80% speed. Since initial attempts to overcome the problem in the test stand proved unsuccessful, a comprehensive effort is currently under way to solve the problem. The results of tests of this hardware will be covered in ensuing progress reports.

3.2 COMPRESSOR RIG MECHANICAL DEVELOPMENT

Heat transfer analyses have indicated the sensitivity of a low flow compressor, such as the AGT 100, to environmental effects. It was thus reasonable to assume that the anomalies between engine and rig results could partly be attributed to differences in system heat transfer characteristics. To address this problem and reduce the sensitivity of the rig to the environment, the following modifications were made:

1. interchangeability of engine and rig dedicated compressor hardware in the compressor rig
2. balancing capability during the buildup process without requiring subsequent rotor disassembly prior to final assembly
3. movement of the rear bearing aft 38.1 mm (1.5 in.) and replacement of the backplate by one made of polyimide and epoxy filled with glass microballoons
4. incorporation of a screw-thread arrangement to enable clearance changes without teardown

All of these modifications were successfully implemented in this reporting period.

The buildup of the modified rig for the engine-to-rig test was completed the last week of June in time for the commencement of diagnostic testing for rig checkout. The results of the tests revealed the successful decoupling of the rig to rear bearing oil temperature.

3.3 COMPRESSOR MECHANICAL DEVELOPMENT

Compressor mechanical development activity this period was limited to gasifier rotor assembly balance, dynamic shaft displacement, and vibration evaluation. The gasifier turbine is affected by this activity. To achieve a complete and integrated presentation, the combined subject is reported in subsection 4.2, Gasifier Turbine Mechanical Development.

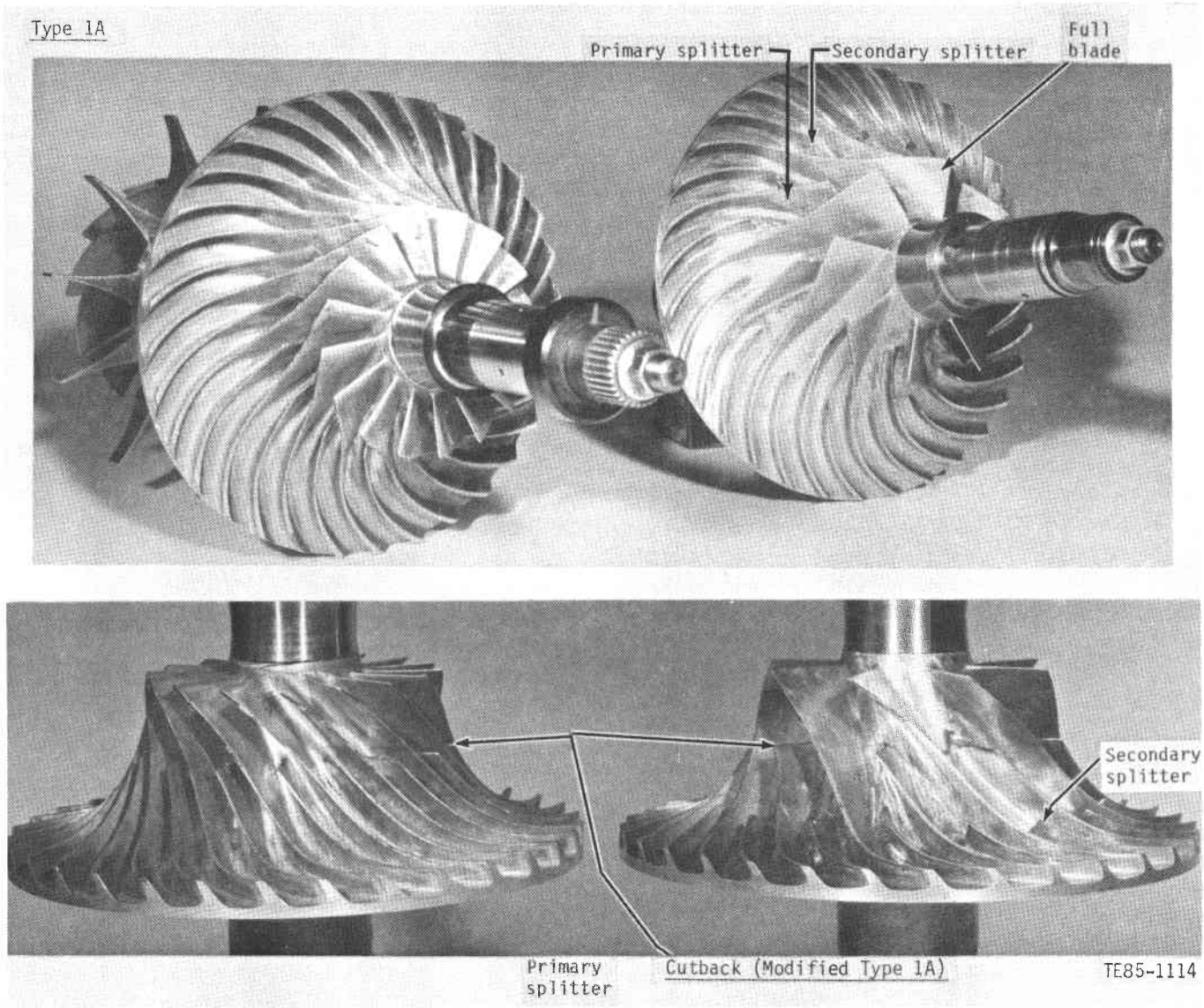

Figure 24. Comparison of type 1A and reduced blade friction impellers.

IV. GASIFIER TURBINE DEVELOPMENT

4.2 GASIFIER TURBINE MECHANICAL DEVELOPMENT

Gasifier turbine mechanical development during this reporting period included the following items:

- vibration investigation
- gasifier turbine rematch modifications
- analysis of rotor clearance measurements

Vibration Investigation

Initial operation of the engine at 100% gasifier speed (S/N 1 BU8) exhibited gasifier shaft vibration levels approaching the established velocity limit at the compressor end. The predominant vibrational frequency coincided with gasifier rotational speed. Subsequent builds (S/N 1 BU9 and S/N 2 BU3) produced overall vibration levels in excess of the established limit when operating in the upper engine speed range. The predominant vibrational frequency again coincided with gasifier speed.

As a result, an investigation was initiated to study the engine test vibration problem. The investigation included an extensive balance study, gasifier assembly analytical modeling, and special instrumentation added on S/N 1 BU 11 to measure bearing motion.

Carbon seal rub was found on some of the shaft sealing surfaces following engine tests that demonstrated vibration levels above the limit. These carbon seal clearances were increased as an interim measure to prevent rub, pending the demonstration of reduced vibration levels at high engine speed.

Balance Study/Test Experience

To prevent undesirable engine vibration, the gasifier rotor assembly must be balanced. The degree of balance required increases with both increased operating speed and decreased rotational mass. A high degree of balance is required for the AGT 100 gasifier rotor since it has a high operating speed range and low mass.

The gasifier rotor assembly is made of several components that must be disassembled after balancing before installation and reassembly in the engine. It is important that a significant balance change not occur due to disassembly and reassembly of the components. A balance repeatability study was conducted to determine how much balance change occurred between successive builds of the gasifier rotor assemblies.

Engine S/N 1 BU 11

During the balance study using S/N 1 components, measurements were taken to determine fit and flatness of interfaces. The spacer and spline designs were modified to improve their interface. Also, the amount of allowable interference between the turbine and impeller shafts under the No. 2 bearing was reduced to improve the axial clamp load distribution. A squeeze film damper was designed for the gasifier assembly front (No. 2) bearing to provide increased tolerance to gasifier unbalance. Changes were incorporated in S/N 1 BU 11 before engine testing.

Turbine shaft elongation during assembly was measured, and a shaft elongation versus axial load test was performed. Maintaining a high clamp load between rotor assembly components during engine operation aided in maintaining balance. The elongation measurements and the elongation versus load test confirmed that the desired load was being built into the assembly by the assembly procedure used.

Balance repeatability within the 2.16 g-mm (0.003 oz-in.) limit at each bearing plane was demonstrated for the balanced gasifier rotor assembly from engine S/N 1 before BU 11. This was accomplished by balancing the assembly, then disassembling and reassembling the rotor assembly twice and checking the unbalance after each assembly. The balancing and checking was done using dummy bearing races instead of the actual engine bearings because of the requirements of the balance machine. The balanced gasifier rotor assembly was installed in BU 11, where vibration levels were low during all test operation, including 1:07 hr at 100% gasifier speed.

Engine S/N 2 BU5

A balance study was also conducted using the gasifier rotor assembly from engine S/N 2 before undertaking BU5. As with S/N 1 rotor components, fit and flatness measurements were taken, the spacer and spline designs were modified, the turbine shaft to impeller shaft fit under the No. 2 bearing was reduced, and shaft elongation testing was done using S/N 2 rotor components. The balance was within the 2.16 g-mm (0.003 oz-in.) limit at each bearing plane for the first two repeatability trials following rotor

assembly balancing. However, on the third trial the unbalance at the No. 1 bearing plane slightly exceeded the limit. Because of the addition of a squeeze film damper (discussed in the analytical modeling section), it was decided to proceed with final balance of the rotor assembly and install it in engine S/N 2 as BU5.

During engine S/N 2 BU5 testing, it was found that the vibration limit at the air inlet splitline reached the established limit when the engine attained 90% gasifier speed. The vibration data indicated that the source of vibration was unbalance.

As in the case of the S/N 1 rotor assembly, this rotor assembly was balanced on dummy bearing races. Calculations indicate that a slight shift in the position of the rotational axis may have severe consequences on balance. A rotational axis shift of 0.0025 mm (0.0001 in.) at the No. 1 bearing has been calculated to produce a balance change of approximately twice the unbalance limit of 2.16 g-mm (0.003 oz-in.). Such a shift may occur when replacing the dummy bearing races with engine bearings due to slight differences in runout and o.d. to i.d. eccentricity. This is a mechanism by which unbalance may be introduced even if the assembly balance is repeatable. To eliminate this variable, a balance fixture was designed and fabricated to allow the gasifier assembly to be check balanced as assembled on engine bearings while installed in the engine bearing support. The balance fixture is discussed later as a separate item.

Engine S/N 2 TD7

The gasifier assembly was not disassembled between S/N 2 BU5 and TD7. Thus, the TD7 gasifier assembly encountered limiting vibration on BU5 near 90% gasifier speed. (No attempt was made to run at 100% gasifier speed on BU6 and BU7.) A check balance of the TD7 gasifier assembly in the balance fixture revealed that it was within unbalance limits at the front bearing and approximately 12 times the unbalance limit at the rear bearing. This suggests that the gasifier assembly either was not within balance limits when initially installed in the engine and/or experienced a balance change during engine testing. If the unbalance was due to the former cause, use of the balance fixture on future builds should allow the problem to be detected before engine testing.

The balance repeatability of the S/N 2 TD7 gasifier assembly was checked in the balance fixture after balancing with temporary weights. The balance was found to repeat within approximately one balance limit for each of two consecutive disassembly/reassembly sequences subsequent to the initial temporary balancing. This result demonstrates balance repeatability on the engine bearings.

Engine S/B 2 BU8

The gasifier assembly on engine S/N 2 BU8 was the first to incorporate a ceramic gasifier turbine rotor during engine testing. Although no formal balance study was made using this rotor, a check balance was performed using the balance fixture with the gasifier as assembled for engine testing. Unbalances of approximately four and six times the unbalance limits were measured at the front and rear bearings, respectively. Because of concern about the magnitudes of the measured unbalances, the rotor was disassembled and reassembled on dummy bearings. When check balanced on the dummy bearings, unbalances of approximately two and four times the unbalance limit were measured at the front and rear bearings, respectively. A decision was made to proceed with disassembling and reassembling the rotor in the engine without doing any additional balancing because BU8 testing was to be limited to speeds significantly below 100% gasifier speed. During BU8 testing, vibration at the compressor splitline increased rapidly when increasing gasifier speed from 43 to 48%. Subsequent analytical modeling of the gasifier assembly incorporating a ceramic rotor revealed that an unbalance at the rear bearing of eight times the unbalance limit is more than enough to bottom the rear bearing mass isolators. This bottoming drives a rotor response mode up in frequency as a result of the increased system stiffness. The mode was driven up into the speed range where the increased vibration was detected. The initial check balance in the balance fixture indicated that a sufficient magnitude of unbalance was present to produce isolator bottoming. This experience is indicative of the balance fixture's potential for detecting problems before engine testing.

Engine S/N 1 BU13

A balance study program was planned for the S/N 1 BU13 gasifier assembly. A new gasifier rotor assembly was assigned to S/N 1 for BU13. Progress was hampered due to hardware deficiencies and excessive dummy bearing race runout. Reworks were initiated to make hardware improvements, including reshafting the impeller with a new shaft. As a result of program plan changes, some gasifier hardware substitutions were made. Balance investigation work using the replacement set of hardware was not started during this reporting period.

Balance Fixture

A special balance fixture was designed and fabricated for checking the rotor assembly unbalance after building it into the engine bearing support structure with engine bearings. The fixture is to be used for checking unbalance both before and after engine testing. It is intended to provide a means for ensuring adequate gasifier assembly balance before engine testing, for checking gasifier assembly balance on teardown, and for gaining insight into any unbalance problems encountered during engine testing. The primary advantages offered by the balance fixture are that it may be used for check balancing the gasifier rotor assembled on engine bearings instead of dummy races and that no disassembly or reassembly is required between check balancing and engine testing.

Difficulties were encountered during the initial use of the fixture on S/N 1 TD12 and S/N 2 BU5 that prevented the fixture from yielding the desired information. (A large indicated unbalance change with rotational speed was observed.) Modifications were made to the fixture to allow use on future engine builds.

A checkout of the balance fixture after modifications indicates that modifications significantly improved the fixture's performance. Some unexpected indicated unbalance change with rotational speed was still noted. This change is due to the current balance machine specifications (1) being exceeded by the combined gasifier assembly and balance fixture mass and (2) exceeding the combined mass and rotational speed specification. A new balance machine with greater capacity is being procured that should eliminate this problem. The data obtained from the current balance machine/balance fixture combination is valuable because indicated unbalances equal or exceed actual unbalances.

Balco Consultation

In conjunction with the balance activities at Allison, input was solicited from The Balancing Company (Balco), Vandalia, Ohio. Balco is recognized as an expert in balancing many types of rotating components and has been involved in balancing and spin testing AGT 100 ceramic gasifier rotors. A gasifier assembly was delivered to Balco late in this reporting period. Balco will make recommendations for ensuring that an adequate degree of balance is present when a gasifier assembly is installed in an engine. Balco's activity will include balance repeatability studies and assessment of the feasibility of balancing the assembly on engine bearings.

Analytical Modeling

An analytical model of the gasifier turbine rotor assembly was employed to study the observed vibration response and to aid in identifying corrective action. Assembly response frequencies and mode shapes were determined for various spring rates of the support structure. The spring rates corresponded to conditions in which the mass isolators supporting the shaft bearing were either active or inactive (bottomed). The design spring rates of 10.5 MN/m (60,000 lb/in.) and 7.0 MN/m (40,000 lb/in.) at the aft (No. 1) and forward (No. 2) bearings, respectively, resulted in system response frequencies of 21,340 cpm (25% gasifier speed) and 44,680 cpm (52% gasifier speed). Bottoming of the forward mass isolator was assumed to change its spring rate to approximately 35.0 MN/m (200,000 lb/in.). This action produced a response frequency near 90% gasifier speed, the speed at which vibration limits were exceeded during engine testing.

To reduce the magnitude of gasifier assembly response to unbalance and avoid a critical speed in the operating range if the forward mass isolator bottoms, a squeeze film damper was evaluated at the forward bearing location. The squeeze film damper adds damping by introducing a fluid layer between two solid surfaces of the support structure. Analytical modeling showed that a damping coefficient of $C = 10$ produced a 30% critical speed margin and offered a significant reduction in response magnitude for a given unbalance. Based on the analysis results, a squeeze film damper was designed. It was initially employed on S/N 1 BU 11 and later on S/N 2 BU5.

Gasifier Turbine Rematch Modifications

As reported during the previous period, a new gasifier metal vane was being defined for the AGT 100 to improve efficiency during reduced temperature engine testing. The vane was originally designed and fabricated for a turbocompound turbine. During this reporting period, after completing layouts, drawings were released for the fabrication of backplates and scrolls to be used in conjunction with the new vane. One scroll assembly and one outer backplate were received. Inspection of the parts revealed that they were dimensionally unacceptable as received. They will be returned to the vendor for reworking.

Analysis of Rotor Clearance Measurements

Using the techniques described in a previous semiannual report (EDR 11577, CR 174629), cold wax clearance measurements and rub pad height

measurements were obtained at both buildup and teardown. These measurements are summarized for engine S/N 1 BU 11 through TD12 in Table IV and for engine S/N 2 BU3 through BU5 in Table V. Measurements are not listed for S/N 1 TD11 or BU12 because TD11 was a partial teardown and the scrolls were not removed. Measurements also are not listed for S/N 2 BU4 or TD4 since BU4 was a mechanical loss test employing unbladed turbine rotors.

The gasifier turbine shroud and inner backplate were recoated, and the rub pads were replaced for BU 11 of engine S/N 1. The cold wax measurement goals for BU 11 were the same as for BU9 except for closing them down by 0.05 mm (0.002 in.) at the backplate. Although the measured cold wax clearances slightly exceeded the goals, they were less than the BU9 measured clearances at the tip, knee, and backplate o.d. (Comparisons are not made to BU10 because TD9 was a partial teardown and BU10 measurements were not taken.) The TD12 rub pad measurements indicate that most of the refurbished rub pads were contacted by the gasifier rotor. None of the rub pads were reduced to zero height during more than 27 hr of operation on BU 11 and BU12, including 1.1 hr at 100% gasifier speed. This suggests that all gasifier rotor build clearances could possibly be reduced. However, a slight rub indication on the shroud exducer near the 12 o'clock position was noted on TD12. Rub had been noted at the same location on previous builds.

The cold wax measurement goals for engine S/N 2 BU3 were the same as for BU1 except for closing them down by 0.05 mm (0.002 in.) at the backplate. The goals were the same as those for engine S/N 1 BU 11. Although the S/N 2 BU3 measured cold wax clearance slightly exceeded the goals, they were simi-

Table IV.
Engine S/N 1 gasifier turbine clearance measurements.

	BU 11 cold wax goals—mm (in.)		BU 11 cold wax measured—mm (in.)		BU 11 rub pads measured—mm (in.)		TD12 rub pads measured—mm (in.)	
Location	Minimum	Maximum	Minimum	Maximum	Minimum	Maximum	Minimum	Maximum
Tip	0.36 (0.014)	0.38 (0.015)	0.41 (0.016)	0.48 (0.019)	0.28 (0.011)	0.33 (0.013)	0.23 (0.009)	0.36 (0.014)
Knee	0.28 (0.011)	0.33 (0.013)	0.31 (0.012)	0.38 (0.015)	0.23 (0.009)	0.25 (0.010)	0.13 (0.005)	0.23 (0.009)
Exducer	0.36 (0.014)	0.43 (0.017)	0.43 (0.017)	0.48 (0.019)	0.31 (0.012)	0.31 (0.012)	0.23 (0.009)	0.23 (0.009)
Backplate, o.d.	0.66 (0.026)	0.71 (0.028)	0.74 (0.029)	0.76 (0.030)	0.64 (0.025)	0.64 (0.025)	0.38 (0.015)	0.43 (0.017)
Backplate, i.d.	0.66 (0.026)	0.71 (0.028)	0.76 (0.030)	0.86 (0.034)	0.64 (0.025)	0.64 (0.025)	0.23 (0.009)	0.28 (0.011)

Table V.
Engine S/N 2 gasifier turbine clearance measurements.

	BU3 cold wax goals—mm (in.)		BU3 cold wax measured—mm (in.)		BU3 rub pads measured—mm (in.)		TD3 rub pads measured—mm (in.)		BU5 cold wax measured—mm (in.)	
Location	Minimum	Maximum	Minimum	Maximum	Minimum	Maximum	Minimum	Maximum	Minimum	Maximum
Tip	0.36 (0.014)	0.38 (0.015)	0.48 (0.019)	0.76 (0.030)	0.31 (0.012)	0.38 (0.015)	0.28 (0.011)	0.36 (0.014)	0.51 (0.020)	0.66 (0.028)
Knee	0.28 (0.011)	0.33 (0.013)	0.38 (0.015)	0.53 (0.021)	0.28 (0.011)	0.31 (0.012)	0.25 (0.010)	0.28 (0.011)	0.38 (0.015)	0.56 (0.022)
Exducer	0.36 (0.014)	0.43 (0.017)	0.41 (0.016)	0.46 (0.018)	0.20 (0.008)	0.25 (0.010)	0.00 (0.000)	0.25 (0.010)	0.36 (0.014)	0.58 (0.023)
Backplate, o.d.	0.66 (0.028)	0.71 (0.030)	0.79 (0.031)	0.89 (0.035)	0.56 (0.022)	0.56 (0.022)	0.31 (0.012)	0.43 (0.017)	0.81 (0.032)	0.86 (0.034)
Backplate, i.d.	0.66 (0.028)	0.71 (0.030)	0.76 (0.030)	0.84 (0.033)	0.56 (0.022)	0.56 (0.022)	0.38 (0.015)	0.48 (0.019)	0.74 (0.029)	0.89 (0.035)

Note: BU5 cold wax goals were the same as BU3.

lar to those measured on BU1. Rub at the gasifier exducer was indicated by one of the exducer rub pads. This indication agreed with the observation of light rub indications at the exducer. The rub was near the 12 o'clock position, resembling rubs noted on engine S/N 1. Elsewhere, the rub pads did not indicate impending rotor rub.

The cold wax measurement goals for engine S/N 2 BU5 were identical to those of BU3, and the BU5 cold wax measurements were similar to BU3 measurements. Analysis of the clearances will be presented pending teardown of S/N 2 BU5.

4.3 CERAMIC GASIFIER TURBINE DESIGN

Gasifier Turbine Alternate Design Scroll

Layout and detail drawings have been completed for an alternate design scroll. The final configuration, (see Figure 25) shows the desired features of a separately fabricated inlet section and a scroll body cast from its outside diameter. The separately cast inlet section eliminates casting a small radius in the area below the inlet where it blends into the scroll body. This was a source of high concentration of indications resulting in rejected castings. The feature of casting only toward the outside diameter eliminates shrinking of the casting onto the mold wall when drying, which was also a cause for rejection due to damage resulting from removal of the casting from the mold.

The alternate scroll was analyzed to obtain transient and steady-state temperatures and corresponding stresses. Two-dimensional finite element analyses were used to generate a comparison between the AA100626 original, the AA101200 alternate, and the AA101160 revised original scrolls. Weibull probabilities of survival were used as a basis of comparison. Table VI presents a reliability comparison of the scrolls with alpha-SiC material. Figure 26 shows the corresponding two-dimensional finite element models. The maximum temperature gradients occurred at different times for each configuration, but in all cases, the values in the table represent the minimum probability for that design during the transient. As seen from the table, the alternate design scroll provides a better probability of survival for this material and these designs. However, the small difference in probability of survival between the alternate and improved designs does not warrant a design change as drastically different as the alternate design.

Scroll configurations, based on Norton NC430 silicon carbide material properties, were also analyzed. Table VII shows a probability of survival comparison of the original design, the alternate design, and the original design with increased shroud wall thickness. Corresponding two-dimensional finite element models are shown in Figure 27. The analysis showed that the original design was superior to the alternate design. The reason for this is that added wall thickness in the highly stressed regions lowers stresses for the original design.

Also, the alternate scroll design does not offer an advantage in fabrication in NC430 because the lower shrink rate of this material does not present great problems when removing the casting from the mold. For these reasons, it has been decided that Norton pursue only the original scroll design.

Gasifier Turbine Rotor

A discussion of the gasifier turbine rotor can be found in subsections 9.2.1 and 9.3.

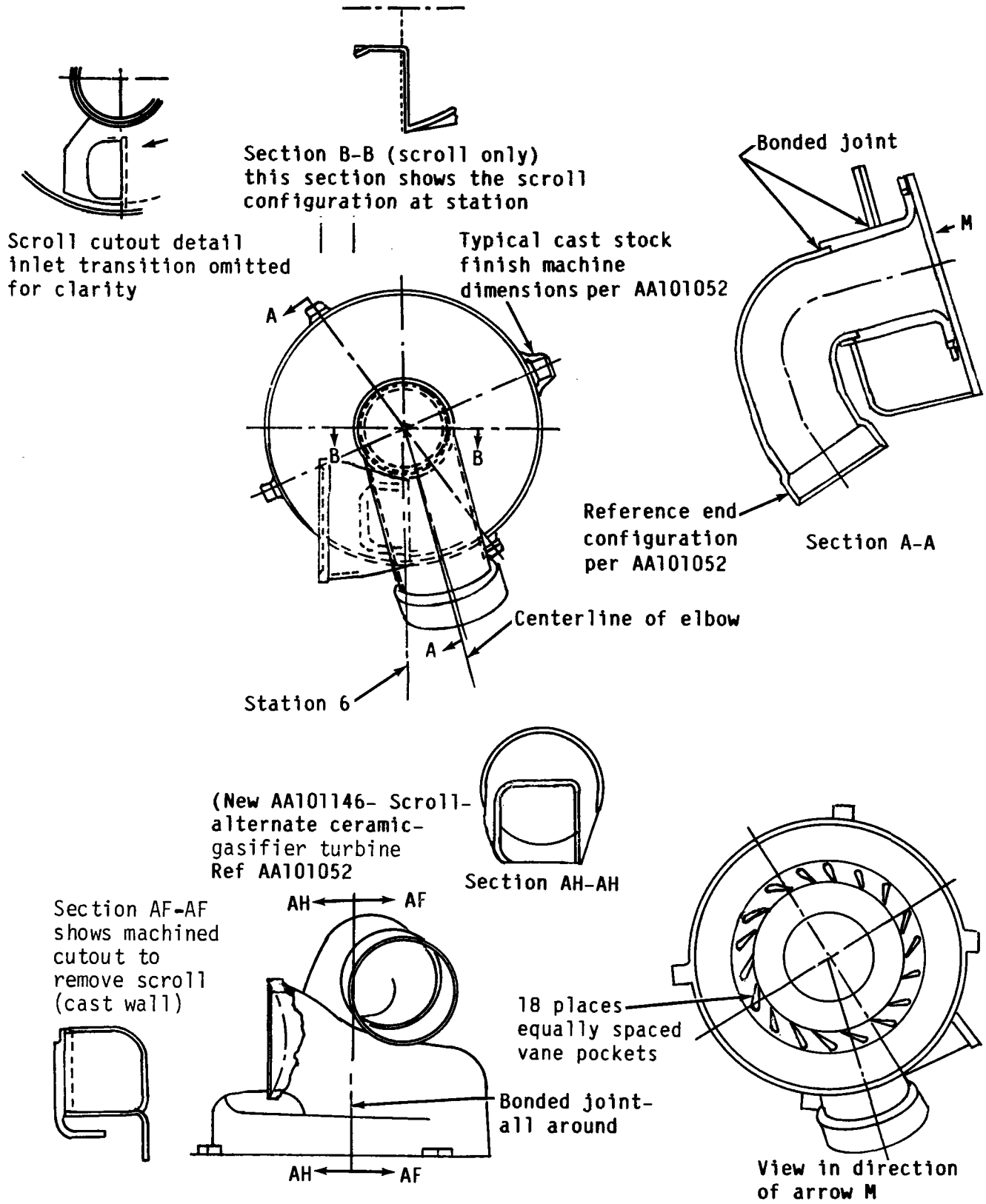

Figure 25. Alternate gasifier scroll configuration.

Table VI.
Probability of survival comparison of CBO alpha-SiC ceramic scroll.*

Inlet temp −°C (°F)	AA101626— original design		AA101160— increased thickness		AA101200— alternate design	
	Steady state	Transient	Steady state	Transient	Steady state	Transient
1080 (1976)	P_v 0.9991 P_s 0.9981 P_t 0.9972	P_v 0.9967 P_s 0.9994 P_t 0.9961	P_v 0.9991 P_s 0.9997 P_t 0.9988	P_v 0.9995 P_s 0.9999 P_t 0.9994	P_v 0.9999 P_s 0.9999 P_t 0.9999	P_v 0.9987 P_s 0.9999 P_t 0.9986
1204 (2200)	P_v 0.9980 P_s 0.9960 P_t 0.9940	P_v 0.9741 P_s 0.9948 P_t 0.9690	P_v 0.9988 P_s 0.9996 P_t 0.9985	P_v 0.9963 P_s 0.9993 P_t 0.9956	P_v 0.9999 P_s 0.9999 P_t 0.9999	P_v 0.9965 P_s 0.9996 P_t 0.9961
1288 (2350)	P_v 0.9986 P_s 0.9972 P_t 0.9958	P_v 0.9033 P_s 0.9788 P_t 0.8842	P_v 0.9984 P_s 0.9995 P_t 0.9979	P_v 0.9826 P_s 0.9969 P_t 0.795	P_v 0.9999 P_s 0.9999 P_t 0.9999	P_v 0.9941 P_s 0.9993 P_t 0.9934

*Characteristic strength is 558 MPa (25,580 lb/in.^{2}) for volume and 706 MPa (48,700 lb/in.^{2}) for surface; Weibull modulus is 8.43 for volume and 8.71 for surface.

Table VII.
Probability of survival of Norton NC430 SiC ceramic scroll.*

Inlet temp −°C (°F)	AA101052		AA101052 with thick wall		Alternate design scroll	
	Steady state	Transient	Steady state	Transient	Steady state	Transient
1080 (1976)	P_v 0.9801 P_s 0.9953	P_v 0.9922 P_s 0.9970	P_v 0.9801 P_s 0.9952	P_v 0.9977 P_s 0.9990	P_v 0.9991 P_s 0.9998	P_v 0.7562 P_s 0.9369
1204 (2200)	P_v 0.9801 P_s 0.9955	P_v 0.9298 P_s 0.9743	P_v 0.9798 P_s 0.9953	P_v 0.9791 P_s 0.9916	P_v 0.9891 P_s 0.9997	P_v 0.4446 P_s 0.8292
1288 (2350)	P_v 0.9780 P_s 0.9951	P_v 0.6446 P_s 0.8603	P_v 0.9776 P_s 0.9949	P_v 0.8717 P_s 0.9498	P_v 0.9989 P_s 0.9997	P_v 0.5880 P_s 0.8642

*Does not include backplate and vanes. MOR is 182.7 MPa (26,200 lb/in.^{2}), with 6 × 3 × 38 mm (0.25 × 0.125 × 1.5 in.) span—1/4 point bending; as fired surface in tension. Weibull modulus is 8.66.

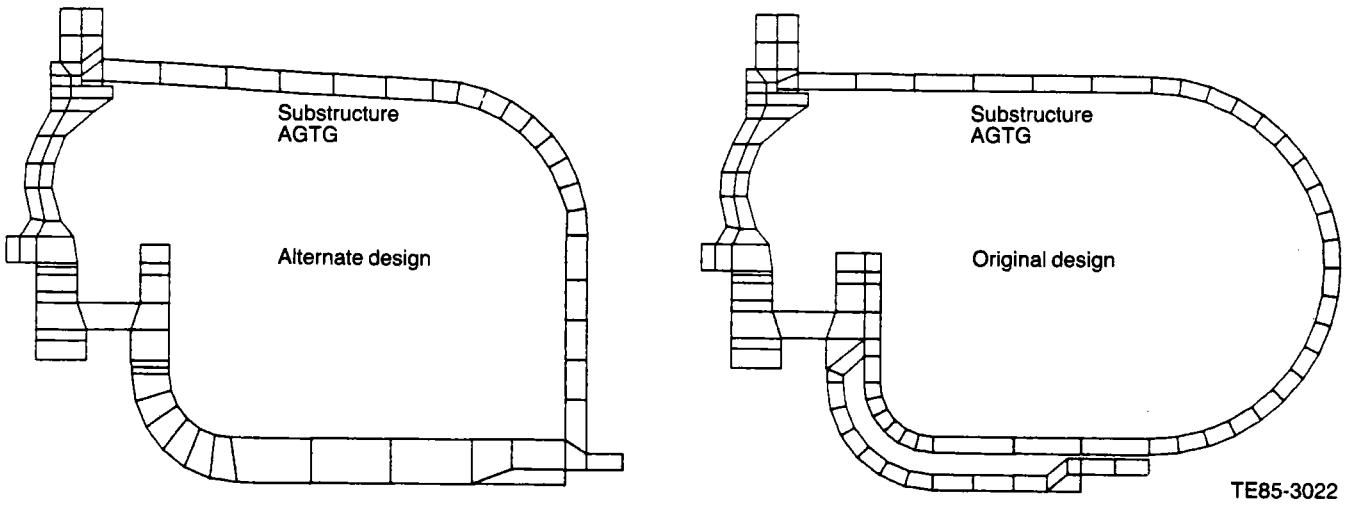

Figure 26. Scroll assembly 2-D finite element models for CBO alpha-SiC.

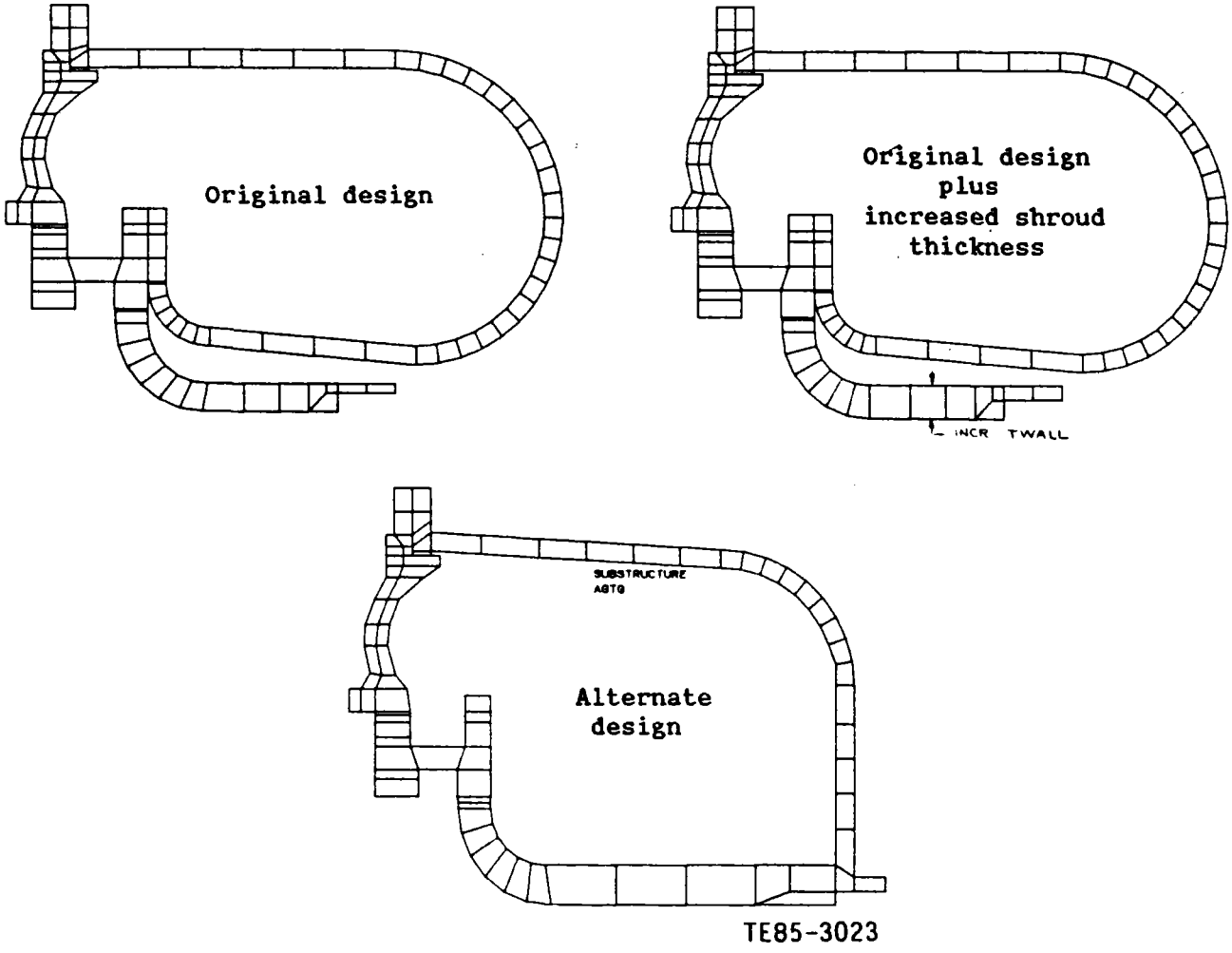

Figure 27. Scroll assembly 2-D finite element models for Norton NC430.

V. POWER TURBINE DEVELOPMENT

5.2 POWER TURBINE MECHANICAL DEVELOPMENT

Power turbine mechanical development during this reporting period included the following items:

- improved component fits
- power turbine rematch modifications
- analysis of rotor clearance measurements

Improved Component Fits

The fits between components of the power turbine assembly were studied after finding that improvements could be made to the fits of the gasifier turbine assembly. The fit between the bearing spacer and the power turbine shaft had more tolerance than desired. The fit tolerance was modified to reduce the amount of unbalance that could be introduced between balancing of the turbine assembly and installation in the engine.

Power Turbine Rematch Modifications

As reported during the previous period, a speed mismatch of the power turbine occurs during reduced temperature engine testing. To achieve improved efficiency, the turbine flow capacity is being adjusted to match the maximum power operating conditions. During this reporting period, drawings were released to allow fabrication of the required hardware. The hardware, consisting of an outer backplate and a scroll assembly, will be incorporated into an upcoming engine build.

Analysis of Rotor Clearance Measurements

Power turbine measurements were obtained in the same manner and for the same builds as described for the gasifier turbine measurements in subsection 4.2. The measurements for engines S/N 1 and S/N 2 are summarized in Tables VIII and IX respectively.

The power turbine inner backplate was recoated and the shroud and inner backplate rub pads were replaced for BU 11 of engine S/N 1. The cold wax measurement goals for BU 11 were the same as for BU9 except for closing them down 0.05 mm (0.002 in.) at the backplate. The measured cold wax clearances met the goals in most cases. They were less than the BU9 measured clearances at the knee, exducer, backplate o.d., and backplate i.d. (Comparisons are not made to BU10 because TD9 was a partial teardown and BU10 measurements were not taken.) The TD12 rub pad measurements indicate that most of the refurbished rub pads were contacted by the gasifier rotor. None of the rub pads were reduced to zero height during more than 27 hr of operation on BU 11 and BU12, although one rub pad on the backplate o.d. measured only 0.03 mm (0.001 in.). Rub indications were not noted on the shroud or backplate. This suggests that all power turbine rotor build clearances could be reduced except at the backplate o.d.

The cold wax measurement goals for engine S/N 2 BU3 were identical to those of BU1 and S/N 1 BU9. The measured cold wax clearances either met or deviated only slightly from the goal values. Following BU3 engine testing, the rub pad measurements did

Table VIII.
Engine S/N 1 power turbine clearance measurements.

	BU 11 cold wax goals—mm (in.)		BU 11 cold wax measured—mm (in.)		BU 11 rub pads measured—mm (in.)		TD12 rub pads measured—mm (in.)	
Location	Minimum	Maximum	Minimum	Maximum	Minimum	Maximum	Minimum	Maximum
Tip	0.48 (0.019)	0.58 (0.023)	0.51 (0.020)	0.53 (0.021)	0.38 (0.015)	0.46 (0.018)	0.38 (0.015)	0.41 (0.016)
Knee	0.38 (0.015)	0.64 (0.025)	0.36 (0.014)	0.46 (0.018)	0.33 (0.013)	0.36 (0.014)	0.31 (0.012)	0.33 (0.013)
Exducer	0.38 (0.015)	0.51 (0.020)	0.33 (0.013)	0.43 (0.017)	0.33 (0.013)	0.36 (0.014)	0.13 (0.005)	0.25 (0.010)
Backplate, o.d.	0.41 (0.016)	0.48 (0.019)	0.38 (0.015)	0.46 (0.018)	0.36 (0.014)	0.38 (0.015)	0.03 (0.001)	0.13 (0.005)
Backplate, i.d.	0.41 (0.016)	0.48 (0.019)	0.38 (0.015)	0.43 (0.017)	0.41 (0.016)	0.41 (0.016)	0.15 (0.006)	0.20 (0.008)

not indicate rub of the power turbine rotor. The shroud exducer rub pad at the 6 o'clock position was the shortest, measuring 0.13 mm (0.005 in.). Light rub was indicated on the shroud exducer approximately 30 deg away from it.

The cold wax measurement goals for engine S/N 2 BU5 were identical to those of BU3, and the BU5 cold wax measurements were similar to BU3 measurements. Analysis of the clearances will be presented pending teardown of S/N 2 BU5.

Table IX.
Engine S/N 2 power turbine clearance measurements.

	BU3 cold wax goals—mm (in.)		BU3 cold wax measured—mm (in.)		BU3 rub pads measured—mm (in.)		TD3 rub pads measured—mm (in.)		BU5 cold wax measured—mm (in.)	
Location	**Minimum**	**Maximum**	**Minimum**	**Maximum**	**Minimum**	**Maximum**	**Minimum**	**Maximum**	**Minimum**	**Maximum**
Tip	0.48 (0.019)	0.58 (0.023)	0.53 (0.021)	0.69 (0.027)	0.43 (0.017)	0.53 (0.021)	0.43 (0.017)	0.56 (0.022)	0.38 (0.015)	0.58 (0.023)
Knee	0.38 (0.015)	0.64 (0.025)	0.43 (0.017)	0.66 (0.026)	0.31 (0.012)	0.38 (0.015)	0.25 (0.010)	0.38 (0.015)	0.43 (0.017)	0.58 (0.023)
Exducer	0.38 (0.015)	0.51 (0.020)	0.31 (0.012)	0.61 (0.024)	0.23 (0.009)	0.36 (0.014)	0.13 (0.005)	0.28 (0.011)	0.38 (0.015)	0.51 (0.020)
Backplate, o.d.	0.46 (0.018)	0.53 (0.021)	0.38 (0.015)	0.46 (0.018)	0.20 (0.008)	0.28 (0.011)	0.15 (0.006)	0.28 (0.011)	0.43 (0.017)	0.51 (0.020)
Backplate, i.d.	0.46 (0.018)	0.53 (0.021)	0.38 (0.015)	0.46 (0.018)	0.18 (0.007)	0.31 (0.012)	0.23 (0.009)	0.28 (0.011)	0.41 (0.016)	0.46 (0.018)

Note: BU5 cold wax goals were the same as BU3.

VI. COMBUSTOR DEVELOPMENT

During this reporting period, combustor development efforts were focused primarily on proof, pilot, ignition, start, and main nozzle testing. Ignition improvements were incorporated into the centerbody of the combustor in the combustion rig. Modifications included the addition of two igniters into the pilotless combustor centerbody. Additional modifications altered the airflow field within the pilot, improving its lean blowout (LBO) characteristics and providing an alternate reliable ignition source for the start and main nozzle fuel flows. Main nozzle testing was confined to additional evaluations of various versions of the pilotless combustor.

6.1 TEST FACILITY

As reported in the eighth semiannual AGT report, a combustor rig test section capable of handling the high temperatures of the RPD cycle has been in use. This facility, as modified in 1983, duplicates the environment expected in the engine — the general flow path, insulating features, combustor orientation, variable geometry control, and fuel systems — as closely as possible. A television camera, positioned to look through a periscope in the combustor exhaust, is connected to a television monitor to allow visual observation of the combustion tests. This arrangement is beneficial in analyzing the combustion phenomena during the continual development of the combustor. Several optical ports have been added to the rig (six for pyrometers and one for a camera) for viewing the combustor outer wall during hot firings. The large optical port allows an infrared camera to view the combustor body axially from planes just below that of the pilot to that of the combustor exit. Circumferentially, the view includes the two dilution holes across from the pilot. This method of observation has removed the need for thermally painting the combustor to determine potential ceramic skin hot spots. The view is located in an area where hot spots have appeared in the past during cold start nozzle operation. These hot spots have been traced to carbon deposition caused by liquid fuel puddling and subsequent expulsion from the pilot.

A preheater, capable of providing combustion inlet air at a temperature of 1024°C (1875°F), has accumulated 90.8 hr of operation to date. This combustor test rig has also been used to evaluate problems with the current engine ceramic combustor that have occurred during pilot, start, and main nozzle operation.

6.2 TEST RESULTS

During this reporting period, 11.87 hr of burning time was accumulated on the combustor and atmospheric pilot test rigs. That time was devoted to proof testing present engine configuration assemblies, improving the pilot ignition system and cold start operation, and developing pilotless combustors incorporating new centerbody injection and ignition systems. Approximately 3.5 hr were devoted to atmospheric pilot testing, 2.4 hr to start nozzle and ignition operation, and 5.97 hr to main nozzle only operation. This total does not include the hours accumulated during engine testing that were directly related to main nozzle development.

6.2.1 Proof Testing

Two Asahi Glass combustor body assemblies were successfully proof tested in February. The first, designated proof test assembly No. 8, was scheduled for engine use. The upstream side of the ceramic dome (that portion resting against the radial swirler assembly) was chipped in two places during the proof test. Analysis revealed that the chips were due to impact loading caused by contact with the radial swirler. The swirler assembly was found to be warped and was remachined. The chips on the dome were not in critical areas and were recontoured through blending procedures and subsequently used in engine testing.

The second proof tested assembly was designated for the combustor rig and is not a numbered engine piece. This latter combustor is being used in the combustion rig.

Two additional combustor body assemblies were proof tested in July. The first, proof test No. 9, was an Asahi combustor. The test was conducted using a centerbody modification in which the exposed main nozzle fuel delivery tubes were water jacketed to reduce fuel tube coking problems. This modification is described in detail in the main nozzle testing section. Initial testing using this centerbody modification and cooling water within the tube manifold jacket resulted in LBO problems. During proof test No. 9, flameouts occurred during setup (of test stand fuel system calibration) and pilot shutoff. Combustion could not be sustained without the pilot at burner inlet temperature (BIT) and burner variable geometry (BVG) conditions, which normally do not require a pilot. These flameouts, which do not automatically shut off fuel flow on

the rig, concurrent with rapid cooldown of the dome face, may have contributed to the failure of the downstream side of the dome during this test. The combustor barrel was undamaged.

The Amercom CVD combustor was also proof tested (No. 10) late in July, using a conventional centerbody injection system, and both the dome and combustor failed during the start nozzle cycle. The flow conditions were to specifications, and the start nozzle was within spray uniformity specifications. Unlike the previous dome failure, this dome failed on the upstream side. The origin of the failure is unclear but may have initiated from one of the bypass holes in which a flaw was found to be present. The Amercom combustor barrel failure occurred in the dilution hole region. Only one dilution hole was involved; the cracks are axial in nature, extending from one side of the dilution hole down to the exit plane and up from the other side of the dilution hole. Origin of the failure is unknown.

6.2.2 Ignition Testing

Pilot Testing

Previous operation on both the rig and engine indicates that the combustor pilot flame could be extinguished early either in the start nozzle or main nozzle cycles due to pilot nozzle flame blowout. Once ignition has been achieved on the start nozzle, continued operation of the combustor is possible as long as the transition from start nozzle to main nozzle operation is performed at BITs above 700°C (~1300°F) and the BVG schedule is programmed for pilotless operations. The pilot may flame out while pilot fuel continues to flow to the extinguished pilot nozzle (see Figure 28). Continued operation in this mode has resulted in pilot operational problems, particularly nozzle tip plugging (coking). While the normal operating mode of the combustor does not require a pilot, it is desirable to retain pilot capability. This capability allows examination of off-design operating conditions and use of the pilot as a backup igniter.

An investigation into the pilot fuel nozzle flameout and coking phenomena was initiated. A change to a gaseous fuel (methane) was successful during atmospheric pressure testing. A specially constructed pilot test rig allowed a range of system pressure difference/inlet pressures ($\Delta P/P$) to be simulated and overall methane injection pressure effects to be evaluated. The pilot flame was easily sustained at all $\Delta P/Ps$, simulating actual combustor conditions. A wide tolerance of overall methane injection pressure allowed operation between rich and lean blowout limits at all combustor operating conditions. These tests were conducted to ensure that, should other modifications fail to alleviate the pilot fuel nozzle flameout problems on liquid fuels, a gaseous fuel could be used as a backup pilot system. The necessity for this requirement has been alleviated, and the methane pilot tests did not proceed beyond those conducted at atmospheric pressures.

Additional atmospheric pressure tests were performed to determine optimal configuration changes to the pilot (primarily those affecting its swirl air volume and flow pattern) using the reference liquid pilot fuel, DF-2. Air shrouds over the pilot axial air swirler were constructed and welded to the pilot tip, shown in place in Figure 28 and in detail in Figure 29. Various geometric shapes were investigated and tested using DF-2 as the fuel in open air and in the combustor rig. The combustor rig hot fire evaluations were necessary since atmospheric testing of the nonshrouded pilot did not duplicate engine or combustor rig flameout and/or coking problems.

The air shroud (see Figure 29) with the smallest allowable exit area exhibited stable operation over the widest operating condition. As pilot fuel flow rate was held nearly constant, the fuel/air ratio was rich at idle varying to lean at the maximum power operating condition. At the latter condition LBO can occur. Stable combustion was reestablished in the rig by slightly increasing the fuel flow rate. A single fuel flow rate was found that exhibited stable combustion over the entire operating range but was fuel rich at the low power operating conditions. Pilot fuel flow scheduling with power operation is recommended if the pilot is retained in the engine.

Engine operation with this shroud configuration did not show the improvement indicated on the combustor rig. Analysis revealed that the gap around the engine combustor pilot igniter was nearly an order of magnitude larger than the hole in the side of the pilot designed to control the airflow to the pilot axial air swirlers, shown in Figure 28. This gap allowed leakage (denoted upper leak) air to flow directly to the same volume supplying air to the pilot swirlers. This excess air resulted in LBO as the operating condition moved away from initial ignition. An increase in this gap area (due to wear) with time may account for the observed long term deterioration of pilot LBO stability. The occurrence of this phenomenon on the combustor rig is reduced due to differences in assembly procedure and the use of material to partially plug this gap. A design and fabrication of a modification to eliminate the upper airflow leak from this gap to the pilot axial air swirlers has been completed.

This modification is conical in nature and, as shown in Figures 28 (as a dotted line) and 30, extends from the swirler dome upstream to the pilot tube support walls.

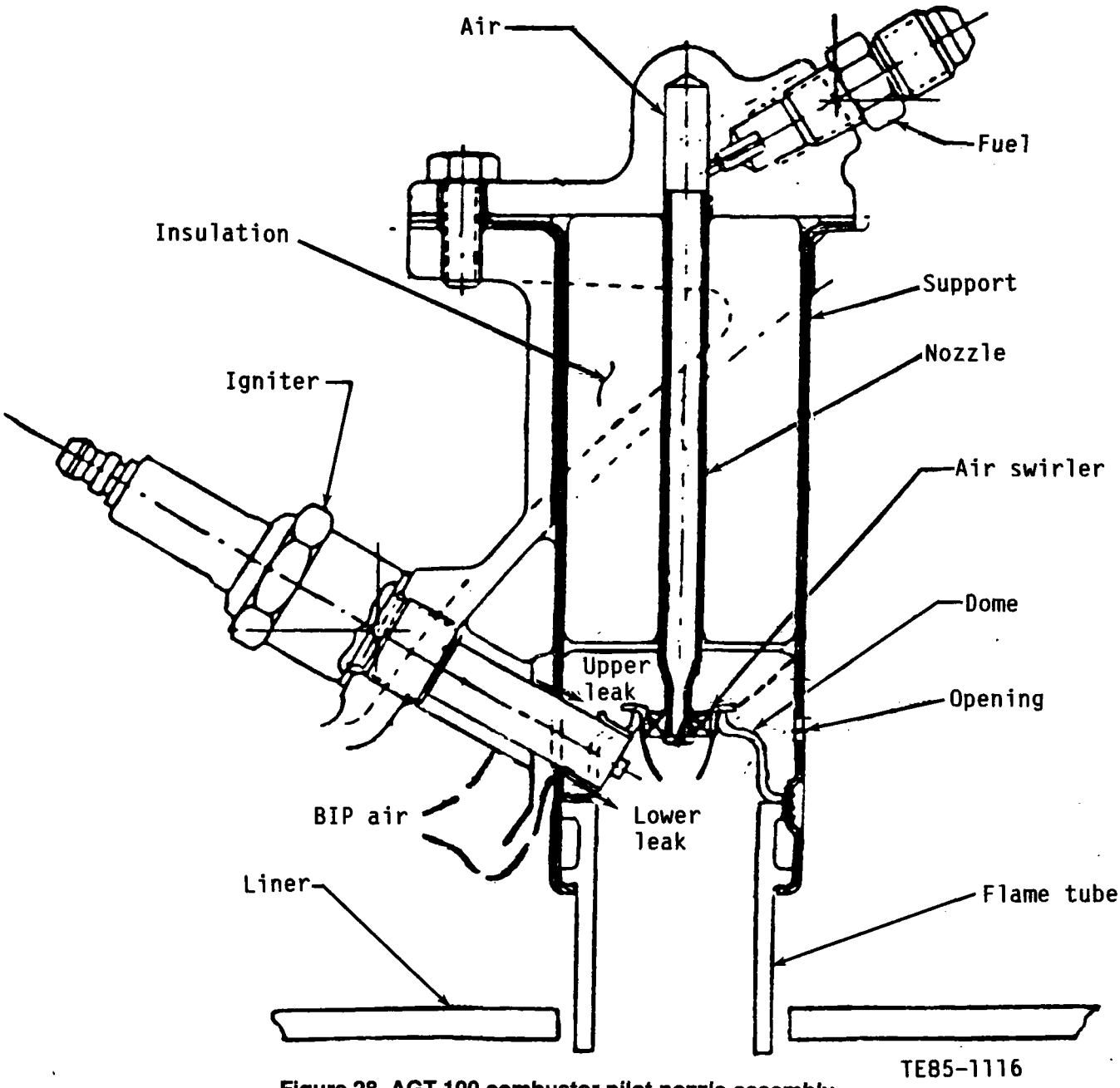

Figure 28. AGT 100 combustor pilot nozzle assembly.

The cone is welded in place and prevents air leakage flow around the igniters from directly entering the pilot axial air swirlers. The flow control hole (opening) in the side of the pilot (see Figure 28) is transferred to an air entry control orifice on the conical surface itself, shown in Figure 30. This new pilot configuration is scheduled to undergo combustor rig and engine test evaluations.

Electrical Igniter Testing

The ultimate goal of the ignition work is the elimination of the pilot flame. This goal has been achieved on the combustor rig. The two igniters on a new pilotless centerbody (see Figures 31, 32, and 33) ignited the start nozzle liquid DF-2 flow at accompanying airflows, producing fuel/air ratios and loadings equivalent to those spanning the engine operating regime from below normal ignition to above idle operating conditions. At a BVG setting of 5 mm (0.2 in.), the usual ignition condition, ignition occurred within 2 to 3 sec, which is within the time required to achieve ignition using the pilot flame. Ignition was achieved at a BVG setting of 7.6 mm (0.3 in.) but required 10 sec, and the range of airflow where ignition was possible was significantly reduced compared with the lower

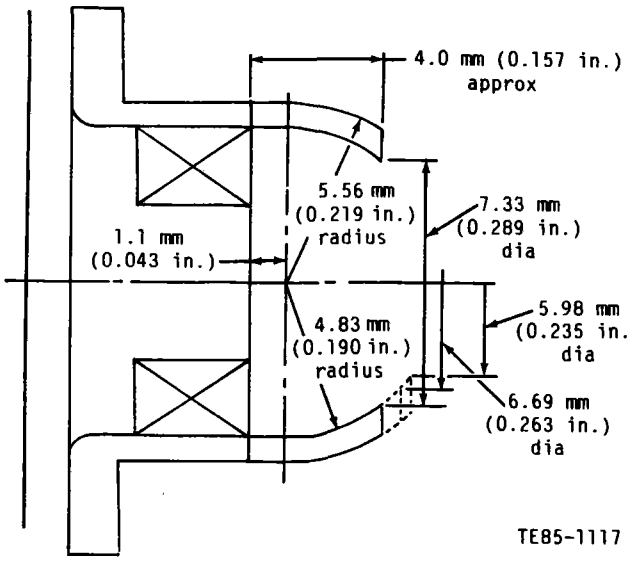

Figure 29. AGT 100 pilot nozzle shroud.

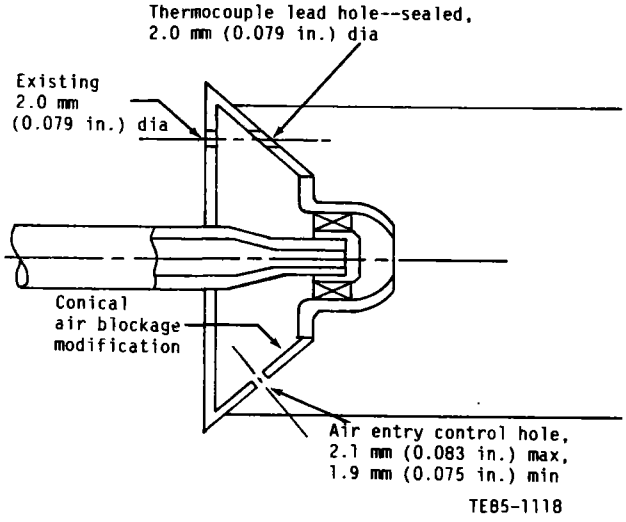

Figure 30. AGT 100 combustor pilot nozzle modification to eliminate upper air leakage to the pilot axial air swirlers.

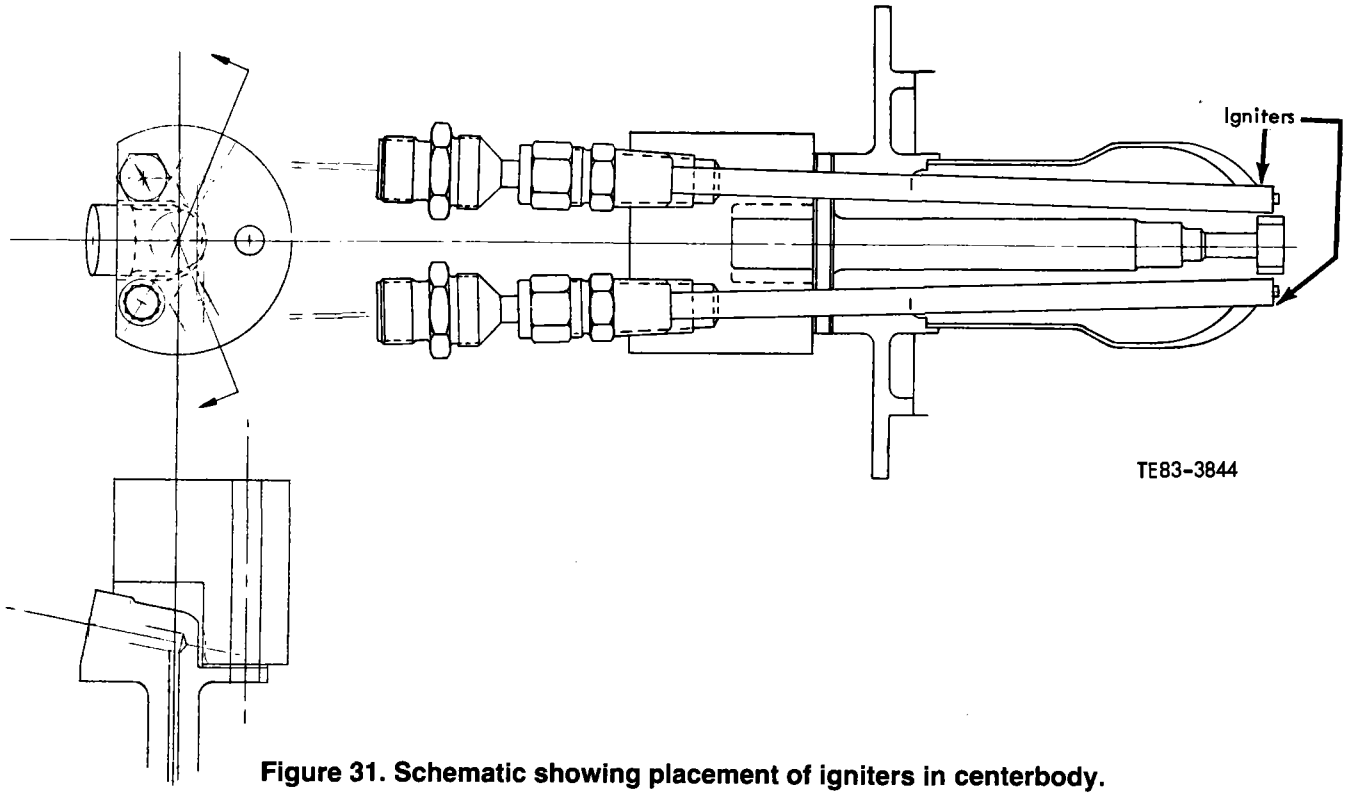

Figure 31. Schematic showing placement of igniters in centerbody.

BVG setting. This reduction confirms that the 5 mm (0.2 in.) BVG setting is near optimum for igniting the flow within the AGT 100 combustor. Ignition stability curves were mapped for the pilotless igniter and pilot flame systems, and the differences are inconsequential, as shown in Figures 34 and 35. The igniters were excited by a standard 12V capacitance system developing about 1 joule at 1 Hz intervals.

6.2.3 Start Nozzle Testing

Start nozzles were reworked early in the program to provide higher idle fuel flow rates, and their flow patternization profiles were found to be skewed 35 to 50% (maximum deviation between any pair of six sectors on the flow patternization rig). The start nozzles were again reworked to provide a more uniform (20%

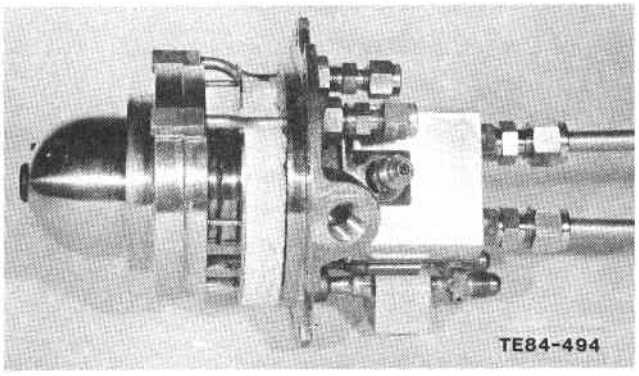

Figure 32. A side view of the pilotless combustor centerbody.

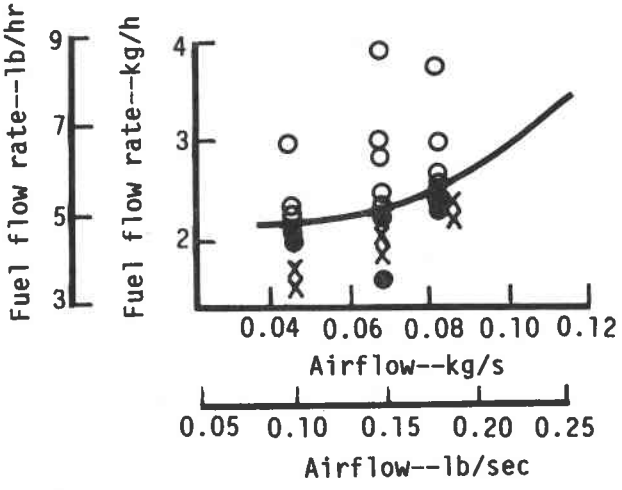

Notes:

1. Fuel flow includes pilot fuel flow of 0.23 kg/h (0.5 lb/hr) except for lean blowout points.
2. Pilot air assist pressure was 27 kPa (8.0 in. Hg) for all points.
3. Start nozzle air assist pressure was 1.7 kPa (0.5 in. Hg) for all points.
4. Variable geometry position was 5.1 mm (0.200 in.) for all points.

Key:

O Ignition

● No ignition

X Lean blowout without pilot

TE85-1119

Figure 34. AGT 100 start nozzle studies with pilot ignition.

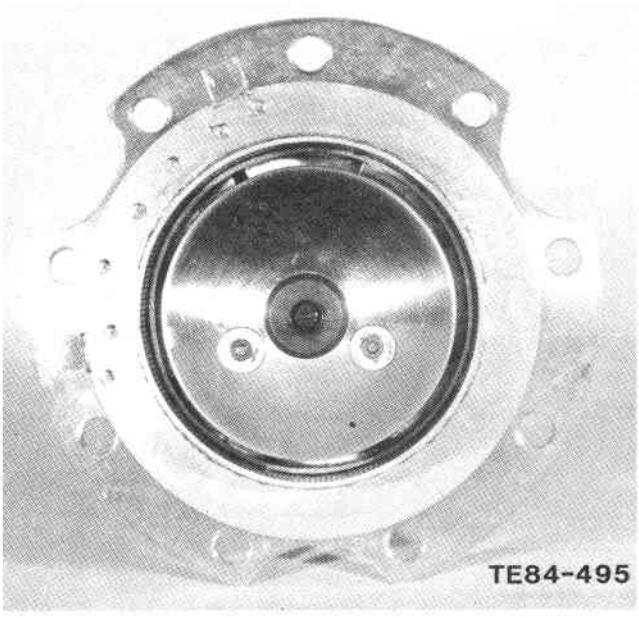

Figure 33. A front view of the pilotless combustor centerbody.

patternization) profile, and combustor testing at the cold start-up condition was successful. The start nozzles were reworked a third time using a newly developed Rochester Products Division method that enhances and smooths the fuel flow patternization profile. The technique is not sensitive to thermal distortion and has been found to improve performance and durability on other Allison combustors. Flow patternization profiles from these nozzles resulted in uniform flow (skew of less than 15%). Results from previous qualification tests indicate that operational characteristics improve as start nozzle uniformity improves.

6.2.4 Main Nozzle Testing

Nearly all of the main nozzle testing involved the development of the pilotless centerbody and pilotless combustor operation. Previous results indicate that a pilot is not required at higher BITs to sustain the main nozzle flame. The new design provides for start nozzle ignition with the placement of the igniters within the centerbody assembly, as described in Figures 31, 32, and 33. Testing was conducted to optimize the placement of the igniters. The present pilotless combustor centerbodies include a new cooling manifold surrounding the fuel tubes to suppress coking tendencies in the main fuel tubes at elevated BITs.

In the absence of a pilot, the combustor can flame out during main nozzle operation while the BIT is below the self-ignition limit of DF-2 (760°C [~1400°F] for the AGT combustor). To sustain combustion during this mode of main nozzle operation,

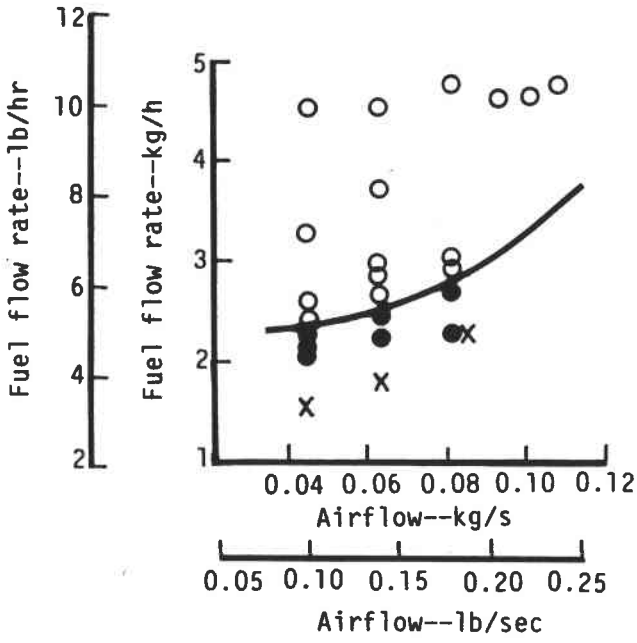

Notes:

1. No pilot fuel.
2. BVG set to 5.1 mm (0.200 in.)
3. Pilot air assist set to 27 kPa (8.0 in. Hg) for all points.
4. Start nozzle set to 1.7 kPa (0.50 in. Hg) for all points.

Key:

O Ignition

● No ignition

X Lean blowout

TE85-1120

Figure 35. AGT 100 start nozzle ignition studies using the centerbody igniter.

the BVG settings were changed to slightly increase the primary zone fuel/air ratio. Original BVG settings were established in the presence of a pilot flame and resulted in a primary zone fuel/air ratio that may be lower than the LBO limit in the absence of a pilot flame. Because little energy is required to sustain the flame at these conditions, the igniters in the centerbody will be energized at BVG settings of 10 mm (0.4 in.) and below to determine if the LBO margin can be widened. Currently, the engine is operating successfully without a pilot on the revised BVG schedule.

Rich-flashback (RFB) continues to be an operational difficulty when DF-2 is used as the fuel. Main nozzle investigation, testing, and modifications are dedicated to the elimination of this problem.

Review and evaluation of the last several months of burner rig and engine testing have been completed. These tests, using two different types of main fuel tube injection, have emphasized long duration continuous testing and have experienced difficulties with LBO and RFB operation. The latter phenomenon has presented severe problems and resulted in termination of many tests. Evaluation of the test results, engine teardown, and inspections indicated that, while the BVG operation and airflow path around the combustor required readjustment and optimization, the primary cause for the LBO and RFB phenomena is the method of fuel injection and filming.

RFB in the AGT 100 at normal operating conditions occurs because of fuel flow maldistribution in the prechamber causing a local increase in fuel/air ratio capable of sustaining flame propagation into the forward portion of the prechamber. Thermocouple and rig periscope video records confirm this observation. RFB at normal operating conditions is not an autoignition phenomenon. Depending on overall fuel/air ratio and the extent of the fuel flow maldistribution, the prechamber often experiences a localized initial flashback in a sector of the annular flowpath around the centerbody.

Fuel flow maldistribution increases with run time and appears to result from two distinct mechanisms. Centerbodies with exposed tubes (no water-cooled tube jacket manifold, as highlighted in Figure 36 by the tube delivery system labeled "old") to deliver the fuel to the filmer surface experience coking of the fuel within the delivery tubes near the elbow in the fuel tube. Because the elbow bends and the surrounding air temperatures are not uniform (circumferentially) from tube to tube, the extent of coking within the tubes is localized and leads to fuel flow maldistribution and subsequent RFB.

To eliminate the coking problem, a centerbody modification that shielded the fuel delivery tubes with a water jacket was designed. It is shown in Figure 36 as the portion labeled "new." The backside of the filmer surface forms one portion of this manifold. Installation of the manifold, of the new design blocks a significant portion of the filmer backside surface from exposure to BIT air. Initial testing using this injection technique with cooling water in the tube manifold jacket resulted in LBO problems. The water cooling of the tubes also affected the temperature of the filmer surface and the extent of fuel premix and prevaporiza-

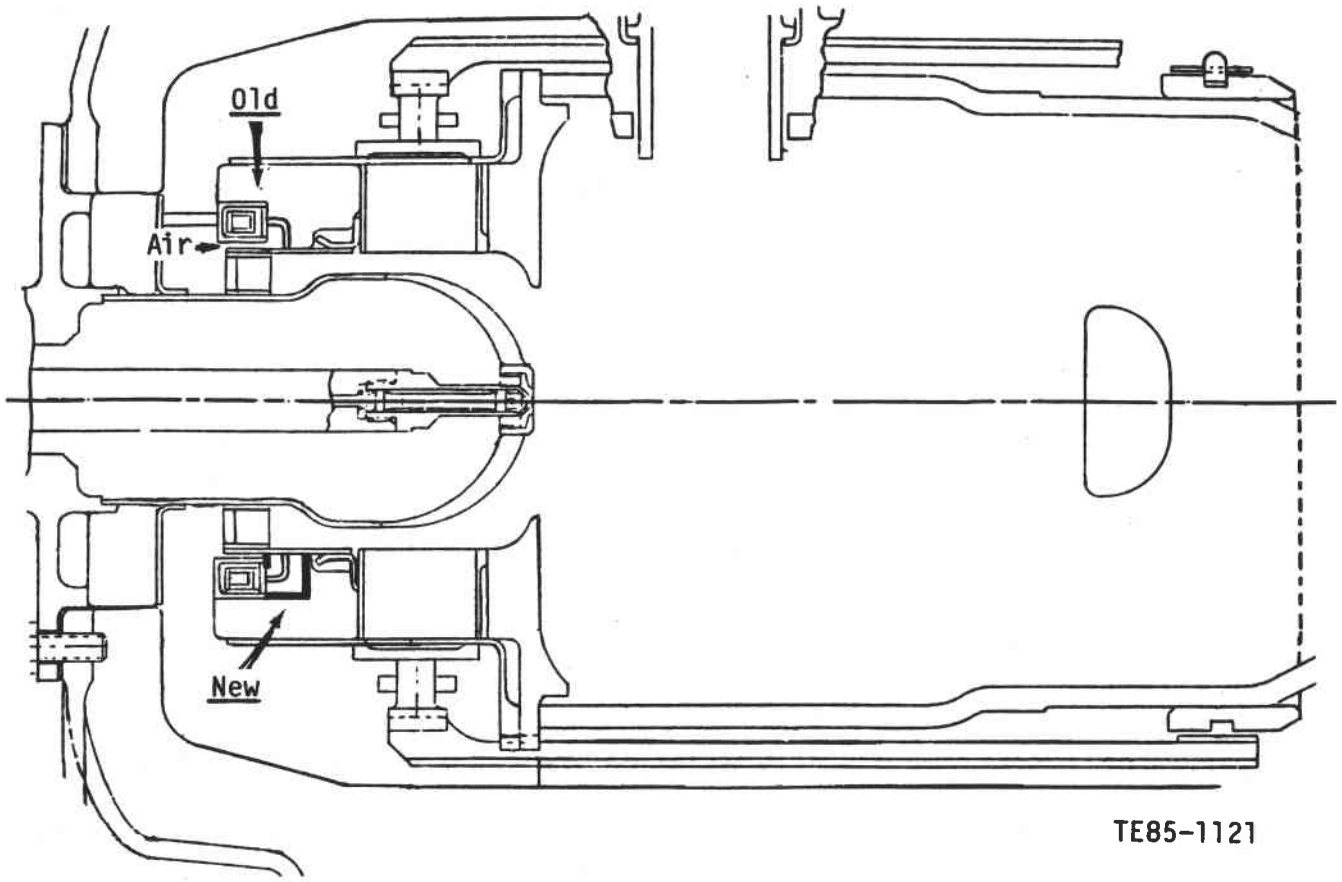

Figure 36. Present centerbody showing original (old) unjacketed main nozzle fuel delivery tubes and modified (new) jacketed main nozzle fuel delivery tubes.

tion. Rig tests using precise water flow rates to the fuel and tube cooling manifolds confirmed the narrowing of the LBO limit.

Engine and rig tests using this centerbody fuel injection modification employed reduced water flow to the fuel cooling manifold and no water flow to the manifold surrounding the fuel delivery tubes to eliminate LBO problems but RFB problems remain. Currently, the mechanism that results in fuel flow maldistribution is carbon buildup on the surface of the filmer. The rate of carbon deposition is sensitive to the filmer surface temperature. In the modified design, even with no water flow through the tube jacket manifold, the backside of the filmer surface is protected from direct exposure to the BIT air, and its temperture has been measured to be about 111°C (200°F) lower than that for the exposed tube centerbody injector, as shown in Figures 37 and 38. This initial difference in temperature is sufficient to initiate fuel fouling and carbon deposition. As expected, posttest inspection reveals that the carbon deposition is not uniform and local RFB conditions can occur following several hours of operation. Thermocouple measurements in the filmer backside are believed to indicate a continual deposition and periodic localized sloughing of carbon, as shown by point B in Figure 38. While the tube jacket cooling manifold has no cooling medium, the sheltering effect virtually eliminates tube coking. Similarly, no carbon deposition has been observed on the filmer surface of the exposed tube centerbody injectors, but the fuel cokes in the tubes near or at the elbow (in the tubes near or at the elbow) where a minimum cross-sectional area occurs.

In an effort to eliminate tube coking or filmer surface carbon deposition (depending on the centerbody/injector type used), rig and engine testing was altered to use cleaner JP-5 fuel. Based on an examination of JP-5 fuel stability characteristics and initial rig data, JP-5 fuel was expected to be more tolerant (with respect to RFB) to localized fuel maldistributions caused by tube coking and/or filmer surface carbon depositions.

Rig tests lasting several hours, using an exposed tube type centerbody design, indicated no problems. Following programming of a new JP-5/DF-2 BVG schedule into the engine controls, engine testing using a fuel tube jacketed manifold centerbody/injection design was also resumed. After several hours of run

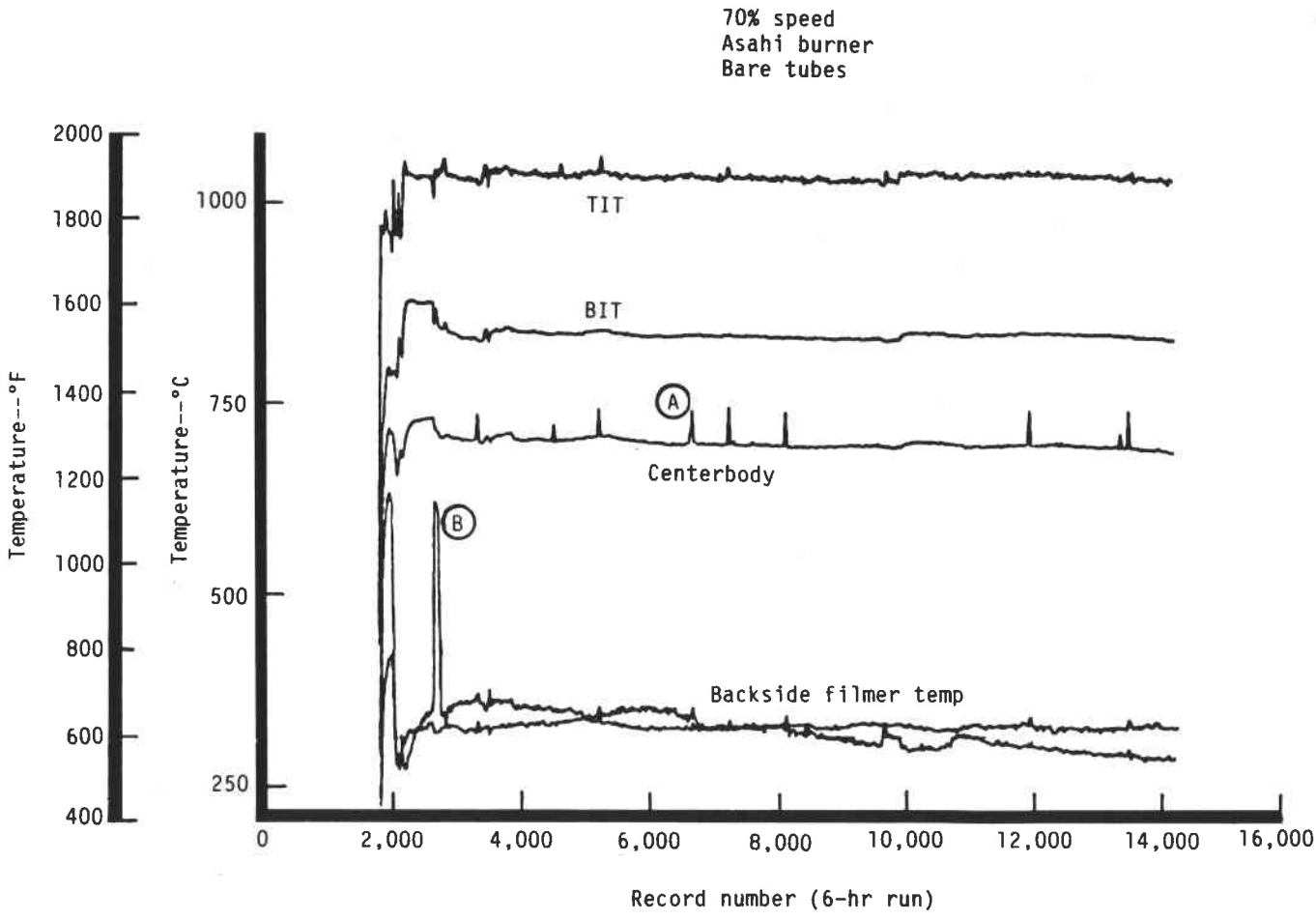

Figure 37. Turbine inlet, burner inlet, centerbody, and backside filmer surface temperatures as a function of time for original centerbody type.

time, no filmer surface carbon deposition occurred. Deposition was observed within this same run time duration when DF-2 was used as the fuel on this centerbody/injector design.

As a result of the evaluation of the DF-2 fuel engine tests (which included some experimental data specifically designed to relate tube coking/filmer surface carbon deposition to operating conditions and the onset of flashback) and the JP-5 fuel tests, a detailed flow and heat transfer analysis of the centerbody/main fuel tube delivery injection system was performed. The results of this study, which is being prepared as an engineering report, relate engine operating conditions (BIT and fuel flow rate) to fuel manifold maldistribution and fuel metal tube temperatures. These results are related to the onset of fuel decomposition, coking, and RFB.

The results of this study also indicate the need for an interim quick-fix centerbody/injector redesign. This redesign involves straightening the present exposed tubes to eliminate the elbow. The outer diameter of the fuel delivery tubes will be reduced to 0.51 mm (0.020 in.) while the inner diameter will become 0.30 mm (0.012 in.). This reduction in fuel tube diameters enhances the uniformity of the fuel flow distribution from the manifold and decreases the heat transfer to the fuel within the tube. Tube coking, as a result of this redesign, should be eliminated up to the point of ideal idle conditions of the present MOD-1 cycle (921°C [1690°F], 1.36 kg/h [3.0 lbm/hr] of fuel flow). Layout of this redesign was completed, and the modification of one of the exposed tube type centerbody designs is in progress. During this modification, provision for electrical igniters will be incorporated into the centerbody.

Results obtained from testing this interim design will help determine the final centerbody/injector design for use in alternate fuel testing. The final design

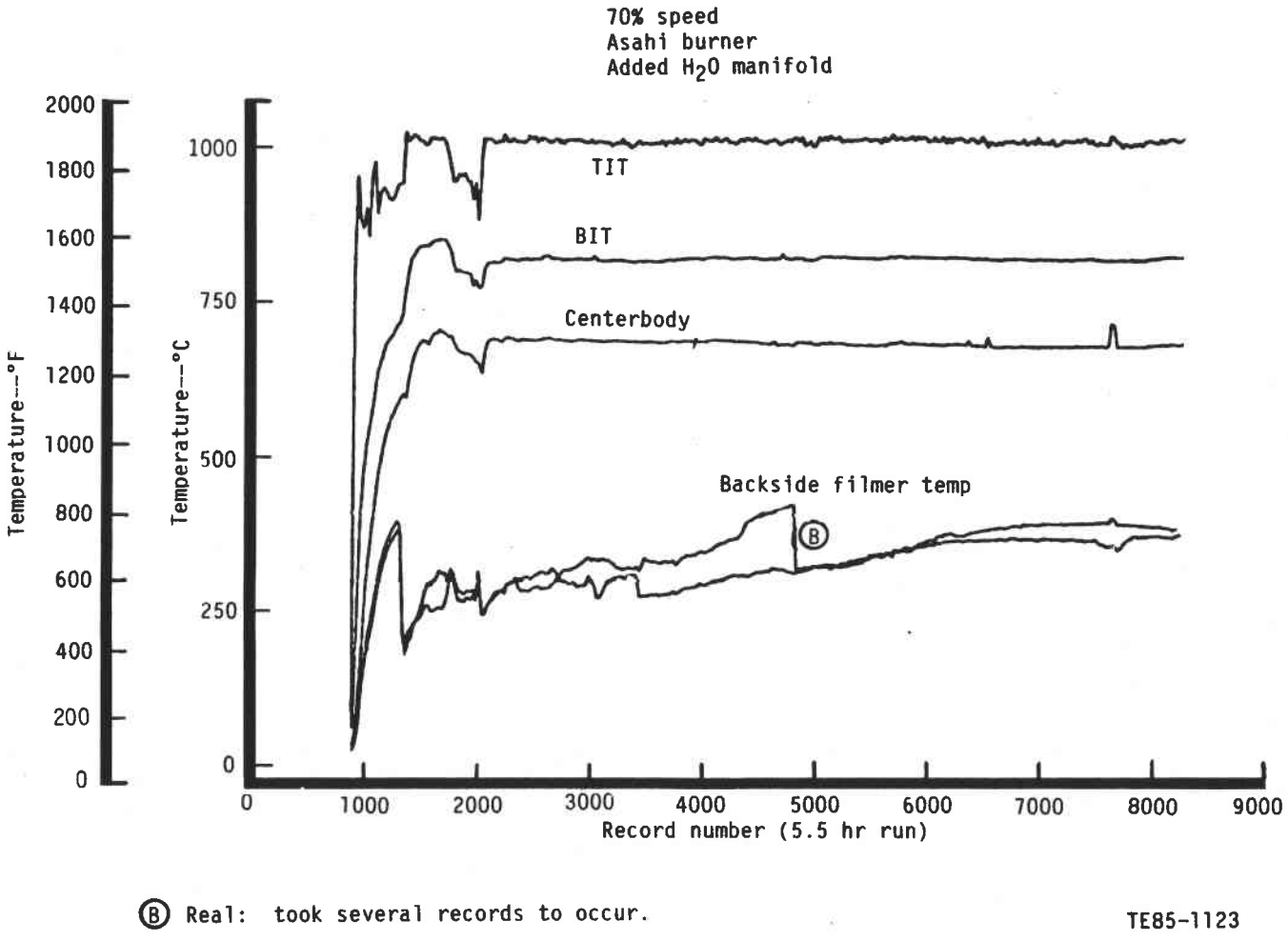

Figure 38. Turbine inlet, burner inlet, centerbody, and backside filmer temperatures as a function of time for modified centerbody type.

will have the capability of eliminating tube coking (regardless of fuel type) up to and including the RPD idle condition, 1024°C (1875°F) BIT and 0.91 kg/h (2 lbm/hr) fuel flow. This flexible fuel design incorporates a centerbody/injector system that lowers the fuel manifold downward toward the fuel filmer surface. Not only is the bend in the main fuel delivery tubes eliminated, the fuel tubes to the filmer surface are shortened to less than one-half their original length. Reduction of the exposed tube surface area to hot BIT air will eliminate main nozzle fuel tube coking at RPD conditions. The design eliminates backside cooling of the film surface by providing BIT air access to this location, similar to the interim design. The final design, shown in Figure 39, also permits splitting of the centerbody to allow access to the fuel delivery tubes for replacement for alternate fuel applications.

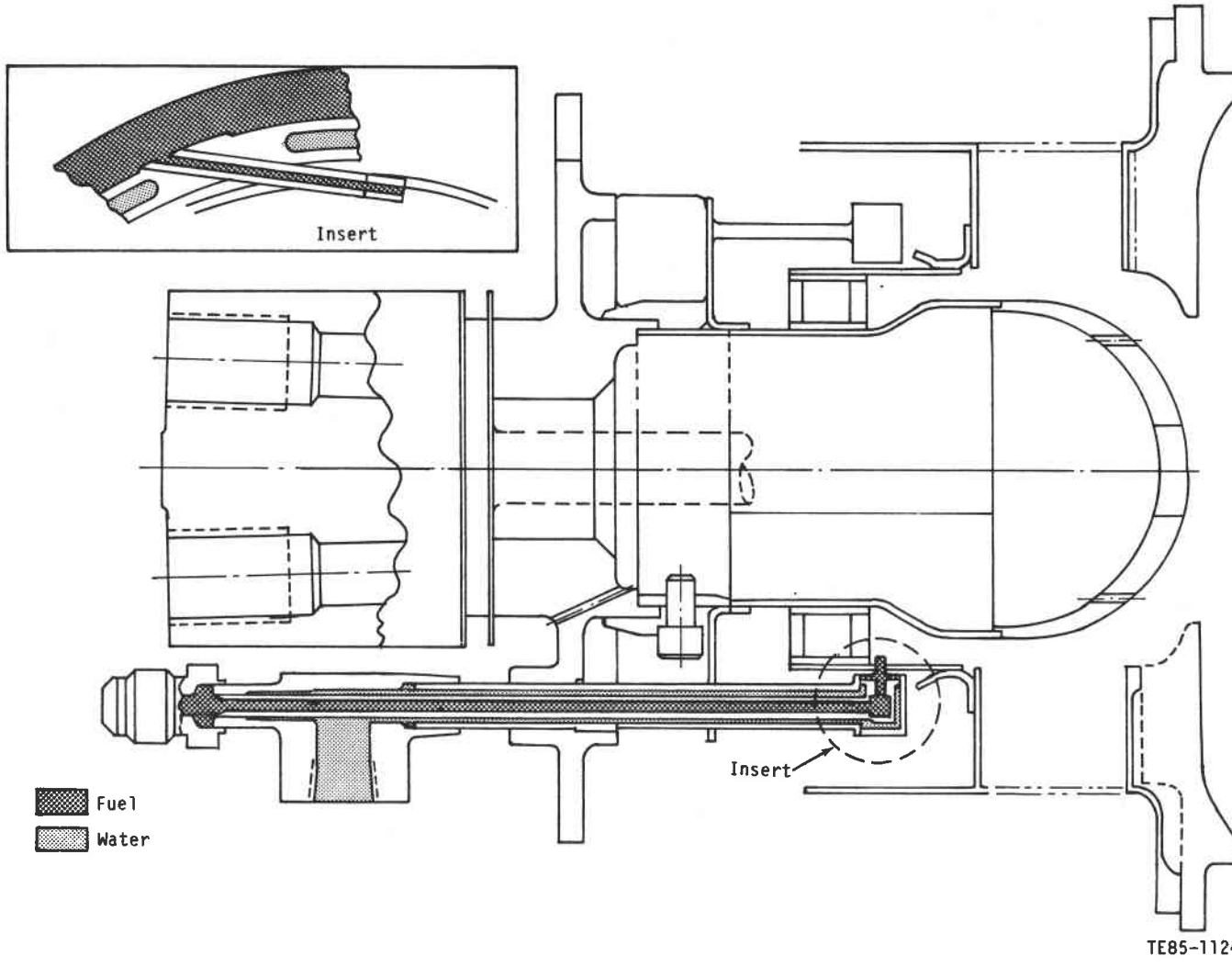

Figure 39. Final multifuel centerbody/injector design.

VII. REGENERATOR DEVELOPMENT

Regenerator development during the period has focused on the fabrication of new seal assemblies, limited rig testing, and the accumulation of engine test experience on the initial design regenerator hardware. Design studies of higher temperature inboard seals continued as work progressed toward the goals of 1065°C (1950°F) regenerator gas inlet temperature operation at system leakage levels of 3.7 to 5.2%.

7.1 DESIGN AND MATERIAL DEVELOPMENT

Design and material development effort, conducted in the following areas during this period, are discussed in detail in this subsection:

- design improvements to the outboard seal committed to hardware and an alternate polyimide material laboratory tested
- design studies of inboard seal wearface and leaf changes continued; fabrication initiated on laboratory test samples
- limited investigation of the cause for failure of the NGK/magnesium aluminum silicate (MAS) disk matrix
- work to certify new source for regenerator hardware with three additional disk/ring gear assemblies and two seal assemblies (one outboard, one inboard) delivered

7.1.1 Outboard Seals

Earlier testing with the molded single piece silicone leaf on a metal platform resulted in thermal distress of the room temperature vulcanizing (RTV) adhesive along the negative crossarm. Two modifications are to be tested: the first has a higher temperature adhesive (Loctite 596), and the second has the addition of a zirconia base thermal barrier applied along the crossarm to lower the heat flux into the silicone leaf adhesive, as shown in Figure 40.

The first monolithic polyimide seal platform/wearface with silicone leaf was rig tested 35 hr before a failure initiated by the shearing of an antirotation tab. A new part has been completed using Vespel SP22. The design was modified to reduce the seal torque loads and to strengthen the antirotation tab. This part has been completed and is ready for hot rig testing over the engine operating range, as shown in Figure 41. An alternate polyimide material, Pure Polybon L, underwent laboratory friction-wear testing; the results, shown in Table X, exhibit improved characteristics compared with the currently used SP22. Unlike SP22, Polybon L can be molded into a single piece to simplify fabrication and lower cost. Work is proceeding with the vendor to initiate tooling for platforms during the next reporting period.

Engine/rig experience is continuing to be accumulated with the current design, and two parts

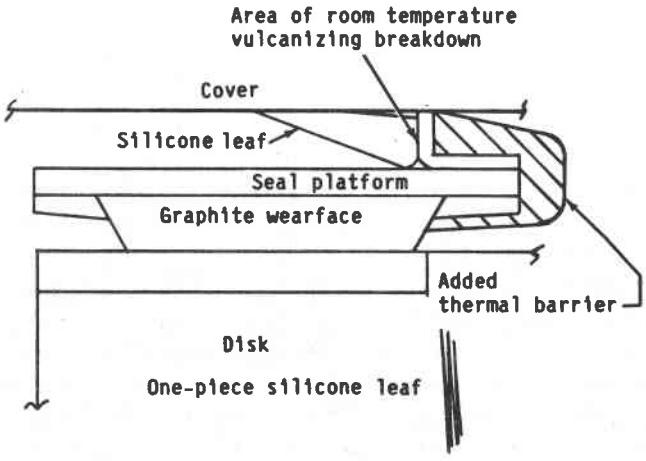

a. Section view illustrating thermal barrier added

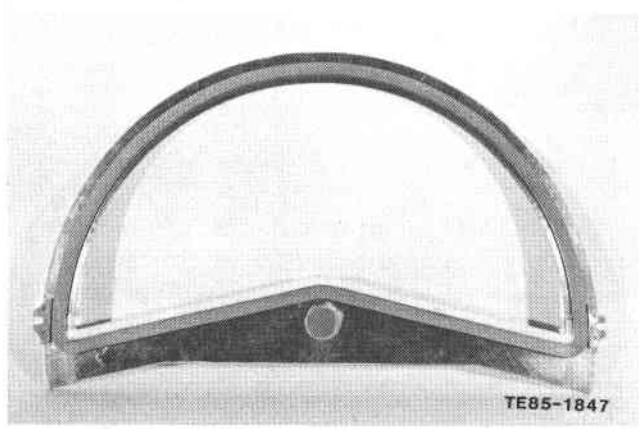

b. Completed seal assembly ready for test

Figure 40. Metal platform/silicone leaf seal assembly with thermal barrier.

Table X.
Friction/wear screening test results (6 hr at 103 kPa [15 lb/in.^{2}] contact pressure).

Material	Test conditions: Sliding velocity—m/s (ft/min)	Test conditions: Temperature—°C (°F)	Results: Coefficient of friction, μ	Results: Wear—mm (in.)
DuPont Vespel SP22	0.05 (10)	204/316 (400/600)	0.12/0.20	
	0.2 (45)	204/316 (400/600)	0.09/0.19	0.03 (0.001)
	0.5 (105)	204/316 (400/600)	0.08/0.16	
Pure Polybon M	0.05 (10)	204/316 (400/600)	0.07/0.12	
	0.2 (45)	204/316 (400/600)	0.07/0.08	0.08 (0.003)
	0.5 (105)	204/316 (400/600)	0.05/0.07	
Pure Polybon L	0.05 (10)	204/316 (400/600)	0.04/0.02	
	0.2 (45)	204/316 (400/600)	0.04/0.14	0.03 (0.001)
	0.5 (105)	204/316 (400/600)	0.03/0.09	

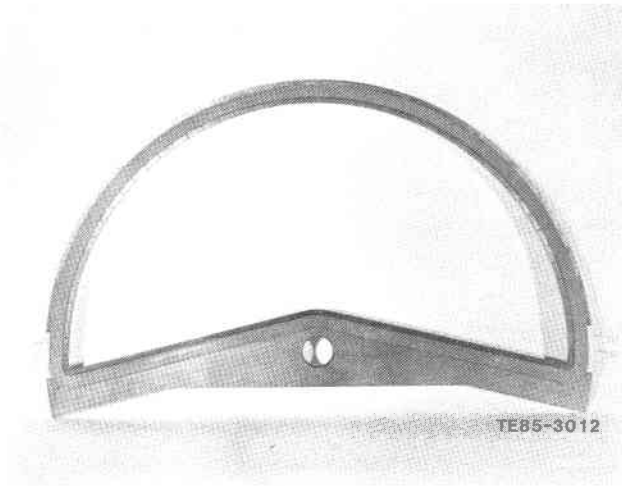

Figure 41. Polyimide platform/silicone leaf seal assembly.

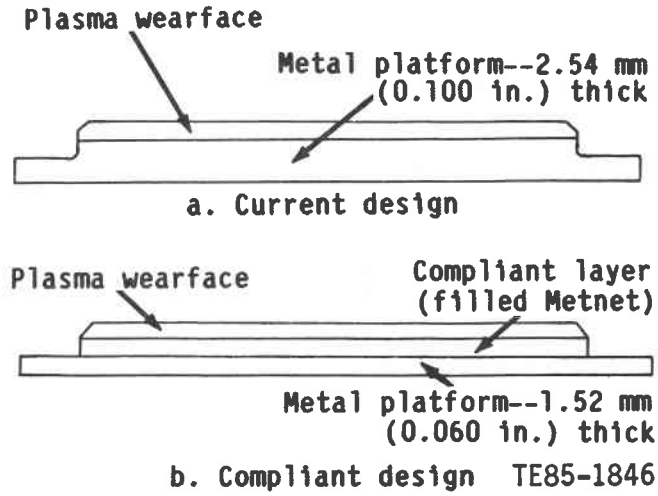

Figure 42. Cross section of inboard seal with compliant crossarm.

have each been tested for 160 hr at all operating conditions between idle and 100%.

7.1.2 Inboard Seals

The present inboard seal design is satisfactorily meeting current engine development objectives; one seal has accumulated approximately 200 hr (rig and engine) of testing, and two additional parts have accumulated 120 hr each. As discussed later, a new vendor, Tri Industries Inc (T-I), is being qualified for regenerator hardware. T-I is presently completing two additional inboard seal assemblies of the current design to provide additional engine test hardware and to establish a performance baseline for parts fabricated by T-I. These two parts are identified as H-5 and H-6. A third seal, H-7, substitutes the higher temperature I-112 plasma crossarm wearface, and a fourth, H-8, incorporates a more compliant crossarm (1.0 mm [0.060 in.] versus 2.5 mm [0.100 in.] thick platform) with a nickel oxide/calcium fluoride wearface applied over a filled Metnet substrate. This latter design change, shown in Figure 42, is based on earlier work (CATE program) where measurable reductions in leakage were obtained.

The next phase in development is to modify the compliant crossarm by introducing air flowing through the Metnet to reduce the heat flux to the platform (see Figure 43). Laboratory test samples of three concepts are being fabricated to determine the best configuration to introduce into seals H-9 and H-10. Also to be included in these later seals is a modified leaf design to eliminate welding of the leaves to the platform. The goal of these changes is to reduce inboard seal leakage (leaf and wearface) and to extend the operating temperature to 1010-1024°C (1850-1875°F).

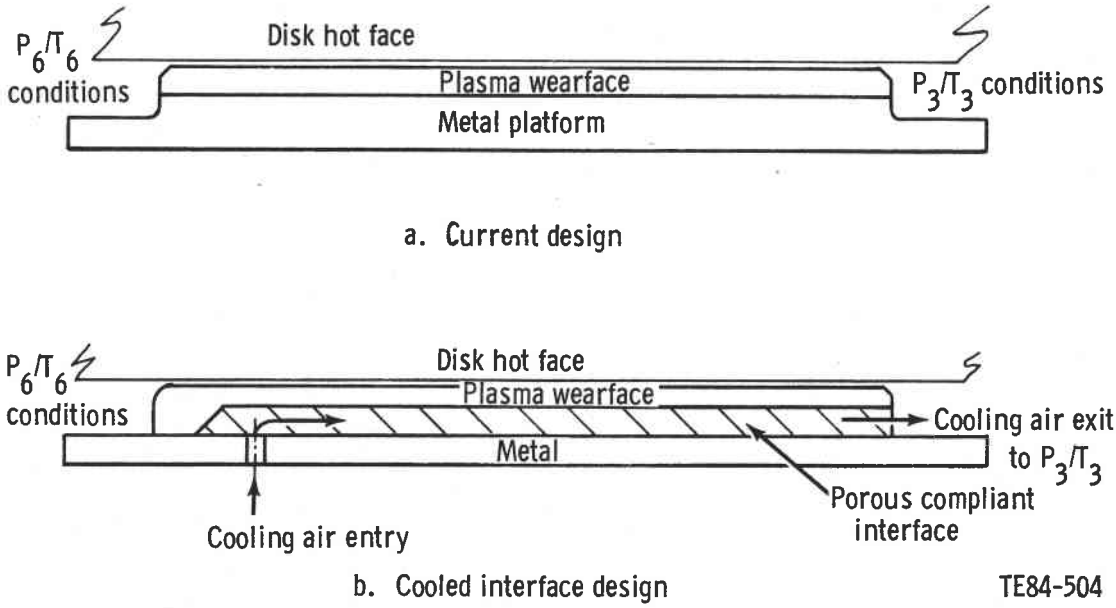

Figure 43. A comparison of the current seal crossarm and a cooling interface concept.

Seal assemblies H-5 through H-8 will be rig tested and engine qualified during the next two months. The laboratory test samples of cooled platform concepts are also nearing completion. In addition, work is continuing with Corning Glass on a ceramic platform (lithium aluminum silicate [LAS]) inboard seal design.

7.1.3 Regenerator Disk

The Corning Glass Works (CGW) code 9461 AS continues to be the prime regenerator disk material for the AGT 100 engine. The high time disk with about 224 hr (rig and engine) continues to be used in engine testing with no serious deterioration noted. Two additional CGW disks with reduced through-wall leakage have been readied for use in the program.

A regenerator material laboratory preliminary evaluation shows that ceramic porosity is the third major variable controlling the strength of CGW ceramic matrices. Previous work in the laboratory established the channel skew angle and separator wall thickness as two of the major variables in determining the tangential modulus of rupture, and these findings were verified by regenerator rig and engine exposed disk failure analyses.

Three out of four disks that failed in the Ceramic Applications in Tube Engines (CATE) and city bus programs ranked in the eight highest leakers out of a total of 40 disks. This ranking suggests a relationship between strength and leakage. The approach selected for this evaluation was to base the work on through-wall leak rate measurements since data of this type were already collected as established quality control criteria for individual engine disks. In addition, by using the standard test bars, the strength level and distribution were linked to the individual leak rate measurement and to the data base of the other variables: wall thickness, skew angle, radius, and disk. Multiple linear regression will be used to reduce the data.

Test data have been expanded to include a much broader range of permeation rate, separator wall thickness, and strength. This increased range was obtained by including data from two additional disks with higher and lower strengths. Figure 44 shows data from the three disks with tangential MOR plotted against permeation rate. Lower permeation provides higher strength. Multiple linear regression will be used next to determine the separate effects of porosity, wall thickness, and passage skew angle.

An extruded MAS matrix, supplied by NGK, was rig tested to evaluate its potential for use on the AGT 100. Forty-six hours of rig testing was completed on the second NGK extruded CO3P matrix disk (S/N G-2) to evaluate mechanical integrity of this latest mosaic disk (earlier CATE disks failed both in the rim and hub regions). The disk completed the testing but several deficiencies were noted, including the loss of rim relief slot filler material (causing excessive leakage) and the appearance of quasicircumferential stains in the hot face that developed into local breakdown of matrix separator walls (as shown in Figure 45). This disk was cut apart and the wall breakdown was found to correspond to extensive cracks in the matrix that extended through to the cold face. The

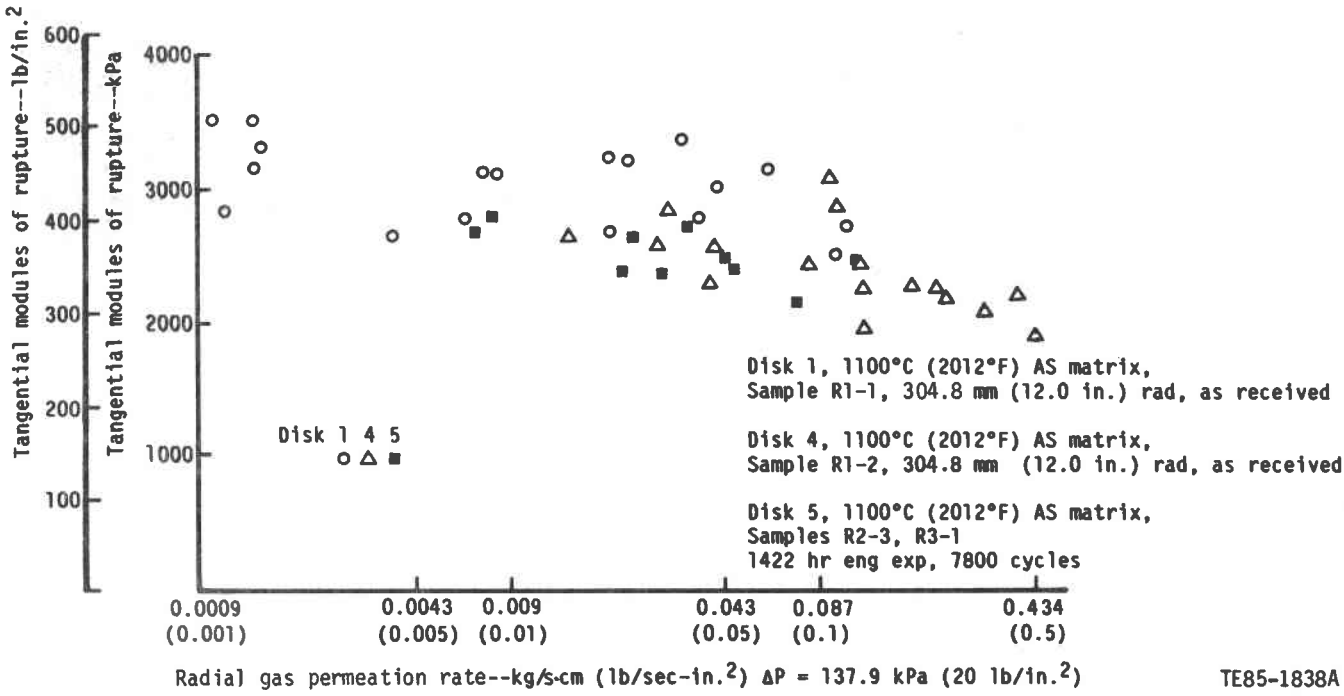

Figure 44. Gas permeation rate versus tangential modulus of rupture, 1100°C (2012°F) AS matrix, for three disks.

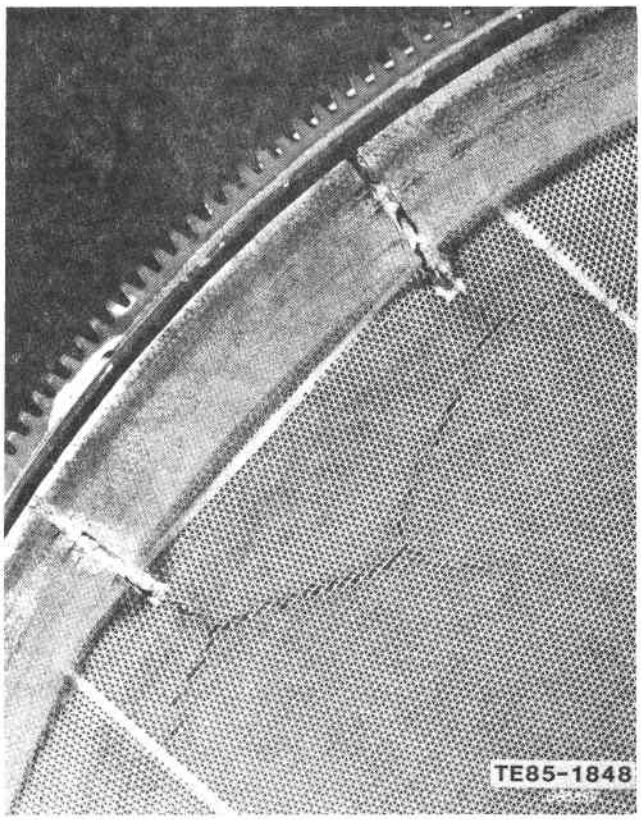

Figure 45. Hot face crack indications on rim of disk S/N G-2.

cracking, shown in Figures 46 and 47, was not visible prior to sectioning of the matrix. The remainder of this disk (G-2) and the first disk (G-1) were returned to NGK for further analysis and laboratory testing.

The NGK laboratories in Japan subsequently verified localized cracking both in G-2 and the initial disk (S/N G-1), which had been returned for repair of the rim filler slots. NGK has concluded that the impregnated (for reduced leakage) MAS matrix will not meet the operational requirements of the AGT 100 regenerator and suggests use of a denser matrix material currently under development at NGK. The addition of the impregnant to the MAS has raised its expansion coefficient, contributing to the failures found in disk G-2.

Laboratory analysis at NGK also defined improved rim slot filler materials that it is believed will operate satisfactorily at AGT 100 conditions (see Table XI). Two alternate materials have been selected for use on disks G-3 and G-4; also, disk G-1 is being repaired with the second alternate filler. A short back-to-back comparative rig test is planned to evaluate these fillers, disk leakage levels, and relative performance as compared with the CGW Code 9461 AS disk.

7.1.4 Parts Fabrication

Work has continued during this period to qualify T-I as a supplier of regenerator parts. As reported

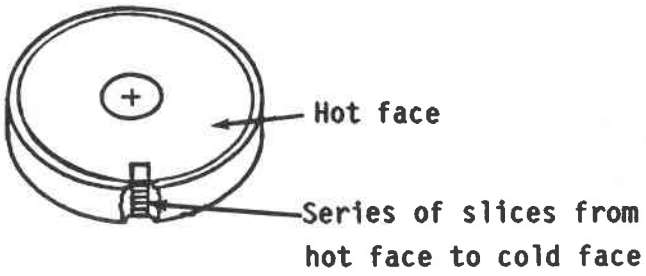

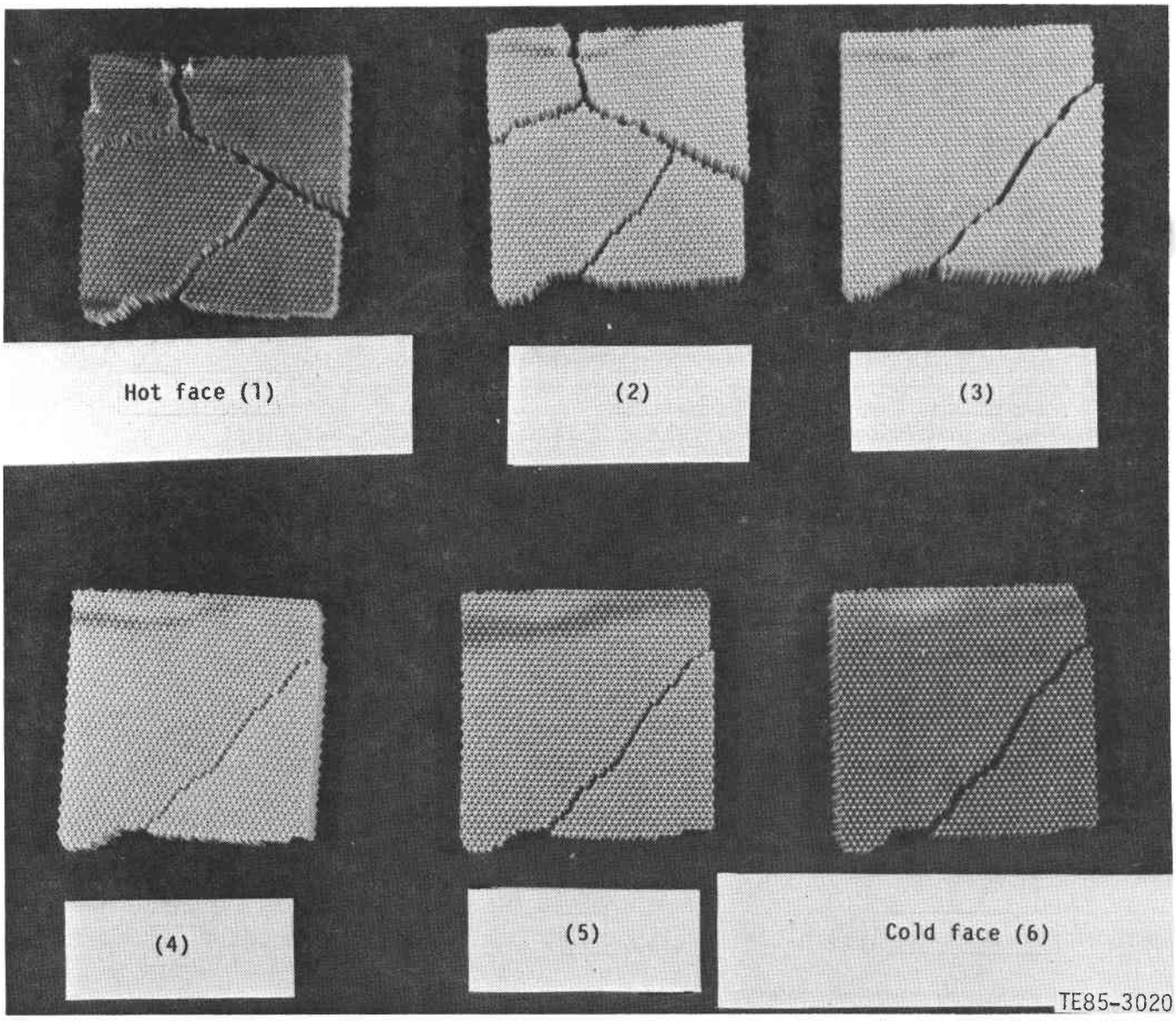

Figure 46. Matrix samples cut from disk S/N G-2 showing crack propagation.

earlier, T-I had delivered several disk/ring gear assemblies and outboard seals. Rig testing of these parts has shown all to be of acceptable quality. Most recently work has been concentrated on the completion of qualified inboard seal assemblies, and delivery of the first part occurred at the end of June. Additional tooling was found to be required, and three additional seal assemblies are scheduled by 1 September.

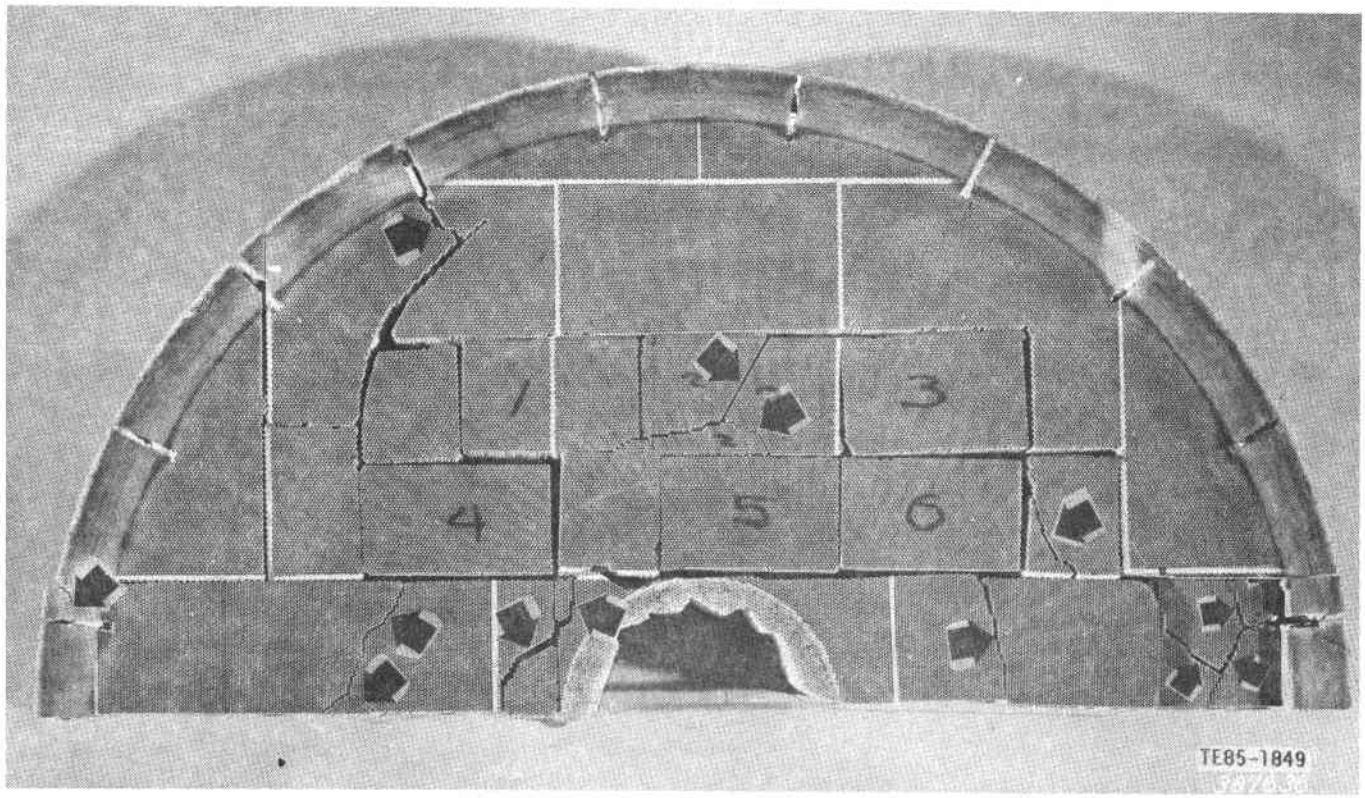

Figure 47. Extensive cracking of NGK extruded MAS regenerator disk S/N G-2.

Table XI.
Disk rim slot filler materials — summary of NGK laboratory evaluation.*

	Original filler— MAS frit/core powder (80/20%) Disk G-1 and G-2	First alternate— alumina cement/ mullite (33/67%) Disk G-3	Second alternate— QF 180/core powder (70/30%) Disk G-4 and G-1**
Bending strength across joint—kPa ($lb/in.^2$)			
Room temperature	0-586 (0-85)	1448-1965 (210-285)	1172-2930 (170-425)
After 800°C (1472°F) HT	0-1069 (0-155)	207-1655 (30-240)	1172-2586 (170-375)
Leakage—$kg/s\text{-}m^2$ ($lb/sec\text{-}in.^2$)			
Room temperature	5.5×10^{-2} (7.8×10^{-5})	$2.0\text{-}2.5 \times 10^{-2}$ ($2.9\text{-}3.5 \times 10^{-5}$)	4.0×10^{-2} (5.7×10^{-5})
After 900°C (1652°F) HT	7.5×10^{-2} (10.6×10^{-5})	$3.5\text{-}4.5 \times 10^{-2}$ ($5.0\text{-}6.4 \times 10^{-5}$)	4.0×10^{-2} (5.7×10^{-5})
Thermal shock resistance (fracture temp)—°C (°F)	650† (1202)	800-900 (1472-1652)	850 (1562)

* Ref TN 84-SC-065, NGK Insulators, Ltd
**S/N G-1 repaired
†Not laboratory tested, cracked in disk during hot rig tests at Allison

During this period, Corning completed the salvage/repair of two ceramic bulkheads damaged earlier in engine testing (due to misalignment/interference with the power turbine/regenerator inlet coupling). CGW removed the damaged section and cemented a mating inlet to each, as shown in Figure 48. These parts are to be pressure proof tested again prior to engine use.

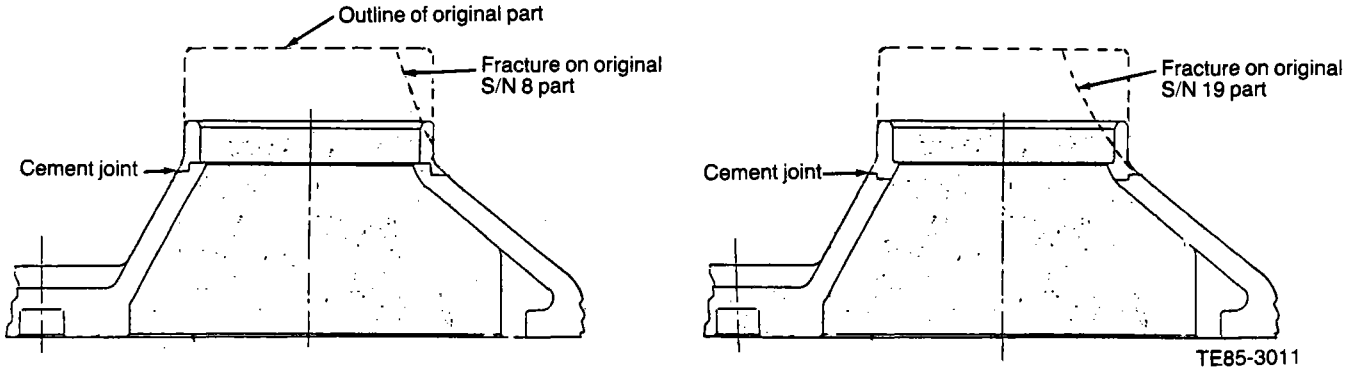

Figure 48. Salvage rework to repair fractured ceramic bulkheads.

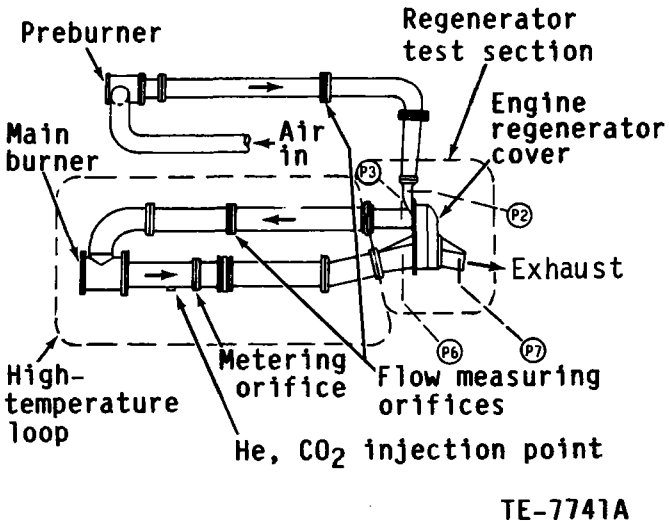

Figure 49. Probe locations for leakage measurement based on gas sampling (high temperature regenerator rig).

7.2 RIG DEVELOPMENT TESTING

Regenerator rig development testing was limited to completion of the NGK disk testing in January and rig checkout in June in preparation for investigation and development work scheduled for summer of 1984. During the inactive period, additional gas sampling probes were added to monitor the flow at the stations shown in Figure 49 (P2, P3, P6, P7), and provisions were made for injecting gas (either $C0_2$ or He) downstream from the main burner. These modifications were made for testing to evaluate the feasibility of using gas samples to determine leakage levels in the engine.

Two approaches are being considered for measuring engine leakage by gas tracing. One is to calculate the amount of air infiltrating the gas path between two points from the decrease in volume concentration of carbon dioxide between the two points. The concentrations are measured using conventional emissions instruments. Use of the hot regenerator rig permits correlation between the rig measured leakage and the leakage calculated from the gas sample data.

The other approach considered for the engine is to seed the gas path with helium at the inlet, exhaust the flow after the compressor, supply clean flow to the turbines through the regenerator, and sample the exhaust for helium leaking past the high pressure seals. The helium concentrations are measured using a mass spectrometer. The leakage is calculated from the ratio of helium in the exhaust to helium in the inlet flow. The regenerator rig will be used to develop the helium seeding and gas sampling techniques but will not provide qualification of this measurement technique.

The first test of the carbon dioxide dilution measurement technique took place 7 July 1984. Gas sample data were obtained for the operating points of 100% speed, 97 km/h (60 mph), 64 km/h (40 mph), and 32 km/h (20 mph). A problem with the gas sample manifold was detected after the 100% point was completed and eliminated these data from consideration.

The gas samples were analyzed using conventional emissions measurement equipment. The volume concentration measurements were translated into a leakage mass fraction using the combustion equation and an equation derived from continuity and species conservation equations.

The results of the shakedown test were encouraging. Comparisons of the rig direct leakage measurements and the indirect tracer gas leakage measurements are given in Table XII.

Further rig testing is planned to refine the technique and to extend its range to smaller quantities of leakage. The seeding of the flow path with CO_2 downstream of station 3 but upstream of station 6 is expected to increase the magnitude of the leakage signal CO_2, thereby improving measurement accuracy for smaller leakage amounts.

7.3 ENGINE TESTING

Three engine builds and 49 hr of hot engine testing were completed during this period; all testing was with a single set of seals and a single disk to accumulate operating experience. Testing was to a maximum of ~925°C (1700°F) regenerator gas inlet temperature. Soakback testing after shutdown was evaluated and temperatures monitored in the regenerator. No excessive temperatures were tracked in the regenerator. One ceramic bulkhead has accumulated more than 40 hr of engine test time. Regenerator performance has remained stable during testing completed in this period.

Table XII.
Comparison of rig and tracer gas leakage measurements.

Condition— km/h (mph)	Rig leakage— % inlet flow	Tracer gas leakage*— % inlet flow
97 (60)	9.92	9.97
64 (40)	10.21	10.64
32 (20)	11.35	6.94

*Leakage fraction is related to inlet flow by the ratio of two rig measured flows.

VIII. SECONDARY SYSTEMS

Progress during 1984 has been made in the following areas:

- power transfer clutch
- oil pump and regulating valve
- mechanical loss test
- bearings
- bearing temperature limits
- carbon seals

8.1 GEARBOX

8.1.1 Power Transfer Clutch

The AGT 100 clutch was dynamically tested for the first time during BU3 running of engine S/N 2. The clutch test entailed locking the clutch at near synchronous rotor speeds. Clutch actuation oil pressure was controlled manually by the electronic control unit. The clutch was locked at 60% speed, and data were subsequently taken at 60% and 70% speeds. The clutch performed satisfactorily with no apparent difficulties. Further dynamic clutch testing will be performed to verify the load carrying capacity and slipping operation of the clutch.

Static testing of the clutch during the previous year verified its torque capability at the regulated system oil pressure of 483 kPa (70 lb/in.^{2}). However, to ensure adequate actuation pressure that will account for part variations between clutches, the actuation pressure has been increased to 586 kPa (85 lb/in.^{2}). This requires a like increase in regulated system oil pressure. These changes will provide greater flexibility in the use of engine hardware.

8.1.2 Oil Pump and Regulating Valve

During BU 11 operation of AGT 100 engine S/N 1, problems with sustaining engine main oil pressure resulted in premature termination of engine testing. Upon engine teardown, the oil pump regulating valve was found stuck in the open or bypass position. This engine pump did not include the modification proposed in the 1983 July-December semiannual report. Since publication of that report, the modified oil pump has also been shown to operate erratically. A more extensive pump redesign has since been developed that provides improved valve seating, which eliminates the previous valve's tendency to become unseated by the oil inlet passage (see Figure 50). In addition, the internal passages of the pump have been modified to reduce losses, and the valve is now guided by the valve spring rather than by the valve chamber to further reduce chances of sticking. The new design also employs a higher rate spring to provide the increased system pressure required for clutch actuation. Both S/N 1 and S/N 2 intermediate gearcases have been modified to accept plumbing for an external test stand oil pump until an engine oil pump incorporating this second modification can be bench-tested.

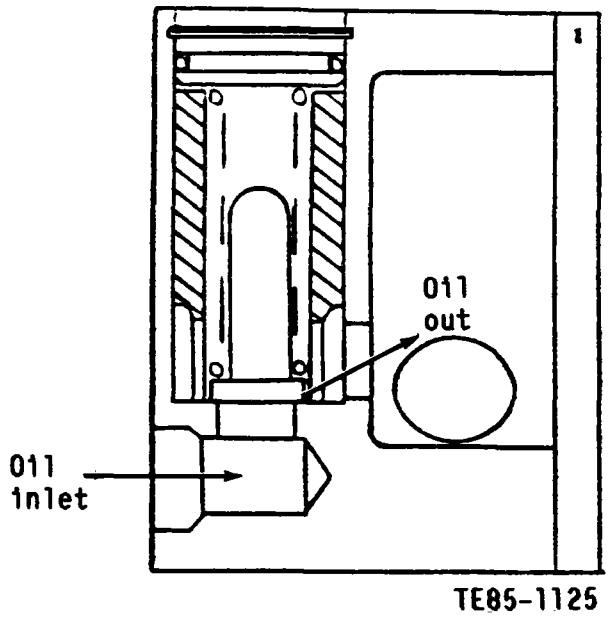

Figure 50. Revised oil regulator design.

8.1.3 Mechanical Loss Test

A special motoring test was performed during BU4 operation of engine S/N 2 to identify the mechanical losses of the engine drivetrain. The test goal was to measure the parasitic power losses associated with the gearbox and engine.

Theory and practice show that reduction power losses vary with speed and torque. Total power losses are the sum of the speed sensitive losses and the transmitted-torque sensitive losses. Speed sensitive losses include four components: windage losses, oil churning losses, mechanical friction losses (due to weight of parts), and oil pump work. Transmitted-torque sensitive losses are mechanical friction losses

resulting from gear tooth loss loads and bearing reaction loads.

The engine was built with bladeless turbine and compressor components to eliminate unrelated aerodynamic losses. Regenerator drive power was obtained from separate testing and added to the results of this test to obtain total system power loss.

The test plan was to measure overall system loss and to investigate the effects of oil temperature, engine speed, and transmitted torque on system loss. The testing followed this plan:

1. gasifier only (no load)
   - 38, 93, 121°C (100, 200, 250°F) oil-in temperature
   - measure drive torque at 50-100% speed at each temperature
2. complete drive train (no load)
   - 38, 93, 121°C (100, 200, 250°F) oil-in temperature
   - measure drive torque at 50-100% speed at each temperature
3. complete drivetrain (with load)
   - 38, 93, 121°C (100, 200, 250°F) oil-in temperature
   - output loads of 3.7, 7.5, 11.2, 14.9 kW (5, 10, 15, 20 hp) (100% rpm)
   - measure drive torque at 50-100% rpm at each temperature and load

Figure 51 depicts loss curves representing total engine losses at 93°C (200°F) oil-in temperature. The load-sensitive loss portion of Figure 51 was estimated using a gear efficiency computer program developed by N. E. Anderson and S. H. Loewenthal. This program was used because test data were only taken up to 7.5 kW (10 hp).

The speed-sensitive measured losses are shown compared with previously estimated losses in Figure 52. Figure 52 shows there is good agreement between the estimated losses and measured losses at the lower speeds, and at higher speeds the estimated losses are slightly lower than the measured losses for both oil jet and oil mist lubrication.

8.2 BEARINGS AND SEALS

8.2.1 Bearings

TD11 of engine S/N 1 revealed damage to the No. 2 bearing separator. The subsequent investigation showed incorrect jet targeting and inadequate separator design to be probable causes of separator distress. The bearing oil jet was incorrectly targeted,

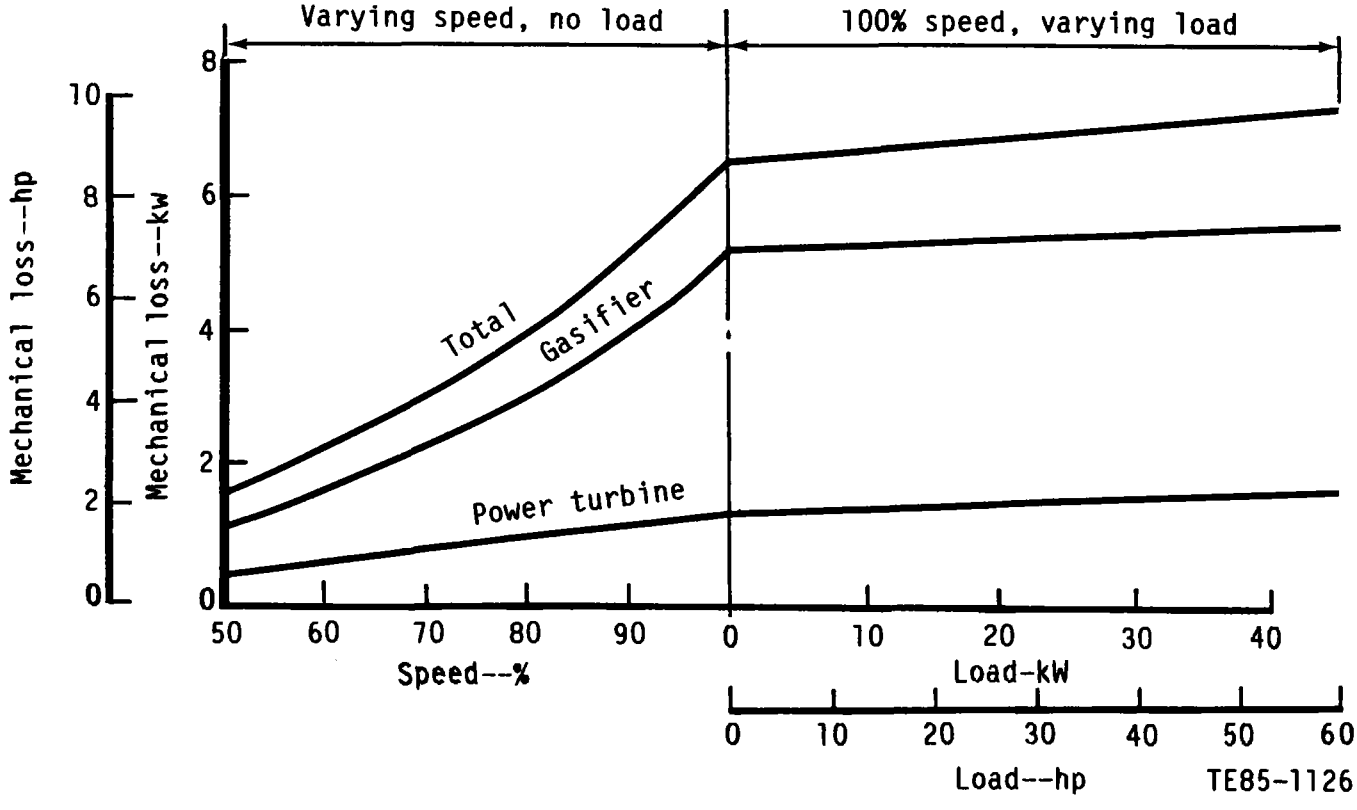

Figure 51. Total system power loss based on measured loss using oil jet lubrication.

resulting in the oil stream being partially deflected by the No. 2 bearing shimpack. The oil jet has been retargeted to avoid the shimpack and provide adequate lubrication for the No. 2 bearing.

1. Measured loss with oil jet lubrication
2. Measured loss with oil mist lubrication (line 1 adjusted)
3. Estimated loss with oil jet lubrication
4. Estimated loss with oil mist lubrication

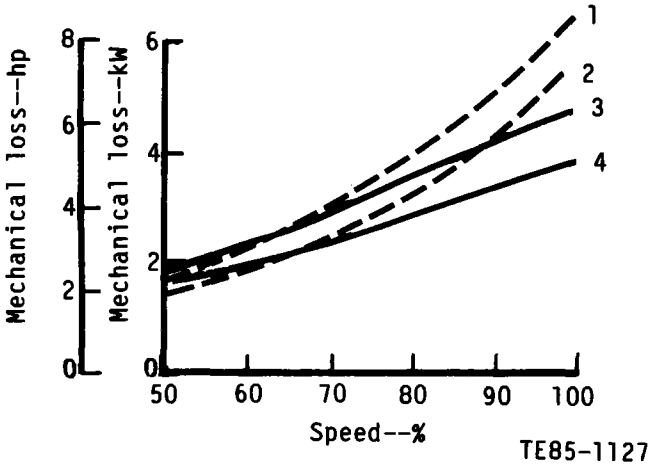

Figure 52. Total loss comparison of measurement with design estimate at no-load condition.

The No. 2 separator was a stamped bronze ribbon design with formed retaining flanges. This separator was replaced with an alternate heavier, fully machined separator as a short term improvement. Longer term steps have been taken to replace all mainshaft bronze separator bearings with fully machined, silverplated, steel separator bearings.

During BU7 running of engine S/N 2, the No. 4 bearing exceeded its temperature limit and forced a premature engine shutdown. The resulting investigation revealed a partially blocked No. 4 bearing jet as the probable cause of bearing overtemperature. In addition, the No. 4 bearing drain was found to be susceptible to blockage induced by coking and debris. The bering jet was deburred and flow-tested to ensure adequate flow and targeting, and the bearing drain was enlarged to reduce its susceptibility to blockage.

8.2.2 Bearing Temperature Limits

During BU3 running of engine S/N 2, specific testing was performed to determine the thermal effects of normal engine shutdown (soakback). All testing until that time had used motoring of the engine after shutdown to maintain low bearing temperatures during soakback. During the soakback testing, the following increased bearing temperature limits were established. These limits are judged to be the maximum soakback temperatures allowable for long bearing life.

Bearing position	Shutdown—°C (°F)
1	302 (575)
2	163 (325)
3	149 (300)
4	302 (575)
5	204 (400)

Two shutdowns were made from 60% speed: one from 982°C (1800°F) turbine inlet temperature and the other from 1038°C (1900°F) turbine inlet temperature. The No. 5 bearing proved to be the most critical by nearly reaching its limit during the 982°C (1800°F) shutdown and reaching its limit during the 1038°C (1900°F) shutdown. As a result of this test, the following soakback temperature limits have been adopted:

Bearing position	Running—°C (°F)	Shutdown—°C (°F)
1	177 (350)	260 (500)
2	149 (300)	149 (300)
3	135 (275)	135 (275)
4	177 (350)	260 (500)
5	177 (350)	191 (375)

8.2.3 Carbon Seals

Carbon seal progress during the past year has been limited by the high levels of shaft whip encountered during AGT 100 engine testing. During BU3 running of engine S/N 2, all three carbon seals on the gasifier shaft assembly were damaged after encountering 0.292 mm (0.0115 in.) of shaft whip. To prevent further shaft and seal rub, the clearances at seal locations behind the impeller and in front of the gasifier and power turbine rotors were increased for BU 11 and BU12 of engine S/N 1 and for BU4 through BU8 of engine S/N 2. These increases are tabulated in Table XIII.

However, as a result of these increased seal clearances, the pressure balance across the air-buffered carbon seals was disrupted. TD12 of engine S/N 1 and TD7 of engine S/N 2 revealed the gasifier carbon seal elements to be severely oxidized, while the power turbine carbon seal elements remained intact. Data obtained during BU5 through BU7 running of engine S/N 2 showed the gasifier seal pressures to be disrupted the worst with backflow of hot gases from the gasifier turbine through the carbon seal evident early in the test.

To address the seal pressure imbalance situation, the AGT 100 secondary airflow computer model will be used to predict carbon seal pressure balances for various seal clearances. The modifications reported in the 1983 July-December semiannual report (i.e., increased gasifier seal cooling and high temperature carbon elements) will continue to be monitored, and alternate seal configurations will continue to be investigated.

Table XIII.
Carbon seal clearances.

	Overall diametral clearance—mm (in.)					
	Seal No. 1A and 1B		Seal No. 2		Seal No. 4A and 4B	
	Mininum	Maximum	Mininum	Maximum	Mininum	Maximum
S/N-1, BU10	0.081 (0.0032)	0.119 (0.0047)	0.076 (0.0030)	0.114 (0.0045)	0.081 (0.0032)	0.119 (0.0047)
S/N-1, BU 11	0.160 (0.0063)	0.198 (0.0078)	0.135 (0.0053)	0.165 (0.0065)	0.180 (0.0071)	0.218 (0.0086)
S/N-2, BU3	0.081 (0.0032)	0.119 (0.0047)	0.076 (0.0030)	0.114 (0.0045)	0.081 (0.0032)	0.119 (0.0047)
S/N-2, BU4-8	0.160 (0.0063)	0.198 (0.0078)	0.135 (0.0053)	0.165 (0.0065)	0.180 (0.0071)	0.218 (0.0086)

IX. MATERIALS DEVELOPMENT

Materials development during this reporting period included effort on zircon thermal barrier material, silicon carbide components (gasifier scrolls and rotors), silicon nitride rotors, and fiber-reinforced glass ceramics.

9.1 THERMAL BARRIER DEVELOPMENT

Material development for thermal barrier applications has concentrated on zircon. The effort has included property consistency, material qualification, process development, and advanced material development.

Zircon Thermal Barrier Material Property Consistency Study

The ZSA-100 zircon material consistency study addressing material variability has continued this reporting period. The goal of this study is the assessment of critical material characteristics (strength, shrinkage, thermal expansion, and microstructure). Four individually processed billets were produced and the modulus of rupture (MOR), density, and percent shrinkage have been measured and reported in the Eighth Semiannual AGT Report, EDR 11684 (CR 174798). These data are reproduced as shown in Table XIV. Work in this period focused on characterization of thermal expansion, phase content, microstructure, and fractographic analysis.

Thermal expansion was measured on two specimens from each billet, as shown in Figure 53. Based on a one-way analysis of variance (95% confidence level), it was concluded that there was no significant difference among the four billets.

Phase content was evaluated by X-ray diffraction analysis (XRDA). In all cases zircon was identified as the major phase, with mullite and cristobalite as minor phases. There was not a discernible difference on a billet to billet basis.

Optical and scanning electron microscopy (see Figure 54) indicated only minor deviation in microstructure. Each billet had a fine grained zircon matrix, a mullite intergranular phase, 1-5 μm porosity, and occasional large voids about 200 μm in size.

Fractographic analysis showed that test bars had 200 μm hollow voids for fracture origins (see Figure 55). Close analysis showed that about 50% of all the bars failed from large hollow voids like the one shown.

In summary the thermal expansion microstructure, phase content, and strength controlling features have been analyzed for four individual billets. Results for this study indicate little to no deviation among billets.

It is desirable for zircon to have consistent thermal expansion behavior. Quite often, different behavior was observed for different batches. Therefore, thermal expansion was studied for two ZSA-100 batches. X-ray fluorescence was used to check for chemical differences.

Variability in thermal expansion was linked to chemical differences between batches. The batch with a slightly higher free silica/zircon ratio gave a higher average coefficient of thermal expansion (CTE), as shown in Figure 56.

The chemical difference was traced to the zircon raw material. Future work will center on the development of methods to compensate for slight chemistry differences.

Material Qualification

Material qualification entailed checking a new lot of spray-dried granules to see if it had the same character as the previous lot (No. 1). The lot No. 21 of ZSA-100 granules was made at the AC Spark Plug

Table XIV.
Critical properties of zircon based thermal barrier material.

Billet No.	Shrinkage—%	True density—g/cm^3	Average 4 pt MOR for machined surface—MPa (lb/in.^{2} × 10^3)	Standard deviation—MPa (lb/in.^{2} × 10^3)	Number of bars
1	16.22	4.038	194.78 (28.25)	31.72 (4.60)	10
2	16.21	4.030	224.15 (32.51)	28.75 (4.17)	10
3	16.66	4.026	215.87 (31.31)	32.89 (4.77)	10
4	16.20	4.020	206.98 (30.02)	19.10 (2.77)	10

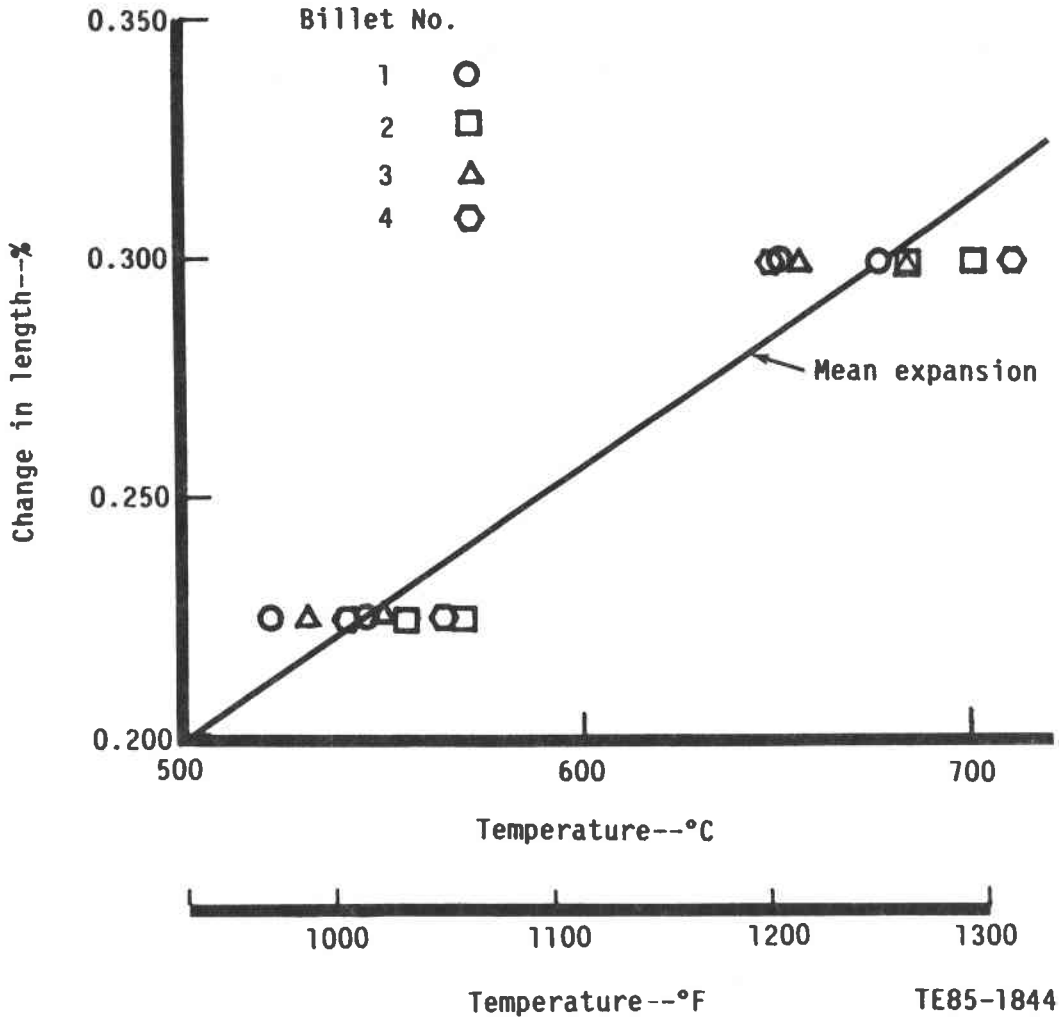

Figure 53. Thermal expansion of ZSA-100 zircon.

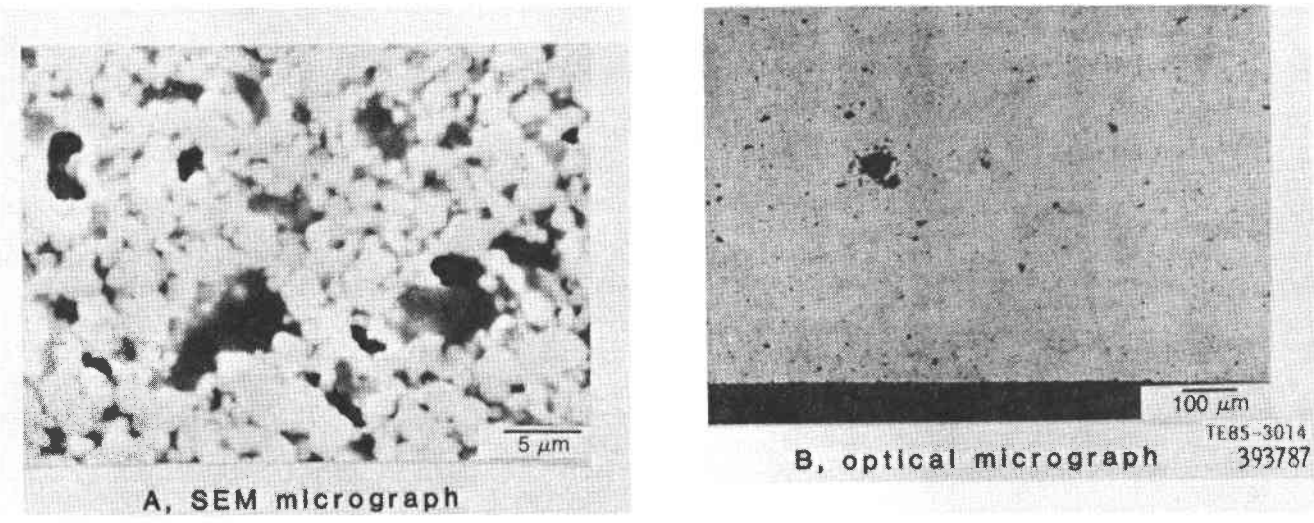

Figure 54. Scanning and optical micrographs of ZSA-100 zircon.

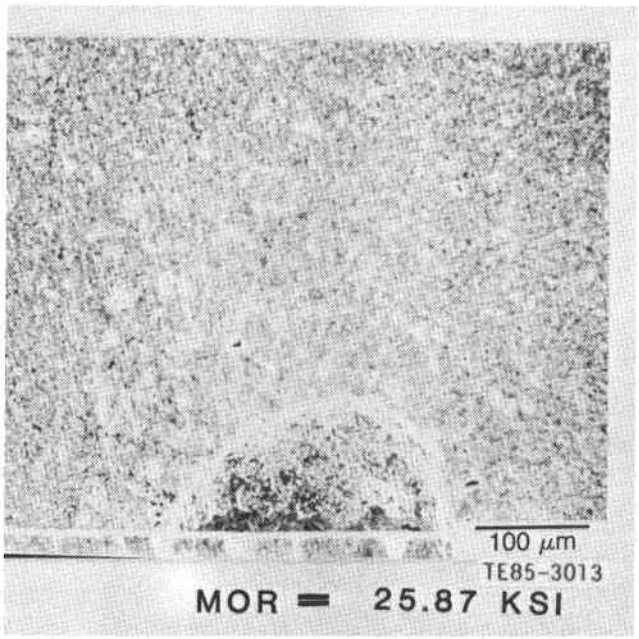

Figure 55. Typical ZSA-100 billet fracture origin.

Division of General Motors Corporation. A comparison with the previous lot was made based on percent shrinkage, density, microstructure, and biaxial strength.

Ten disks were made from each spray lot. Minus 60 mesh granules of lot No. 1 and 2 were die pressed to 137.9 MPa (20,000 lb/in.^{2}) followed by isopressing to 206.8 MPa (30,000 lb/in.^{2}). They were all fired simultaneously in air to 1425°C (2597°F).

The qualification results are listed in Table XV. The results indicate that no significant difference exists between the two powder lots. The percent shrinkage was found to vary by only 0.2%, and the density ranged from 4.014 to 4.016 g/cm^3 (lot No. 2). Also, the biaxial strength of lot No. 2 (314.06 MPa [45,550 lb/in.^{2}]) was very close to that of lot No. 1 (320.19 MPa [46,440 lb/in.^{2}]).

One disk from each group was sectioned for microstructure evaluation. Figure 57 shows a representative micrograph for each disk. There was no difference between the microstructures. On the basis of

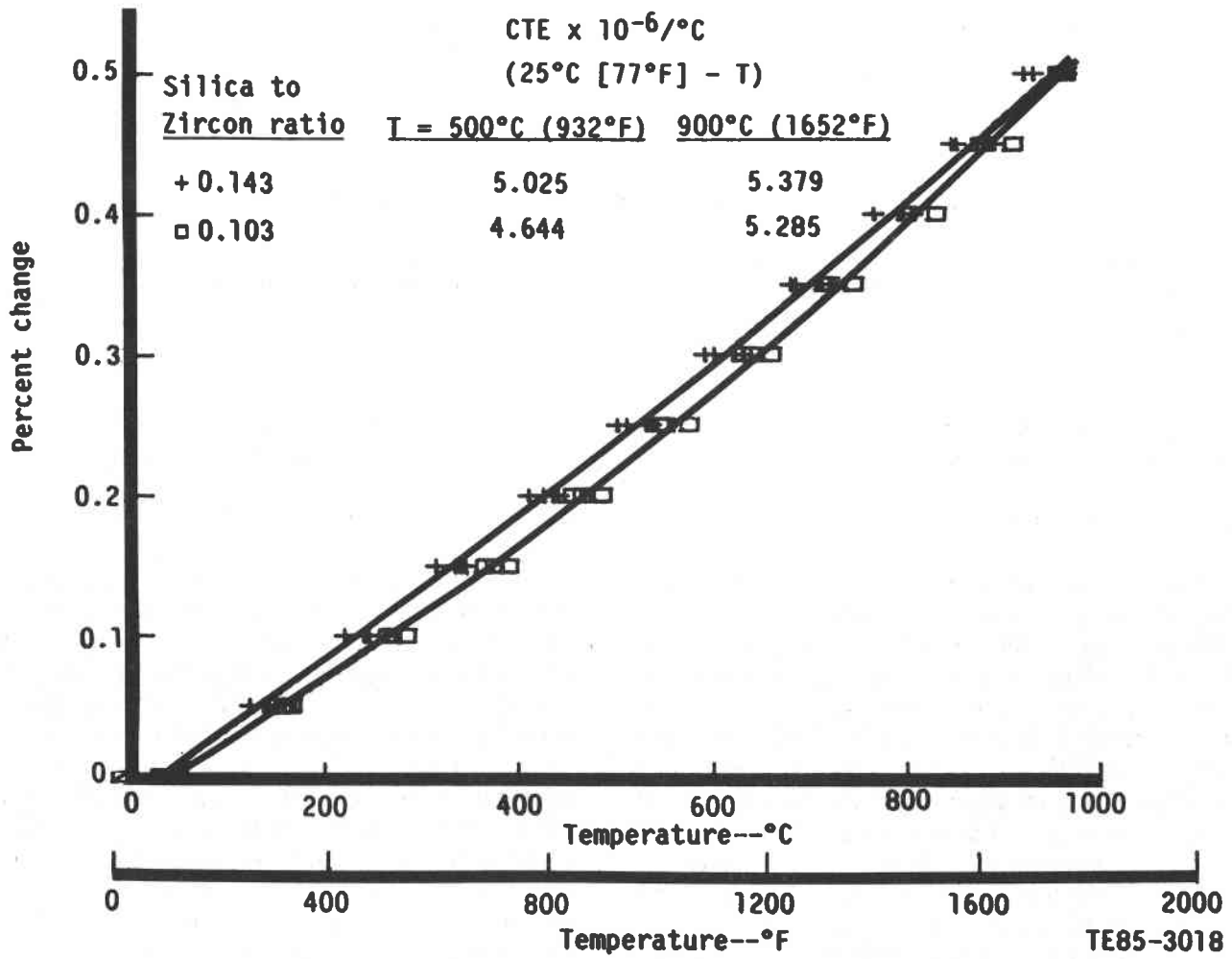

Figure 56. Thermal expansion measurements.

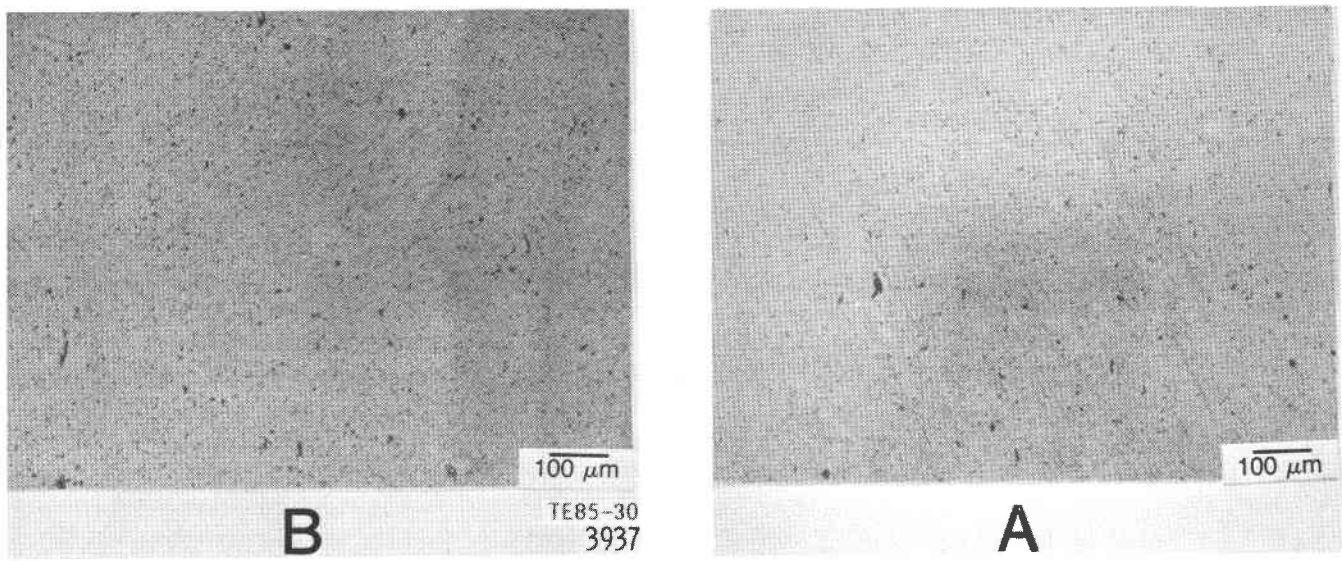

Figure 57. Microstructure of ZSA-100 material qualification sample.

Table XV. Spray lot qualification results.

	Lot No. 1	Lot No. 2
Percent shrinkage	15.87, 0.08	16.07, 0.06
Density (g/cm^3)	4.014, 0.005	4.016, 0.007
Biaxial strength—MPa ($lb/in.^2$)	320.19, 62.60	314.06, 47.85
	(46,440, 9,080)	(45,550, 6,940)

Table XVI.
Room temperature MOR for ZSA-100, machined tensile surfaces.

Process routing	Mean MOR (4 point)—MPa ($lb/in.^2$)		Standard deviation—MPa ($lb/in.^2$)		Number
Original	210.43	(30,520)	28.13	(4.08)	40
New	267.31	(38,770)	24.13	(3.50)	8

these results the second spray lot is considered qualified for fabrication of zircon thermal barriers.

Process Development

Strength studies have been addressed to optimize MOR in zircon thermal barriers. A new process routing has been established that increased MOR by 27%. In the original routing, large hollow voids were the strength limiting features (see Figure 54). It is suggested that entrapped air was being retained in the fired microstructure. To resolve the entrapped air problem, the original single plunger die was replaced with a double-action (two plunger) die. This permitted die compaction to higher pressures, thereby giving a compact with a lower pore fraction as pressed. The compact was then de-aired and isopressed.

The MOR for both processes is given in Table XVI; the new process has 27% higher MOR. Examination of fracture surfaces indicated that the new process samples did not have entrapped air.

Advanced Material Development

Research in advanced materials addresses improved strength, thermal expansion matching, and fabrication potential of new compositions. Results to date have indicated that zircon purity can affect reproducibility of thermal expansion. In-house effort has centered on acid leaching the raw material to obtain high purity zircon. The resulting material, ZSA-300X, has been explored. Previous work (see EDR 11684, CR 174798) based on density (4.57 g/cm^3) indicated it was about 99% pure. However, it was 25% lower in strength than ZSA-100. The process is also lengthy, thus limiting the quantities of ZSA-300X. Therefore, the 1985 goal is to explore commercial sources of high purity raw materials.

High purity raw material samples have been acquired from two vendors. The samples have slightly different chemical and particle characteristics. Sinterability will be established, and scale-up spray drying will be done for the more promising compositions. Compaction behavior will be characterized, and billets will be made for strength and thermal expansion measurement.

9.2 SILICON CARBIDE COMPONENT DEVELOPMENT

9.2.1 Gasifier Rotor

The status of the process development of the alpha-SiC material gasifier turbine rotor is summarized in Table XVII. The evaluation of groups 1 and 2 was completed in 1983. The current report period addresses the evaluation of group 3. Groups 4 through 8B were in experimental trials (1984) culminating in the group 8C and 8D processes that support the 1985 gasifier rotor requirements. As noted in Table XVII, groups 5 through 8B were contaminated by metallic material from a damaged compound mixer. The contaminant became evident when a pock marked surface appeared during the sinter operation.

The Eighth Semiannual AGT Report (EDR 11684, CR 174798) explained the successful fixturing during the sinter operation that resulted in dimensional conformance. Dimensional checks of the group 3A and 3B rotors for this period again demonstrated dimensional conformance. Additional parameters such as strength, visual inspection, fluorescent penetrant inspection (FPI), and spin test, are summarized in the following paragraphs.

Standard-size four-point modulus of rupture (MOR) test bars were cut from various locations in one of the group 3A rotors (FX34280) to test material strength characterization. These test bars were also used to determine the nature and location of the strength-controlling defects. Strength measurements were taken on material from both the rotor backface region (radial direction) and from the rotor hub near the exducer (axial direction), as shown in Figure 58.

Test material from the backface region (radial) had an average MOR of 347.28 MPa (50,369 lb/in.^{2}). An average strength of 339.57 MPa (49,250 lb/in.^{2}) was seen in bars cut in the axial direction near the exducer. The primary strength-controlling defects found in these test bars were internal pores; the secondary defects were surface pores and surface flaws.

The results of the nondestructive evaluation (NDE), spin tests, and disposition of the group 3 rotors is summarized in Tables XVIII and XIX. Fractographic evaluation of the spin test rotors is itemized in Tables XX and XXI. Note the considerable reduction in average burst speed of group 3 rotors in comparison with those in group 1.

Postfailure investigation of the rotors was conducted by fractographic analysis of both the group 1 and group 3A rotors to address the difference in average burst speed. Of the six rotors from group 1 with identifiable fracture origins, as listed in Table XX, four failed because of surface flaws and two failed because of internal pores. The surface flaws, shown in Figure 59, were primarily seen on the rotor backface near the shaft and are believed to be the result of incomplete knitting of the injection molding strands. The remaining two rotors failed from large internal pores. A typical example of these internal pores is shown in Figure 60. The spin test and fractographic results for the CBO group 3A rotors are summarized in Table XXI. All three rotors for which fracture origins could be determined failed from surface flaws similar to those in the group 1 rotors.

Additional fracture surface analysis was conducted on both group 1 and group 3A rotors to determine the stress at fracture according to the following relationship:

$$\sigma_f = Ar^{-1/2}$$

where

σ_f = fracture stress
A = material constant
r = radius of the fracture mirror

These results are summarized in Table XXII. The stresses calculated from the fracture mirror radii correlate well with the stress levels predicted by the finite element analysis.

Based on the identification of surface and subsurface flaws in the backface region (see Figure 61), eight rotors (see Table XVIII, group 3A) were prepared for spin test by matching, blending, and polishing in the backface area, including the shaft fillet. The backface was machined to a 3.5 deg conical surface, as shown in Figure 62. Another example of seven (see Table XIX, group 3B) was hand blended. Of these 15 rotors, 12 were spin tested. The results are listed in Table XXIII. Seven rotors were successfully proof-spin tested to 86,200 rpm, and the remaining five exhibited an average burst speed of 83,660 rpm. Both speeds were in excess of the average burst speed (77,050 rpm) for the as-received (no backface rework) rotors from the same process sample (group 3).

Table XVII.
Process development, gasifier turbines.

Part No.	No. molded	CBO serial no.	As-molded B − or better	Sintered rotors Quality	Sintered rotors Date	Fabrication Parameters	
				Actual			
AA100395 (oval shaft)	42	486 to 527	14	9	6/3/83	Reed + microprocessor	Group 1
	90	528 to 617	21	20	6/8	Reed + microprocessor	
	110	618 to 727	33	29	7/18	Reed (65.09 mm [2.5625 in.] shot)	
	16	728 to 743	0			Reed (66.68 mm [2.6250 in.] shot)	
AA100932 (round shaft)	138	744 to 881	16	12	7/29	SB-1, N-1 experimental	Group 2
	15	882 to 896	7	6	8/5	SB-1, N-1 (15)	
	20	897 to 916	5	4	8/22	SB-2, N-2 (20-same as 15)	
	33	917 to 949	13	10	9/13	SB-2, N-2 experimental	
	15	950 to 964	10	8	9/30	SB-2, N-2 (15)	
	15	965 to 979	7			SB-3, N-1 experimental	
	20	980 to 999	8	12	11/8	SB-3, N-1 (20)	
	100	1000 to 1099	17	9	11/21	SB-2, N-2 (100) without heat	Group 3A
	100	1100 to 1199	29	28		SB-2, N-2 (100) with heat	
	76	1200 to 1275	0	0	1/19/84	Variable conditions	
	100	1276 to 1375	27	27	1/25	SB-2, N-2 (100) with heat	
	100	1376 to 1575	64	20	4/27	SB-2, N-2 (100)	Group 3B
				20	5/18	With heat	
				19	6/8	Invariant conditions	
				233 received as of 30 June 1984			
	125	1576 to 1700	8	8	8/31	Reed + microprocessor but with round shaft (see group 1)	Group 4
AA101151 (green body machining of backface, baud curve)	212	1701 to 1912	93	9	8/17	SB-2, N-2 with heat. Adjusted	Group 5*
				13	8/27	parameters but invariant from 1783 on. Extra stock, backface, and shaft.	
AA101155	42	1913 to 1954	20	10	None delivered (experimental)	KX02 material, ECR tool (oversize) high polymer mix	Group 6*

Code:
Reed = type of compounder
SB-1, -2, -3 = three sizes for the injection mold sprue bushing
N-1, -2 = two sizes for the injection mold nozzle

*Damaged compounder—metallic contamination of injection mold compound

Table XVII. (cont)

Part No.	No. molded	CBO serial no.	As-molded B – or better	Sintered rotors Quality	Date	Fabrication Parameters	
AA100932	24	1955 to 1978	23	6	None delivered (experimental)	Experimental compound based on blade matrix high mold yield	Group 7*
AA101156	60	1979 to 2038	49	12	None delivered (experimental)	Shaft end injection, extra stock base and shaft, invariant conditions	Group 8A*
AA101156	10	2039 to 2048	8	6	None delivered (experimental)	Shaft end injection, extra stock base and shaft, invariant conditions	Group 8B*
				263 received as of 31 December 1984			
AA101242	96	2049 to 2145	66	Estimated	February 1985	Shaft end injection, extra stock nose, base and shaft, invariant conditions	Group 8C-1
AA101243	75	2146 to 2220	50		March 1985	Shaft end injection, experimental mix, extra stock nose, base and shaft. Three conditions.	Group 8D-1
AA101243	52	2221 to 2272	48		April 1985	Shaft end injection, experimental mix, extra stock nose, invariant conditions.	Group 8D-2
AA101242	78	2273 to 2350	32		May 1985	Shaft end injection, extra stock nose, four conditions	Group 8C-2
AA101151	63	2351 to 2413	15		June 1985	Extra stock base and shaft — replicate group 5	Group 5B

Code:
Reed = type of compounder
SB-1, -2, -3 = three sizes for the injection mold sprue bushing
N-1, -2 = two sizes for the injection mold nozzle

*Damaged compounder—metallic contamination of injection mold compound

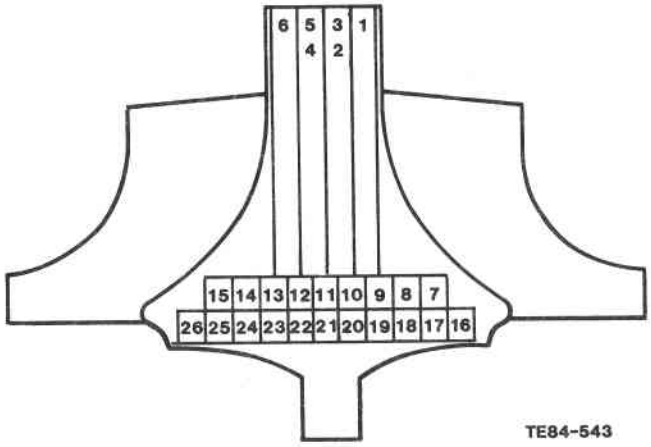

Figure 58. Orientation of test bars cut from ceramic rotor.

	Stress	
	MPa	lb/in.^{2}x10^3
A	22.3	3.23
B	44.5	6.46
C	66.9	9.70
D	89.1	12.93
E	111.4	16.15
F	133.6	19.38

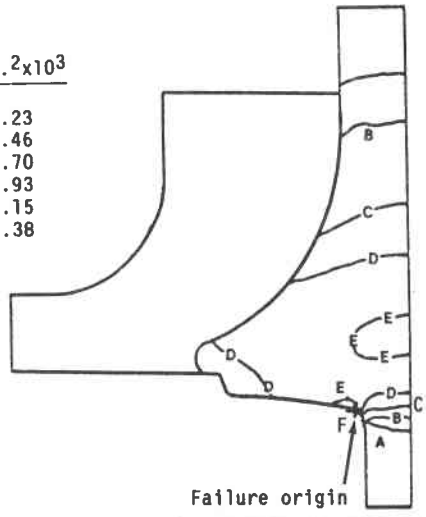

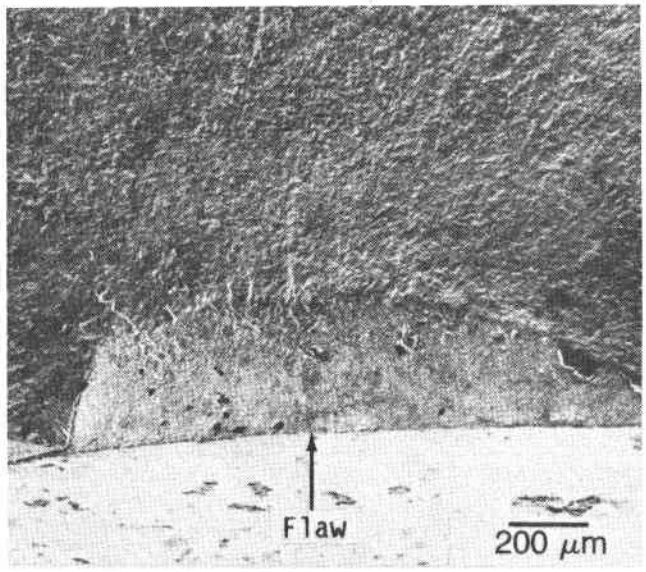

Figure 59. Typical failure (surface flaw) observed in CBO group I gasifier rotors; burst speed of rotor FX34166 was 89,500 rpm.

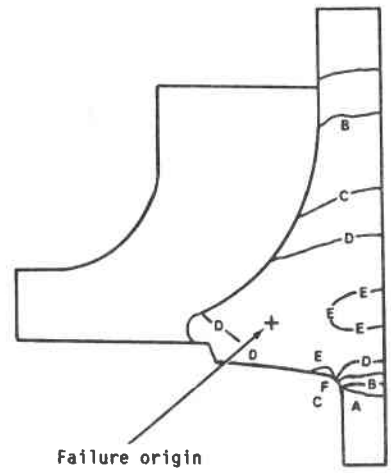

	Stress	
	MPa	lb/in.^{2}x10^3
A	18.7	2.71
B	37.4	5.42
C	56.1	8.14
D	74.8	10.85
E	93.5	13.56
F	112.2	16.27

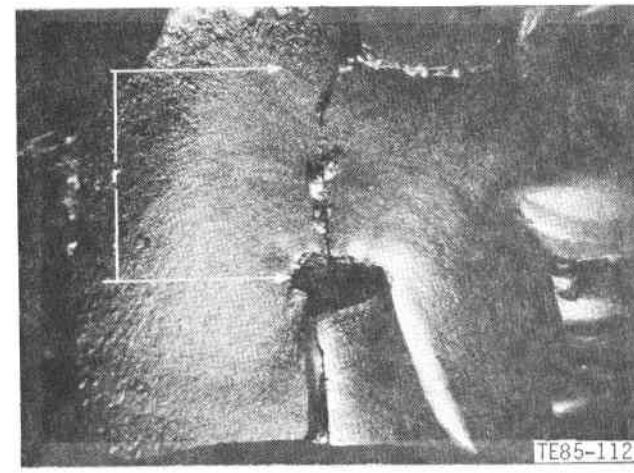

Figure 60. Typical failure (internal pore) observed in CBO group I gasifier rotor FX34172; burst speed was 82,000 rpm.

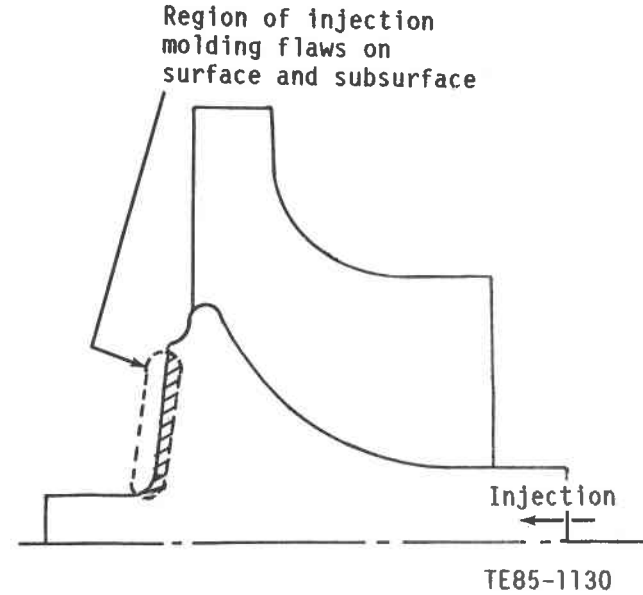

Figure 61. Location of typical backface flaws on injection-molded rotors.

Table XVIII.
Development summary of group 3A rotors.

No.	CBO S/N	Allison S/N	NDE*	Comment	Disposition
1	1102	FX34258	A	Broken airfoil	Scrap
2	1103	FX34259	N	Machined backface, 3.5 deg	Spin burst 98,100 rpm
3	1108	FX34260	A	Broken airfoil	Reserve
4	1109	FX34261	A		Spin burst 95,000 rpm
5	1110	FX34262	A	Chip at base of airfoil	Scrap
6	1113	FX34263	A		Spin burst 78,500 rpm
7	1114	FX34264	A		Spin burst 87,600 rpm
8	1118	FX34265	A		Spin burst 92,200 rpm
9	1124	FX34266	A		Spin burst 76,200 rpm
10	1126	FX34267	A	Distorted inducer	Scrap
11	1130	FX34268	N	Machined backface, 3.5 deg	1.5 deg taper shaft
12	1131	FX34269	N	Broken inducer	Scrap
13	1135	FX34270	N	Machined backface, 3.5 deg	Spin burst 86,200 rpm
14	1136	FX34271	N	Chipped inducer	Scrap
15	1140	FX34272	A	Broken airfoil	Scrap
16	1141	FX34273	A		Spin burst 63,300 rpm
17	1142	FX34274	N	Broken exducer	Scrap
18	1143	FX34275	N	Broken inducer	Scrap
19	1145	FX34276	N	Broken airfoil	Scrap
20	1149	FX34277	A	Broken inducer	Spin burst 76,100 rpm
21	1150	FX34278	A	Broken inducer	Spin burst 61,900 rpm
22	1152	FX34279	A		Spin burst 61,000 rpm
23	1174	FX34280	A	Broken airfoil	MOR bars
24	1177	FX34281	N	Machined backface, 3.5 deg	Spin burst 87,000 rpm
25	1178	FX34282	N	Distorted inducer	Scrap
26	1180	FX34283	N	Chipped inducer	Scrap
27	1187	FX34284	A		Spin burst 72,600 rpm
28	1191	FX34285	N		Scrap
29	1281	FX34286	N	Machined backface, 3.5 deg	Proof test 86,200 rpm
30	1282	FX34287	N		Scrap
31	1285	FX34288	N	Broken exducer	Scrap
32	1287	FX34289	N		Scrap
33	1296	FX34290	N	Distorted inducer	Scrap
34	1297	FX34291	N	Distorted inducer	Scrap
35	1300	FX34292	N		Scrap
36	1311	FX34293	N		Scrap
37	1321	FX34294	N		Scrap
38	1324	FX34295	N	Broken exducer	Scrap
39	1326	FX34296	A	Machined backface, 3.5 deg	1.5 deg taper shaft
40	1327	FX34297	N		Scrap
41	1340	FX34298	A		Spin burst 74,500 rpm
42	1344	FX34299	A		Spin burst 76,800 rpm
43	1345	FX34300	A		Spin burst 86,000 rpm
44	1346	FX34301	A	Broken inducer	Scrap
45	1352	FX34302	N		Scrap
46	1353	FX34303	N		Scrap

*NDE based on visual and FPI inspection
A = acceptable, including defects present that can be machined out to meet all NDE requirements
N = not acceptable

Table XVIII. (cont)
Development summary of group 3A rotors.

No.	CBO S/N	Allison S/N	NDE*	Comment	Disposition
47	1354	FX34304	N	Machined backface, 3.5 deg	Spin rig failure 70,000 rpm
48	1356	FX34305	A	Broke insulator during grind	Proof spin 86,200 rpm
49	1357	FX34306	N	Broken airfoil	Scrap
50	1358	FX34307	N	Machined backface, 3.5 deg	Proof test 86,200 rpm
51	1359	FX34308	A	Distorted inducer	Scrap
52	1369	FX34309	N		Scrap
53	1371	FX34310	N		Scrap
54	1372	FX34311	A		Proof spin 86,200 rpm
55	1373	FX34312	A		Proof spin 86,200 rpm

*NDE based on visual and FPI inspection
A = acceptable, including defects present that can be machined out to meet all NDE requirements
N = not acceptable

Table XIX.
Development summary of group 3B rotors.

No.	CBO S/N	Allison S/N	NDE*	Comment	Disposition
1	1383	FX34313	N	Chipped inducer	Scrap
2	1395	FX34314	N		Scrap
3	1399	FX34315	N		Scrap
4	1405	FX34316	N		Scrap
5	1410	FX34317	N		Scrap
6	1413	FX34318	N		Scrap
7	1416	FX34319	N		Scrap
8	1421	FX34320	A	Machine backface Baud curve	Proof test 95,000 rpm
9	1427	FX34321	A	Machine backface Baud curve	Proof test 96,200 rpm
10	1430	FX34322	N	Broken exducer	Scrap
11	1431	FX34323	A	Machine backface Baud curve	Spin burst 95,000 rpm
12	1432	FX34324	A	Local blend of backface	Proof test 86,200 rpm
13	1433	FX34325	A	Machine backface Baud curve	Proof test 95,000 rpm (broken inducer—handling)
14	1434	FX34326	A	Machine backface Baud curve	Spin burst 75,000 rpm
15	1435	FX34327	A	Machine backface Baud curve	Scrap-chipped airfoil
16	1437	FX34328	A	Machine backface Baud curve	Spin burst 64,000 rpm

*NDE based on visual and FPI inspection
A = acceptable, including defects present that can be machined out to meet all NDE requirements
N = not acceptable

Table XIX. (cont)
Development summary of group 3B rotors.

No.	CBO S/N	Allison S/N	NDE*	Comment	Disposition
17	1438	FX34329	N		Scrap
18	1445	FX34330	N		Scrap
19	1449	FX34331	N		Scrap
20	1452	FX34332	N	Short shaft	Scrap
21	1453	FX34333	N	Short shaft	Scrap
22	1456	FX34334	A	Local blend of backface	Proof test 90,100 rpm
23	1458	FX34335	A	Local blend of backface	Proof test 86,200 rpm
24	1459	FX34336	N		Scrap
25	1464	FX34337	N		Scrap
26	1466	FX34338	N	Broken inducer	Scrap
27	1467	FX34339	N		Scrap
28	1469	FX34340	A	Local blend of backface	Proof test 86,200 rpm
29	1474	FX34341	A	Local blend of backface	Spin burst 66,500 rpm
30	1476	FX34342	N		Scrap
31	1478	FX34343	N		Scrap
32	1480	FX34344	N		Scrap
33	1481	FX34345	A	Local blend of backface	Spin burst 80,500 rpm
34	1482	FX34346	A	Local blend of backface	Proof test 86,200 rpm
35	1488	FX34347	N		Scrap
36	1489	FX34348	N		Scrap
37	1490	FX34349	N		Scrap
38	1491	FX34350	N		Scrap
39	1499	FX34351	A	Machine backface Baud curve	Spin burst 94,600 rpm
40	1500	FX34352	A	Machine backface Baud curve	Spin burst 94,800 rpm
41	1504	FX34353	A	Machine backface Baud curve	Spin test pending
42	1511	FX34354	N		Scrap
43	1512	FX34355	N		Scrap
44	1513	FX34356	A	Machine backface Baud curve	Spin test pending
45	1514	FX34357	A	Machine backface Baud curve	Spin test pending
46	1515	FX34358	A	Machine backface Baud curve	Proof test 95,000 rpm
47	1520	FX34359	A	Machine backface Baud curve	Spin burst 66,000 rpm
48	1521	FX34360	A	Machine backface Baud curve	Proof test 94,400 rpm
49	1522	FX34361	A	Machine backface Baud curve	Spin test pending
50	1523	FX34362	A	Machine backface Baud curve	Proof test 95,000 rpm
51	1529	FX34363	A	Machine backface Baud curve	Spin burst 78,400 rpm

*NDE based on visual and FPI inspection
A = acceptable, including defects present that can be machined out to meet all NDE requirements
N = not acceptable

Table XIX. (cont)

No.	CBO S/N	Allison S/N	NDE*	Comment	Disposition
52	1531	FX34364	A	Machine backface Baud curve	Spin burst 89,500 rpm
53	1533	FX34365	A	Machine backface Baud curve	Spin burst 103,800 rpm
54	1536	FX34366	A	Machine backface Baud curve	Proof test 92,200 rpm
55	1540	FX34367	N		Scrap
56	1543	FX34368	A	Machine backface Baud curve	Spin test pending
57	1545	FX34369	A	Machine backface Baud curve	Proof test 95,100 rpm
58	1570	FX34370	A	Machine backface Baud curve	Crack in fillet—scrap
59	1571	FX34371	A	Machine backface Baud curve	Spin failure 60,000 rpm released inducer blade

*NDE based on visual and FPI inspection
A = acceptable, including defects present that can be machined out to meet all NDE requirements
N = not acceptable

Table XX.
Spin test and fractographic evaluation of CBO group 1 gasifier rotors.

Serial No.*	Failure speed—rpm	Fracture origin
FX34141	92,500	Surface flaw
FX34152**	102,500	Missing
FX34157**	105,000	Missing
FX34159**	100,500	Missing
FX34162	93,400	Missing
FX34166	89,500	Surface flaw
FX34167	99,000	Missing
FX34169	82,000	Surface flaw
FX34170**	100,000	Missing
FX34171	89,200	Missing
FX34172	89,000	Internal pore
FX34173	106,000	Missing
FX34174**	101,500	Missing
FX34175	95,000	Surface flaw
FX34183**	95,500	Missing
FX34184**	105,000	Missing
FX34185	107,050	Missing
FX34186**	100,500	Internal pore
FX34192	77,000	Missing

* Acceptable quality
**Average failure speed = 99,330 rpm

Table XX. (cont)
Spin test and fractographic evaluation of CBO group 1 gasifier rotors.

Serial No.*	Failure speed—rpm	Fracture origin
FX34194	70,500	Missing
FX34195**	102,000	Missing

* Acceptable quality
**Average failure speed = 99,330 rpm

Table XXI.
Spin test and fractographic evaluation of CBO group 3A gasifier rotors.

Serial No.*	Failure speed—rpm	Fracture origin
FX34261	95,000	Missing
FX34263	78,500	Missing
FX34264	87,600	Missing
FX34265	92,200	Missing
FX34266	76,200	Missing
FX34273	63,300	Missing
FX34277	76,100	Missing
FX34278	61,900	Missing
FX34279	61,000	Missing
FX34284	72,600	Missing
FX34298	74,500	Surface flaw
FX34299	76,800	Surface flaw
FX34300	86,000	Surface flaw
FX34305	(86,300) proof	—
FX34311	(86,300) proof	—
FX34312	(86,300) proof	—

*All acceptable quality
Note: Average failure speed = 77,050 rpm

Table XXII.
Fracture stress of spin tested CBO SiC rotors.

Rotor lot	Serial No.	Failure speed—rpm	Fracture mirror stress—MPa (ksi)	Predicted stress—MPa (ksi)	
				Radial	Max principal
Group 1	34141	92,500	105.5 (15.3)	83.4 (12.1)	99.3 (14.4)
Group 1	34166	89,500	100.0 (14.5)	117.2 (17.0)	120.0 (17.4)
Group 1	34169	82,000	90.3 (13.1)	93.8 (13.6)	96.5 (14.0)
Group 1	34172	82,000	87.6 (12.7)	72.4 (10.5)	81.4 (11.8)
Group 1	34175	95,000	110.0 (16.1)	91.7 (13.3)	81.7 (13.3)
Group 1	34186	100,500	119.3 (17.3)	97.2 (14.1)	115.8 (16.8)
Group 3A	34298*	74,500	—	—	
Group 3A	34299	76,800	79.3 (11.5)	76.5 (11.1)	98.6 (14.3)
Group 3A	34300	86,000	95.2 (13.8)	88.9 (12.9)	116.5 (16.9)

*Fracture mirror missing (damaged)

Table XXIII.
Summary of spin test results—first sample of blended backface.

Source	Serial number	Spin test
Group 3A, machined backface, 3.5 deg	1. FX34259*	Burst 98,100 rpm
	2. FX34268	Tapered shaft attachment dev
	3. FX34270*	Burst 86,200 rpm
	4. FX34281*	Burst 87,000 rpm
	5. FX34286	Proof 86,200 rpm
	6. FX34296	Tapered shaft attachment dev
	7. FX34304	Rig wreck 70,000 rpm
	8. FX34307	Proof 86,200 rpm
Group 3B hand—blended backface	1. FX34324	Proof 86,200 rpm
	2. FX34334	Proof 86,200 rpm
	3. FX34335	Proof 86,200 rpm
	4. FX34340	Proof 86,200 rpm
	5. FX34341*	Burst 66,500 rpm
	6. FX34345*	Burst 80,500 rpm
	7. FX34346	Proof 86,200 rpm

*Average burst speed = 83,660 rpm (versus 77,050 rpm average burst speed for nonblended backface, as in Table XXI).

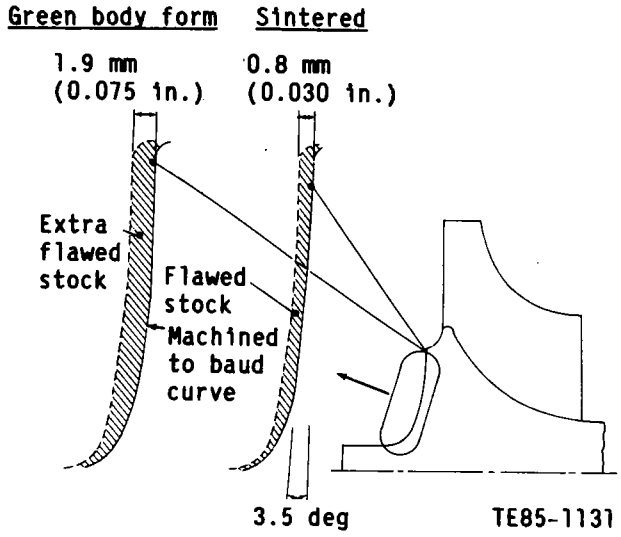

Figure 62. Revised backface contours for green and sintered rotors.

Based on the identification of backface injection molding flaws and the previously noted spin test results, processing that features the green body form molded with extra stock in the backface and shaft region was initiated. This extra stock, potentially flawed, is machine removed in the green state. This approach is graphically illustrated in Figure 62. As part of this effort a recontour of the backface was investigated to address the goal of reducing the peak stress in the shaft fillet area. In **Stress Concentration Factors** (R. E. Peterson, John Wiley & Sons, New York, 1974), Peterson suggested a particular contour identified as the Baud curve as an optimum contour that would minimize the stress level at the shaft fillet.

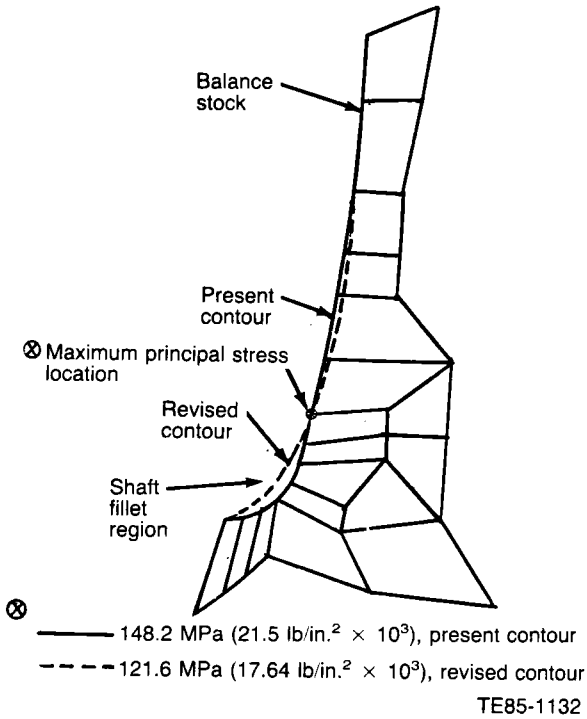

Figure 63. Calculated shaft fillet maximum principal stresses, present and revised rotor backface contour (shown in finite element model format).

This contour was incorporated in the rotor finite element model and the stresses calculated. The contour comparison with the present backface is shown in Figure 63. The Baud curve contour reduced the peak fillet stress by 18%. Based on this result, the contour of the backface of the group 5 rotors is being machined to the Baud curve, thus addressing the re-

moval of molding flaws and also minimizing shaft fillet peak stress.

Statistical analysis of group 3B (machined backface) rotor spin tests resulted in a predicted average burst speed of 92,300 rpm with a 6.44 Weibull modulus. (Proof tests were considered as suspended items.) This compares with an average burst speed of 99,330 rpm and a Weibull modulus of 6.9 for the group 1 rotors (see Table XX).

The analyses have also included calculation of probability of survival for various conditions. The results are listed in Table XXIV for the present and recontoured backface. The as-molded configuration includes machining stock on the airfoils. The engine condition is for the planned initial trial of the rotor in the engine (machined airfoils) at 1080°C (1976°F) rotor inlet temperature (RIT), steady-state conditions (SS), and design speed (100% N_1). Note that for the engine condition and the recontoured backface the calculated probability of survival, P_s, is 0.9862. This exceeds the design goal of 0.97.

The benefit of cold spin proof testing on the operational rotor reliability at 1080°C (1976°F) RIT is shown in Figure 64. Data are presented for no cold proof and for proof test speeds of 105% and 110% as a function of material strength. The rejection rate is also presented for each speed.

Thermal shock proof testing for the 1080°C (1976°F) RIT case was analytically studied. The objective of the study was to assess the potential improvement in the engine rotor reliability as a result of successfully passing a fluidized bed thermal shock test. Figure 65 shows a schematic of the fluidized bed rig and the thermal transients that can be achieved. Note that two conditions were considered: (1) a heatup from room temperature to 871°C (1600°F) and (2) a cooldown from 871°C (1600°F) to 204°C (400°F). Analyses indicated the cooldown transient developed the most severe stresses in the rotor. Based on this result, the probability of survival of the rotor was calculated as a function of time for the following:

1. fluidized bed thermal shock
2. 1080°C (1976°F) RIT engine condition operating steady state at design speed after successfully completing step 1

Steps 1 and 2 were calculated for a range of material MOR strengths: 344.74 MPa (50 lb/in.^{2} × 10^3), 379.21 MPa (55 lb/in.^{2} × 10^3), and 413.7 MPa (60 lb/in.^{2} × 10^3). The results are summarized in Figure 66 and show little improvement in operational reliability for the 1080°C (1976°F) RIT steady-state engine condition.

Rotor/Shaft Attachment

Table XVIII lists several rotors successfully spin tested at 86,200 rpm (100% N_1). Of these, serial numbers FX34286, FX34305, FX34307, FX34311, and FX34312 were committed to joining with semifinished shafts as the first engine candidate assemblies. The ceramic rotor/metal shaft joint is illustrated in Figure 67. The disposition of each rotor is described in Table XXV. Following the first trial (with rotor S/N FX34305) of grinding the insulator to length and diameter, the next three rotors fractured across the rotor stub shaft typically, as shown in Figure 68.

Postfailure examination of rotors S/N FX34311 and FX34312 revealed multiple and similar fractures for both assemblies. Sectioning of the attachment and

Table XXIV.
Calculated probability of survival for a gasifier rotor.

	Present backface				Recontoured backface (Baud curve)			
	Per drawing		Ground to recontour shape				30% discontinuous (balance)	
Condition	Max σp—MPa (lb/in.^{2} × 10^3)	P_s	Max σp—MPa (lb/in.^{2} × 10^3)	P_s	Max σp—MPa (lb/in.^{2} × 10_3)	P_s	Max σp—MPa (lb/in.^{2} × 10_3)	P_s
As-molded 100% N_1, RT spin	148.1 (21.48)	0.994	125.5 (18.2)	0.9939	129.94 (17.54)	0.994	129.9 (18.84)	0.9933
Machined, steady state, 100% N_1, 1080°C (1976°F) RIT	300.4 (43.57)	0.9757			244.84 (35.51)	0.9862		
Machined, steady state, 100% N_1, 1080°C (1976°F) RIT (after 100% spin proof)	300.4 (43.57)	0.977			244.84 (35.51)			

Note: Weibull, material properties used

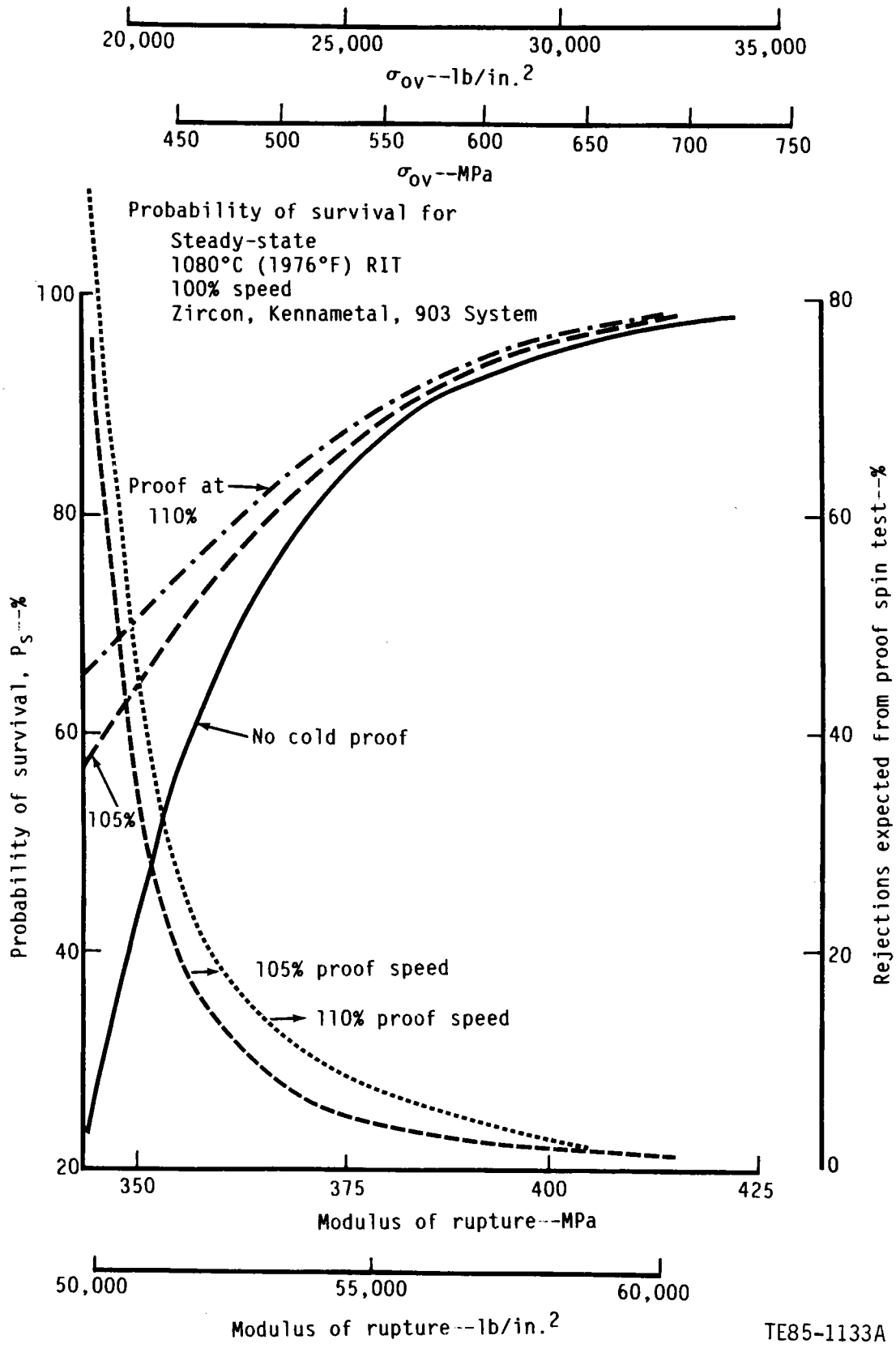

Figure 64. Rotor operational reliability (1080°C [1976°F] RIT) versus material strength at selected proof test speeds.

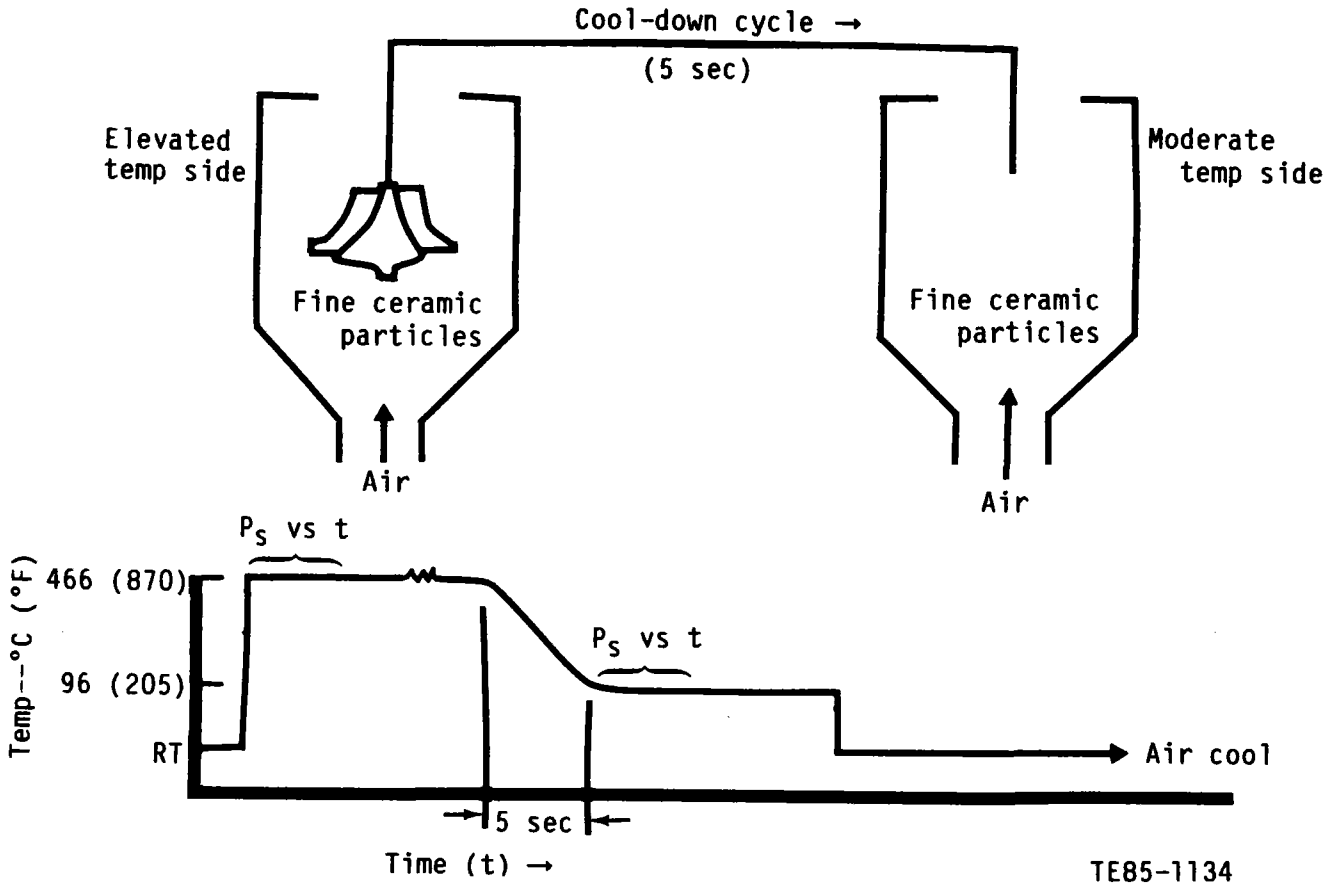

Figure 65. Schematic of fluidized bed thermal shock rig.

examination of the rotor stub shaft fracture (nearest the backface) indicates the failure origin was in an area of localized contact of the insulator with the rotor stub shaft. A controlled-size green body insulator is sintered to the SiC stub shaft, and the associated shrinkage of the insulator engages the shaft. The rotor shaft was an as-fired irregular surface that resulted in the localized contact and failure. The corrective action is to finish machine the rotor stub shaft.

Concurrent with the failure investigation of the SiC rotor shaft assemblies was an effort to determine the strength level of the attachment system and evaluate the fracture mechanism. Three shaft attachment specimens were assembled to duplicate the actual rotor attachment design, using a cylindrical isopressed SiC rod in place of the SiC rotor shaft. A bending stress was generated by applying bending loads in 0.56 N-m (5 in.-lb) increments until failure. The specimens were rotated through 360 deg after application of the load to stress the attachment uniformly. A schematic of the attachment specimens and test procedure is shown in Figure 69. The results of this testing are summarized in Table XXVI.

All specimens had fracture origins on the surface of the SiC rod, with no apparent defect at the origin. A typical fracture surface is shown in Figure 70. The fracture surfaces of the shaft attachment specimens were similar to the fractures observed in the rotor shaft assemblies.

The other fractures, through the sleeve, insulator, and rotor shaft, were the subject of an extensive finite element stress analysis. The analysis addressed the original configuration (the two failures) and a modified configuration. The results of the analysis are summarized in Figure 71. The figure compares the predicted stresses for the original and modified rotor shaft blank assemblies, as illustrated in Figure 72. The specific case presented is that of the interference fit, rotor/shaft assembly stresses at the attachment. The modified shaft blank features a semifinished contour that is closer to the finished contour. The result is reduced radial stiffness, which favorably influences the component stresses at assembly.

The modified attachment was analyzed for predicted reliability at various conditions by finite element simulation. The results are summarized in Table XXVII. The following four conditions were analyzed:

- room temperature spin and 100% speed (86,240 rpm)

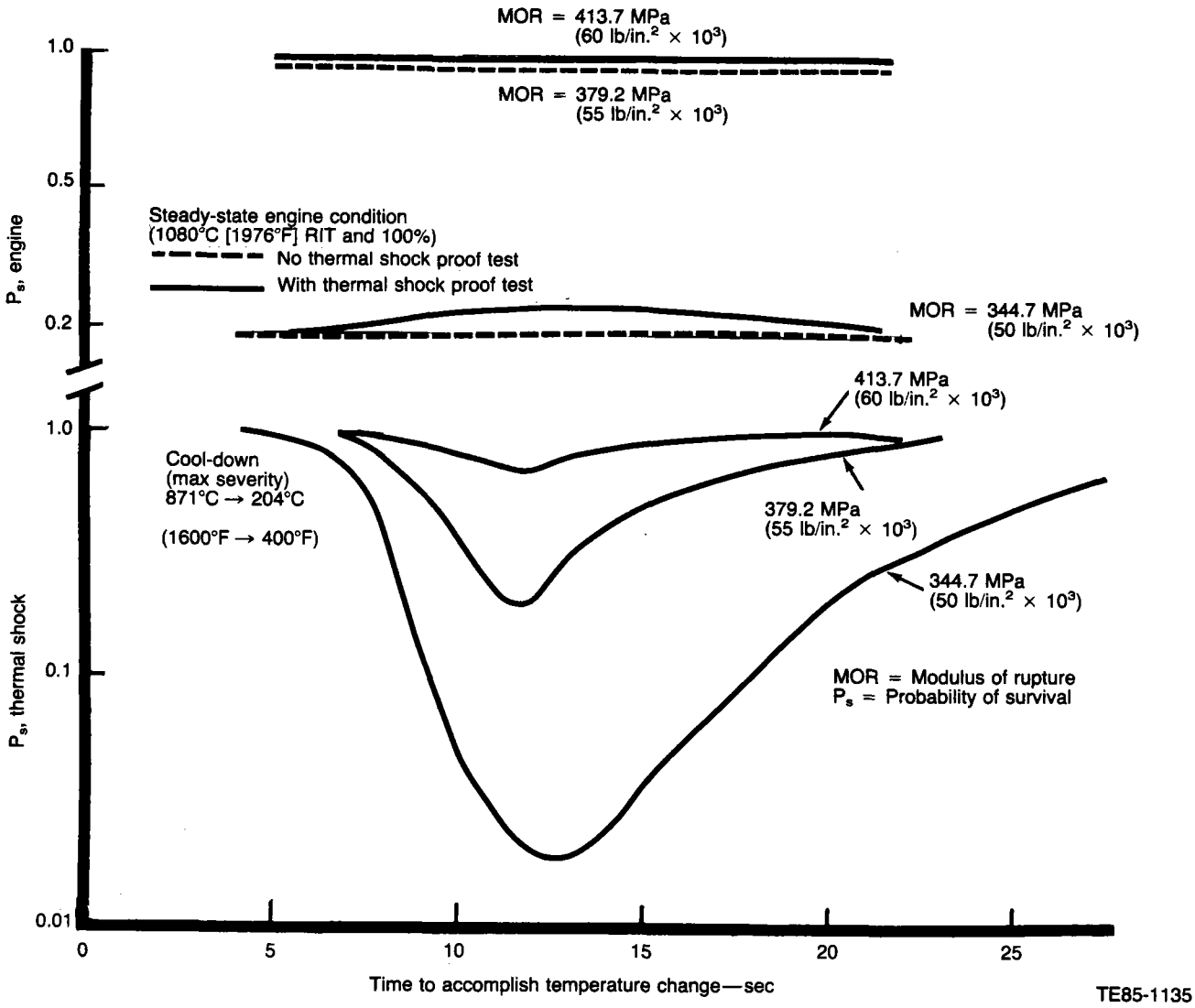

Figure 66. Rotor thermal shock proof test and corresponding effect upon operational reliability.

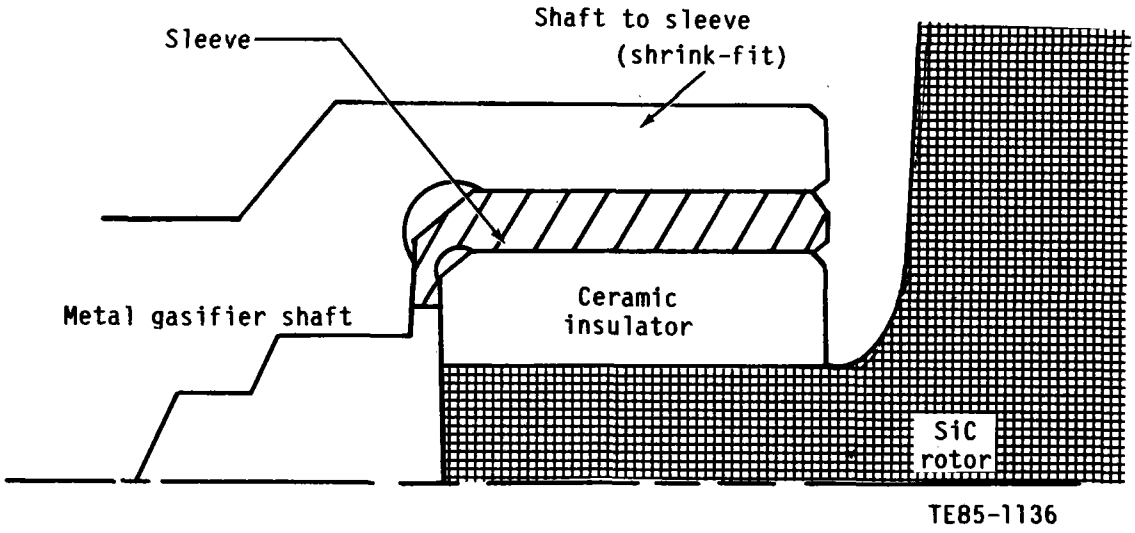

Figure 67. Schematic of ceramic rotor to metal shaft attachment system.

Table XXV.
Status of engine candidate gasifier rotor assemblies.

No.	Rotor S/N	Rotor-only spin test	Insulator installed	Joined to shaft	Machined	Inspected	Rotor/shaft spin test	Installed in engine	Comments
1	FX34305	X	X						The insulator and rotor shaft were damaged during finish grind of the o.d. and length. (Joining of the insulator to the rotor shaft is the first step in the assembly buildup.) Stub shaft was not usable.
2	FX34311	X	X	X					Complete rotor/shaft assembly was successfully built. Rotor stub shaft fractured (see Figure 68) during routine handling at Allison.
3	FX34312	X	X	X					Complete rotor/shaft assembly was successfully built. Rotor stub shaft fractured during lathe setup for matching at Atlas. (Fracture was similar to FX34311.)
4	FX34307	X	X	X	X	X			Fractured during bearing assembly at Balco.
5	FX34286	X	X	X	X	X	X	X	Final spin test limited to 77,000 rpm due to equipment; operated in engine S/N 2 BU8.
6	FX34334	X	X	X	X	X			Failed at 52,000 rpm due to defective spin equipment.
7	FX34340	X	X						Two chipped airfoils at exducer section due to handling.
8	FX34346	X	X						Inducer airfoil broken in handling; not usable.
9	FX34321	X	X						Proofed to 95,000 rpm; two airfoils broken in handling; not usable.
10	FX34362	X							Proofed to 95,000 rpm.
11	FX34366	X	X	X					Proofed to 95,000 rpm.
12	FX34360	X	X	X					Proofed to 95,000 rpm.
13	FX34369	X	X						Proofed to 95,000 rpm.
14	FX34320	X							Proofed to 95,000 rpm.
15	FX34325	X							Proofed to 95,000 rpm.
16	FX34358	X							Proofed to 95,000 rpm.
17	FX34371	X							Proofed to 95,000 rpm; two included blades released; not usable.

Notes:
X = completed
Items 4-8 had 3.5 deg backface and machined stub shaft.
Items 9-17 had Baud curved backface and machined stub shaft.

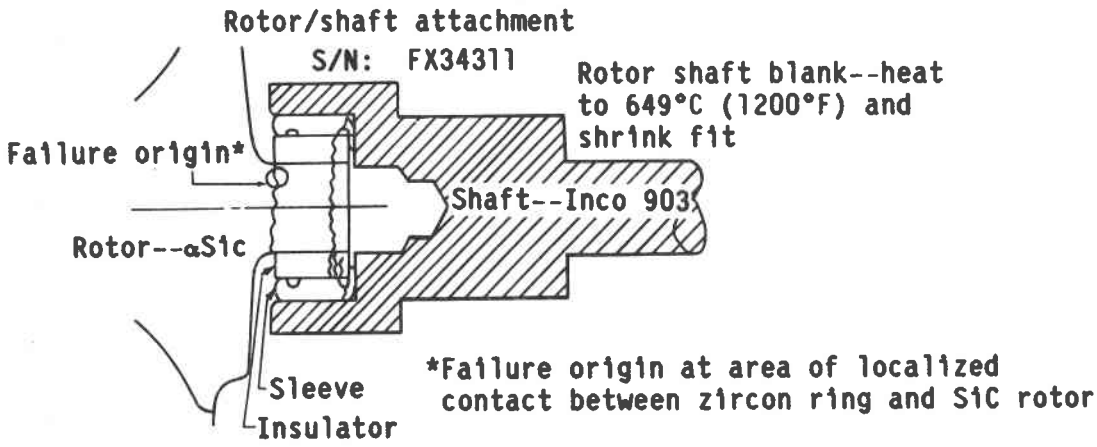

Figure 68. Results of first assembly of ceramic rotor and metal shaft (S/B FX34311).

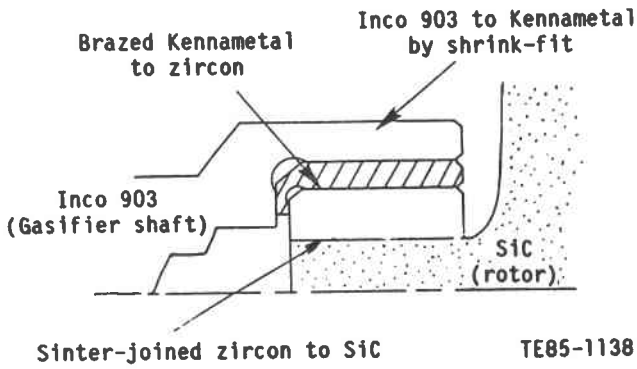

Figure 69. Schematic of ceramic rotor to metal shaft attachment system.

Table XXVI.
Shaft attachment specimen test results.

Specimen No.	Fracture stress—MPa (lb/in.^{2} × 10^3)
1	133.90 (19.42)
2	93.63 (13.58)
3	106.25 (15.41)
Average	111.26 (16.14)

- steady-state idle at 1080°C (1976°F) RIT and 50% speed
- steady-state at 1080°C (1976°F) RIT and 100% speed
- steady-state at 1288°C (2350°F) RIT and 100% speed (engine design point)

Stress and reliability were calculated for the range of interference fit of the shaft to the sleeve (Δr = 0.0457 mm [0.0018 in.] to 0.0508 mm [0.002 in.]). Review of Table XXVII shows that the predicted reliability is acceptable.

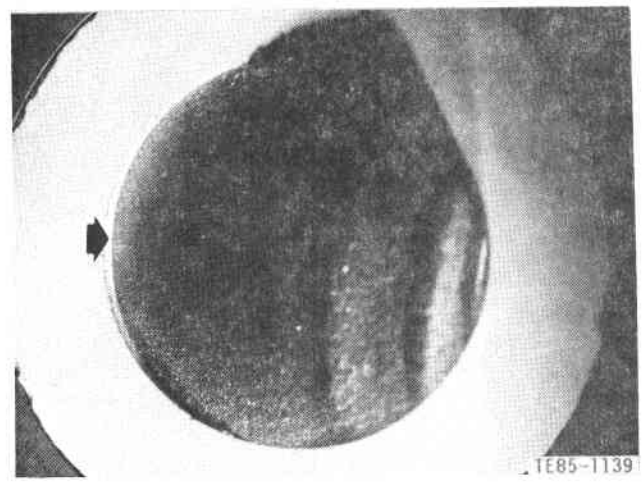

Figure 70. Typical fracture origin of shaft attachment specimens; fracture initiated from surface of SiC rod (at arrow) at a stress of 93.63 MPa (13,580 lb/in.^{2}.)

Following identification of the rotor backface region enhancement by machining (see Table XXIII) and the modified shaft attachment design, additional engine candidate rotor assemblies were committed incorporating both features. As shown in Table XXV, rotors numbered 4 through 8 incorporate a backface machined on a 3.5 deg taper and rotors numbered 9 and higher incorporate a backface machined to the Baud curve. Rotors numbered 4 through 6 were assembled with the modified shaft attachment design. The three completed assemblies are reviewed in detail in the following paragraphs.

Rotor S/N FX34307 (see Table XXV)

The semifinished rotor/shaft assembly is illustrated in Figure 73. This assembly was successfully

Shrink fit assembly stresses--
0.0457 mm (0.0018 in. radial)

	Original		Modified	
Stub shaft, αSiC	MPa	lb/in.^{2}x10^3	MPa	lb/in.^{2}x10^3
Max principal	78.6	11.4	52.4	7.6
Max axial	75.85	11.0	49.9	7.2
Min radial	-255.1	-37.0	-143.4	-20.8
Zircon insulator				
Max principal	353.0	51.2	128.9	18.7
Max axial	100.7	14.6	65.5	9.5
Min radial	678.5	-98.4	248.9	-36.1
Kennametal ring				
Max axial	506.8	73.5	280.6	40.7
Max radial defl	-0.012 mm	-0.00047 in.	-0.0055 mm	-0.00022 in.
Inco 903 shaft				
Max equiv	1176.9	170.7	1174.9	170.4
Max tangential	461.3	66.9	513.7	74.5

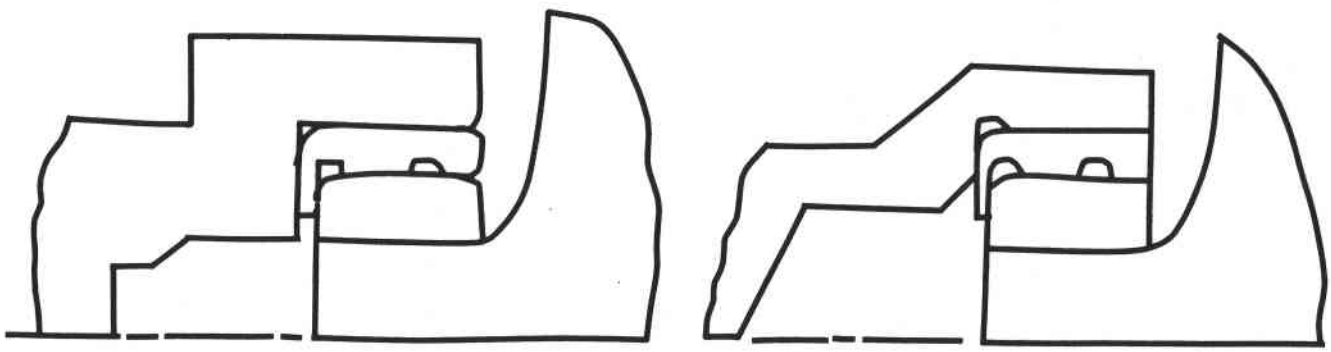

TE85-1140

Figure 71. Shrink fit assembly stresses for original and modified gasifier rotor/shaft attachment.

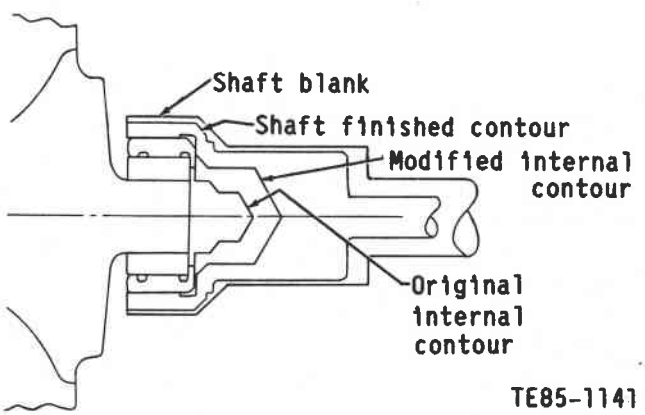

Figure 72. Modified shaft blank contour, second rotor/shaft attachment trial.

machined (as shown in Figure 74) by Atlas Tool and Die Company and delivered to Allison 28 September. Dimensional inspection demonstrated that the assembly conformed to the drawing, and FPI inspection cleared the assembly of any surface indications. A final proof spin test was planned to clear the assembly for engine installation. During installation of the No. 1 bearing on the ceramic rotor assembly, the rotor stub shaft fractured, as shown in Figure 75. The fracture occurred during handling of the rotor with no reported load on the attachment. Postfailure investigation revealed no feature or flaw at the fracture surface that would explain the failure. The remainder of the attachment (encapsulated in the metal shaft) revealed no cracks (after sectioning) as were seen in the first attachment design (see Figure 68).

Table XXVII.
Calculated (FEM) stresses and reliability for the ceramic gasifier rotor.

	RT spin 100% N	Steady state, 1080°C (1976°F) Idle (50% N)		Steady state, 1080°C (1976°F, 100% N		Steady state, 1288°C (2350°F), 100% N	
Probability of survival*							
Rotor	0.9981	0.9992	0.9991	0.9903	0.9902	0.9602	0.9594
Insulator	0.9990	0.9985	0.9937	0.9840	0.9852	0.9132	0.9232
Peak stresses—MPa (lb/in.^{2} × 10^3)							
Rotor	137.55	223.67	227.25	223.87	225.11	279.79	281.03
	(19.95)	(32.44)	(32.96)	(32.47)	(32.65)	(40.58)	(40.76)
Insulator	149.82	175.20	185.88	166.37	166.44	187.68	187.74
	(21.73)	(25.41)	(26.95)	(24.13)	(24.14)	(27.22)	(27.23)
Ring	108.25	492.91	488.22	507.80	503.04	637.14	632.32
	(15.7)	(71.49)	(70.81)	(73.65)	(72.96)	(92.41)	(91.71)
Shaft	541.93	383.83	432.85	385.97	433.47	398.52	446.09
	(78.6)	(55.67)	(62.78)	(55.98)	(62.87)	(57.80)	(64.70)
Radial fits, shaft/sleeve —mm (in.)	−0.0457 (−0.0018)	−0.457 (−0.0018)	−0.0508 (−0.0020)	−0.0457 (−0.0018)	−0.0508 (−0.0020)	−0.0457 (−0.0018)	−0.0508 (−0.0020)

*Material properties, Weibull characterization

	σ_{ov}	m_v	σ_{os}	m_s
Rotor	686.4 MPa (32,293 lb/in.^{2})	8.62	661.1 MPa (53,004 lb/in.^{2})	10.915
Insulator	366.45 MPa (15,800 lb/in.^{2})	8.0	479.86 MPa (31,000 lb/in.^{2})	8.0

Rotor S/N FX34286 (see Table XXV)

This finish-machined assembly successfully passed dimensional, FPI, and static load tests. The static load test consisted of stepwise increasing bending moments across the rotor/shaft attachment plane up to a maximum of 6-78 N-m (60 in.-lb). This resulted in a maximum bending stress at the attachment of 24.82 MPa (3.6 lb/in.^{2} × 10^3) and corresponds to the maximum stress that could be developed if the rotor were balanced to the drawing specified limit. The assembly was rotated through 360 deg to proof stress every point on the rotor stub shaft.

Illustrated in Figure 76 is the rotor/shaft assembled with the No. 1 engine bearing and other components for a proof clearance spin test in the two-bearing rig. The spin test balance magnitudes were as follows:

- as assembled
  - backface — 32.4 g-mm (0.045 oz-in.) at 10 deg
  - nose — 12.97 g-mm (0.018 oz-in.) at 330 deg
- final balance
  - backface—1.44 g-mm (0.002 oz-in.) at 100 deg
  - nose—1.44 g-mm (0.002 oz-in.) at 360 deg

Drawing tolerance is 7.0 g-mm (0.01 oz-in.). Figure 77 shows the rotor in the two-bearing rig suspended from the spin facility cover. The assembly was successfully spin tested to 77,000 rpm with a 10 sec dwell. The maximum speed was limited to 77,000 rpm as a result of rig seal rub. The seal clearances were increased for future spin tests.

Figure 78 shows the ceramic turbine rotor assembled with the compressor for engine S/N 2. The assembly is shown on the engine bearing support. The inducer tip of two blades was nicked (small chip) during assembly (handling). These were blended and FPI showed the blended area was without cracks.

The assembly balance magnitudes were as follows:

- as assembled
  - impeller—34.04 g-mm (0.047 oz-in.)
  - turbine—16.0 g-mm (0.0222 oz-in.)
- final balance
  - impeller—3.55 g-mm (0.005 oz-in.)
  - turbine—8.64 g-mm (0.012 oz-in.)

Drawing tolerance is 2.16 g-mm (0.003 oz-in.). The final balance magnitude is for the gasifier assembly prior to its disassembly and reassembly into the

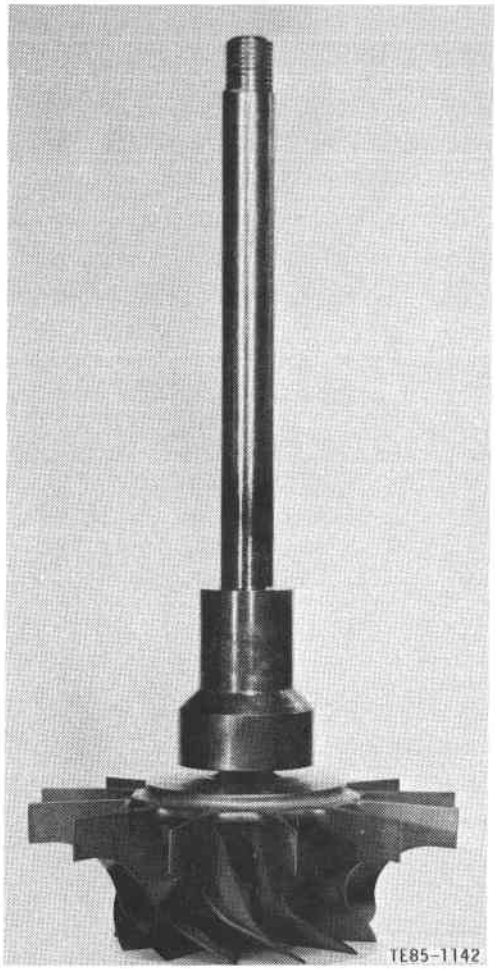

Figure 73. Semifinished rotor/shaft assembly 13.5 deg machined taper rotor backface and second iteration attachment design.

engine support. Also, the final balance magnitudes, although two to four times the drawing limit, were considered acceptable for the planned running to a maximum of 50% N_1.

The engine successfully ran for approximately 42 minutes at 43% N_1. The first 11 minutes were at ambient inlet conditions; the other 31 minutes were at heated inlet air. The test is fully described in subsection 2.2.2, Experimental Engine Testing. To summarize, the test was terminated because of an increase in gasifier shaft whip and compressor inlet vibration associated with an increase in speed to 48% N_1. The gasifier shaft whip is measured at the pinion coupling (compressor end of assembly). The whip response and sequence of events progressing from steps 1 through 4 are illustrated in Figure 79. Step 1 was a slow acceleration to 47.7% N_1 speed and was followed by a deceleration (step 2) because of rapidly increasing whip. The pullback reduced the whip to prior levels, so another acceleration (step 3) was attempted. A shift in the whip response from 0.071 mm (0.0028 in.) to 0.122 mm (0.0048 in.) occurred during step 3, and the engine was immediately decelerated (step 4). Based on prior experience, the change in whip (step 3) seemed to be a shift in rotor balance. The prudent action was to inspect the gasifier.

Teardown inspection revealed that the ceramic gasifier turbine had failed, losing approximately 15 mm (0.6 in.) from all inducer blade tips, as illustrated in Figure 80. A ceramic rotor in the thermal shock rig used to straighten the flow experienced a similar failure. This rotor was nonrotating, and therefore the inducer tips were subjected to a large angle of attack by the flow. All of the inducer tips were broken but more erratically, losing approximately 10 to 20 mm (0.4 to 0.8 in).

Teardown inspection (engine S/N 2) further revealed impact surface damage on the gasifier guide vanes, as shown in Figure 81, but no evidence of airfoil rub on the shroud (see Figure 82).

A postfailure investigation was conducted addressing the gasifier whip (see Figure 79), the rotor/shaft attachment, and the failed inducer airfoils. Calculations were made to predict the dynamic response of the gasifier to various levels of ceramic turbine unbalance. The results are shown in Figure 83. The system, as designed with a squeeze film damper (SFD) at the compressor and spring bar isolator at the turbine, results in a rotor system mode at 20,000 rpm. However, with sufficient unbalance, 11.53 g-mm (0.016 oz-in.), the turbine end isolator bottoms and increases the 20,000 rpm rotor system mode to approximately 40,000 rpm. The rotor was built with 8.46 g-mm (0.012 oz-in.) at the turbine and additional unbalance of 3.55 g-mm (0.005 oz-in.) at the compressor. The whip response seen during the acceleration from 43% to 47.7% N_1 (step 1, Figure 79) is possibly explained by a bottomed turbine isolator.

Postfailure investigation of the attachment showed it was structurally sound by clearing FPI and repeating the drawing (machining) dimensions; no slippage was evident in the assembly.

Postfailure investigation of the attachment showed it was structurally sound by clearing FPI and repeating the drawing (machining) dimensions; no slippage was evident in the assembly.

Potential explanations for the inducer airfoil failure were identified. These were then divided into remote and potential classifications. They are the following:

- remote failure modes
  - overspeed
  - rub

} no evidence

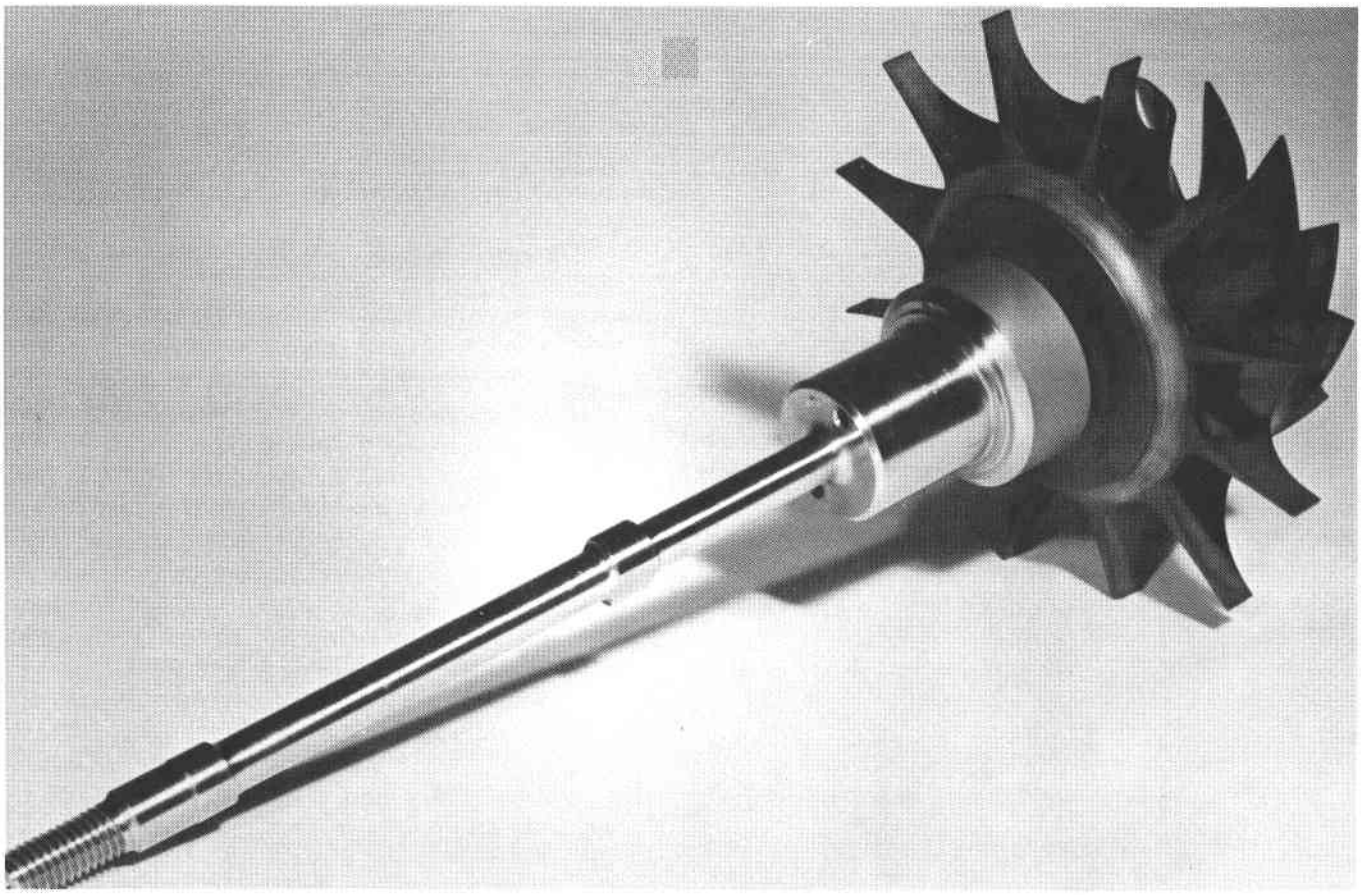

Figure 74. First finish-machined gasifier rotor/shaft assembly, serial number FX34307.

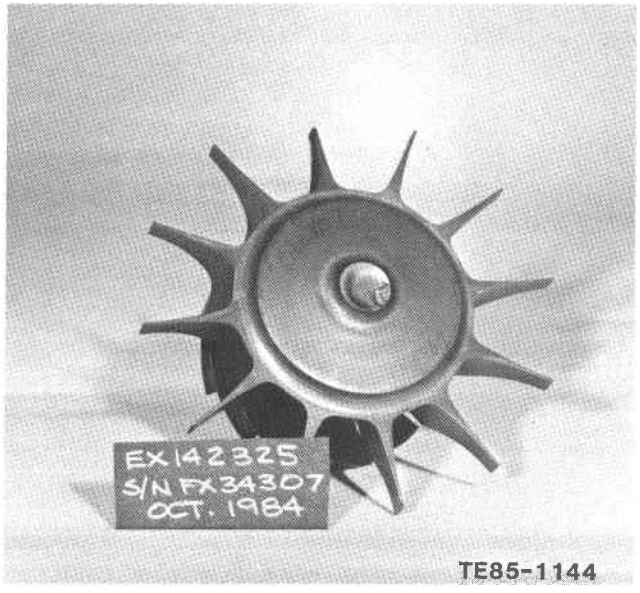

Figure 75. Fracture on rotor S/N FX34307 (first assembly, modified attachment design).

- thermal stress gradient } no evidence
- tip release at chip location — area of near zero centrifugal (radial) stress
- material flaw — no discernible feature/flow per fractographic analysis of the 12 failed airfoils, but the surfaces are battered by the failure debris

- potential failure modes
  - foreign object damage — any particle(s) passing through the flow path and impacting the ceramic rotor (For example, the combustor pilot flame tube [ceramic] was known to be chipped at assembly. At teardown, the chipped condition was again noted with the concern that additional chipping may have occurred.)
  - vibration (nozzle vane passage) — gasifier diagram of rotor blade frequency versus speed shown in Figure 84 (Note that in accelerating to 43% N_1 speed, a potential exducer response to vane passage excitation existed at 30,000 rpm. Transition through this speed was successful with no exducer airfoil failure. The next area of

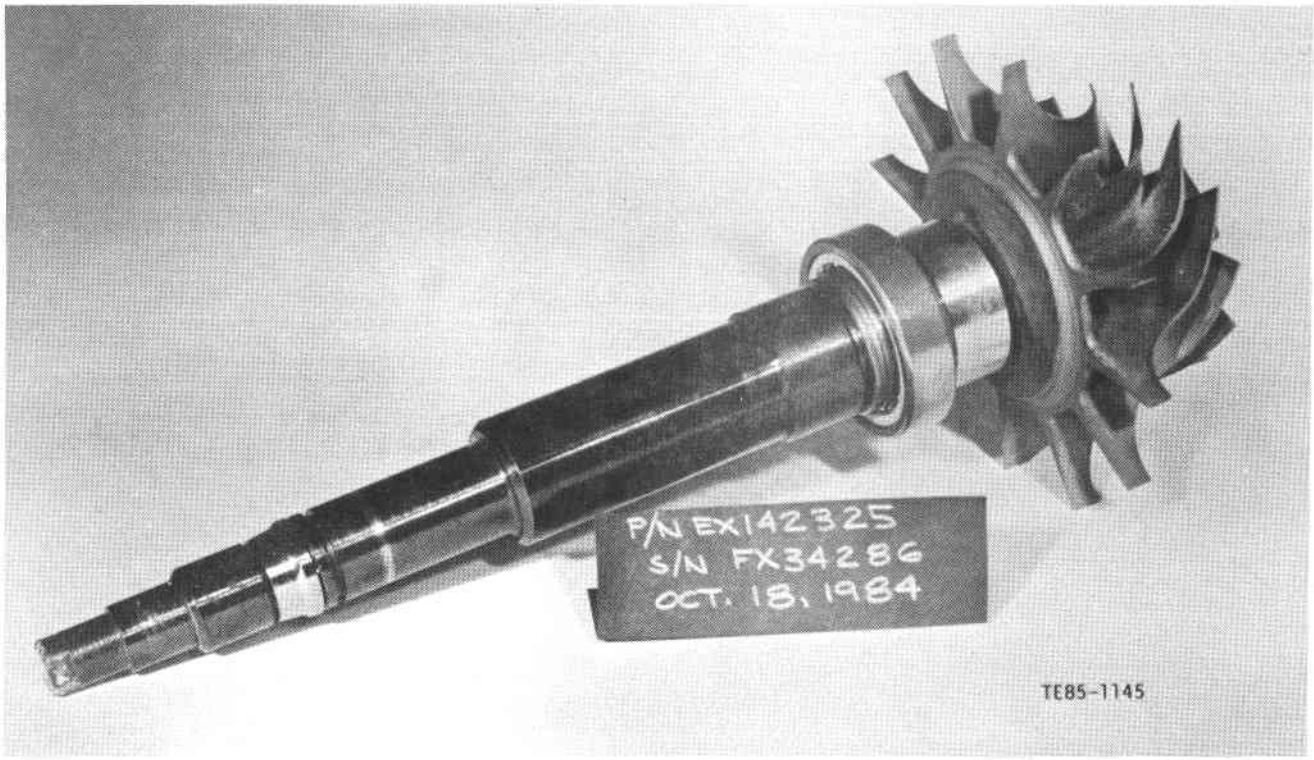

Figure 76. Finish-machined engine candidate rotor assembly prepared for proof clearance spin test.

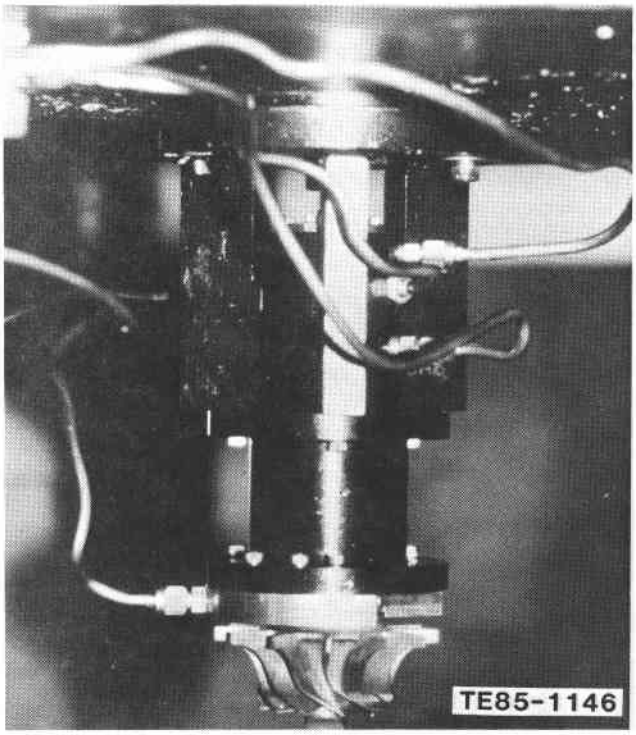

Figure 77. Engine candidate rotor assembly S/N FX34286 installed in the two-bearing spin rig.

concern was inducer response at approximately 45,000 rpm for this rotor [S/N FX34286]. Review of Figure 79 indicates that the step change in whip response occurred at about 36,000 rpm. This does not correspond to a coincidence with vane passage frequency per Figure 84. However, the calculated inducer mode shape, shown in Figure 85, lies in the region of the observed failure.)

In summary, the potential causes for failure of the inducer region of the airfoils in engine S/N 2, BU8 are foreign (loose) object damage and/or forced vibration.

To characterize inducer blade dynamic response further, a test program has been initiated. Room temperature tests of a nonrotating rotor will consist of the following:

1. determination of first inducer mode response versus excitation frequency through resonance
2. determination of the fracture stress at resonance
3. determination of the influence of inducer airfoil length on the natural frequency

Future engine builds will include a measurement of the natural frequencies for every airfoil.

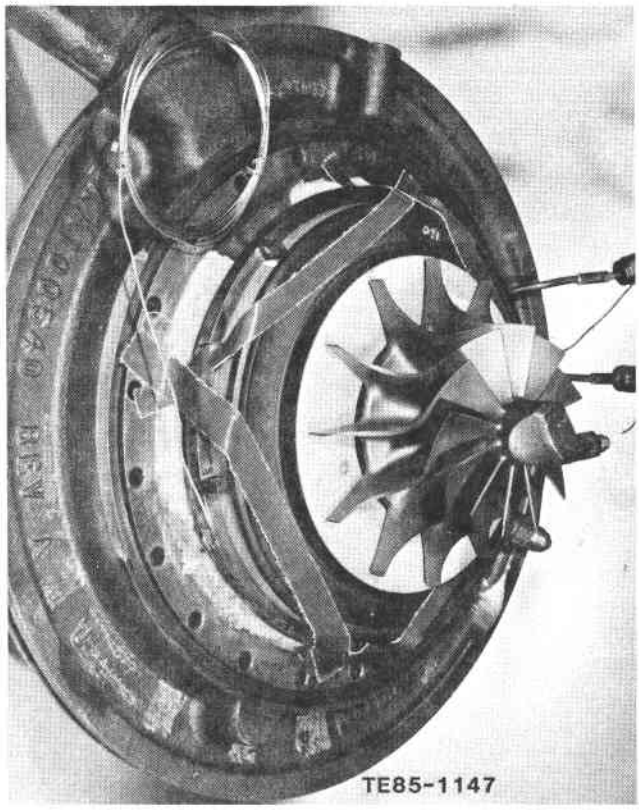

Figure 78. Ceramic gasifier rotor (S/N FX34286) assembled in engine S/N 2 bearing support.

Rotor S/N FX34334 (see Table XXV)

Rotor S/N FX34334 was another fully machined engine candidate assembly that successfully passed dimensional, FPI, and static load tests. The assembly proceeded to the final proof clearance spin test but experienced a spin rig bearing failure at 52,500 rpm that destroyed the rotor.

The status of the balance of the engine candidate gasifier rotors (see Table XXV) is summarized as follows:

- FX34340 — Second attempt in joining to the metal shaft is pending. The first attempt resulted in only partial engagement during the interference fit process.
- FX34346 — This rotor was not usable. Airfoils were broken during machining of the insulator.
- FX34321 — This rotor was not usable. Handling damage followed proof spin clearance test.
- FX34362 — Firing of the insulator to the rotor is pending.
- FX34366 — Being machined (Ahaus Tool Company) with delivery projected for the week of 28 January 1985, this assembly is expected to be available for engine build during the week of 18 February 1985. The attachment was structurally tested by a 100 lb axial load check.

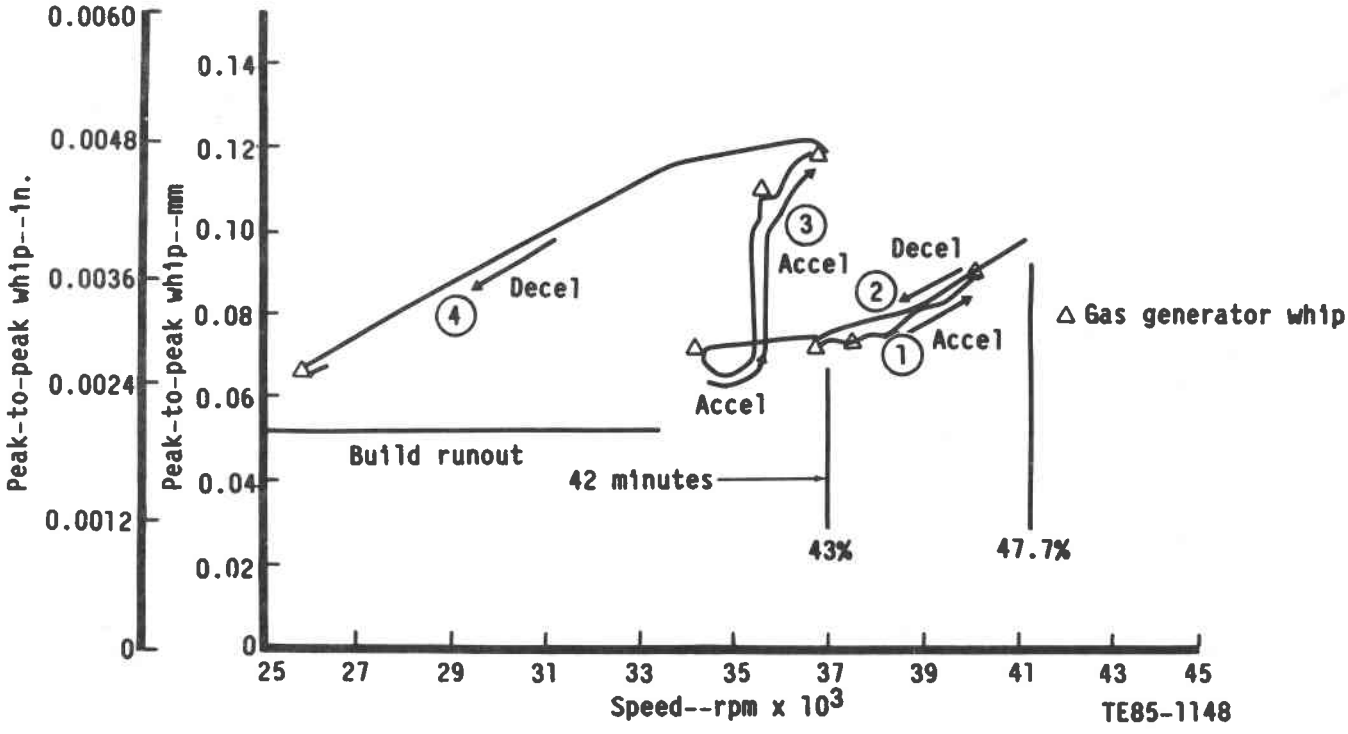

Figure 79. Gasifier rotor whip versus speed.

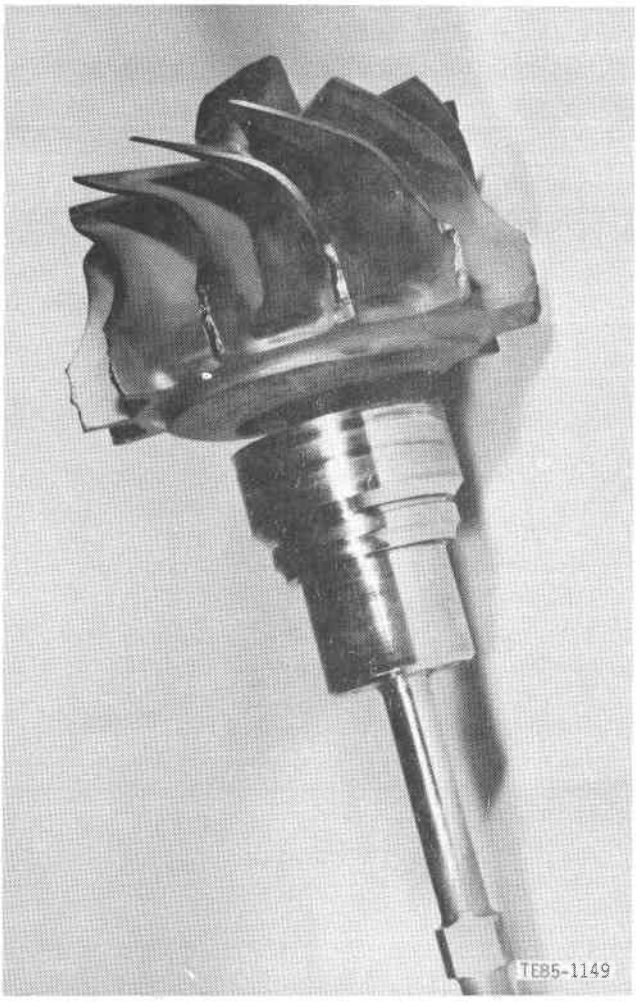

Figure 80. Failed ceramic gasifier rotor (S/N FX34286), engine S/N 2, TD8.

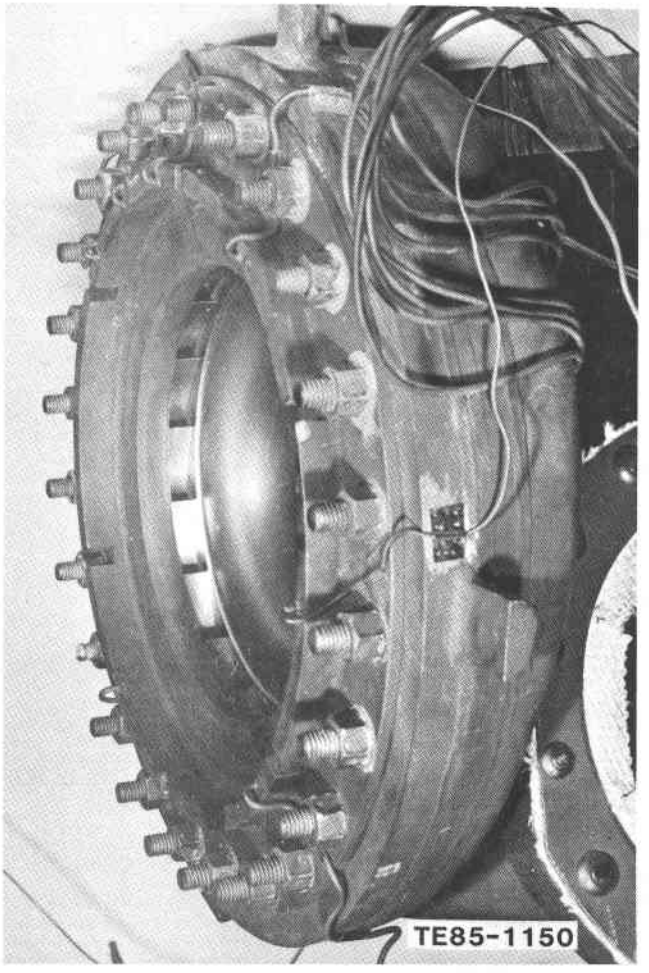

Figure 81. Gasifier inlet guide vanes, engine S/N 2, TD8.

- FX34360 — This rotor directly follows FX34366 in machining. Two small FPI indications were observed in the end face of the insulator. However, the attachment successfully passed the 100 lb axial load check.
- FX34369 — Joining to the metal shaft is pending. Two of the exducer airfoils are broken but judged acceptable.
- FX34320 — In queue for firing of the insulator to the rotor.
- FX34325 — In queue for firing of the insulator to the rotor.
- FX34358 — In queue for firing of the insulator to the rotor.
- FX34371 — In queue for firing of the insulator to the rotor.

Alternate Shaft Attachment

An alternate attachment scheme that uses a glass bond for joining the insulator to the SiC material

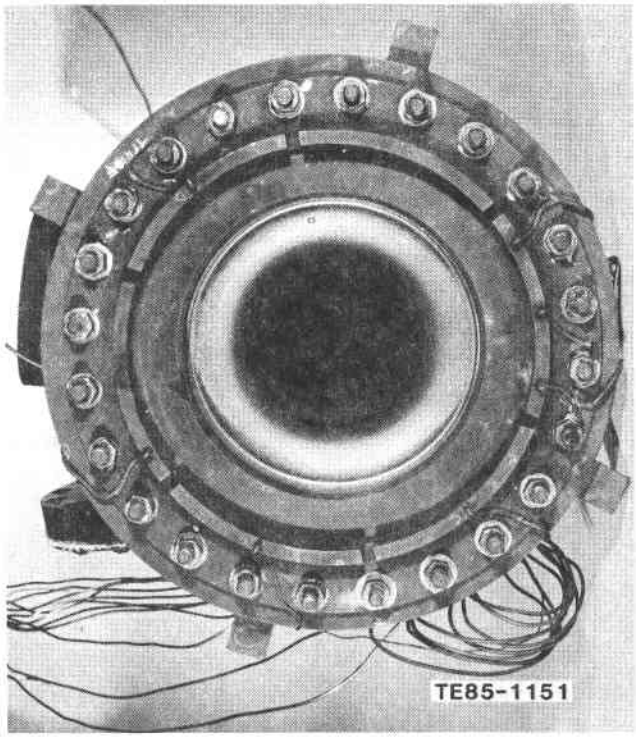

Figure 82. Gasifier shroud (no airfoil rub), engine S/N 2, TD8, ceramic rotor S/N FX34286.

rotor shaft is being investigated. Two rotors, S/N FX34268 and FX34296, are being used to investigate the alternate attachment.

The backface (3.5 deg plane), fillet, and stub shaft were machined, and the insulator was joined to each rotor. The insulator was machined on rotor S/N FX34286, and the proof spin clearance test is pending. Machining of the insulator for rotor S/N FX34296 is pending. Following successful spin clearance tests, completing the attachment and testing the assembly are planned.

Rotor Analyses

Rotor and attachment reliability analyses were updated for the modified attachment (see Figure 71) and revised material parameters for the zircon insulator. The zircon properties are based on a sample of approximately 40 MOR test bars and use a Weibull characterization for the unit surface and volume strength. Tabulated in Table XXVIII are the calculated probability of survival and peak stress values for the ceramic rotor and insulator for various conditions. For reference, temperature and stress plots are included.

The stress plots are selected plots for areas of high stress. For the brittle materials, the rotor, insulator, and sleeve (see Figure 67), maximum principal stresses are presented. For the metal shaft (ductile material), maximum equivalent stresses are provided. The location of the peak stresses noted in Table XXVIII can be identified in the plots. A listing of the plots follows (see Table XXVIII):

- assembly (semifinished shaft, RPD rotor) — interference, shaft/sleeve, Δr = 0.046 mm (0.0018 in.); isotemperature plots — none (uniform room temperature); isostress plots — shown in Figures 86, 87, 88, 89, and 90
- room temperature spin at 100% N_1 (86,240 rpm) (finished shaft, RPD rotor) — interference, shaft/sleeve Δr = 0.046 mm (0.0018 in.); isostress plots — shown in Figures 91, 92, 93, 94, 95, and 96
- steady-state, 649°C (1200°F) RIT, and 50% N_1 engine conditions (subidle) for the finished shaft and RPD rotor; isotemperature plot — shown in Figure 97; isostress plots — shown in Figures 98 and 99
- steady-state, 954°C (1750°F) RIT, and 60% N_1 engine conditions (idle) for the finished shaft and RPD rotor; isotemperature plot — shown in Figure 100; isostress plot — shown in Figures 101, 102, 103, and 104
- steady-state, 1080°C (1976°F) RIT, and 100% N_1 engine conditions for the finished shaft and RPD rotor; isotemperature plots — shown in Figures 105 and 106; isostress plots — shown in Figures 107, 108, 109, and 110
- steady-state, 1288°C (2350°F) RIT, and 100% N_1 engine conditions (design point) for the finished shaft and RPD rotor; isotemperature plot — shown in Figure 111; isostress plots—shown in Figures 112, 113, 114, and 115

9.2.2 Gasifier Turbine Scroll Assembly

Activity this period has addressed the areas of design analysis, parts fabrication, and rig fabrication/assembly. Design analysis was performed on two alternate ceramic gasifier scrolls. One was based on CBO SiC material and a modified component shape designed to simplify manufacture. The other alternate used Norton NC430 material. The analysis results of both alternate scrolls, presented in subsection 4.3.2, were positive, thus generating interest in fabricating and evaluating these ceramic components. Norton was selected to conduct fabrication development of an NC430 scroll as part of an existing Allison Independent Research and Development project. The status of this effort, CBO's efforts on fabricating the original design scroll, and the fabrication/assembly of the thermal shock rig is presented in the following paragraphs.

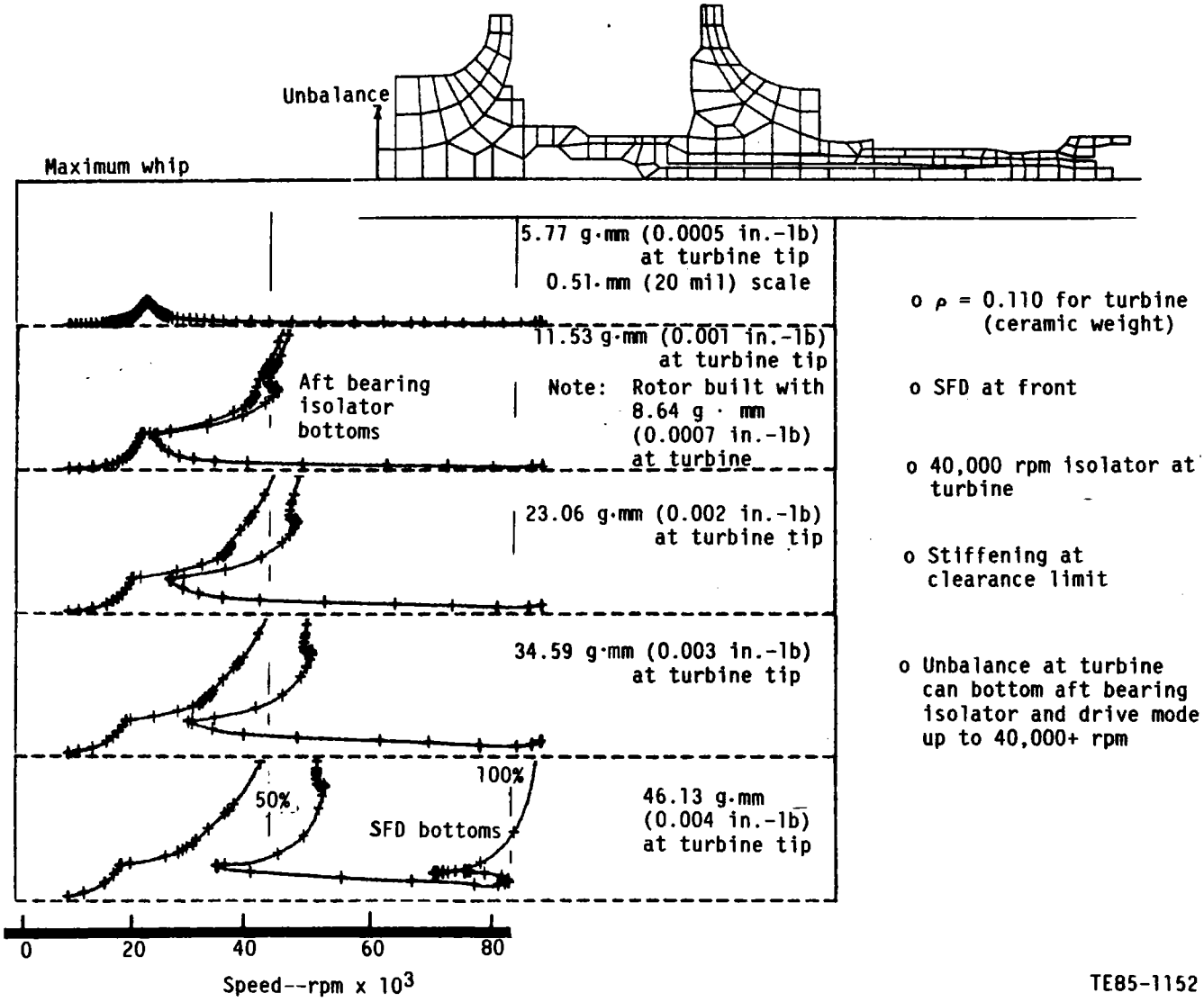

Figure 83. Calculated dynamic response of gasifier rotor for various levels of turbine unbalance.

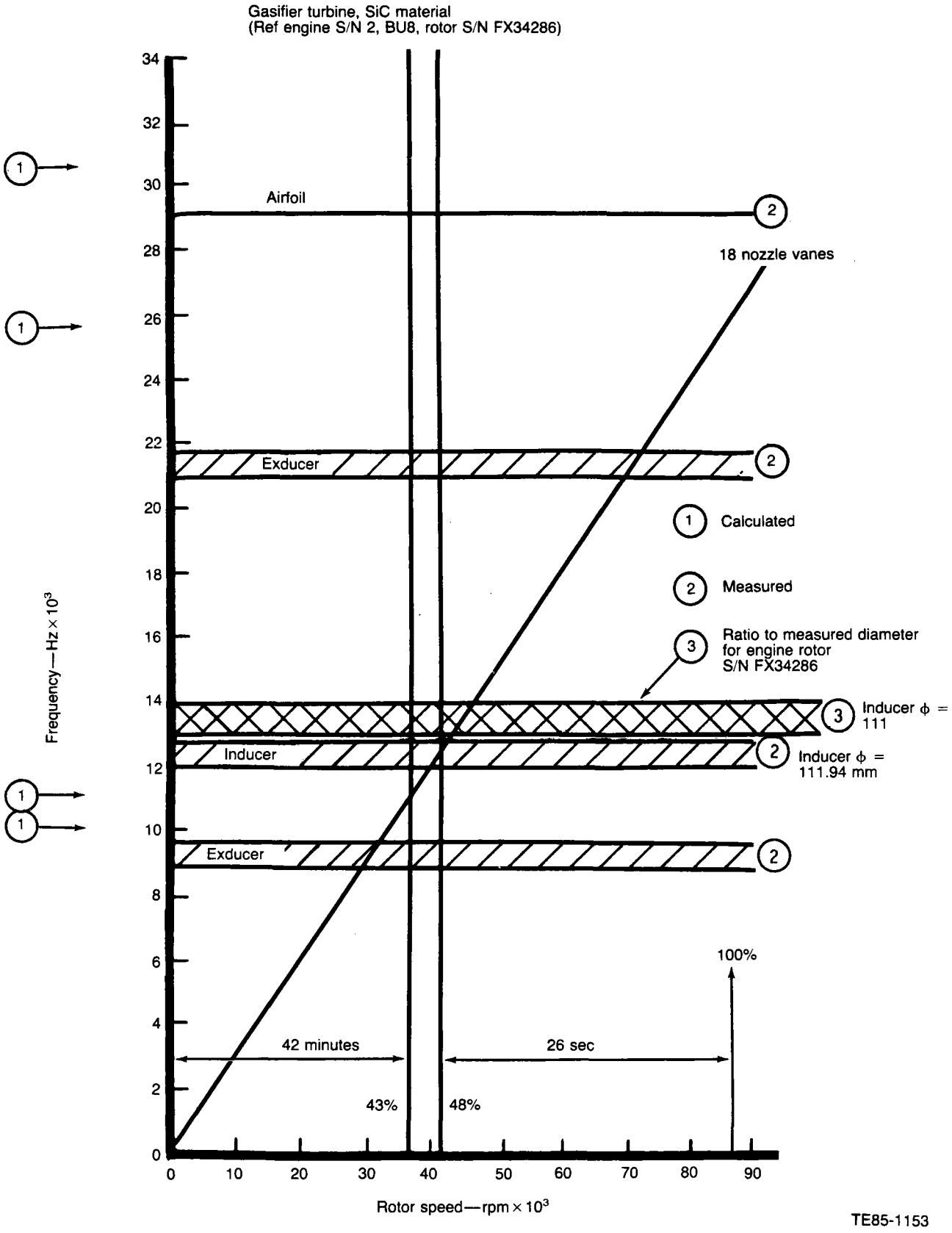

Figure 84. Frequency/speed diagram for ceramic rotor blades.

Table XXVIII.
Calculated ceramic rotor and attachment (finite element) probability of survival and peak stress.

	Assembly	RT spin 100% N	SS, 649°C (1200°F) 50% N	SS, 954°C (1750°F) 60% N	SS, 1080°C (1976°F) 100% N	SS, 1288°C (2350°F) 100% N
Probability of survival						
Rotor	0.9999	0.9981	0.9999	0.9999	0.9911	0.9739
Insulator	0.9999	0.9994	0.9993	0.9954	0.9705	0.8481
Peak stresses—MPa ($lb/in.^2 \times 10^3$)						
Rotor	43.37	112.04	116.11	174.44	218.08	260.55
	(6.29)	(16.25)	(16.84)	(25.3)	(31.63)	(37.79)
Insulator	350.44	149.82	118.18	156.17	173.75	211.05
	(18.72)	(21.73)	(17.14)	(22.65)	(25.20)	(30.61)
Ring	−711.88	108.25	—	426.30	491.94	603.98
	(−103.25)	(15.7)	—	(61.83)	(71.35)	(87.60)
Shaft	1174.87	541.93	—	376.80	381.00	386.38
	(170.4)	(78.6)	—	(54.65)	(55.26)	(56.04)
Radial fit—mm (in.)						
Shaft/ring	−0.0018	−0.0018	−0.0018	−0.0018	−0.0018	−0.0018

Weibull parameters

	Surface	Volume
Rotor		
σ_o	53.004	32.293
M	10.91	8.62
Insulator		
σ_o	28.19	14.9
M	8.93	5.96

Note: Modified attachment

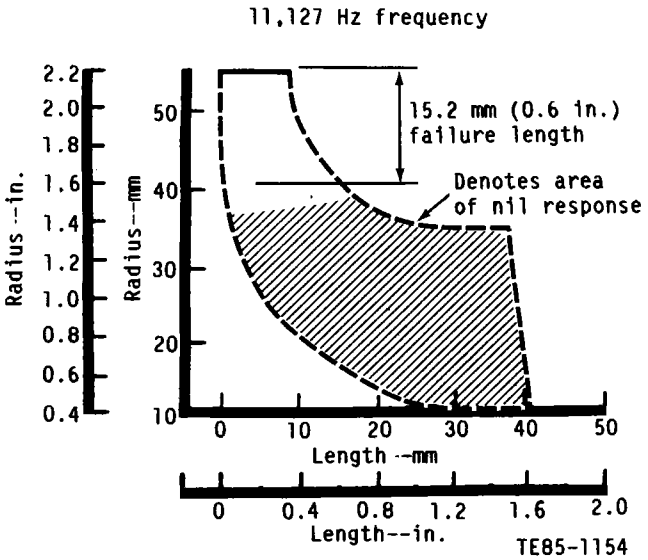

Figure 85. Calculated first inducer mode shape for ceramic material gasifier turbine.

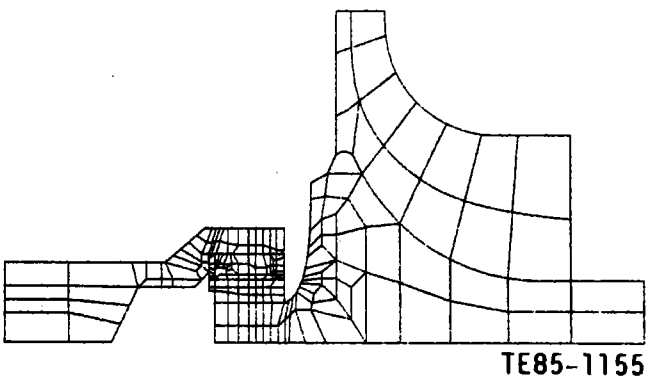

Figure 86. Rotor/shaft assembly case finite element model.

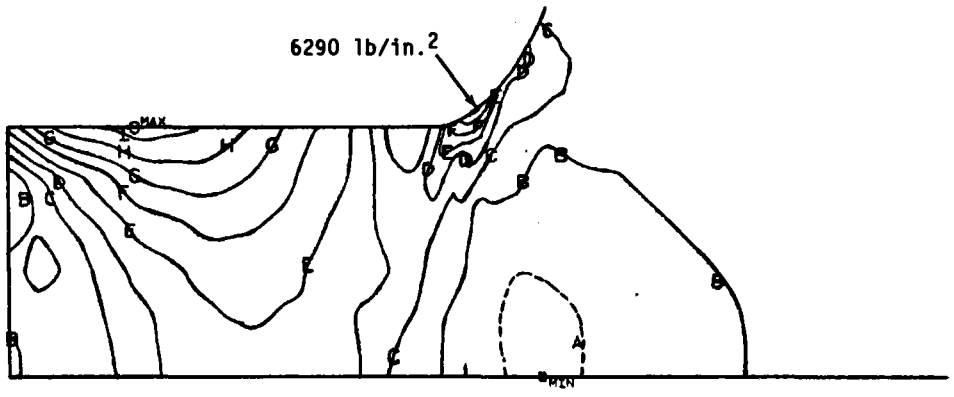

	Stress	
	MPa	lb/in.^{2}x10^3
A	-6.9	-1.00
B	0	0
C	6.9	1.00
D	13.8	2.00
E	20.7	3.00
F	27.6	4.00
G	34.5	5.00
H	41.4	6.00
I	48.3	7.00
Max	52.2	7.57
Min	-9.8	-1.42

TE85-1156

Figure 87. Rotor/shaft assembly case maximum principal stress for SiC rotor stub shaft.

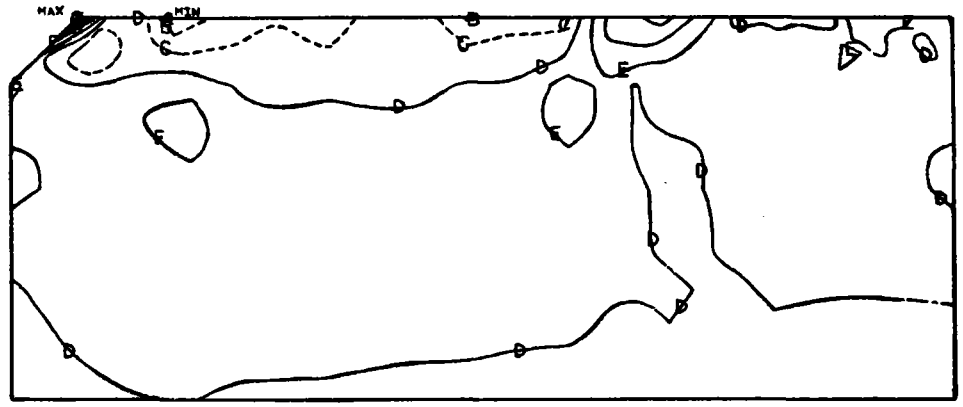

	Stress	
	MPa	lb/in.^{2}x10^3
A	-62.1	-8.00
B	-41.4	-6.00
C	-20.7	-3.00
D	0	0
E	20.7	3.00
F	41.4	6.00
G	62.1	9.00
H	82.7	12.00
I	103.4	15.00
J	124.1	18.00
Max	129.1	18.72
Min	-63.1	-9.15

TE85-1157

Figure 88. Rotor/shaft assembly case maximum principal stress with insulator.

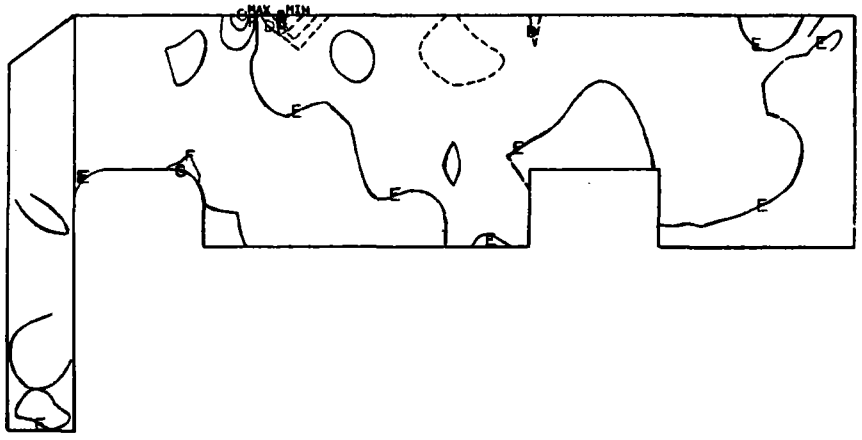

	Stress	
	MPa	lb/in.^{2}x10^3
A	551.6	-80.00
B	413.7	-60.00
C	275.8	-40.00
D	137.9	-20.00
E	0	0
F	137.9	20.00
G	275.8	40.00
Max	390.9	56.69
Min	638.0	-92.54

TE85-1158

Figure 89. Rotor shaft assembly case maximum principal stress for sleeve.

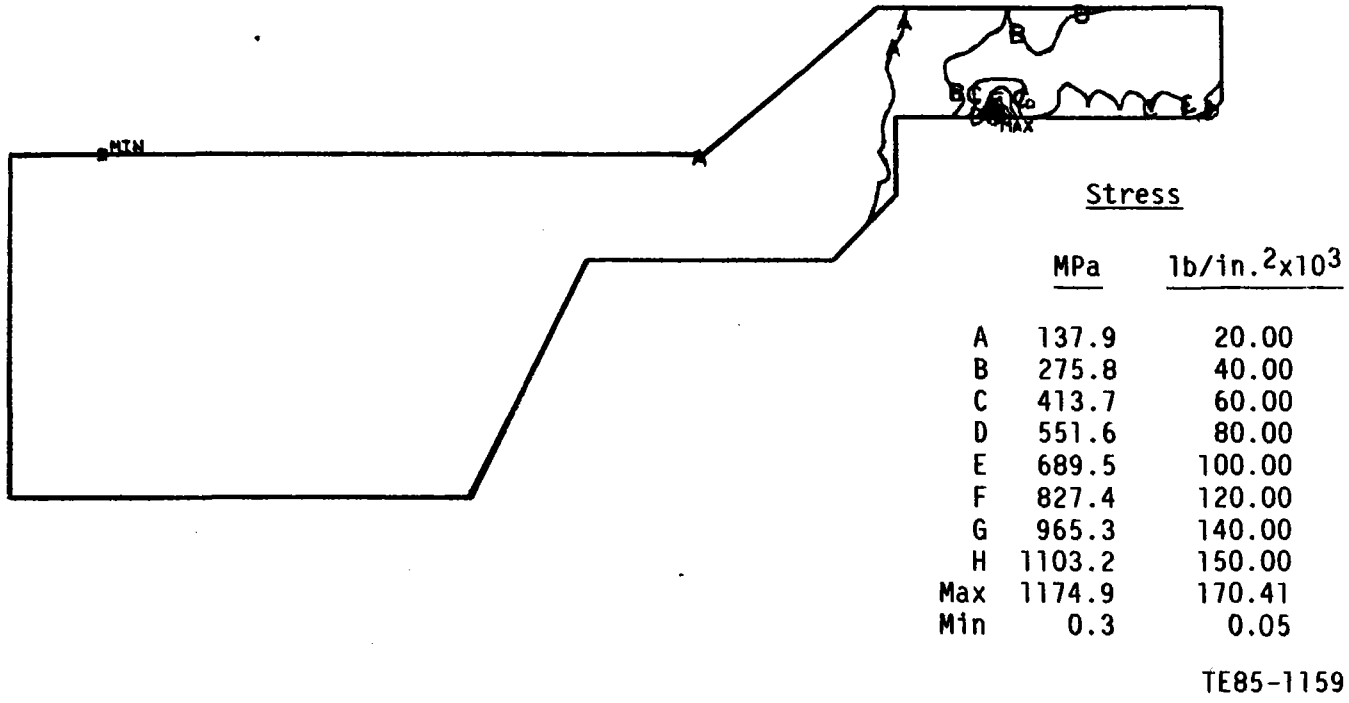

Figure 90. Rotor shaft assembly case combined equivalent stress for shaft.

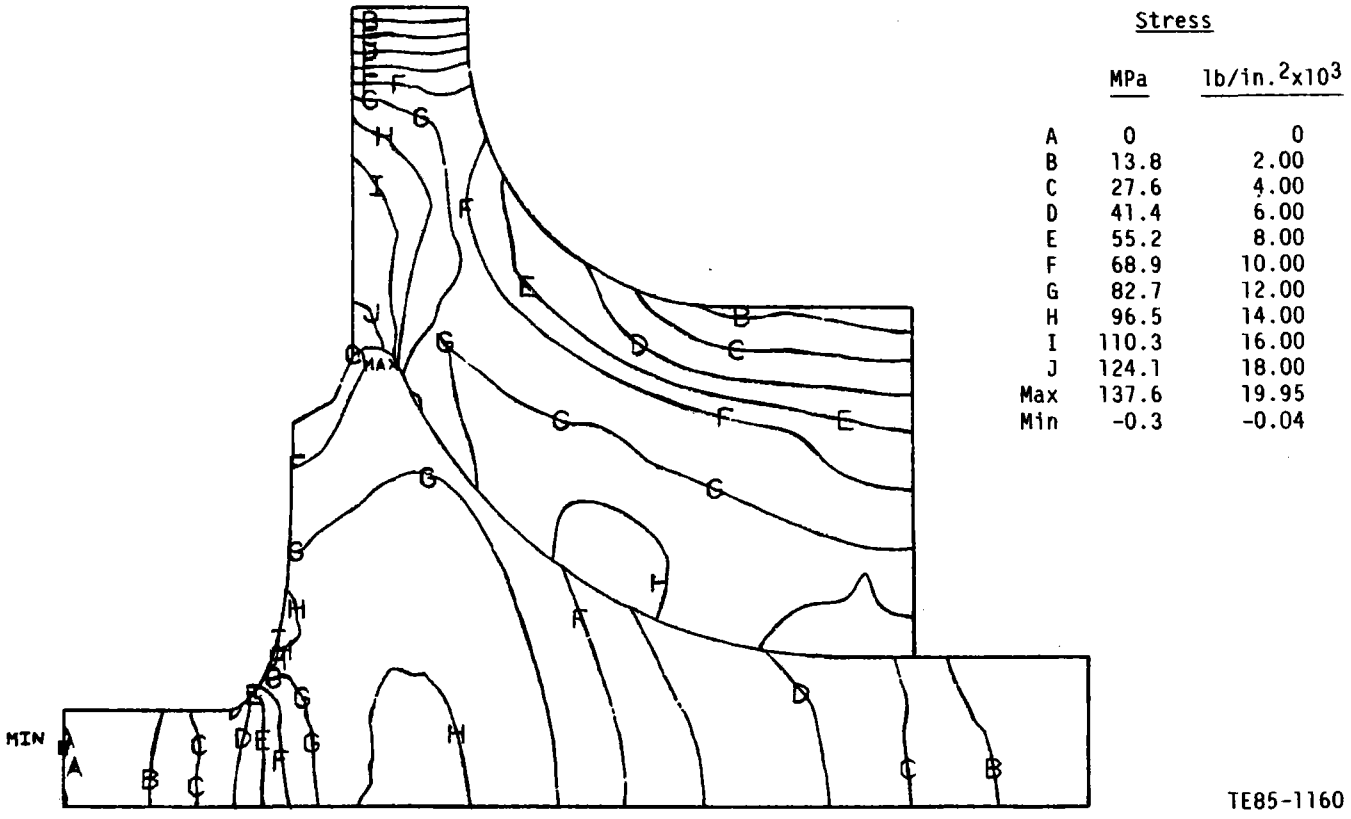

Figure 91. Rotor maximum principal stress for room temperature spin at 100% speed.

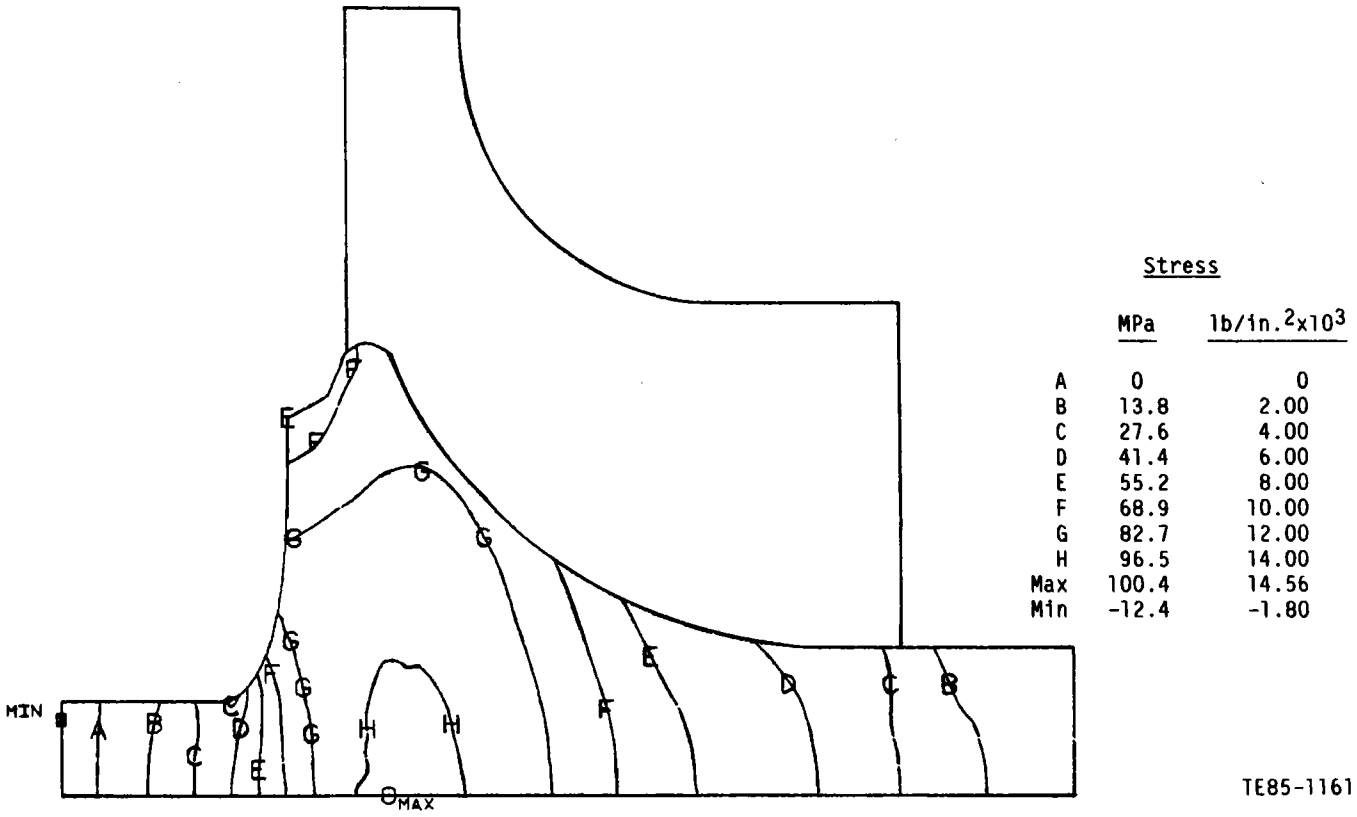

Figure 92. Rotor tangential stress for room temperature spin at 100% speed.

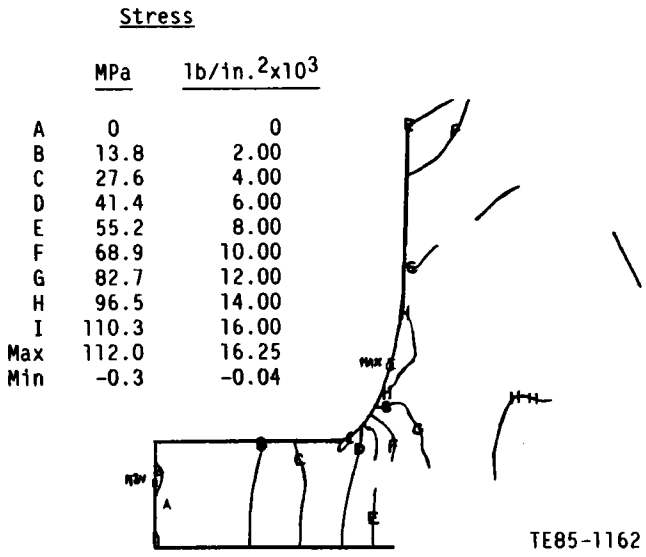

Figure 93. Rotor stub shaft maximum principal stress for room temperature spin at 100% speed.

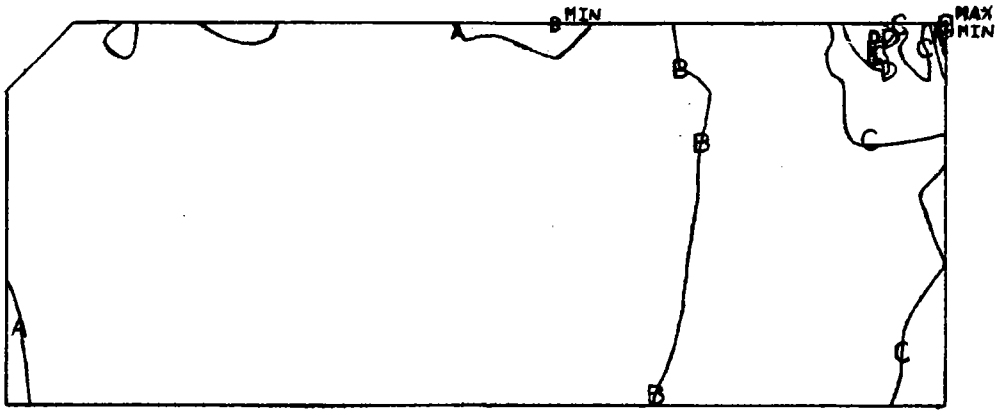

	Stress	
	MPa	lb/in.^{2}x10^3
A	0	0
B	20.7	3.00
C	41.4	6.00
D	62.1	9.00
E	82.7	12.00
F	103.4	15.00
G	124.1	18.00
H	144.8	21.00
Max	149.8	21.73
Min	-15.5	-2.26

TE85-1163

Figure 94. Insulator maximum principal stress for room temperature spin at 100% speed.

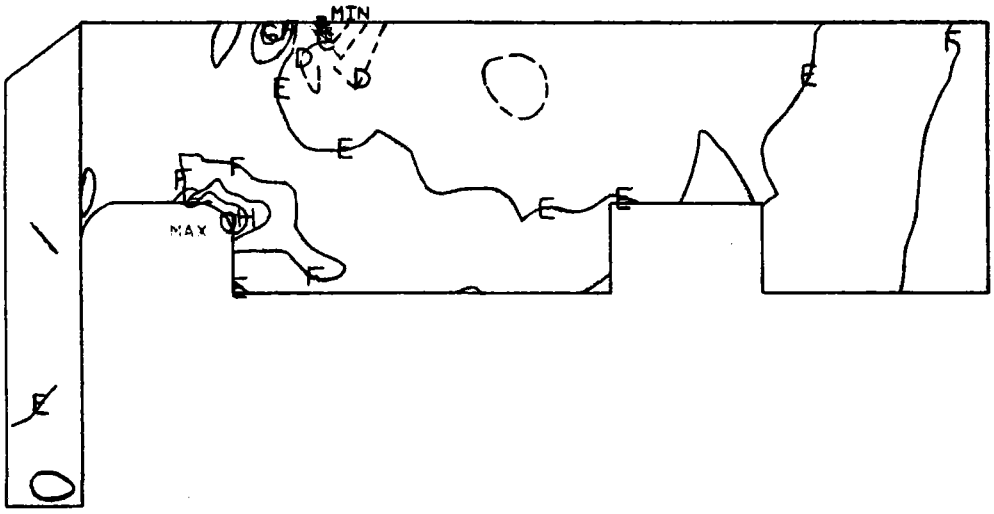

	Stress	
	MPa	lb/in.^{2}x10^3
A	-275.8	-40.00
B	-206.8	-30.00
C	-137.9	-20.00
D	-68.9	-10.00
E	0	0
F	68.9	10.00
G	137.9	20.00
H	206.8	30.00
I	275.8	40.00
Max	313.2	45.43
Min	-309.9	-44.94

TE85-1164

Figure 95. Sleeve maximum principal stress for room temperature spin at 100% speed.

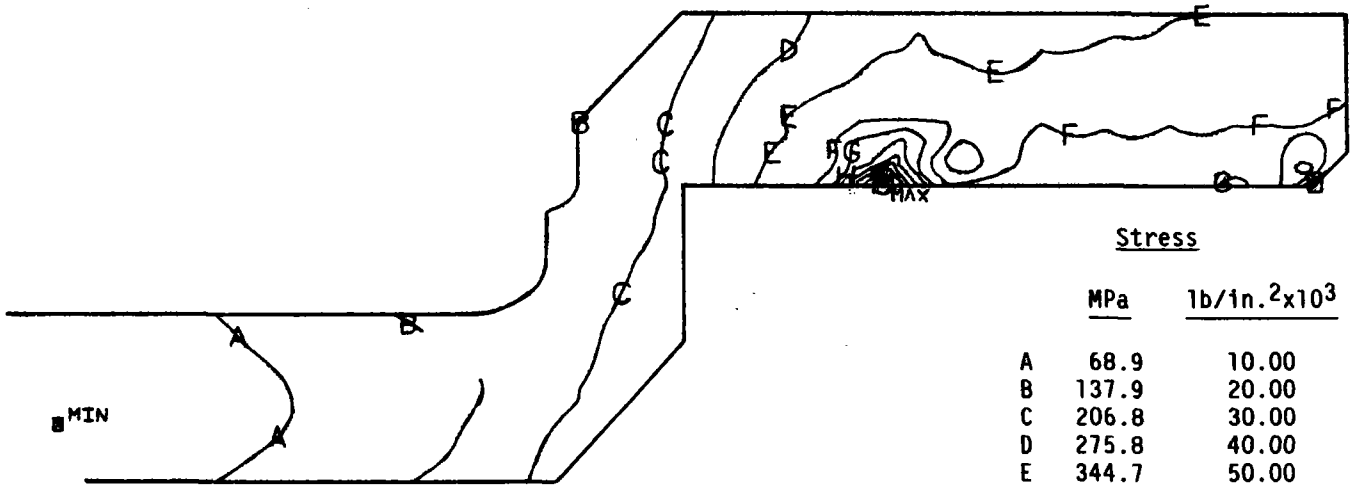

	Stress	
	MPa	lb/in.^{2}x10^3
A	68.9	10.00
B	137.9	20.00
C	206.8	30.00
D	275.8	40.00
E	344.7	50.00
F	413.7	60.00
G	482.6	70.00
H	551.6	80.00
I	620.5	90.00
J	689.5	100.00
K	758.4	110.00
L	827.4	120.00
M	896.3	130.00
N	965.3	140.00
Max	978.4	141.90
Min	35.9	5.21

TE85-1165

Figure 96. Gasifier shaft combined equivalent stress for room temperature spin at 100% speed.

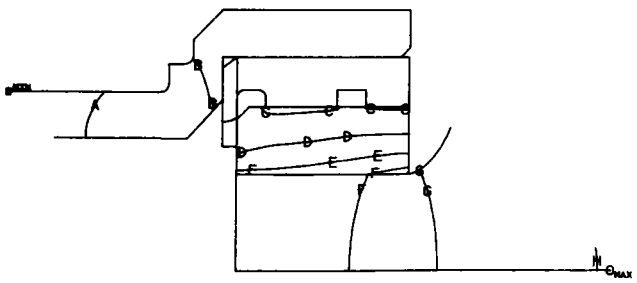

	Temperature	
	°C	°F
A	182.2	360.00
B	232.2	450.00
C	282.2	540.00
D	332.2	630.00
E	382.2	720.00
F	432.2	810.00
G	482.2	900.00
H	532.2	990.00
Max	534.0	993.26
Min	176.5	349.67

TE85-1166

Figure 97. Rotor/shaft attachment region temperature for steady-state, 649°C (1200°F) RIT, and 50% speed engine conditions.

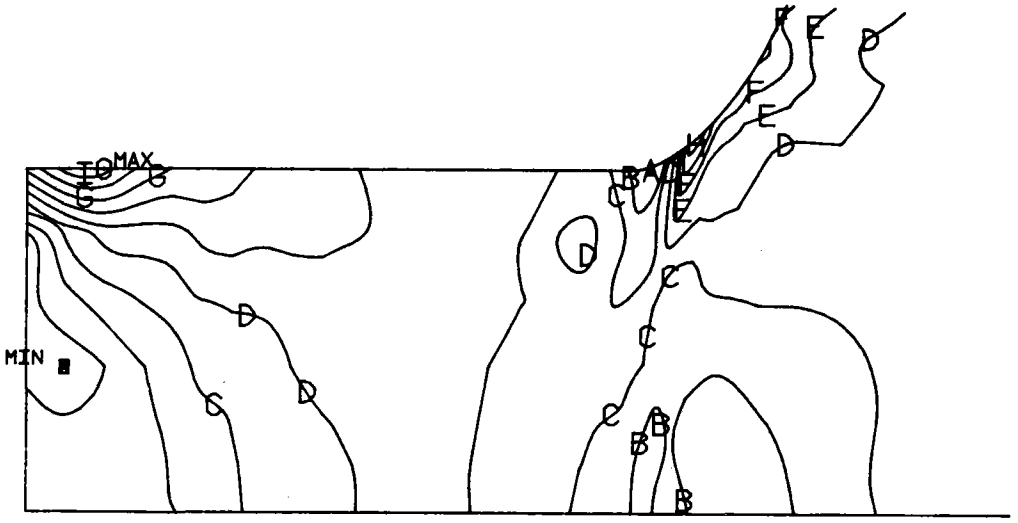

	Stress MPa	Stress lb/in.^{2}x10^3
A	0	0
B	13.8	2.00
C	27.6	4.00
D	41.4	6.00
E	55.2	8.00
F	68.9	10.00
G	82.7	12.00
H	96.5	14.00
I	110.3	16.00
Max	116.1	16.84
Min	-8.1	-1.17

TE85-1167

Figure 98. Rotor stub shaft maximum principal stress for 649°C (1200°F) RIT and 50% speed engine conditions.

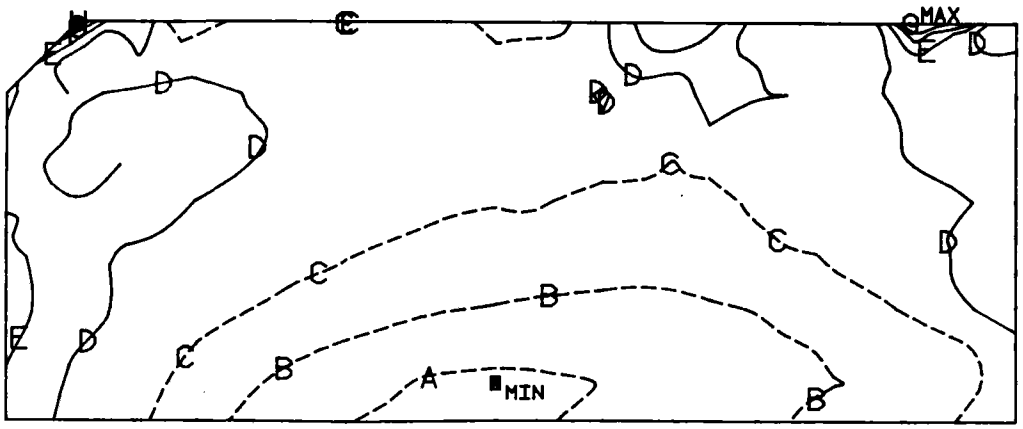

	Stress MPa	Stress lb/in.^{2}x10^3
A	-82.7	-12.00
B	-55.2	-8.00
C	-27.6	-4.00
D	0	0
E	27.6	4.00
F	55.2	8.00
G	82.7	12.00
H	110.3	16.00
Max	118.2	17.14
Min	-90.2	-13.08

TE85-1168

Figure 99. Insulator maximum principal stress for 649°C (1200°F) RIT and 50% speed engine conditions.

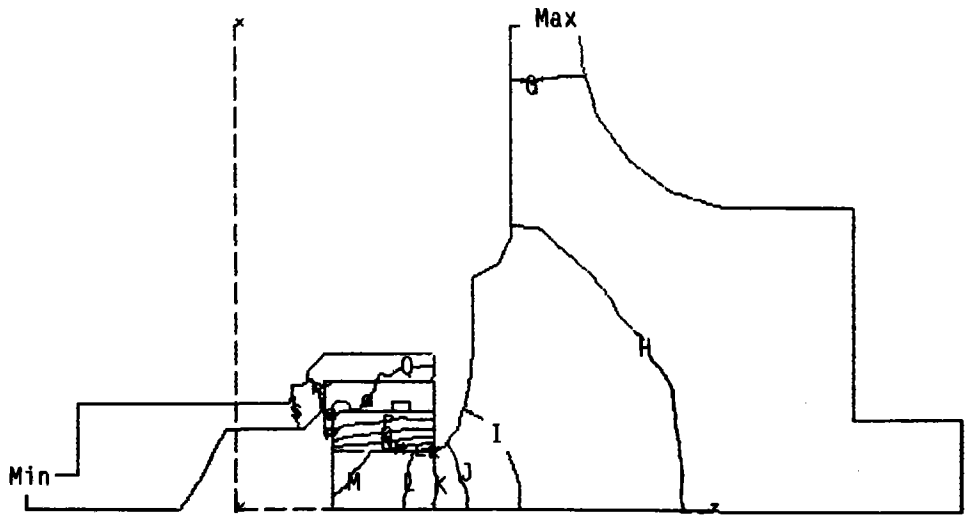

	Temperature °C	Temperature °F
G	871.1	1600.00
H	815.6	1500.00
I	760.0	1400.00
J	704.4	1300.00
K	648.9	1200.00
L	593.3	1100.00
M	537.8	1000.00
N	482.2	900.00
O	426.7	800.00
P	371.1	700.00
Q	315.6	600.00
R	260.0	500.00
S	204.4	400.00
Max	880.7	1617.29
Min	130.0	200.81

TE85-1169

Figure 100. Rotor/shaft temperatures for steady-state, 954°C (1750°F) RIT, and 60% speed (idle) engine conditions.

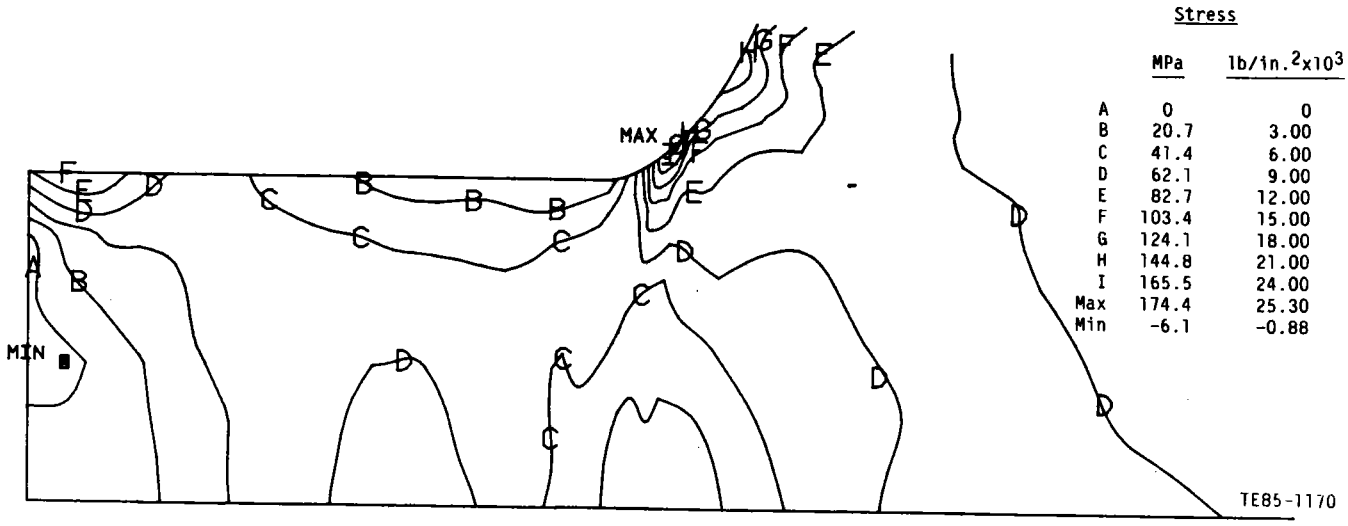

Figure 101. Rotor stub shaft maximum principal stress for steady-state, 954°C (1750°F) RIT, and 60% speed (idle) engine conditions.

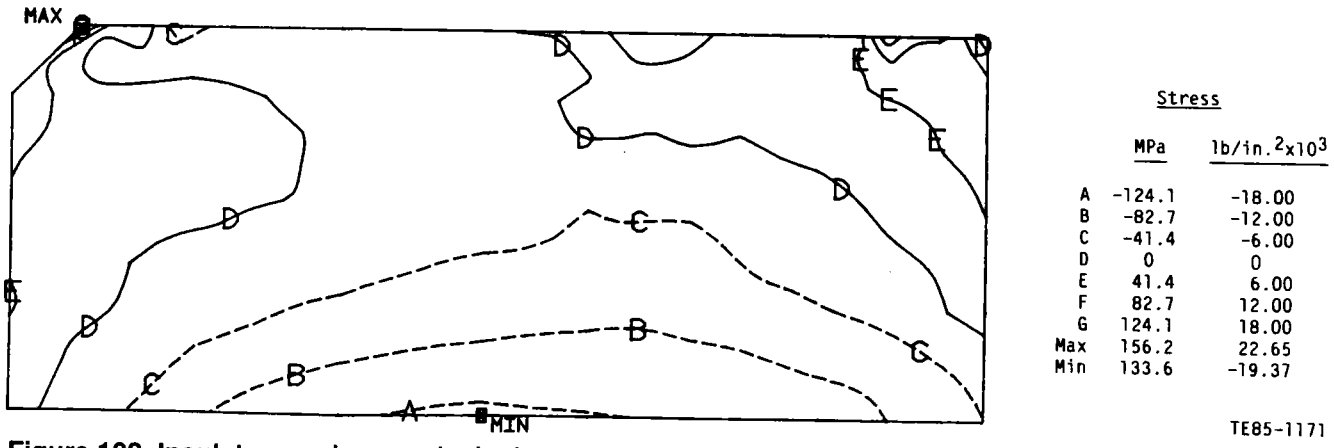

Figure 102. Insulator maximum principal stress for steady-state, 954°C (1750°F) RIT, and 60% speed (idle) engine conditions.

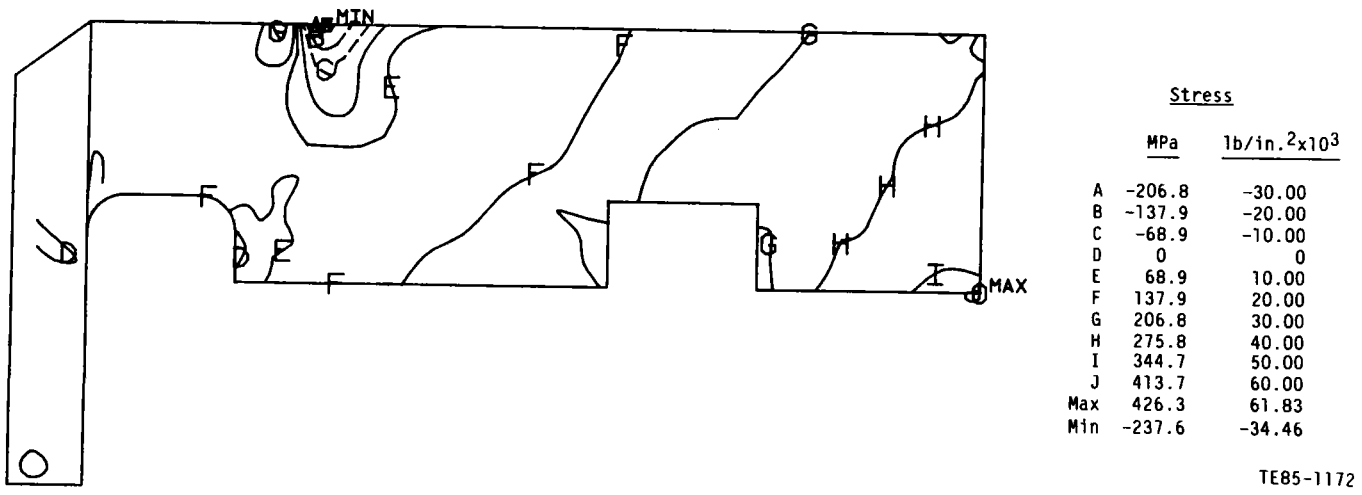

Figure 103. Sleeve maximum principal stress for steady-state, 954°C (1750°F) RIT, and 60% speed (idle) engine conditions.

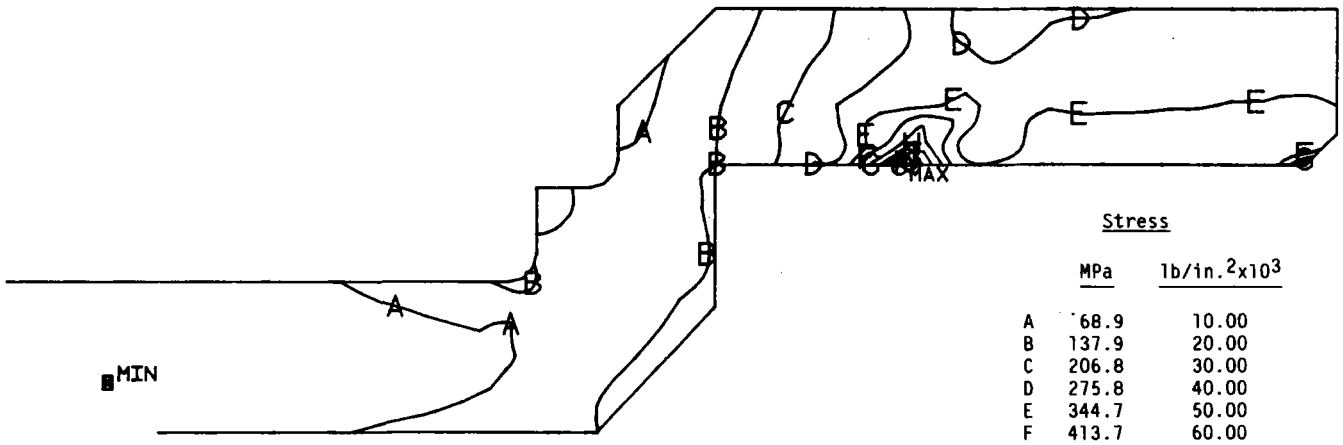

Stress	MPa	lb/in.^{2}x10^3
A	68.9	10.00
B	137.9	20.00
C	206.8	30.00
D	275.8	40.00
E	344.7	50.00
F	413.7	60.00
G	482.6	70.00
H	551.6	80.00
I	620.5	90.00
J	689.5	100.00
K	758.4	110.00
Max	809.9	117.47
Min	7.8	1.13

TE85-1173

Figure 104. Gasifier shaft combined equivalent stress for steady-state, 954°C (1750°F) RIT, and 60% speed (idle) engine conditions.

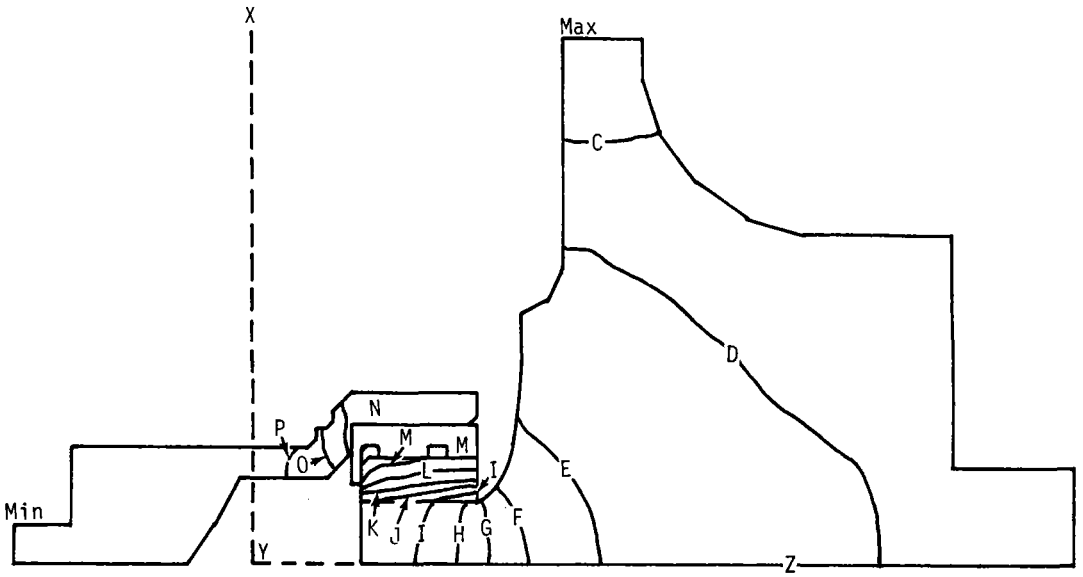

Temperature	°C	°F
A	1037.8	1900.00
B	982.2	1800.00
C	926.7	1700.00
D	871.1	1600.00
E	815.6	1500.00
F	760.0	1400.00
G	704.4	1300.00
H	648.9	1200.00
I	593.3	1100.00
J	537.8	1000.00
K	482.2	900.00
L	426.7	800.00
M	371.1	700.00
N	315.6	600.00
O	260.0	500.00
P	204.4	400.00
Q	148.9	300.00
R	93.3	200.00
Max	965.5	1769.84
Min	174.6	346.20

TE85-1174

Figure 105. Rotor temperatures for steady-state, 1080°C (1976°F) RIT and 100% speed engine conditions.

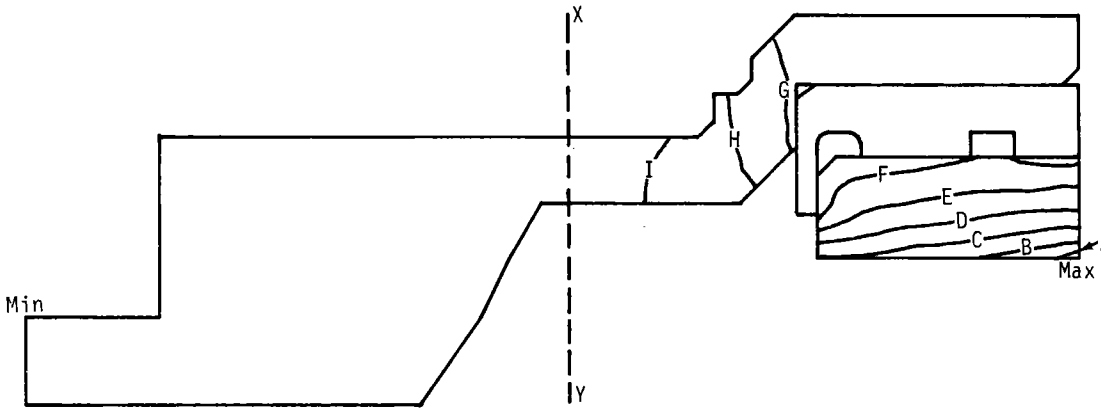

Temperature	°C	°F
A	648.9	1200.00
B	593.3	1100.00
C	537.8	1000.00
D	482.2	900.00
E	426.7	800.00
F	371.1	700.00
G	315.6	600.00
H	260.0	500.00
I	204.4	400.00
Max	684.4	1263.93
Min	174.6	346.20

TE85-1175

Figure 106. Rotor/shaft attachment temperatures for steady-state 1080°C (1976°F) RIT and 100% speed engine conditions.

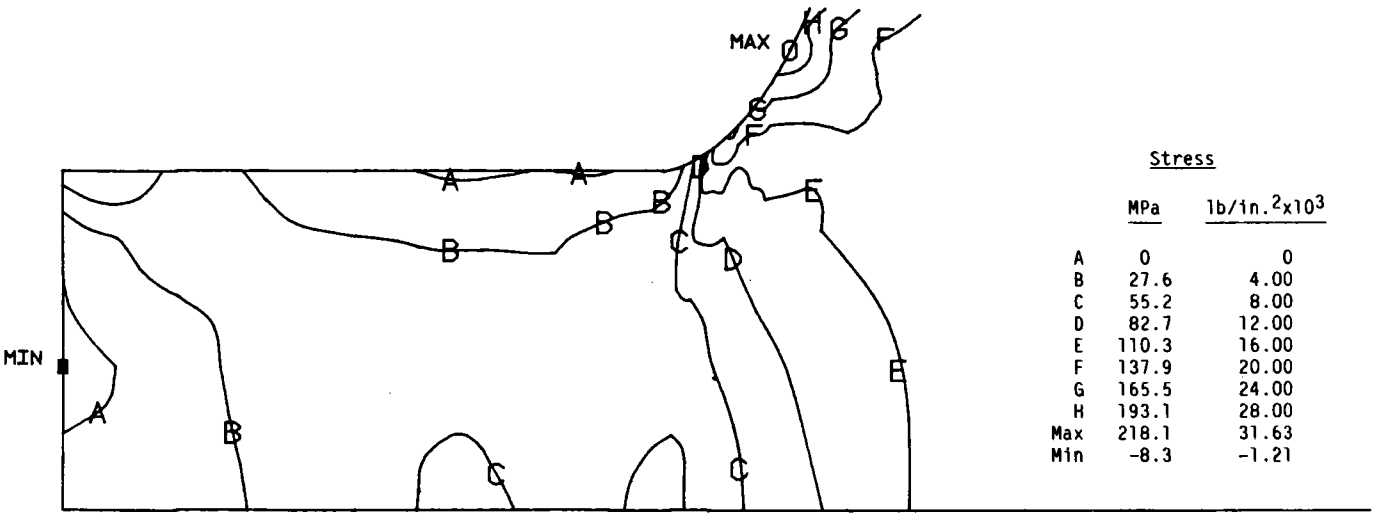

Stress	MPa	lb/in.^{2}x10^3
A	0	0
B	27.6	4.00
C	55.2	8.00
D	82.7	12.00
E	110.3	16.00
F	137.9	20.00
G	165.5	24.00
H	193.1	28.00
Max	218.1	31.63
Min	-8.3	-1.21

TE85-1176

Figure 107. Rotor stub shaft maximum principal stress for steady-state, 1080°C (1976°F) RIT and 100% speed engine conditions.

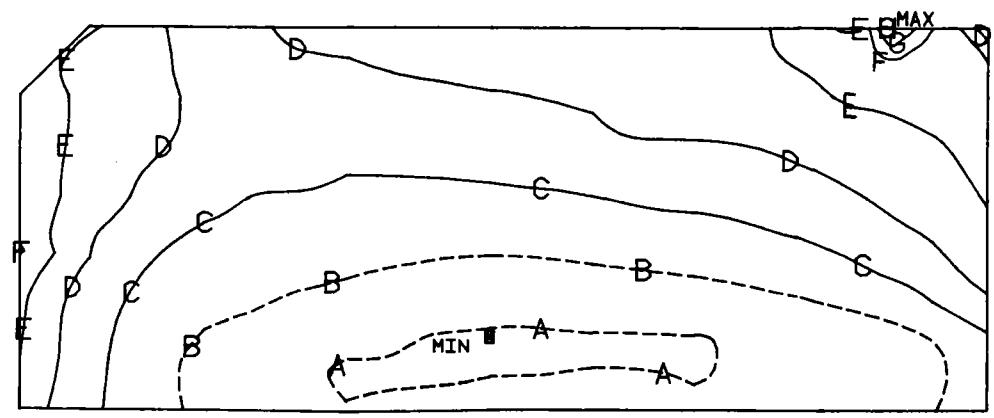

Stress	MPa	lb/in.^{2}x10^3
A	-68.9	-10.00
B	-34.5	-5.00
C	0	0
D	34.5	5.00
E	68.9	10.00
F	103.4	15.00
G	137.9	20.00
H	172.4	25.00
Max	173.7	25.20
Min	72.1	-10.46

TE85-1177

Figure 108. Insulator maximum principal stress for steady-state, 1080°C (1976°F) RIT, and 100% speed engine conditions.

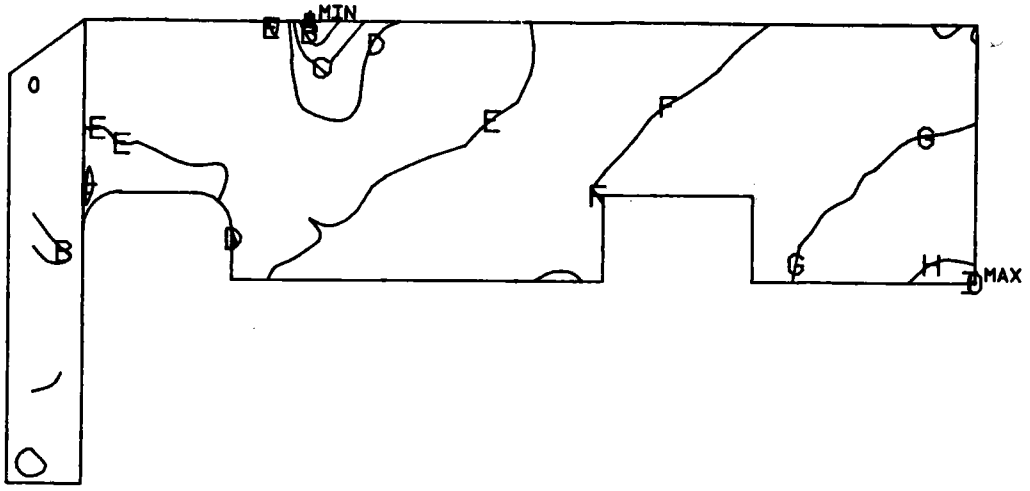

Stress	MPa	lb/in.^{2}x10^3
A	-68.9	-10.00
B	0	0
C	68.9	10.00
D	137.9	20.00
E	206.8	30.00
F	275.8	40.00
G	344.7	50.00
H	413.7	60.00
I	482.6	70.00
Max	491.9	71.35
Min	-71.8	-10.42

TE85-1178

Figure 109. Sleeve maximum principal stress for steady-state, 1080°C (1976°F) RIT, and 100% speed engine conditions.

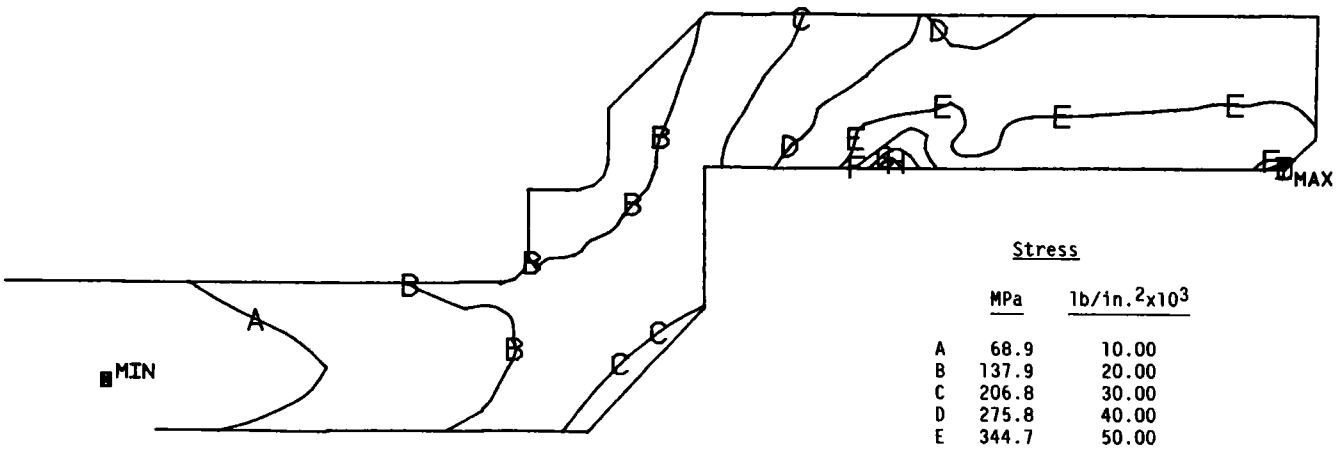

Stress	MPa	lb/in.^{2}x10^3
A	68.9	10.00
B	137.9	20.00
C	206.8	30.00
D	275.8	40.00
E	344.7	50.00
F	413.7	60.00
G	482.6	70.00
H	551.6	80.00
I	620.5	90.00
Max	674.5	97.83
Min	34.0	4.93

TE85-1179

Figure 110. Gasifier shaft combined equivalent stress for steady-state, 1080°C (1976°F) RIT, and 100% speed engine conditions.

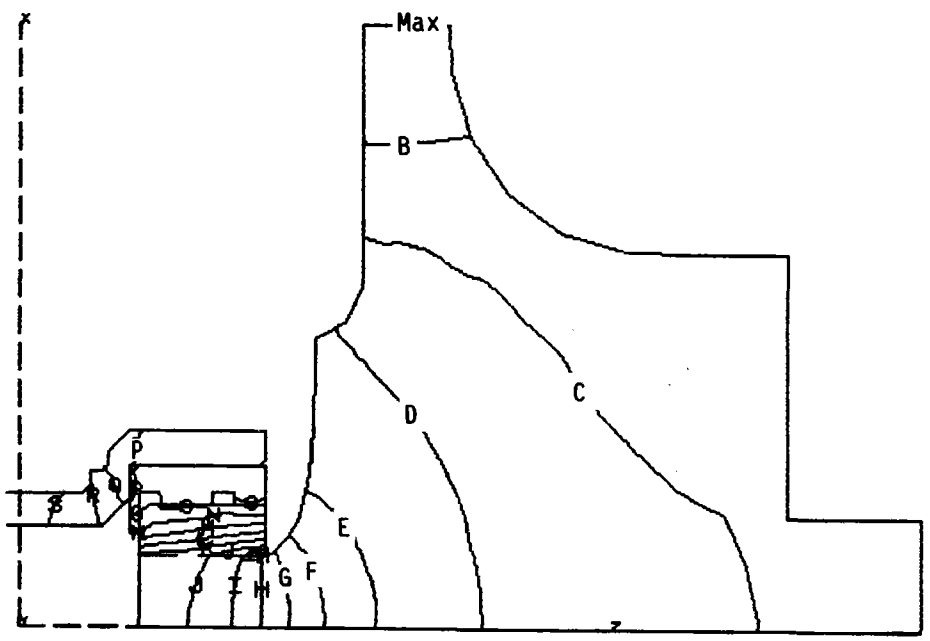

Temperature	°C	°F
B	1148.9	2100.00
C	1093.3	2000.00
D	1037.8	1900.00
E	982.2	1800.00
F	926.7	1700.00
G	871.1	1600.00
H	815.6	1500.00
I	760.0	1400.00
J	704.4	1300.00
K	648.9	1200.00
L	593.3	1100.00
M	537.8	1000.00
N	482.2	900.00
O	426.7	800.00
P	371.1	700.00
Q	315.6	600.00
R	260.0	500.00
S	204.4	400.00
Max	1191.3	2176.33
Min	175.3	347.55

TE85-1180

Figure 111. Rotor/shaft assembly temperature for steady-state 1288°C (2350°F) RIT, and 100% speed engine conditions.

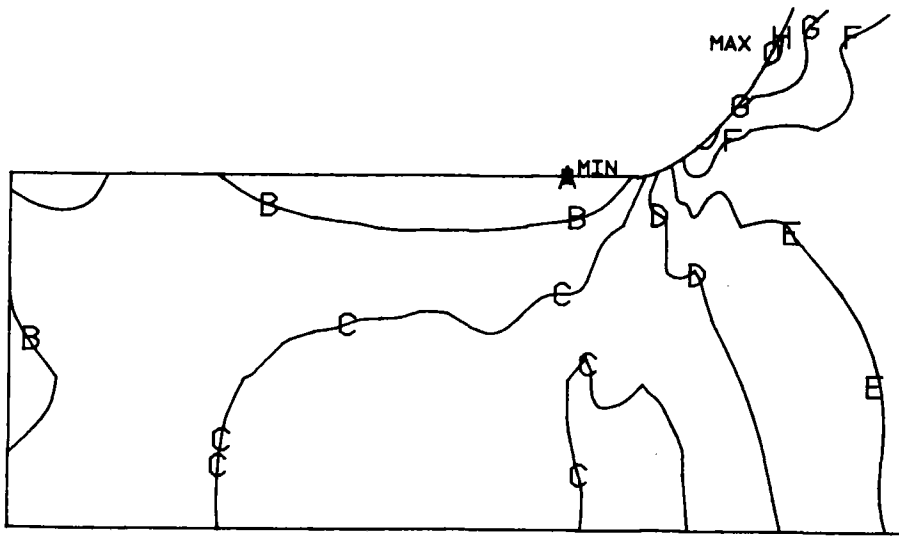

Stress	MPa	lb/in.^{2}x10^3
A	-41.4	-6.00
B	0	0
C	41.4	6.00
D	82.7	12.00
E	124.1	18.00
F	165.5	24.00
G	206.8	30.00
H	248.2	36.00
Max	260.6	37.79
Min	-41.6	-6.04

TE85-1181

Figure 112. Rotor stub shaft maximum principal stress for steady-state, 1288°C (2350°F) RIT, and 100% speed (design point) engine conditions.

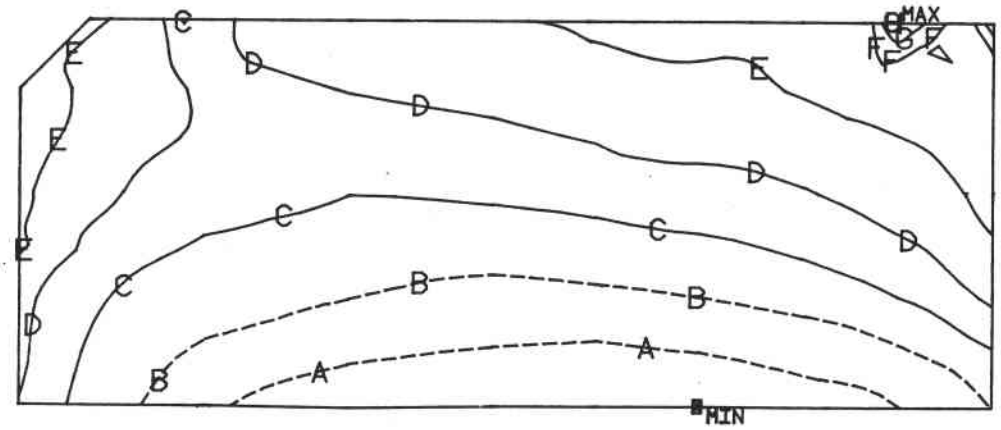

Stress	MPa	lb/in.^{2}x10^3
A	-82.7	-12.00
B	-41.4	-6.00
C	0	0
D	41.4	6.00
E	82.7	12.00
F	124.1	18.00
G	165.5	24.00
H	206.8	30.00
Max	211.0	30.61
Min	-111.9	-16.23

TE85-1182

Figure 113. Insulator maximum principal stress for steady-state, 1288°C (2350°F) RIT, and 100% speed (design point) engine conditions.

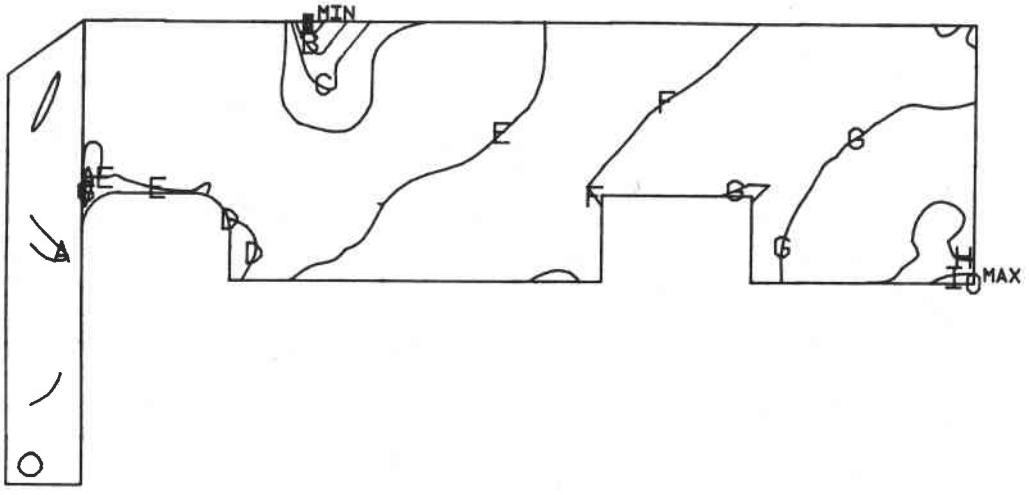

Stress	MPa	lb/in.^{2}x10^3
A	0	0
B	68.9	10.00
C	137.9	20.00
D	206.8	30.00
E	275.8	40.00
F	344.7	50.00
G	413.7	60.00
H	482.6	70.00
I	551.6	80.00
Max	604.0	87.61
Min	-37.7	-5.47

TE85-1183

Figure 114. Sleeve maximum principal stress for steady-state, 1288°C (2350°F) RIT, and 100% speed (design point) engine conditions.

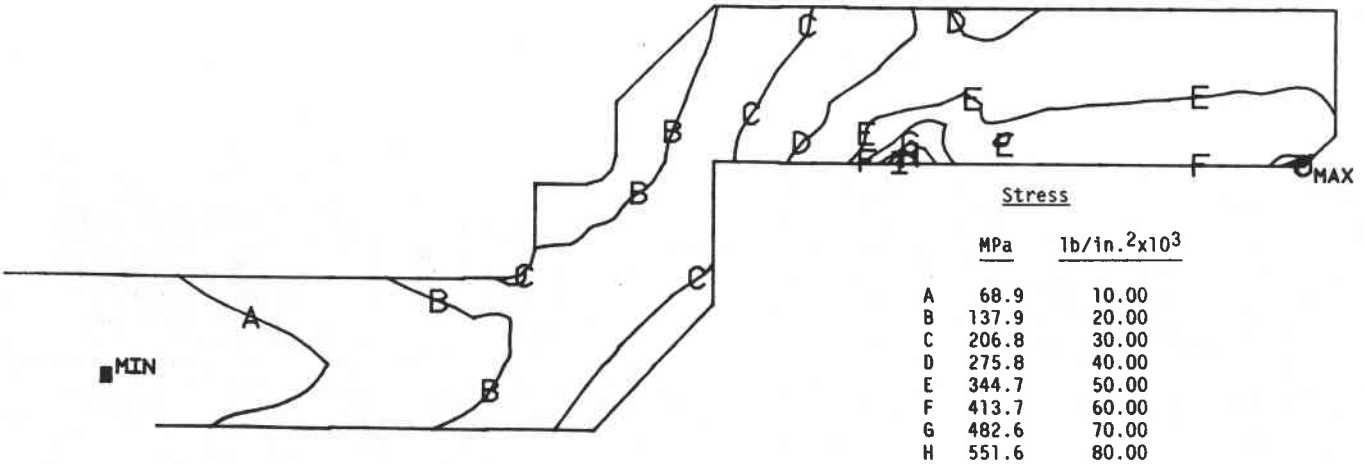

Stress	MPa	lb/in.^{2}x10^3
A	68.9	10.00
B	137.9	20.00
C	206.8	30.00
D	275.8	40.00
E	344.7	50.00
F	413.7	60.00
G	482.6	70.00
H	551.6	80.00
I	620.5	90.00
J	689.5	100.00
Max	756.8	109.76
Min	33.2	4.82

TE85-1184

Figure 115. Gasifier shaft combined equivalent stress for steady-state, 1288°C (2350°F) RIT, and 100% speed (design point) engine conditions.

Carborundum

Four sintered alpha-SiC scroll assemblies were fabricated by CBO during this reporting period. One piece was inspected and machined by Atlas Tool Company and is ready for rig testing (see Figure 116). Two pieces were sent to Ahaus Tool Company for machining; one was dimensionally unmachinable. The second is in the process of being machined. The fourth piece had flaws in the braze joints and was sent back to CBO for repairs.

One siliconized silicon carbide scroll assembly was fabricated by CBO during this reporting period. The part was sent to Atlas for machining. Upon inspection of the machined part, it was found that some of the vane pockets were machined too deep; however, the part will be retained for rig testing.

Norton

The Norton High Performance Ceramics Division is producing NC430 silicon carbide scroll assemblies.

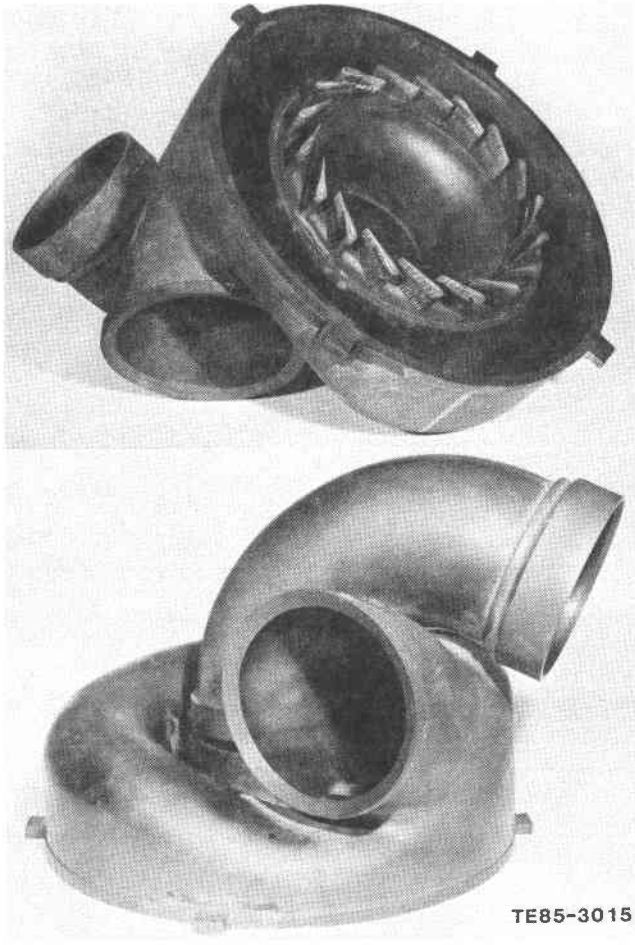

Figure 116. Finish-machined Carborundum alpha-SiC scroll assembly.

Fabrication of the required patterns and molds for slip casting the gasifier scroll assembly components has been completed (see Figure 117). Eleven scroll bodies were successfully cast (see Figure 118), prefired, and analyzed dimensionally. Measurements indicated that the actual shrinkage was slightly different from the anticipated value. This necessitated remaking the patterns for the scroll body, elbow, and shroud. However, siliconization of the existing scroll bodies was continued to allow refinement of the process. This siliconization was successful on all eleven bodies.

Refabrication of the patterns and molds and recasting of scroll components have been completed. Following prefiring, five sets of components were machined and are ready for the bonding process.

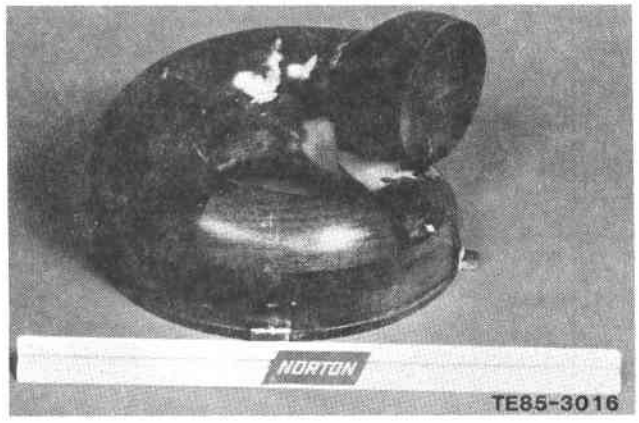

Figure 117. Pattern for Norton NC340 scroll assembly.

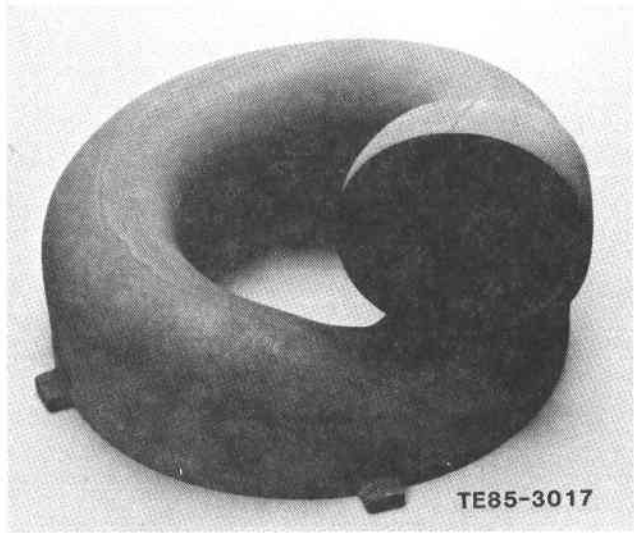

Figure 118. Prefired Norton NC430 scroll body.

9.2.3 Turbine Scroll Static Components Thermal Simulation Rig

Assembly of the turbine scroll static components thermal simulation rig (also known as the scroll thermal shock rig) began in May 1984. The rig is designed to produce AGT 100 engine combustor outlet conditions within an environment that duplicates the engine airflow paths, temperatures, and pressures. The rig was designed to provide a thermal simulator suitable for testing nonrotating ceramic components as a demonstration of their engine readiness.

The installation of the scroll thermal shock rig in the combustion laboratory facility is depicted in Figure 119. As shown in Figure 119, the exhaust piping and the rig baseplates are air cooled (water cooling is also available) to allow continuous operation at engine temperatures. The rig itself, as depicted in Figure 120, has the internal capability to test the gasifier turbine and power turbine scrolls together.

Since a ceramic gasifier turbine scroll assembly is the first unit scheduled in hot fire proof testing on this rig, the initial gasifier turbine only rig configuration, as shown in Figure 121, has been used for this reporting period. This initial configuration replaced the power turbine flow-path components with a ceramic transition duct (detail 1) and used a modified ceramic exhaust transition (detail 2). The exhaust duct was connected to the gasifier scroll by a modified ceramic coupling/piston ring that was retained in position by cerachrome felt insulators. A modified, nonrotating, ceramic rotor was initially incorporated to prevent excessive swirl (detail 3).

Allison conducted more than 5.5 hr of hot fire testing during cold start and main nozzle flow shakedown, checkout, and calibration of this rig. These tests were conducted using a metal gasifier scroll in place of the ceramic scroll. Several revisions of the rig design were required to bring the rig to operational status. One ceramic scroll was proof tested at idle airflow rate and 705°C (~1300°F) BIT conditions. This test was a heated air only ceramic scroll checkout run. The rig is now ready for hot fire ceramic scroll engine readiness demonstration proof tests.

Initial Metal Gasifier Scroll Shakedown and Calibration Tests

The purpose of these tests was to ensure proper rig operation and correlate rig instrumentation with instrumentation on the metal gasifier scroll assembly. An instrumented gasifier scroll assembly was borrowed from engine S/N 1. The rig and future engine configurations will measure and monitor the BOT through thermocouples placed within the gas stream that are attached to a newly installed ring fitted between the combustor outlet and the scroll inlet. Previous tests have monitored the TIT upstream from the guide vanes through gas flow immersed thermocouples attached to the inside of the metal gasifier scroll at circumferential locations. The metal gasifier scroll is

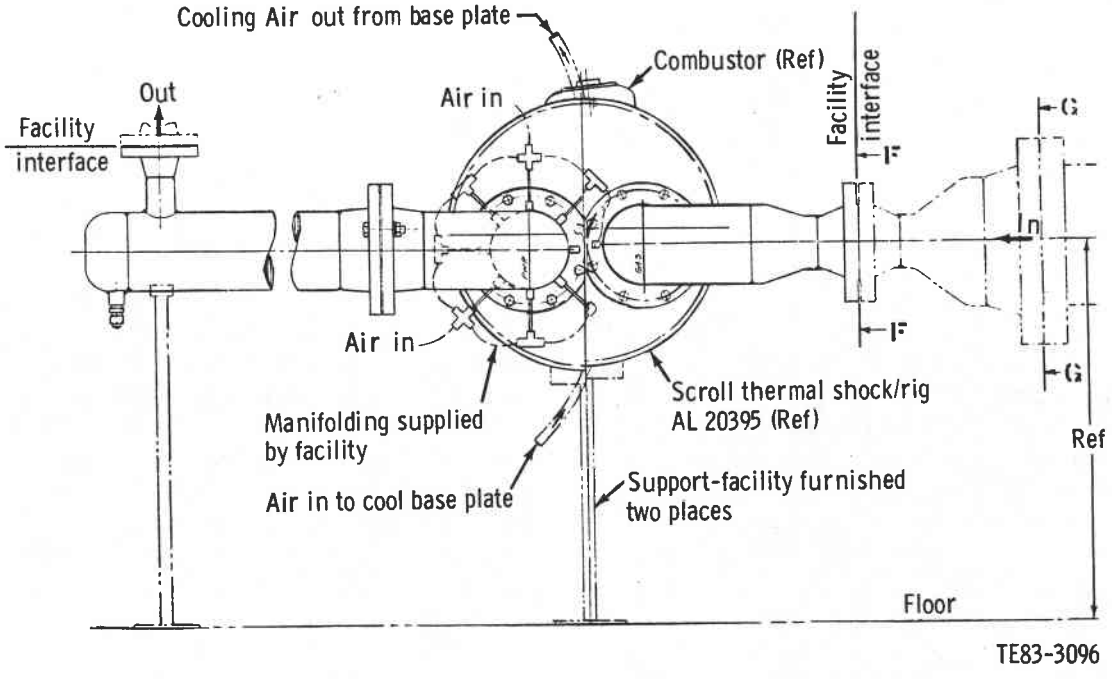

Figure 119. AGT 100 turbine scroll static components thermal simulation rig facility installation.

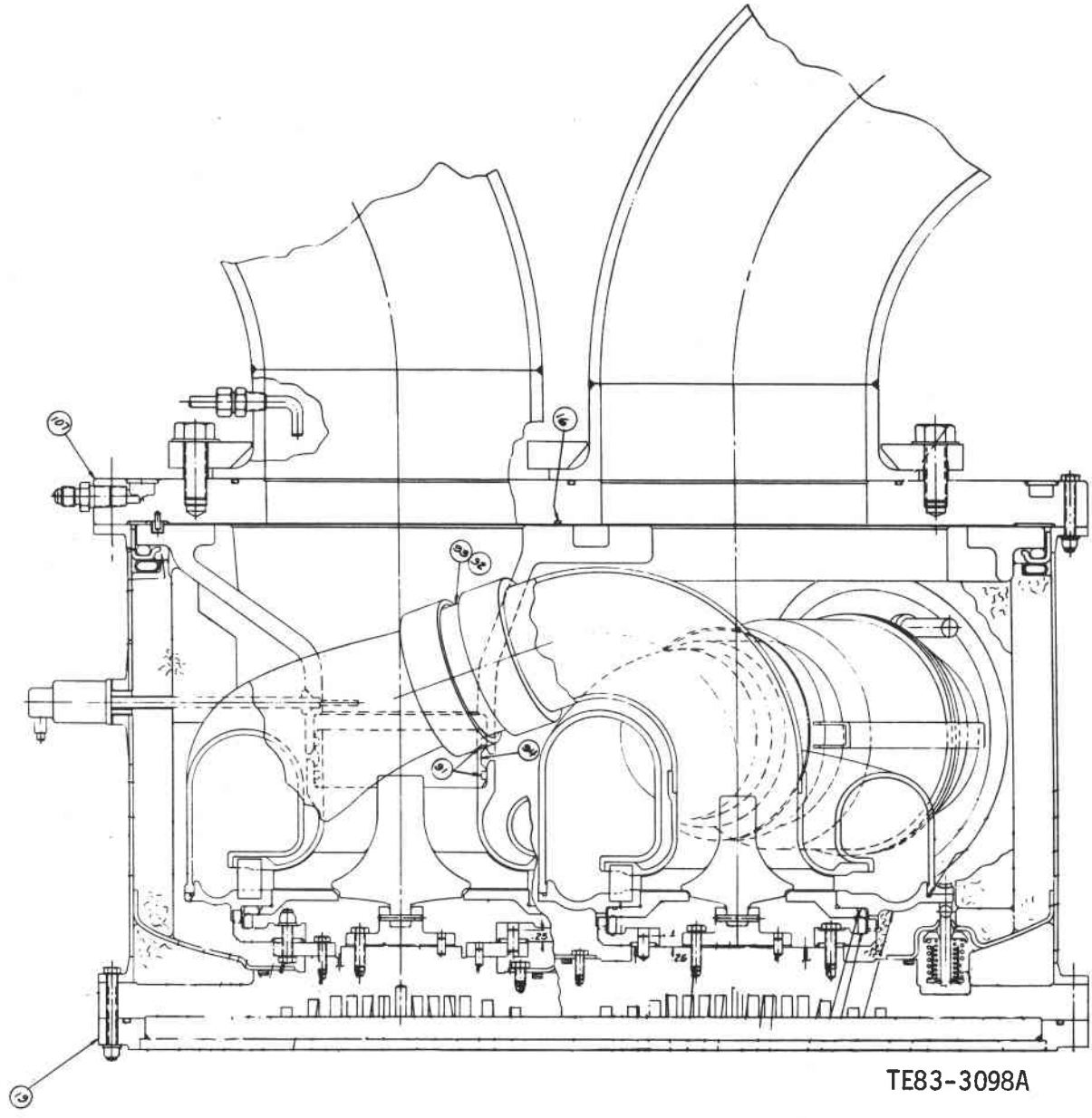

Figure 120. Sectional view of AGT 100 scroll thermal shock rig showing configuration to test both gasifier and power turbine scrolls together.

instrumented to record metal skin temperatures along the outer scroll wall and inner backplate and to measure pressure drops across the guide vanes and static turbine rotor. Since this instrumentation is absent on the ceramic scrolls, one of the purposes of the metal gasifier scroll shakedown and calibration tests is to correlate the TITs measured in the metal gasifier scroll with the BOTs measured using the new ring thermocouples. Turbine exit, exhaust duct, outer scroll, and inner backplate temperatures and guide vane and static turbine rotor pressure drops can be correlated as a function of ring BOT and operating conditions. The environmental data obtained on the metal gasifier scroll is not expected to differ significantly from that within the ceramic gasifier scroll, due to similarities in the heat transfer of the materials at elevated temperatures. Correlation of rig instrumentation (BOT ring data, etc) with instrumentation on the metal gasifier scroll assembly calibrates the rig instrumentation for use in testing ceramic scrolls and achieving the desired environmental conditions within them.

The first test was an initial rig checkout with a metal scroll assembly and a limited set of ceramic

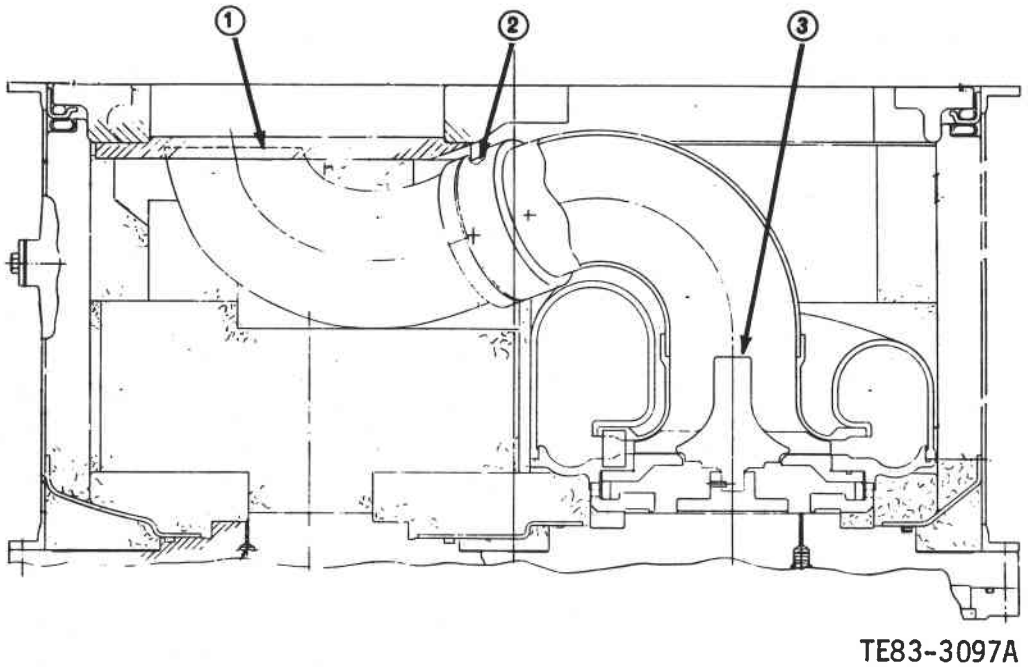

Figure 121. Gasifier-turbine-only configuration for AGT 100 thermal shock rig.

components. The following ceramic components were installed:

- combustor assembly (SiC)
- flow straightening rotor (SiC)
- two gasifier turbine vanes (SiC)
- shim (Zr)
- thermal barrier rings (Zr)
- interturbine coupling with two piston rings (SiC)
- modified bulkhead (LAS)
- exhaust elbow (SiC)

The initial test procedure was similar to that used for proof testing combustors. Testing began on 22 August 1984 on the north rail in the Combustion Research Laboratory.

An operating temperature of 316°C (600°F) inlet temperature was established for this test. Due to the known air leak at the bulkhead, airflow was increased until the measured combustor pressure drop was high enough that prior calibration indicated the proper amount of air was going through the combustor. The assembly was successfully proof tested, using JP-5 fuel, on the start nozzle. However, the built-in leakage to allow air to flow over the scroll and out an annulus surrounding the exhaust (preventing localized heating in the bulkhead) proved to be too large. Approximately two-thirds of the inlet flow was directed to the leakage path and one-third to the combustor scroll inlet. The rig was subsequently disassembled and modified to allow about 20% of the inlet airflow to leak around the exhaust outlet. This modification involved the installation of a rope seal (ceramic fiber) to partially plug the large gap around the exit duct at the LAS bulkhead exit hole.

This was an on-site installation, and no unusual conditions were observed during the teardown. An inlet temperature of 316°C (600°F) was established. The rope seal was determined to be working, since proper airflow was achieved as judged by combustor ΔP/P and fuel flow versus BOT data. Two start nozzle cycles were completed at a BOT average of 899°C (1650°F). These retests were necessary to obtain measured temperatures on the metal scroll that accurately reflected those within the engine.

The next series of checkout tests involved the main nozzle thermal shock cycle. A BIT of 649°C (1200°F) was established with a targeted 1038°C (1900°F) BOT maximum flow rate proof test using the main nozzle injection system. Continuous monitoring of the rig data during BIT heat-up revealed that the rope seal failed as indicated by changes in the combustor ΔP values. Airflow was increased to compensate for the loss, but another ΔP/P was noted. Fired conditions were not conducted. The rig was shut down, removed from the test rail, and disassembled to investigate the changing combustor ΔP/P values. Observations upon disassembly in the test facility are shown in Figure 122.

The ceramic bulkhead under the inlet and exhaust backplate was severely cracked on both its outer ring (exhaust side) and across the plate through which the gasifier exhaust tube passes. Three-inch

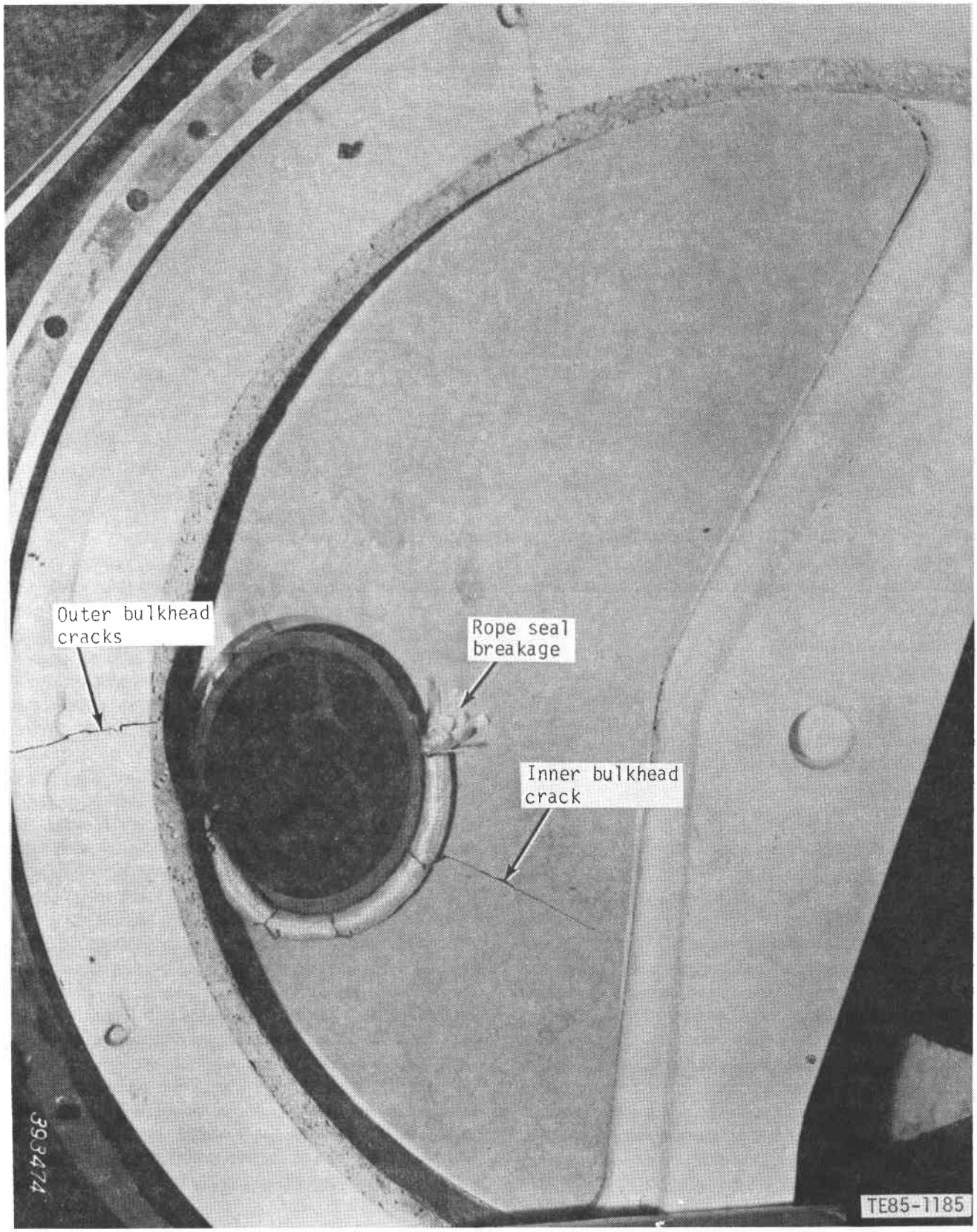

Figure 122. Scroll thermal shock rig ceramic bulkhead and rope seal failure.

segments of both the upper and lower rope seal were missing in approximately the same circumferential location. The breaks in the rope were clean, suggesting the possibility that the wires used to retain the rope seal contributed to the failure. The bulkhead was removed from the rig in several pieces and sent to the ceramic material laboratory for analysis. The ceramic combustor assembly and exhaust elbow appeared to be intact. Further teardown was completed after the rig was removed to the assembly floor. An examination of the dissassembled rig revealed that the flow straightener used at the normal turbine rotor position was broken. This flow straightener was made from a ceramic turbine rotor by removing the cambered exducer portion of the vanes. The vane inducer regions were broken off, either by air loading or flow induced vibration. The two broken ceramic guide vanes were chipped by material flying off the breaking rotor blades.

Laboratory analysis revealed that the ceramic bulkhead portion under the inlet and exhaust backplate failed due to thermal distortion of the retaining metal parts. The inboard seal platform (the ceramic plate through which the gasifier tube passed) failure occurred because of the induced distortion of the bulkhead to which it was attached and/or a significant pressure differential across it. The rope seal that failed was mounted to this part. These parts were not engine pieces and were not designed or stressed for the loads experienced in the scroll rig tests.

A redesign of the scroll rig was completed to eliminate the entire ceramic bulkhead and seal platform by fabricating a new exhaust port duct that carries the hot exhaust gas from the ceramic tube to the exit in the backplate. The necessity for the rope seal was eliminated by using a close tolerance gap to minimize leakage, as shown in Figures 123 and 124.

Because of the air loads encountered within the gasifier scroll, a metal version of the previous ceramic flow straightener was prepared from a metal cast turbine wheel, (see Figure 125). A distortion of the metal parts was reduced by changes to the rig endplate water cooling circuits (air is used in place of water) and by increased use of internal insulation. The redesigned system is appropriate for near-term testing up to BOT of 1093°C (2000°F).

Ceramic Gasifier Scroll Heated Air Proof Test

Following the preliminary checkout and numerous revisions of the scroll rig resulting from the hot fire tests using the metal gasifier scroll, a decision was made to proceed to a heated air (705°C [1300°F], idle flow rate) test of the ceramic gasifier scroll. This decision was made for two reasons: (1) The scroll rig had been revised so that it was considered checked out and calibrated, at least up to start-nozzle flow conditions, 899°C (1650°F), idle flow rate; and (2) a preliminary checkout of the ceramic scroll assembly would allow potential interference fits to be discovered, located, and fixed.

The external dimensions of the ceramic scrolls were difficult to control to tight tolerances and some interference fits were expected. These interferences, such as the scroll and outer backplate tang thickness over which the hold-down clamps fit, were minor and required simple machining. The lower dilution band of the burner assembly contacted the scroll body when the BVG position was below 12.7 mm (0.5 in.) and created a serious interference. This contact precluded a hot fire start nozzle test that required a BVG setting of 5 to 7.6 mm (0.2 to 0.3 in.).

A solution to this problem has been achieved by scalloping the dilution band, which removes the interference and allows the dilution holes to be opened. A second option is being explored that would raise the dilution holes on the combustor body. This method would allow complete BVG movement without contact interference (unmachined combustor bodies exist for this option).

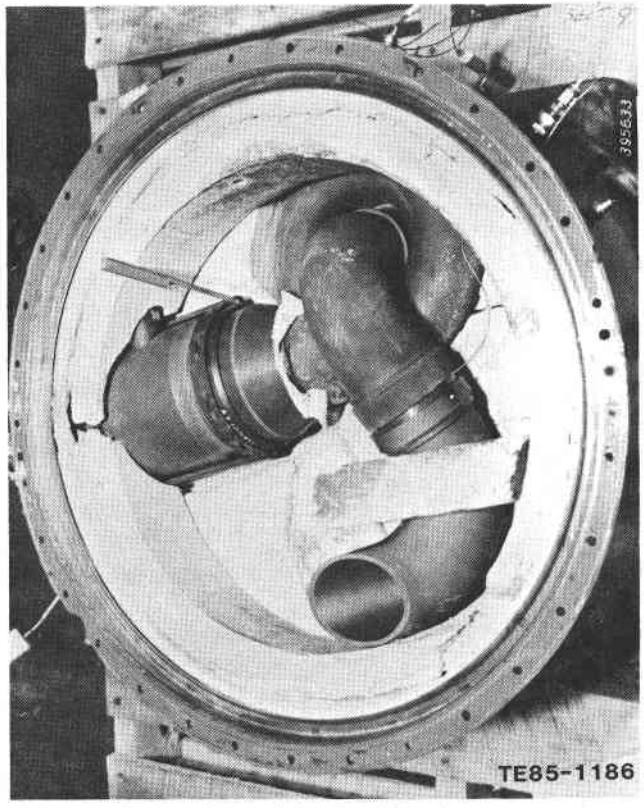

Figure 123. Installed view of combustor, metal gasifier scroll, and ceramic exhaust duct in scroll thermal shock rig.

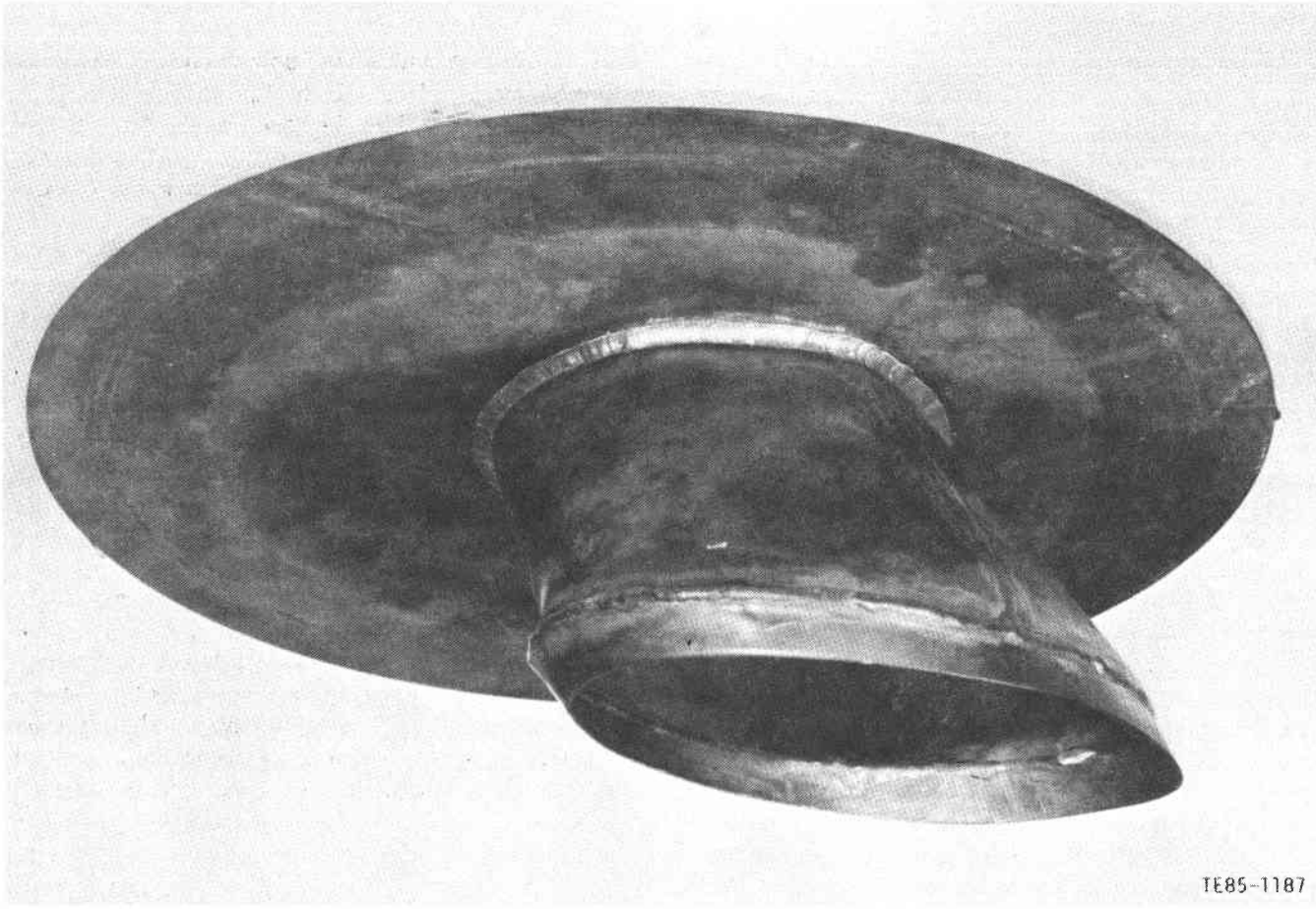

Figure 124. Redesigned metal transition exhaust port duct attaches directly to gasifier ceramic crossover tube.

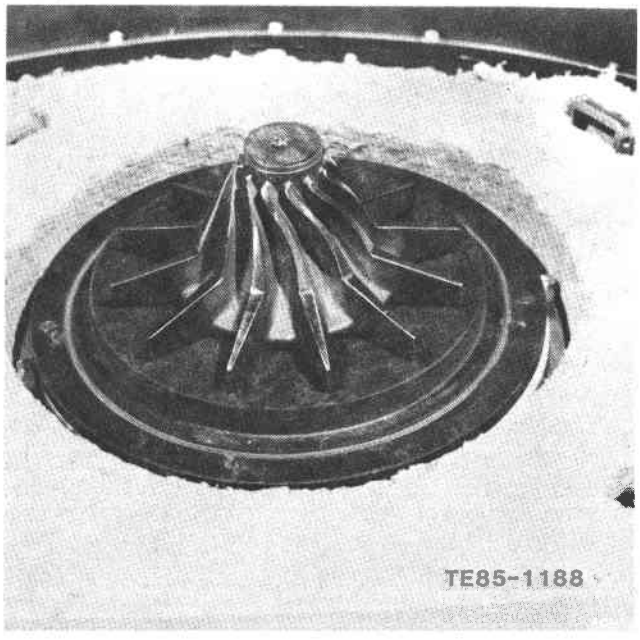

Figure 125. Metal version of flow straightener.

At the time of the initial ceramic scroll test, none of these solutions existed and a start nozzle flow condition was simulated within the ceramic scroll. This condition was achieved by setting the BVG to the maximum position (closed dilution holes, radial swirler wide open) and flowing heated air at 705°C (1300°F) at idle flow rate. The components, ceramic type, and vendor for this configuration were as follows:

• scroll assembly	αSiC	Carborundum
• outer backplate	αSiC	Carborundum
• vanes (18)	αSiC	Carborundum
• inner backplate	BMAS	Corning
• combustor assembly	αSiC	Carborundum
• pilot flame tube	αSiC	Carborundum
• piston ring (2)	Refel SiC	Pure Carbon
• shims	Zirconia	Feldmuhle
• exhaust elbow	αSiC	Carborundum

The entire assembly was tested in November over a 4-hr hot airflow test duration. The test plan called for stabilization at 649 to 704°C (1200 to 1300°F) over a 1-hr period, cool and shutdown, and

inspection of the ceramic components. The first 0.5 hr of the high temperature stabilization period of this test is presented in Figure 126.

The various curves represent internal scroll rig heated air temperatures. TT30A and B are near the air inlet into the rig while TT30G, F, and H are the measured air temperatures around the radial swirlers at the inlet to the combustor. Because these air temperatures are closer to the outer combustor case, they are affected by localized heat transfer to the surroundings.

Continuation of Metal Gasifier Scroll Calibrations — Start and Main Nozzle Testing

Following the ceramic scroll test, the thermal shock rig was refitted with metal scrolls to further characterize internal temperatures and complete the calibration of the rig instrumentation, particularly for main nozzle flows up to maximum power conditions. One purpose of these tests, beyond the instrumentation calibrations described previously, was to conduct the initial testing of the operational test cycle to be used for ceramic components. Detailed investigation of the engine fuel control system indicated that, following ignition light-off, the rate of temperature increased within the engine combustor, and the gasifier scroll could be controlled to 14°C (25°F) per minute.

Since the ceramic scrolls are in the developmental stage, they should be initially exposed to the lowest practical thermal shock rate. Minimum failure and maximum design information can be gained using this operational procedure. The ceramic scrolls can be gradually subjected to more severe thermal shock rates. Thus, the initial operational test cycle to be used in the scroll rig should not subject the ceramic scrolls to thermal loads higher than those present within the engine. Consequently, the remaining scroll rig calibration tests using the metal gasifier scrolls were conducted at thermal loads simulating the testing of a ceramic scroll, i.e., heating and cooling rates of 14°C (25°F) per minute.

Because the operational test cycle described had not been used in previous tests, the start nozzle hot fire flow test was repeated before main nozzle calibration testing. The rig operating conditions chosen to simulate engine operation are shown in Tables XXIX and XXX.

While the entire main nozzle test matrix, as outlined in Table XXX, will be conducted using the metallic scrolls to obtain temperature correlations, only main nozzle tests 2 (80% of present maximum engine power) and 3 (100% of present maximum engine power) will be conducted using the ceramic scrolls. These main nozzle test cycles for the metal and ceramic scrolls will be identical.

Typical results from the start nozzle and 60% speed main nozzle tests are presented in Figures 127 through 135. The start nozzle fire-up record is presented in Figure 127, while the stabilization, 899°C (1650°F) BOT, record of the same run is shown in Figure 128.

Agreement between the averages of the thermocouple measured scroll BOT (actually, the turbine in-

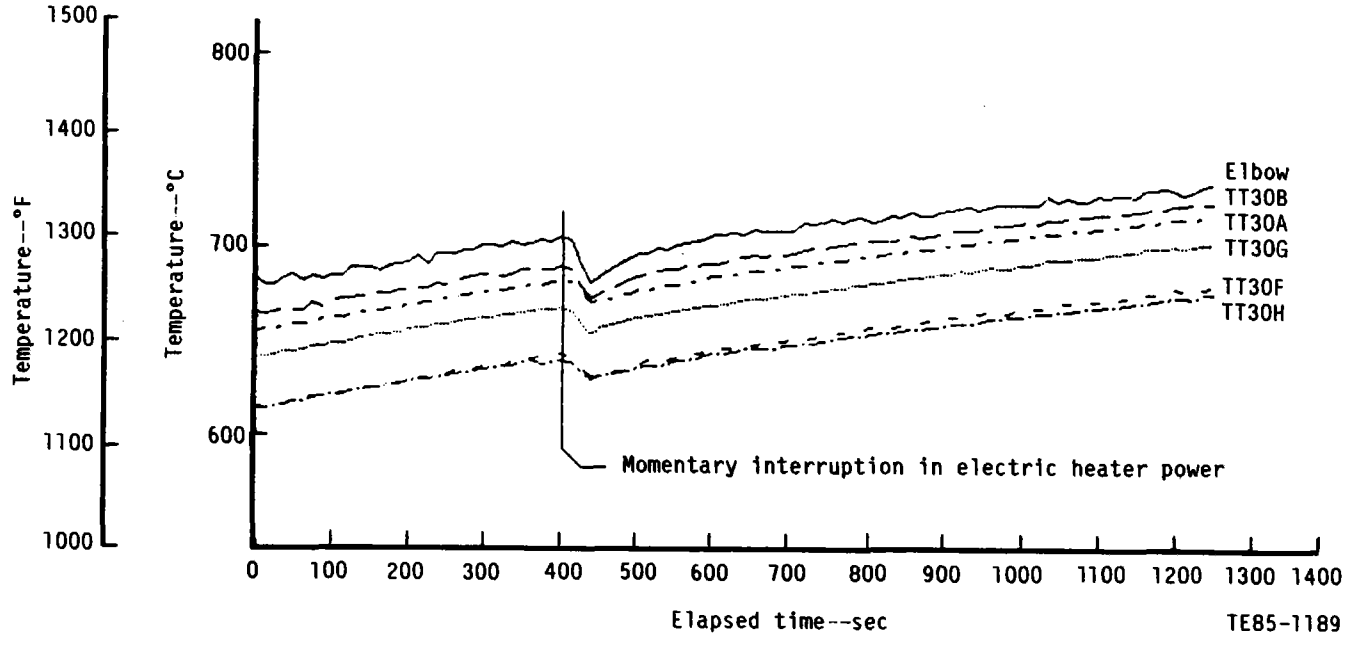

Figure 126. Thermal shock rig ceramic gasifier scroll test: heated air start nozzle flow conditions, first half of thermal stabilization period.

let temperature) and ring BOT is excellent. This agreement occurred despite the fact that the ring BOT thermocouple data (at the combustor exit) indicated a pattern factor of 0.26 (based on °F) at stabilization (see Figure 129) while the scroll BOT data (see Figure 130) indicated a pattern factor of less than 0.03 for this same test condition.

This discrepancy occurred throughout the start nozzle and, to a lesser extent, in the main nozzle test cycles. A more uniform temperature profile at the inlet to the guide vanes (at various circumferential locations around the scroll, i.e., the scroll BOT data) was expected because of the additional induced mixing of the high swirl velocity flow exiting from the combustor. This additional flow mixing is a result of increased length before contact with the first scroll BOT thermocouple and the strong secondary flows set up by the turning of the flow within the scroll. However, the temperature variations (high pattern factor) observed at the combustor exit (BOT ring) during these tests were extreme compared with data obtained in prior tests of both the scroll rig and the burner rig. In the burner rig, the BOTs are measured in a straight exhaust duct close to the burner exit. All of the burner rig tests indicated pattern factors of less than 0.15 for the start nozzle and 0.10 for the main nozzle. A calibration of the platinum/rhodium BOT ring thermocouples indicated that the observed temperature readings during this set of scroll rig tests were correct. The discrepancy between the scroll rigs measured ring BOT and scroll BOT pattern factors was eventually found to be a result of radial and axial swirler blockage due to loose insulation. The combustor was removed and examined following the first set of main nozzle tests. Some of the internal rig insulation had torn loose and blown into the radial and axial swirler passages. The result was an approximate 60% blockage of the radial swirler passages and a 20% nonuniform blockage of the axial swirler. The insulation blockage was removed, and a quick check fire-up indicated that the BOT ring pattern factors had returned to normal. The insulation in the scroll rig has been reworked to prevent recurrence of the problem.

Main nozzle test results at the 60% speed airflow rate are presented in Figures 131 through 135. The main nozzle fire-up record is presented in Figure 131, while the main nozzle flow acceleration to and stabilization record for the same run at 1052°C (1925°F) is shown in Figure 132.

Agreement between the averages of the scroll BOT and ring BOT is excellent. The ring BOT thermocouple data, shown in Figure 133, indicates a more nonuniform temperature profile than does the scroll BOT data, shown in Figure 134. Representative metal temperatures are presented in Figure 135.

The inner backplate and gasifier backplate cavity will be cooled in future runs by the addition of a small cool air purge. This addition simulates engine cool air design leakage to these areas.

Following completion of the 60% speed airflow rate main nozzle test, testing was resumed to complete the main nozzle calibration test matrix. On starting the airflow, the system and combustor ΔP values were much lower than had been observed during the previous running. The main nozzle was fired at a BIT of 707°C (1305°F) to verify the leakage rate through BOT fuel flow comparisons. Postrun inspection revealed that the radial and axial swirlers were clear. The rig was removed from the stand, and it was found that a large piece of the ceramic exhaust tube had broken off, as shown in Figure 136. The broken part was not recovered, and the rig was returned to the assembly floor for teardown and inspection.

The probable cause of the fracture was contact loading between the ceramic exhaust tube and the sheet metal shroud holding it in place at the exhaust outlet. The exact cause of the contract loading is unknown, but thermal distortion is suspected. The scroll rig is being rebuilt with a metal tube replacing the ceramic exhaust duct. When metal gasifier scroll main nozzle flow calibrations are complete, ceramic hot fire gasifier scroll proof testing will begin.

Table XXIX.
Conditions simulating engine operation.

Start nozzle** (60% engine speed)	Main nozzle (operated over a variation of airflows and BOTs)
BIT—600°F (use swirler inlet thermocouples during no-fire condition)	BIT—1400°F or highest temperature attainable less than 1400°F (use swirler inlet thermocouples during no-fire condition)
BOT—Steady state, 1250°F increasing to 1650°F (BOTs will be monitored by using a comparison TT41F; these are the scroll BOT thermocouples.)	BOT—temperatures will be monitored by using a comparison of TT411A and the average of TT41A and TT41F
Maximum individual TT41, T/C—1850°F	Maximum individual TT41, T/C—2000°F
BIP—26.0 lb/in.^{2} W_a—0.25 F/A—0.0096 to 0.161 maximum W_f—8.64 lbm/hr to 14.49 lbm/hr BVG—0.3 in. at light-off increasing to 0.4 in. during transition from 1250 to 1650°F (0.2 in. setting at light-off may be required at low fuel rates; transition to 0.3 in. to occur shortly after stable ignition achieved)	BIP W_a F/A W_f BVG these parameters vary with BOT†

*Units are in English because this is the cycle given to the test engineer.
**Start nozzle flows and test cycles for the metal and ceramic scrolls will be identical.
†Variations of parameters are shown in Table XXX.

Table XXX.
Main nozzle test matrix.*

				1650°F BOT			1775°F BOT			1925°F BOT		
Step	Speed—% max	Airflow—lbm/sec	BIP—lb/in.^{2}	F/A ratio	Fuel flow—lbm/hr	BVG—in.	F/A ratio	Fuel flow—lbm/hr	BVG—in.	F/A ratio	Fuel Flow—lbm/hr	BVG—In.
1	60	0.25 (1300°F BIT)	26	0.0056	5.04	0.40	0.0076	6.84	0.40 −0.50	0.0101	9.09	0.55 −0.65
2	80	0.42 (1300°F BIT)	40	0.0056	7.26	0.40	0.0076	9.85	0.40 −0.50	0.0101	13.09	0.55 −0.65
3	100	0.58 (max present engine, 1400°F BIT)	61	0.004	8.35	0.40	0.00605	12.63	0.425 −0.52	0.0086	17.96	0.60 −0.80
4	100	0.70 (max RPD cycle, 1400°F BIT)	66	0.004	10.08	0.40	0.00605	15.25	0.425 −0.525	0.0086	21.67	0.60 −0.80

*Units are in English because this is the cycle given to the test engineer.

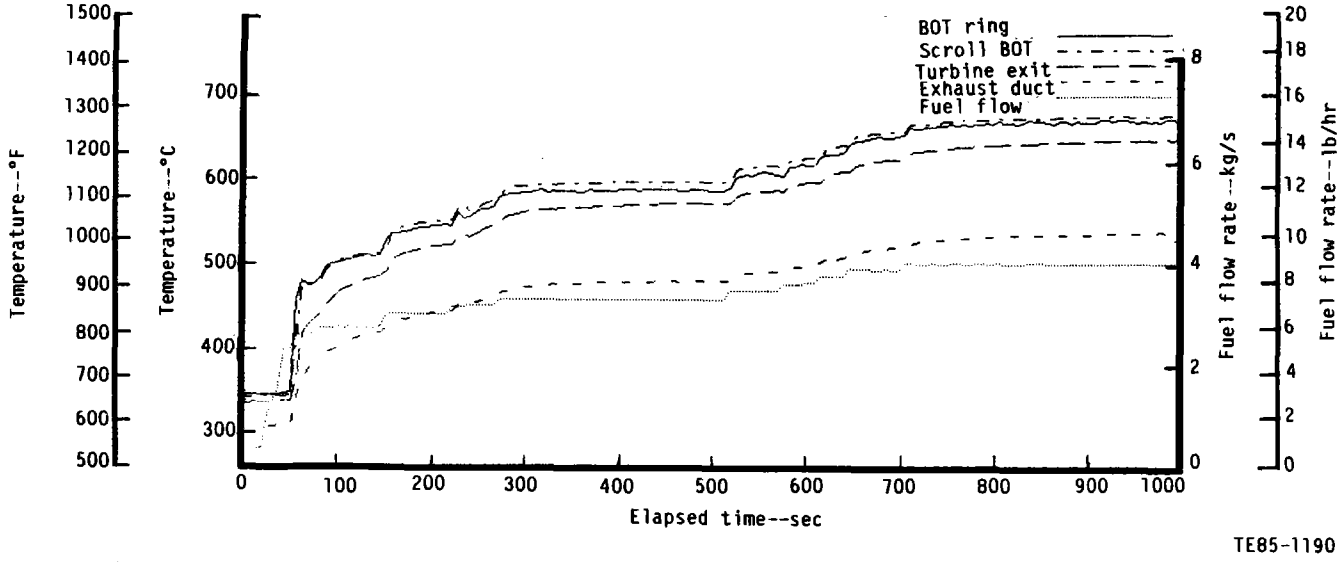

Figure 127. Thermal shock rig metal gasifier scroll calibration tests: start-nozzle fire-up record.

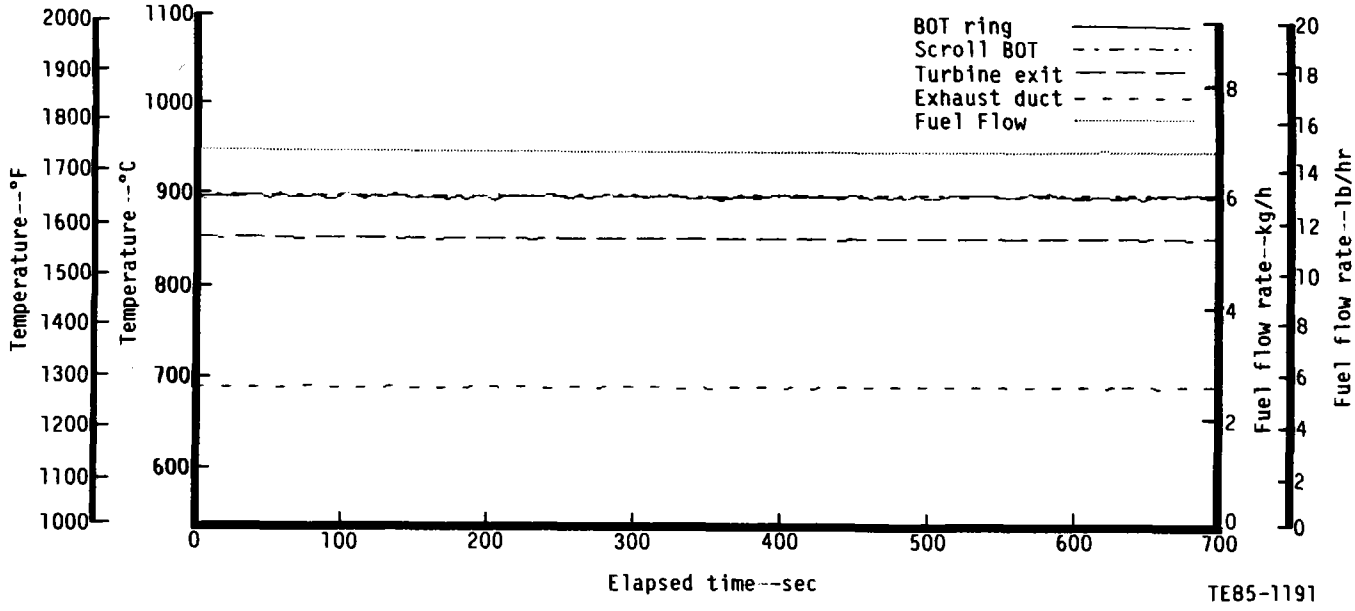

Figure 128. Thermal shock rig metal gasifier scroll calibration tests: start-nozzle stabilization (899°C [1650°F] BOT) record.

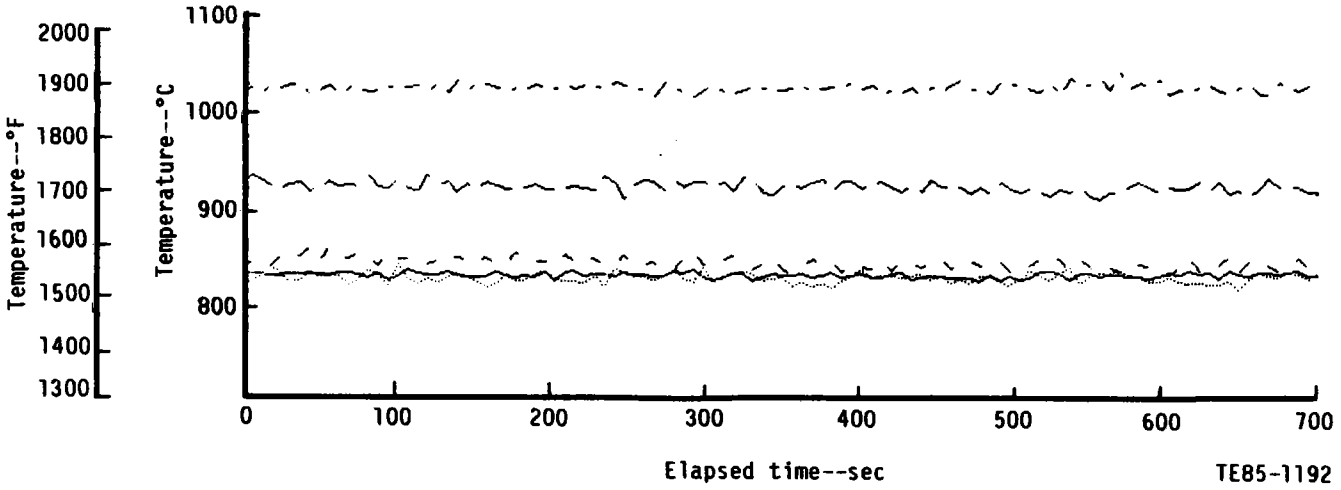

Figure 129. Thermal shock rig metal gasifier scroll calibration tests: start-nozzle stabilization ring BOT thermocouple data.

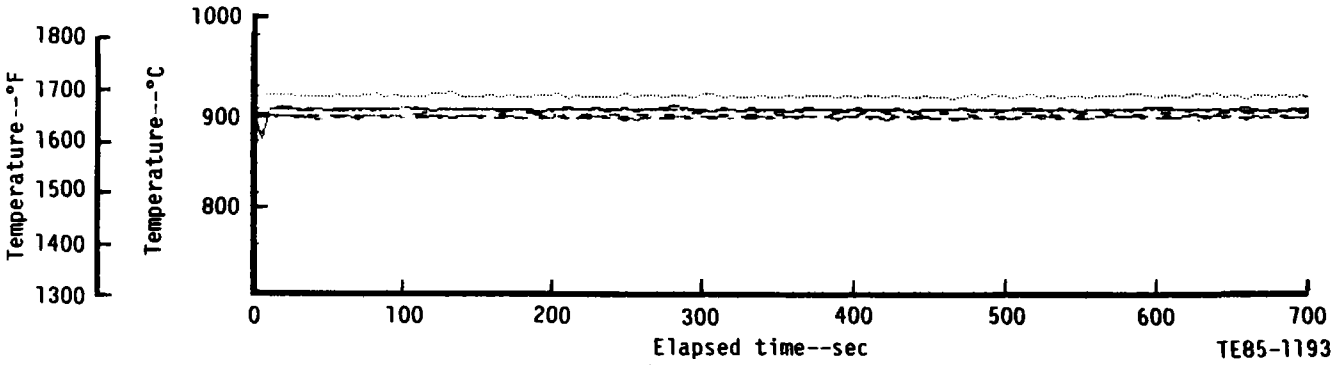

Figure 130. Thermal shock rig metal gasifier scroll calibration tests: start-nozzle stabilization scroll BOT thermocouple data.

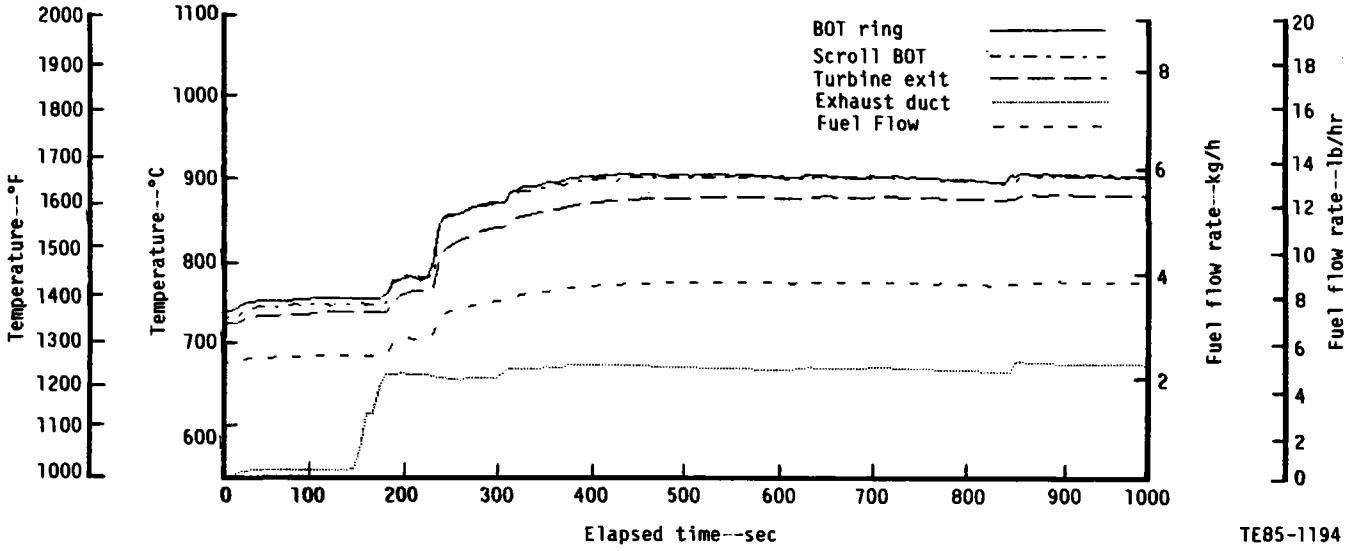

Figure 131. Thermal shock rig metal gasifier scroll calibration tests: main-nozzle fire-up and low BOT temperature stabilization record.

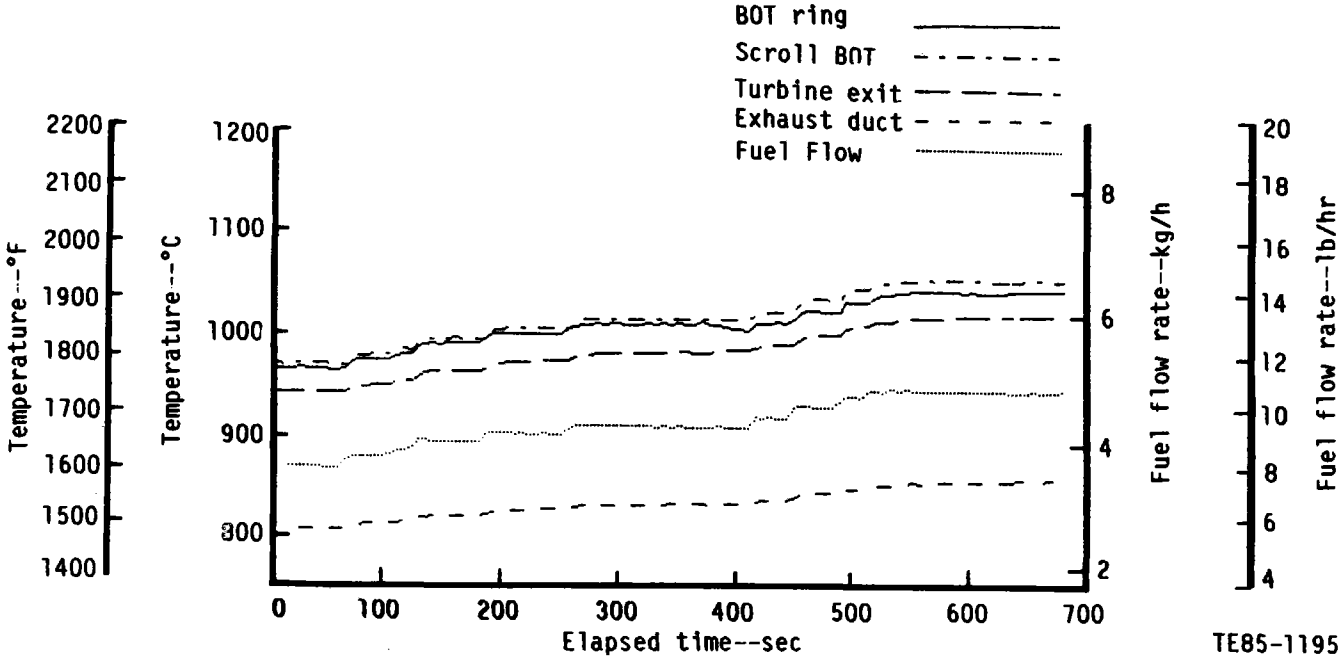

Figure 132. Thermal shock rig metal gasifier scroll calibration tests: main-nozzle acceleration and stabilization (1052°C [1925°F] BOT) record.

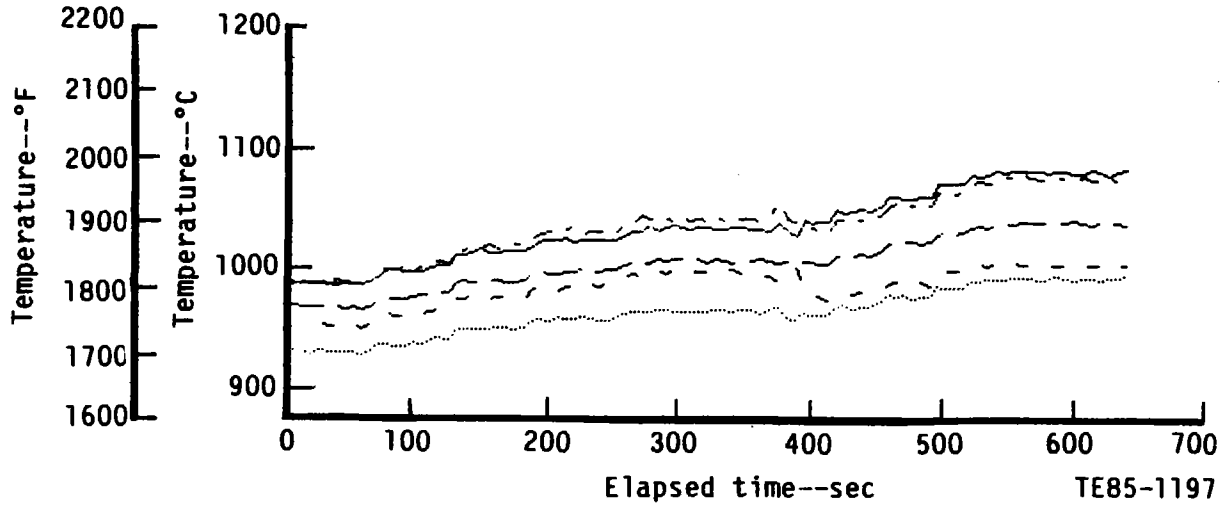

Figure 133. Thermal shock rig metal gasifier scroll calibration tests: main-nozzle stabilization, ring BOT thermocouple data.

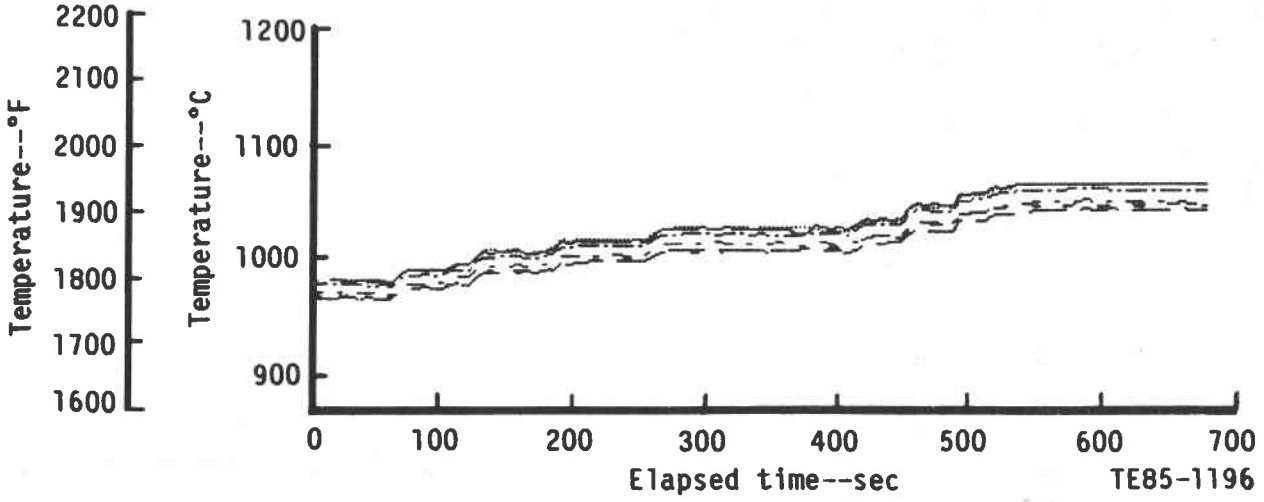

Figure 134. Thermal shock rig metal gasifier scroll calibration tests: main-nozzle stabilization, scroll BOT thermocouple data.

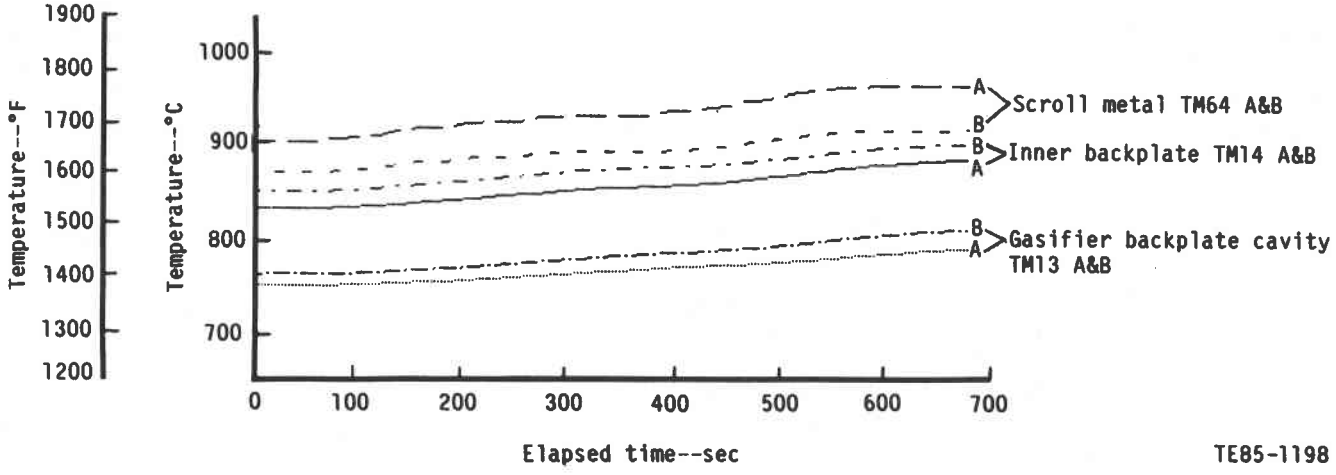

Figure 135. Thermal shock rig metal gasifier scroll calibration tests: main-nozzle stabilization, selected metal temperatures.

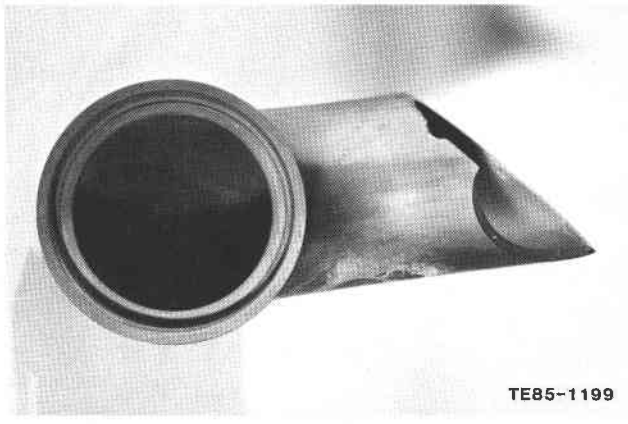

Figure 136. Failed ceramic exhaust tube.

9.3 KYOCERA SILICON NITRIDE ROTORS

Two Si_3N_4 gasifier rotors were received during this reporting period from Kyocera International. These rotors, shown in Figure 137, were fabricated of slip-cast SN22OM sintered Si_3N_4. Nondestructive inspection (visual and fluorescent penetrant) revealed no objectionable discontinuities. Dimensional evaluation indicated that all dimensions were within print tolerances with the exception of a minor closing of the exducer throat spacing. This closing is believed to be caused by drooping of the exducer airfoils during sintering and will be corrected by the use of additional fixturing in subsequent rotors.

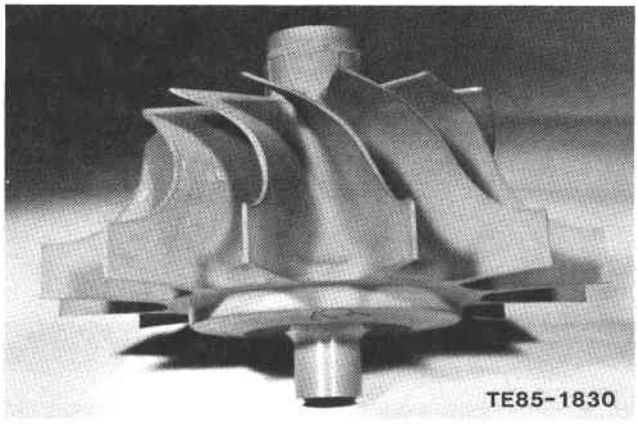

Figure 137. Kyocera slip-cast SN220M sintered silicon nitride gasifier turbine rotor.

To evaluate material strength characteristics and component performance, three additional SN22OM Si_3N_4 rotors were subjected to room temperature spin tests at Kyocera. These spin test results are summarized in Table XXXI.

Further strength characterization was conducted on standard-size MOR test bars cut from slip-cast billets. These results are summarized in Table XXXII. The average room temperature fracture strength of material tested with an as-fired surface condition measured 514.00 MPa (74,550 lb/in.^{2}) with a standard deviation of 30.27 MPa (4390 lb/in.^{2}).

The strength-controlling flaws were pores located either on the tensile surface or at the base of surface depressions, as shown in Figure 138. Bars tested with a machined surface had an average strength of 762.28 MPa (110,560 lb/in.^{2}) with a standard deviation of 71.22 MPa (10,330 lb/in.^{2}). The typical fracture

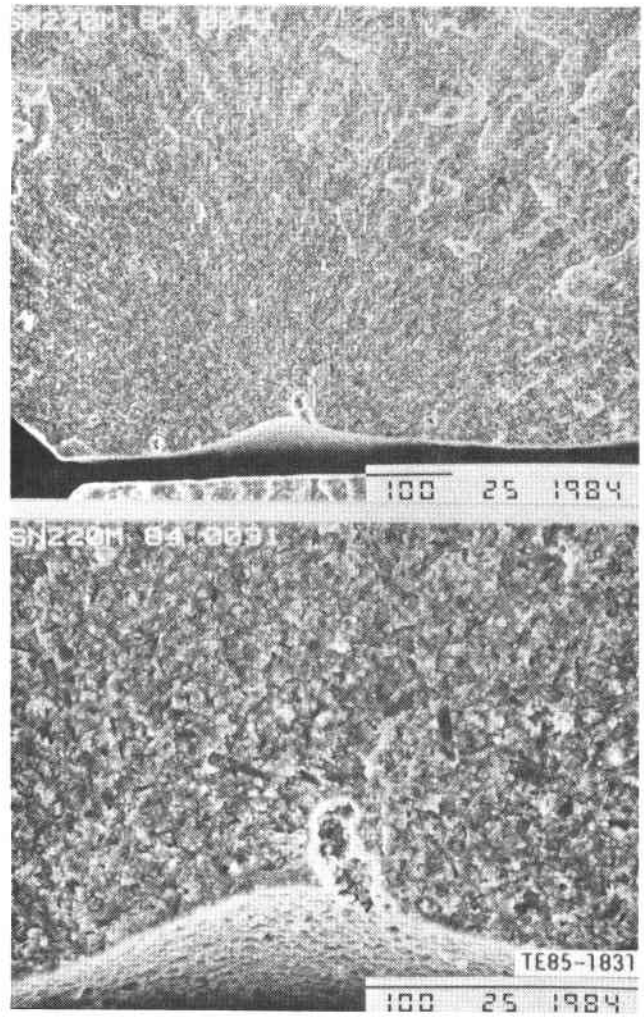

Figure 138. Typical fracture origin (surface pore) in as-fired Kyocera SN220M Si_3N_4 tested at room temperature.

Table XXXI.
Spin test results of Kyocera SN220M Si_3N_4 rotors.

Rotor No.	Maximum speed	Comments
1	134,000 rpm	Rotor intact*
2	137,800 rpm	Rotor burst
3	138,000 rpm	Rotor intact*

*Maximum speed achievable with test equipment.

Table XXXII.
Elevated temperature strength of Kyocera SN220M Si_3N_4.

Surface condition	Fracture strength—MPa (lb/in.^{2})		
	Room temperature	1000°C (1832°F)	1150°C (2102°F)
Machined	762.28 (110.56)	602.67 (87.41)	333.78 (48.41)
As-fired	514.00 (74.55)	— —	275.79 (40.00)

origins were internal inclusions, either a glassy phase rich in aluminum, calcium, yttrium, and silicon (see Figure 139) or a cluster of large grains rich in iron, chromium, titanium, and silicon (see Figure 140).

The average strength of bars tested at 1000°C (1832°F) with a machined tensile surface measured 602.67 MPa (87,410 lb/in.^{2}) with a standard deviation of 21.03 MPa (3050 lb/in.^{2}). Fracture was initiated from small surface pores. At a test temperature of 1150°C (2102°F), the average strength of bars with a machined surface decreased to 333.78 MPa (48,410 lb/in.^{2}) with a standard deviation of 8.69 MPa (1260 lb/in.^{2}), while as-fired bars averaged 275.79MPa (40,000 lb/in.^{2}) with a standard deviation of 18.75 MPa (2720 lb/in.^{2}). All bars tested at 1150°C (2102°F) were heavily oxidized, with the as-fired surface oxidized more than the machined surface. The strength-controlling flaws were glassy bubbles near the tensile surface, as shown in Figure 141.

9.4 FIBER REINFORCED GLASS CERAMICS

Two fiber reinforced glass ceramic composite inner backplates were received from Corning Glass Works this reporting period, one LAS-III (lithium aluminosilicate) and one BMAS-II (barium magnesium aluminosilicate). Both composite backplates contain approximately 30-40% by volume ceramic grade Nicalon 102 silicon carbide fibers from Nippon Carbon. Fabrication of fiber reinforced glass ceramic composites consists of three stages. In the first stage, called prepregging, the fibers are passed through a slurry of powdered glass suspended in water, wound on a faceted drum, and allowed to dry in sheets. The second stage, layup, consists of cutting the prepreg sheets into the desired geometry and stacking them to obtain the desired fiber orientation (42 layers of 0/±45/90 deg for the inner backplates). Consolidation

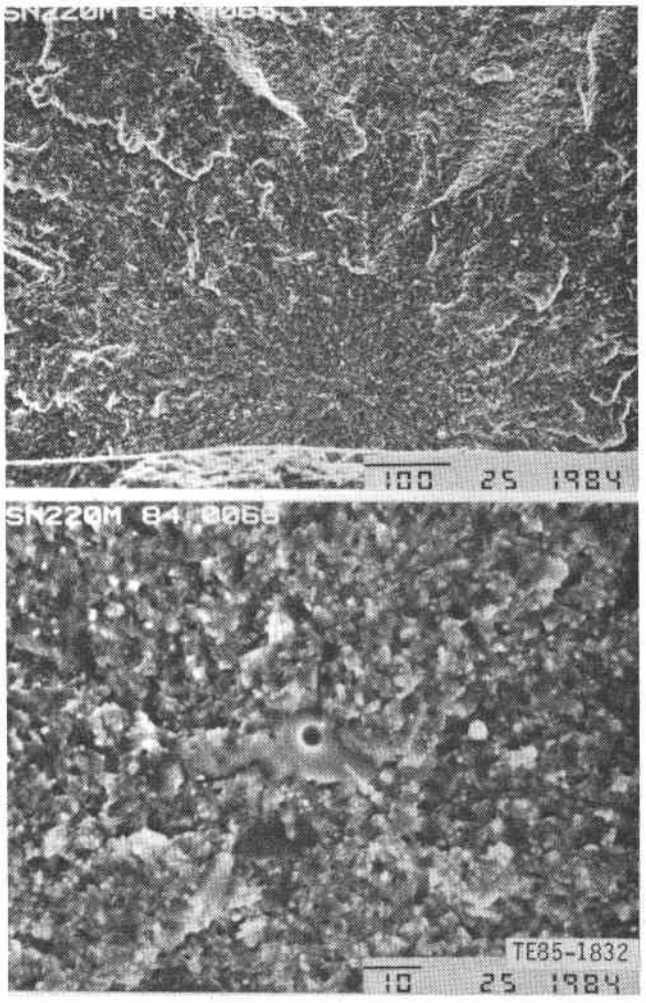

Figure 139. Typical fracture origin (glassy phase inclusion) in machined Kyocera SN220M tested at room temperature.

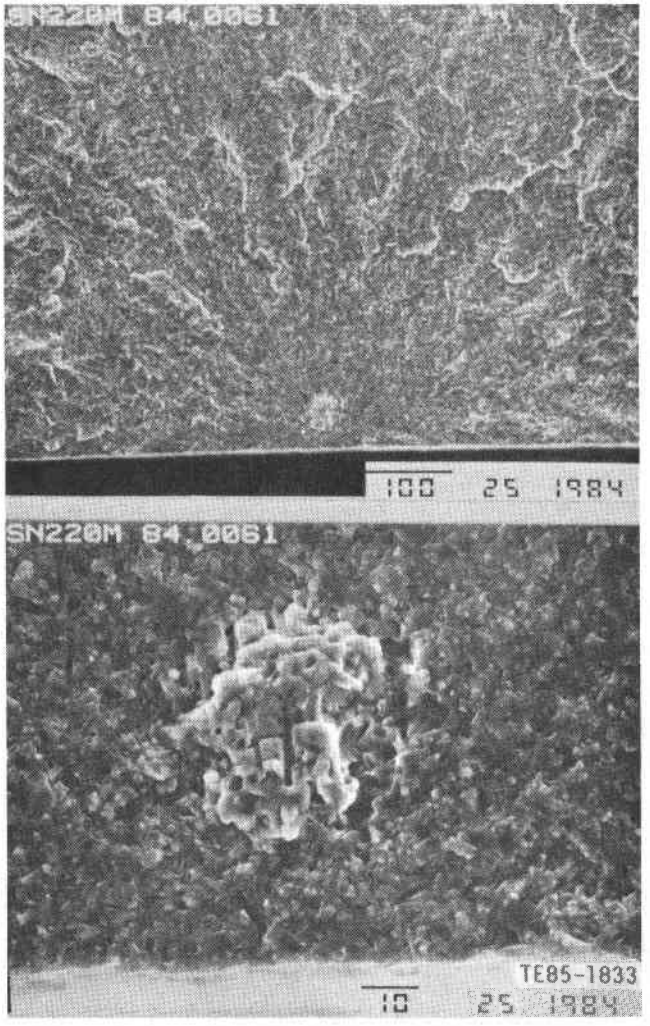

Figure 140. Typical fracture origin (internal inclusion) in machined Kyocera SN220M tested at room temperature.

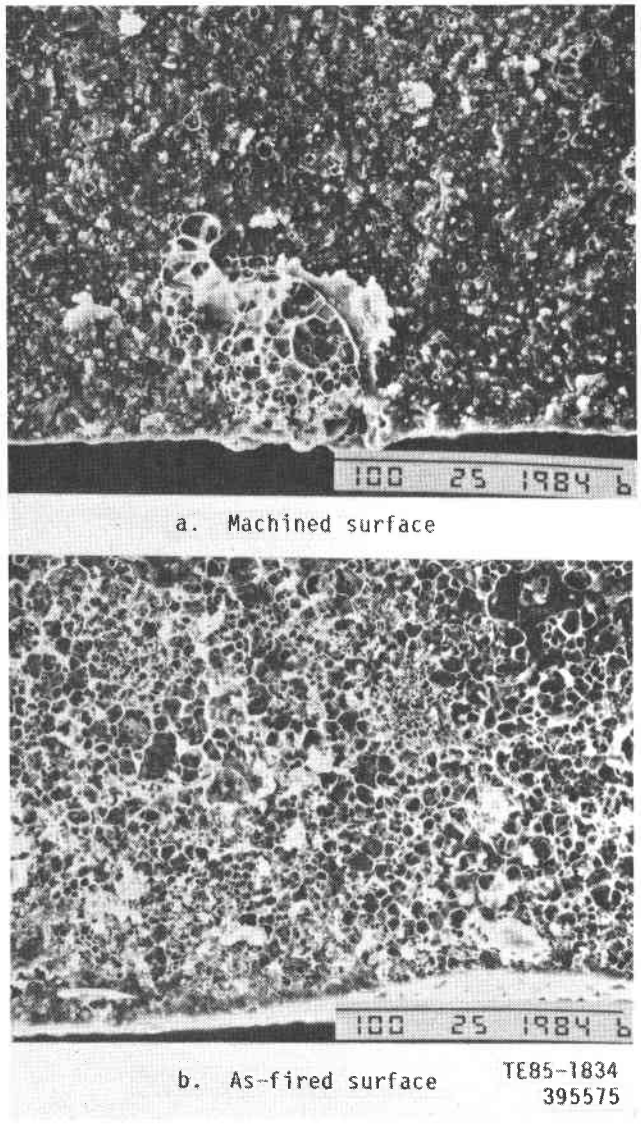

Figure 141. Typical fracture origin (glassy bubbles) observed in Kyocera SN220M Si_3N_4 tested at 1150°C (2102°F).

is the final stage of composite fabrication, involving hot pressing the prepreg and machining to required dimensions.

To evaluate material strength characteristics, test bars measuring 69.85 × 3.18 × 2.54 mm (2.75 × 0.125 × 0.10 in.) were machined from two BMAS-II composite billets, one with fibers oriented 0/0 deg and the other with a 0/90 deg fiber orientation. Bars from each billet were tested in three-point bending with a test span of 50.80 mm (2.0 in.), corresponding to a test span to specimen depth ratio of 20:1. The average room temperature strength of the 0/0 deg orientation test bars measured 802.07 MPa (116,330 lb/in.^{2}) with a standard deviation of 131.90 MPa (19,130 lb/in.^{2}). The typical fracture mode observed is pullout of the fibers from the BMAS matrix, shown in Figure 142. Test bars with a 0/90 deg fiber orientation exhibited an average strength of 369.35 MPa (53,570 lb/in.^{2}) with a standard deviation of 57.02 MPa (8270 lb/in.^{2}). The fracture mode of the 0/90 deg test bars was observed to be both brittle and fibrous. Scanning electron microscope (SEM) fractographs, shown in Figure 143, indicated that brittle fractures developed in the matrix phase, along with fibers of 0 deg orientation pulling out of the BMAS matrix.

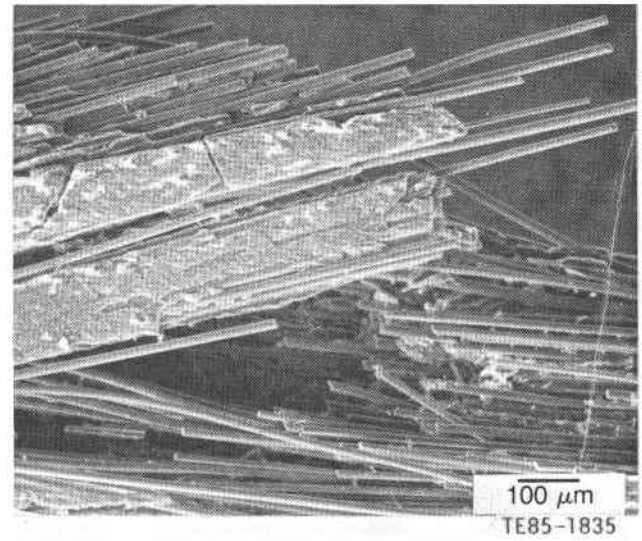

Figure 142. Fracture surface at Corning BMAS-II fiber-reinforced glass ceramic composite test bars with fibers in 0/0 deg orientation; fracture mode is fiber pullout from BMAS matrix.

The results of the elevated temperature strength tests are summarized in Table XXXIII. The average strength of the test bars with a 0/0 deg fiber orientation decreased from the room temperature value of 802.07 MPa (116,330 lb/in.^{2}) to 546.48 MPa (79,260 lb/in.^{2}) at 900°C (1652°F) and 473.74 MPa (68,710 lb/in.^{2}) at a temperature of 1100°C (2012°F). Test material with a 0/90 deg fiber orientation had an average strength of 369.35 MPa (53,570 lb/in.^{2}) at room temperature, 202.15 MPa (29,320 lb/in.^{2}) at 900°C (1652°F), 221.39 MPa (32,110 lb/in.^{2}) at 1000°C (1832°F), 200.43 MPa (29,070 lb/in.^{2}) at 1100°C (2012°F), and 238.28 MPa (34,560 lb/in.^{2}) at 1200°C (2192°F). The failure mechanism in the elevated temperature tests was observed to be a brittle fracture along the tensile surface with fiber pullout at the center of the specimens, shown in Figure 144.

Table XXXIII.
Elevated temperature strength of Corning BMAS-II composite material.

Temperature	Fracture strength—MPa (lb/in.^{2})	
	0/0 deg orientation	0/90 deg orientation
Room temperature	802.07 (116,330)	369.35 (53,570)
900°C (1652°F)	546.48 (79,260)	202.15 (29,320)
1000°C (1832°F)	—	221.39 (32,110)
1100°C (2012°F)	473.74 (68,710)	200.43 (29,070)
1200°C (2192°F)	—	238.28 (34,560)

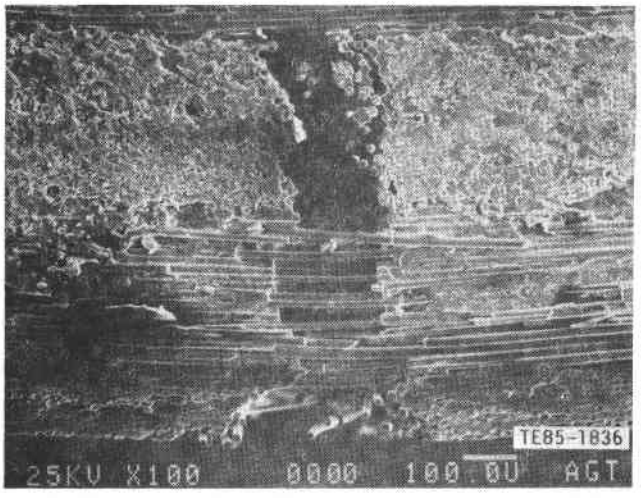

Figure 143. Fracture surface of Corning BMAS-II fiber-reinforced glass ceramic composite test bars with SiC fibers in 0/90 deg orientation; fracture mode consists of both brittle fracture and fiber pullout.

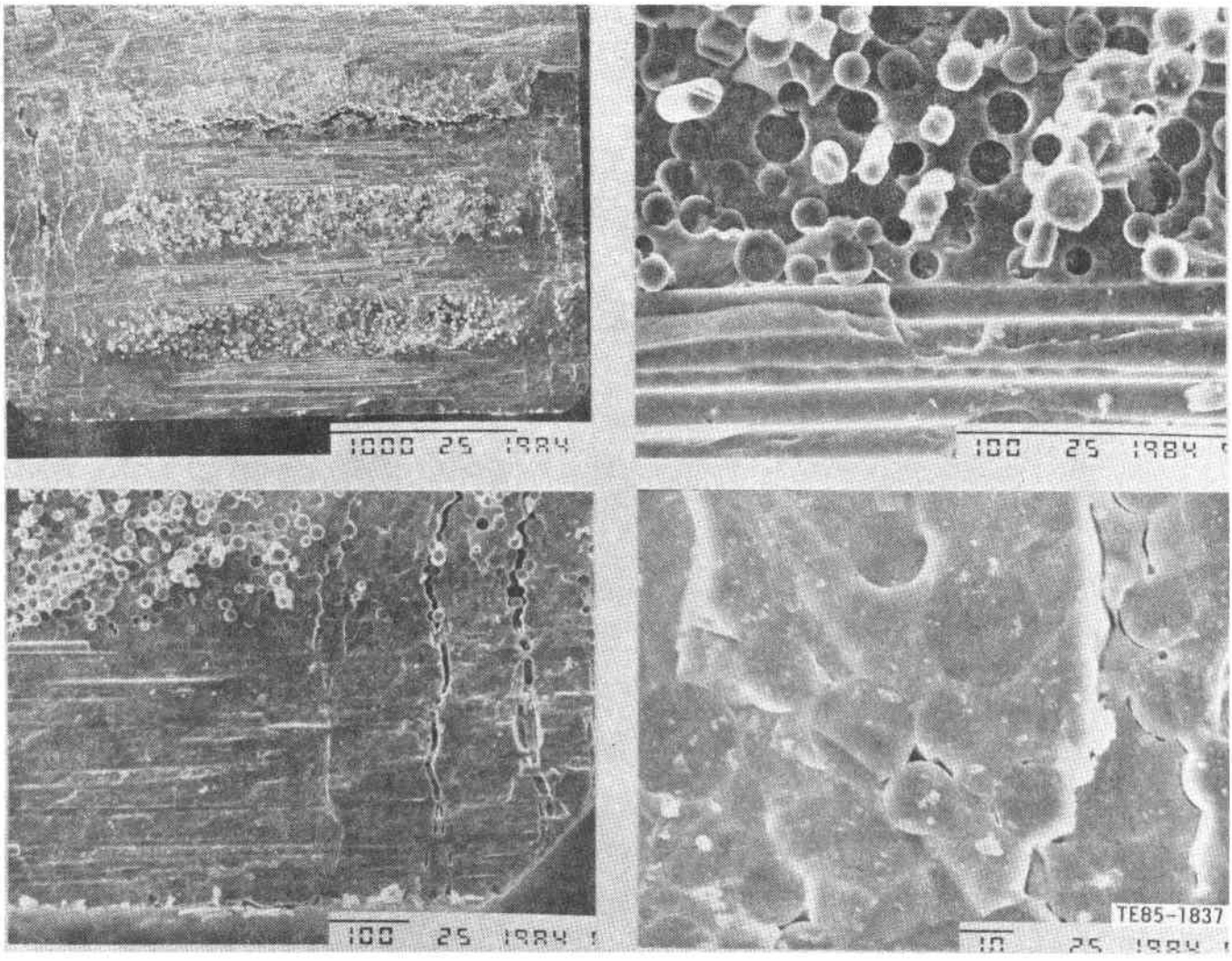

Figure 144. Typical fracture surfaces observed in Corning BMAS-II/SiC composite bars with 0/90 deg orientation tested at 900°C (1652°F).

X. CONTROLS DEVELOPMENT

10.1 IMPROVED FUEL SYSTEM

The improved fuel pump and metering valve were engine tested during the report period. This upgraded system proved less complicated and is suitable for continued engine operation. Elements of this system are discussed in the following paragaphs.

10.1.1 Fuel Pump

A small dc motor driven fuel pump replaces a skid-mounted workhorse pump. The pump is a miniature, lightweight, self-priming, hydraulically balanced positive displacement pump that uses a cammed-vane principle, shown in Figure 145, and is manufactured by Weldon Tool Company, Cleveland, Ohio. Figure 146 shows the performance characteristics that make the pump ideal for AGT 100 use.

10.1.2 Metering Valve

A direct metering valve replaced an indirect valve and provides the following advantages for AGT 100:

- less sensitivity to manifold volume and fuel nozzle pressure
- improved accuracy of burner variable geometry settings
- pilot flow independent from start/main flow

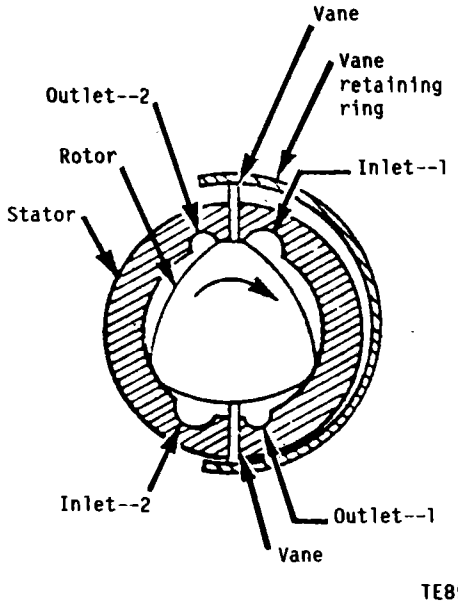

Figure 145. Fuel pump operating principle.

Independent pilot flow allows pilot fuel to be shut off for development testing without the complications required in the previous system. The design makes the calibration insensitive to pilot atomizing air pressure and corrects a failure mode where start/main fuel could have gone high if the pilot fuel nozzle were plugged. The operating principles of the old and new systems can be compared by referring to Figure 147.

Direct metering is accomplished in the start/main path by positioning a variable orifice, across which is held a constant differential pressure. Positioning is controlled by a proportional solenoid. Pilot metering is similar except the orifice is a two-stage fixed restriction controlled by a solenoid valve.

The indirect metering method was accomplished in the bypass path. In this case, a variable throttling (bypass) valve orifice was positioned by a torquemotor with a second in-line flow control valve for pilot metering. Pilot metering was also two-stage. In this design, if the pilot nozzle was completely plugged, the second in-line valve would close the bypass path, disallowing start/main flow modulation.

The new AGT 100 fuel valve is manufactured by South Bend Controls, South Bend, Indiana. Steady-state flow characteristics are shown in Figure 148 and frequency response is shown in Figure 149.

10.2 SOFTWARE CHANGES TO SUPPORT ENGINE TESTING

Software changes were made to the electronic control to be compatible with the new fuel metering

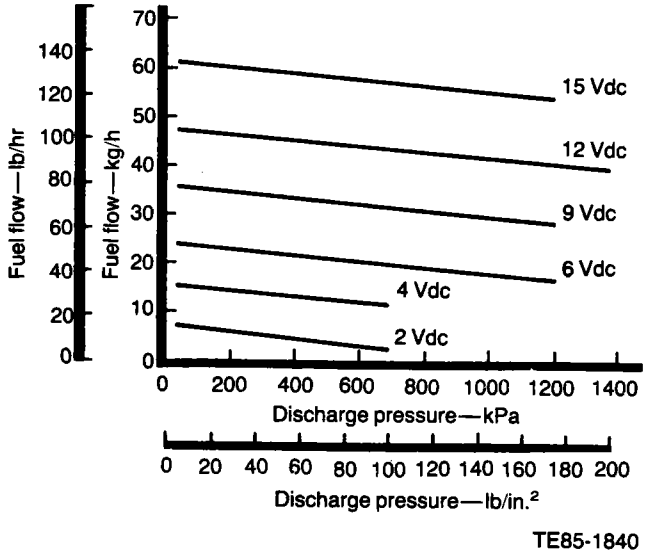

Figure 146. Fuel pump performance.

valve. Considerable simplification was permitted as a result of the direct metering principle. At the same time, the engine airflow curve was updated to improve the accuracy in calculating fuel/air ratio for positioning burner variable geometry.

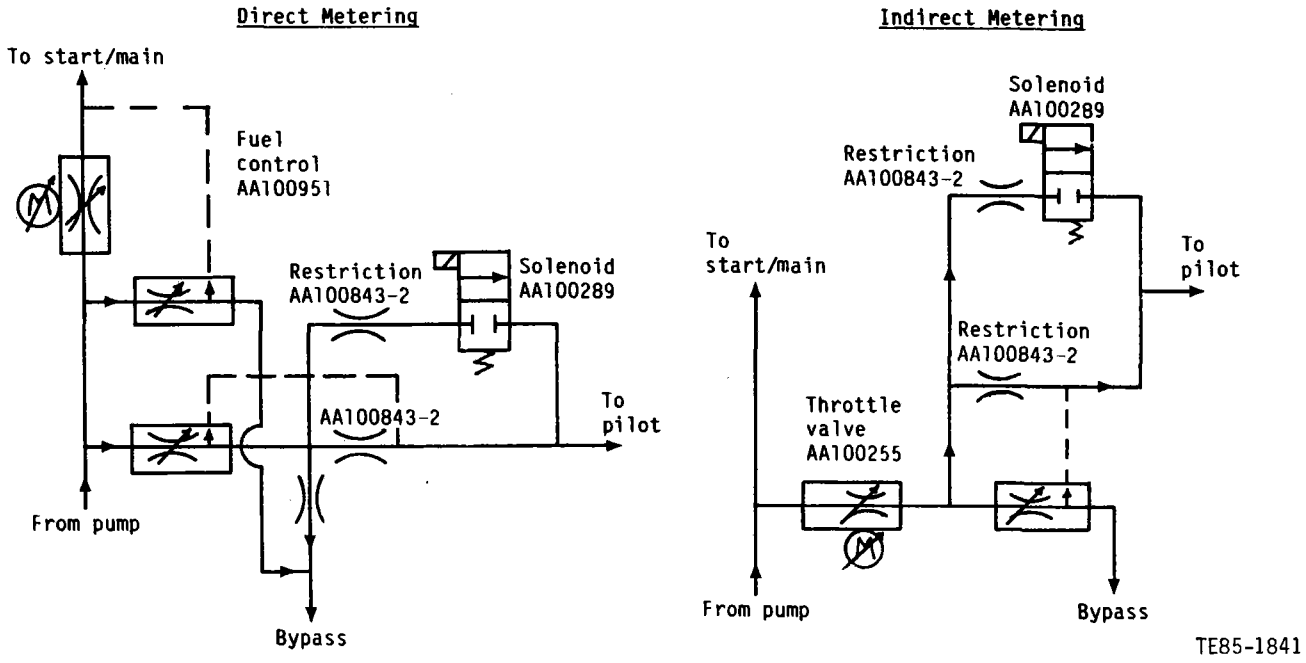

Figure 147. Fuel valve operating principle.

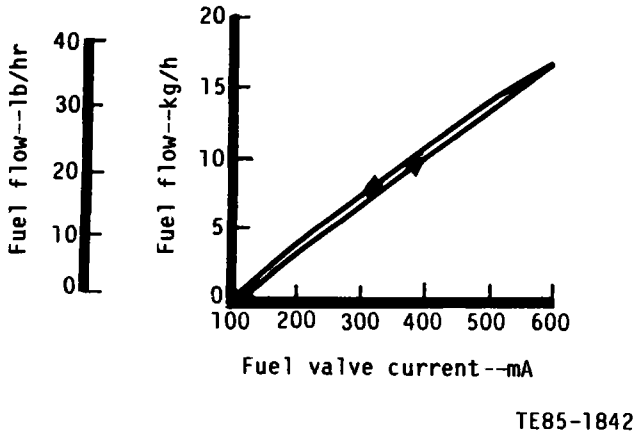

Figure 148. Fuel valve characteristics.

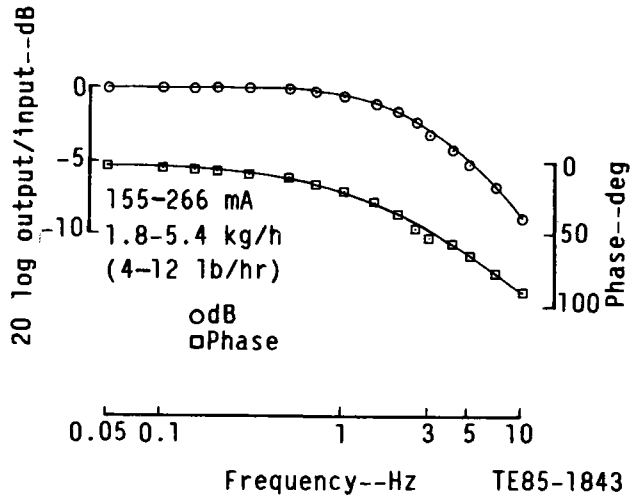

Figure 149. Fuel valve frequency response.

XII. SUPPORTIVE MANUFACTURING, COST, AND MARKETABILITY

12.1 MANUFACTURING FEASIBILITY

The effort at Pontiac during this reporting period was devoted to an experimental die development and parts fabrication program on the combustion case assembly. The objectives of this program were as follows:

- verify the manufacturing feasibility of the combustion case assembly incorporating design revisions as previously proposed and included in the manufacturing and cost analysis for the RPD engine
- determine the feasibility of using an expansion forming die process to produce the combustion case assembly on a high-volume production basis
- gain experience with the draw and forming characteristics of SAE 4130 steel
- gain experience regarding the downstream machining requirements based on the outcome of actual parts fabrication

The RPD design revisions proposed for the combustion case assembly included elimination of separate combustor support and mounting flange castings by including these formations in the sheet metal case (Ref: Fifth Semiannual AGT Report, Section XII). An expansion forming die process was proposed for the formation of these areas.

An experimental expansion forming die incorporating the proposed features was constructed, and a series of parts was made. During the die tryout program, the mounting flanges were successfully formed, but metal near the top surface of the combustor support area fractured before reaching the specified height. Various techniques tried during the die tryout program, including preforming the support area, did not alleviate the fracturing. The flow of metal during the forming process also resulted in deformation of surfaces adjacent to the support area.

The conclusions from this program were as follows:

- The depth of draw in the combustor support area with the existing design and material specification exceeds the capability of the expansion forming process.
- The mounting flanges can be formed by using either an expansion forming or a conventional roll forming process.
- The expansion forming process can be used for sizing and qualifying the concentricity of the inside diameter of the case.
- A conventional draw die program should be initiated to verify formability of the combustor support area.

The new program was initiated, and conventional draw die tooling to verify formability of the case combustor support area was under construction at the end of this reporting period.

APPENDIX A. TERMS AND DEFINITIONS

A-body	a class or size of General Motors automobile body
AGT	advanced gas turbine
AGT 100	the AGT model being developed by Allison
AREQ	equivalent area ratio
AS	aluminum silicate
BIP	burner inlet pressure
BIT	burner inlet temperature
BU	buildup number
BVG	burner variable geometry
C	damping coefficient
°C	degrees Centigrade
CATE	Ceramic Applications in Turbine Engines Program
CBO	Carborundum Company
BDT	compressor discharge temperature
CGW	Corning Glass Works
cm	centimeter
CO_2	carbon dioxide
cpm	cycles per minute
CTE	coefficient of thermal expansion or cyclic thermal evaluation
CY	calendar year
DF-2	diesel fuel number 2
DOE	U.S. Department of Energy
E	Young's modulus
ECR	engine configuration rotor
ECU	electronic control unit
EDR	Allison Engineering Report
EMI	electromagnetic inspection
EMTL	Energy Materials Testing Laboratory
°F	degrees Fahrenheit
f/a	fuel-to-air ratio
FPI	fluorescent penetrant inspection
ft	foot
GM	General Motors Corporation
GTE	General Telephone and Electronics Corporation
h or hr	hour
HIP	hot isostatically pressed
hp	horsepower
Hz	Hertz
I/B	inboard
i.d.	inside diameter
IGV	inlet guide vane
in.	inch
kg	kilogram
km	kilometer
kPa	kilopascal
ksi	thousands of pounds per square inch
kW	kilowatt
L	liter
LAS	lithium aluminum silicate
lb	pound
lbm	pound mass
LBO	lean blowout
m	meter
mA	milliampere
Metnet	a foamed metal later filled with wearface material
MAS	magnesium aluminum silicate
mg	milligram
mil	one thousandth of an inch
min	minutes
mm	millimeter
MOR	modulus of rupture
MPa	megapascal
m_s	Weibull modulus based on surface characteristics
m_v	Weibull modulus based on volume characteristics
mpg	miles per gallon
N	force (Newton) or speed or rotation (rpm)
N_1	gasifier speed of rotation
N_2	power turbine speed of rotation
NASA	National Aeronautics and Space Administration
NDE	nondestructive evaluation
NGK	ceramics manufacturing company in Japan
O/B	outboard
o.d.	outside diameter
P	probability of survival
PMD	Pontiac Motor Division of General Motors
P_s	probability of survival based on surface characteristics
psig	pounds per square inch gage
P_t	total probability of survival
P_v	probability of survival based on volume characteristics
RBSiC	reaction-bonded silicon carbide
Ref	reference
RFB	rich flashback
RIT	rotor inlet temperature
RPD	reference power-train design
rpm	revolutions per minute
RT	room temperature
RTV	room temperature vulcanizing
s or sec	second

SAE 4130	low alloy, medium strength steel
S/N	serial number
S/N 1	first experimental AGT 100 engine
S/N 2	second experimental AGT 100 engine
SiC	silicon carbide
Si_3N_4	silicon nitride
SS	steady state
T/C	thermocouple
TD	teardown
T-I	Tri Industries Incorporated
TIT	turbine inlet temperature
TMOR	tangential modulus of rupture
TOT	turbine outlet temperature

v	volt
Δ	difference between two measurements, e.g., temperature or pressure
ηR	regenerator effectiveness
μ	coefficient of friction
μm	micrometer ("micron")
σ	stress
σ_o	Weibull characteristic strength
σ_{os}	Weibull characteristic strength — surface flaw strength distribution
σ_{ov}	Weibull characteristic strength — volume flaw strength distribution

1. Report No.	2. Government Accession No.	3. Recipient's Catalog No.
NASA CR-175018		

4. Title and Subtitle	5. Report Date
ADVANCED GAS TURBINE (AGT) TECHNOLOGY PROJECT	June 1985
	6. Performing Organization Code

7. Author(s)	8. Performing Organization Report No.
Engineering Department, Allison Gas Turbine Division	EDR 12070
	10. Work Unit No.

9. Performing Organization Name and Address	11. Contract or Grant No.
Allison Gas Turbine Division of General Motors Corporation P.O. Box 420 Indianapolis, IN 46206-0420	DEN 3-168
	13. Type of Report and Period Covered Contractor Report January-December 1984

12. Sponsoring Agency Name and Address	14. Sponsoring Agency Code
U.S. Department of Energy Office of Vehicle and Engine Research Development Washington, D.C. 20545	DOE/NASA

15. Supplementary Notes

Annual report, prepared under Interagency Agreement DE-AI01-77CS51040.
Project Manager P. T. Kerwin, Transportation Propulsion Division,
NASA Lewis Research Center, Cleveland, OH 44135

16. Abstract Engine testing, ceramic component fabrication and evaluation, component performance rig testing, and producibility experiments at Pontiac comprised AGT 100 activities of this period, January-December 1984. Two experimental engines were available and allowed the evaluation of eight experimental assemblies. Operating time accumulated was 115 hr of burning and 156 hr total. Total cumulative engine operating time is now 225 hr. Build number 11 and 12 of engine S/N 1 totaled 28 burning hours and constituted a single assembly of the engine core--the compressor, both turbines, and the gearbox. Build number 11 of engine S/N 1 included a 1:07 hr continuous test at 100% gasifier speed (86,000 rpm). Build number 8 of engine S/N 2 was the first engine test with a ceramic turbine rotor. A mechanical loss test of an engine assembly revealed the actual losses to be near the original design allowance. Component development activity included rig testing of the compressor, combustor, and regenerator. Compressor testing was initiated on a rig modified to control the transfer of heat between flow path, lubricating oil, and structure. Results show successful thermal decoupling of the rig and lubricating/cooling oil. Rig evaluation of a reduced-friction compressor was initiated. Combustor testing covered qualification of ceramic parts for engine use, mapping of operating range limits, and evaluation of a relocated igniter plug. Several seal refinements were tested on the hot regenerator rig. An alternate regenerator disk, extruded MAS, was examined and found to be currently inadequate for the AGT 100 application. Also, a new technique for measuring leakage was explored on the regenerator rig. Ceramic component activity has focused on the development of state-of-the-art material strength characteristics in full-scale hardware. Injection-molded sintered alpha-SiC rotors were produced at Carborundum in an extensive process and tool optimization study. Correlation of spin-to-burst rotor tests with fracture surface analyses revealed that backface flow and knit-line indications were the frequent cause of rotor bursts at relatively low speeds. A modified fabrication/rework procedure, for both green and sintered rotors, was identified whereby these surface imperfections may be removed. The exploration of injection molded GTE Si_3N_4 rotors included evaluation of 10 hot isostatically pressed (HIP) rotors. Burst testing demonstrated that HIP processing raised burst speed. Gasifier turbine scroll assemblies, in SiC material, are being fabricated by both Carborundum and Norton. Carborundum units are awaiting hot-rig test; engine test will follow successful rig testing. Fiber reinforced glass-ceramic composite turbine backplates were fabricated by the Corning Glass Works. Different materials were considered, and evaluation was initiated with room temperature bend testing of test bars.

17. Key Words (Suggested by Author(s))	18. Distribution Statement
Automotive gas turbine Ceramic components Engine configuration rotors Alternate propulsion systems Improved fuel economy	

19. Security Classif. (of this report)	20. Security Classif. (of this page)	21. No. of Pages	22. Price*
Unclassified	Unclassified	268	

* For sale by the National Technical Information Service, Springfield, Virginia 22151